Determination of gluon polarisation in the nucleon from events with high-pT hadron pairs in COMPASS experiment

Konrad Klimaszewski
Department of High-Energy Physics
Soltan Institute for Nuclear Studies
Świerk-Otwock

Submitted in partial fulfillment
of the requirements for the degree of
Doctor of Philosophy in Physics

Supervised by prof. dr hab. Jan Paweł Nassalski[†]
and doc. dr hab. Andrzej Sandacz

Warsaw, 1st June 2010

[†]Deceased

In memory of Professor Jan Paweł Nassalski.

Great Scholar, Great Tutor.

Abstract

The main goal of the COMPASS experiment at CERN is the determination of the gluon spin contribution to the nucleon spin. It is measured using cross section spin asymmetries in Deep Inelastic Scattering of polarised muons off polarised nucleons. The COMPASS uses polarised muon beam of $160\,$GeV energy and a polarised ^{6}LiD target. The gluons in the nucleon are accessed through a Photon Gluon Fusion process which is tagged by two signatures: an open charm production and pairs of hadrons with high transverse momenta. In this thesis we present the latter analysis performed for the $Q^2 > 1\,\text{GeV}^2$ region and based on the data collected during 2002-2004 years. A novel method of $\Delta G/G$ extraction based on Neural Networks is discussed. The result $\Delta G/G = 0.08 \pm 0.1(stat.) \pm 0.05(syst.)$ is consistent with zero within the measurement uncertainty. It is compatible with other lepton-nucleon scattering results (COMPASS, SMC, HERMES) and with results from the proton-proton interactions (STAR, PHENIX). The obtained result is currently one of the two most precise direct measurements of the gluon polarisation.

Contents

Chapter 1

Introduction

The concept of intrinsic angular momentum called spin, which emerged in the twenties, have a profound impact on our understanding of the design of Nature. After it was demonstrated in late sixties in Deep Inelastic Scattering (DIS) of the electrons on the nucleons at SLAC [1] that the nucleon is a composite object, a following intriguing question became legitimate. Is it possible to explain the nucleon spin, a quantised entity measured to be[1] $1/2$, in terms of its partonic components, quarks and gluons?

In the frame of the QCD improved parton model the spin of the nucleon can be decomposed into the contributions of the quark spins $(\Delta\Sigma)$, the gluon spins (ΔG) and the orbital angular momentum of the partons in the nucleon $(L_{q,g})$. This is expressed by a sum rule:

$$\frac{1}{2} = \frac{1}{2}\Delta\Sigma + \Delta G + L_{q,g}.$$

From theoretical considerations that include relativistic effects we expect the $\Delta\Sigma$ to be ~ 0.6.

In another SLAC experiment [2] performed a decade after the first DIS experiment, this time with deep inelastic scattering of both the polarised electrons and protons, sizable cross section spin asymmetries were observed in a kinematic region, where valence quarks dominate. Thus it was demonstrated that polarised DIS is a powerful tool to study the spin structure of the nucleon. However, it was only after another decade when the EMC experiment at CERN, covering significantly larger kinematic range than experiments at SLAC, discovered that the quark contribution is much smaller than expected [3, 4]. This puzzle, named the "Spin Crisis of the nucleon", became and still is an intriguing issue.

The findings of the EMC experiment were confirmed by the SMC at CERN [5], the SLAC experiments [6, 7] and the HERMES [8]. Currently the quark contribution is known quite precisely and according to one of the recent global analysis it is $\Delta\Sigma = 0.30 \pm 0.01 \pm 0.02$ [9]. Thus the quark contribution is well below theoretical predictions and is not sufficient to explain alone the nucleon spin.

To further our knowledge of the nucleon structure it is crucial to measure the contributions of the gluon spins and the orbital angular momentum of partons. The gluon contribution can be estimated from the evolution of measured g_1 structure function with virtuality Q^2. Unfortunately even the most recent results have large uncertainties: $|\Delta G| = 0.2 \div 0.3$ with both negative and positive values allowed. Therefore a direct measurement of the gluon contribution is required.

An unique possibility for such measurement lies in Deep Inelastic Scattering of polarised leptons on polarised nucleons with selection of hadrons in the final state. There, in the Photon Gluon Fusion (PGF)

[1] Throughout this thesis $\hbar = c = 1$ is assumed.

process the virtual photon is used to probe the gluons in the nucleon. Therefore we can directly measure the spin dependent gluon distribution. Such measurement is the main goal of the COMPASS experiment, a successor of the SMC and EMC experiments.

Two methods are used to select events that originate from PGF. In the first one we ask for a charmed meson in the final state. As the charmed quark in LO QCD can be produced only via the PGF process, this ensures that obtained sample is clean from background processes. However due to a significant combinatorial background and a small cross-section the precision of this measurement is limited. The results of this analysis have been published in Ref. [10].

In the second approach we search for two hadrons of high transverse momentum in the final state. Such analysis performed for $Q^2 > 1\,\mathrm{GeV}^2$ kinematic region is the topic of this thesis. In this case we consider production of light quarks and as such the contribution of other processes besides PGF cannot be neglected. They have to be taken into account relying on Monte Carlo simulations. However, the available statistical precision is significantly larger than in the open-charm case.

Third analysis was performed in COMPASS for the same channel but for the $Q^2 < 1\,\mathrm{GeV}^2$. The results are published in Ref. [11]. This analysis allows to collect enormous amount of events at cost of increased theoretical uncertainty. Therefore the three analyses should be considered as complementary.

In the analysis performed as a topic of this thesis a new method of background processes treatment based on the neural networks approach is proposed. As opposed to the analysis performed by the SMC [12] the neural network is not used to select a sample enriched in PGF events. Instead it is used to estimate the probability for an event to originate from PGF or one of the background processes which then enables us to build a weight of the event. Such weighted method allows us a precise treatment of the background processes contributions to the measured asymmetry as well as increases the statistical precision of the measurement.

Structure of the thesis

The thesis consists of twelve chapters. After *Introduction,* in Chapter 2 the theoretical description of polarised Deep Inelastic Scattering of leptons on nucleons is presented, followed by discussion of the structure of the nucleon in the frame of the Parton Model. Afterwards the QCD formalism describing the nucleon structure is introduced. The theoretical introduction is followed by an overview of the status of current experimental results for the gluon polarisation in the nucleon presented in Chapter 3. Chapter 4 describes the COMPASS experiment, in particular the polarised muon beam, the polarised target and the spectrometer. Chapters 5 and 6 focus on the description of the muon beam momentum reconstruction and on the precise determination of the positions of all the detectors of the spectrometer. The author was actively participating in the implementation of both of these technical tasks, which are crucial for all analyses performed at COMPASS. In Chapter 7 details of the ΔG extraction are presented. First and foremost the motivation behind the selection of events with a pair of high p_T hadrons is provided. Then various methods of the spin asymmetry determination as well as extraction of the ΔG from measured asymmetry are described. Finally the details of event selection are discussed. As the ΔG extraction depends on MC simulations a detailed study of the description of experimental data by the MC simulations is presented in Chapter 8. The novel method of the neural networks application and the basic introduction into the topic are discussed in Chapter 9. Chapter 10 gives an overview of studies performed to determine systematic uncertainties due to the experimental setup, MC simulations and neural networks. Finally the Chapter 11 presents the obtained value of $\Delta G/G$ in

comparison to world results. The performed work and its results are summarised in Chapter 12.

Responsibilities of the author[2] in the COMPASS experiment and the analysis of the data

The contributions of the author to the COMPASS experiment are twofold. It comprises task providing tools for a common use with an impact on all COMPASS analyses of the data, and also tasks oriented towards extraction of ΔG.

The author was responsible for the extension of the beam momentum reconstruction algorithm to include the information from a newly build, additional detector plane, as well as for the validation of the beam momentum reconstruction performance. The results of this work are summarised in Chapter 5.

Also the author was responsible for the *alignment* of the COMPASS spectrometer during 2005-2006 years and a part of 2008. The alignment of the detector planes is crucial for proper reconstruction of tracks of charged particles. The alignment procedure and the illustration of results of author's work on the alignment are presented in Chapter 6.

The analysis of the experimental data to extract the ΔG required several specific technical tasks to be carried out by the author. These included:

1. Modification of the asymmetry calculation program to extract asymmetries using second order weighted method and the implementation of the neural networks for extraction of ΔG.
2. Implementation of basic features of the COMPASS spectrometer acceptance in LEPTO generator, for quick studies of the acceptance.
3. Implementation of the Radiative Correction tables into the COMPASS MC simulations.
4. Inclusion of the RAPGAP generator into the MC generator abstraction layer used at COMPASS.
5. Determination of the efficiencies of the trigger hodoscope planes and their application in the MC simulations.
6. Modification and installation of the COMPASS analysis software to be used at the LHC Computing Grid.

[2]Konrad.Klimaszewski@fuw.edu.pl

Chapter 2

Theoretical framework

2.1 Deep Inelastic Scattering

2.1.1 Kinematic variables

In inelastic scattering of the point-like lepton l off a nucleon N, the nucleon brakes up

$$l + N \rightarrow l' + X, \tag{2.1}$$

where X denotes the final hadronic state. The schematic representation of the process is shown in Fig. 2.1. To describe the kinematics of the process two independent variables are needed, *e.g.* the energy E' of scattered lepton and the scattering angle θ. However usually two independent Lorentz invariants are used

$$\nu = \frac{P \cdot q}{M} \overset{lab}{=} E - E', \tag{2.2}$$

$$Q^2 = -q^2 = -(k - k')^2 \overset{lab}{\simeq} 4EE' sin^2 \frac{\theta}{2}, \tag{2.3}$$

where $P = (M, \vec{0})$ is the four-momentum of the initial nucleon at rest and M is the nucleon mass, $q = (\nu, \vec{q})$ denotes the four-momentum of the exchanged virtual photon. The four-momenta of incoming and outgoing leptons are denoted by $k = (E, \vec{k})$ and $k' = (E', \vec{k'})$ respectively. The variable ν defined by Eq. 2.2 is the virtual photon energy in the laboratory system. The quantity $q^2 (= -Q^2)$ defined by Eq. 2.3 is the squared mass of the virtual photon. In the approximation for the last term of Eq. 2.3 the lepton mass is neglected.

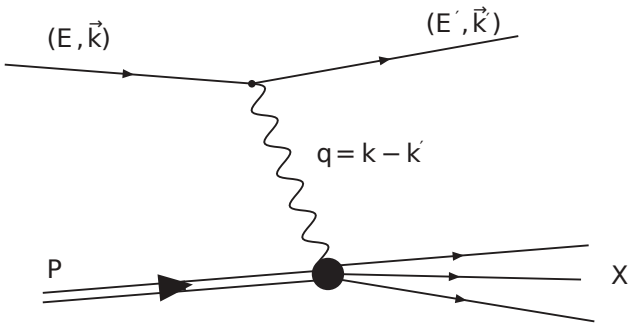

Figure 2.1: Schematic representation of the DIS process.

In addition to ν and Q^2, the dimensionless scaling variables x and y are defined

$$x = \frac{Q^2}{2P \cdot q} = \frac{Q^2}{2M\nu}, \tag{2.4}$$

$$y = \frac{P \cdot q}{P \cdot k} \overset{lab}{=} \frac{\nu}{E}. \tag{2.5}$$

The variable x is known as the Bjorken scaling variable. It has a clear physics interpretation within the Quark Parton Model (see Sec. 2.2.1). In the frame of the infinite nucleon momentum x corresponds to the fraction of the nucleon momentum carried by the struck quark. The variable y is a fraction of the incoming lepton's energy transferred to the nucleon in the laboratory frame.

Another quantity used to describe the scattering, is the invariant mass W of the final hadronic state X

$$W^2 = (P+q)^2 = M^2 + \frac{Q^2}{x} - Q^2 = M^2 + 2M\nu - Q^2. \tag{2.6}$$

The kinematic region where $W^2 \gg M^2$ and $\nu \gg M$ is referred as inelastic region of the lepton-nucleon scattering. While the Deep Inelastic Scattering (DIS) region is defined by the condition $Q^2 > 1\,\text{GeV}^2$.

2.1.2 Lepton-nucleon scattering cross section

The differential cross section for lepton-nucleon scattering, where the scattered lepton has an energy between E' and $E' + dE'$ and is found in the solid angle $d\Omega$, can be written in general form as [13]

$$\frac{d^2\sigma}{dE'd\Omega} = \frac{\alpha^2}{Q^4}\frac{E'}{ME} L_{\mu\nu} W^{\mu\nu}, \tag{2.7}$$

where $L_{\mu\nu}$ is the leptonic tensor, $W^{\mu\nu}$ the hadronic tensor and $\alpha = e^2/4\pi$ is the electromagnetic fine-structure constant (for a detailed derivation of Eq. 2.7 see [14, 15]). The leptonic tensor $L_{\mu\nu}$ describes the emission of a virtual photon by a lepton of mass m and spin s

$$L_{\mu\nu}(k, s, k', s') = \bar{u}(k', s')\gamma_\mu u(k, s)\bar{u}(k, s)\gamma_\nu u(k', s'), \tag{2.8}$$

where u, $\bar{u}$ are Dirac spinors, s (s') is the incoming (outgoing) lepton spin four-vector, such that it is orthogonal to its momentum $s \cdot k = 0$ ($s' \cdot k' = 0$) and satisfying $s^2 = -1$ ($s'^2 = -1$). For the incoming leptons polarised along their momentum direction this leads to $s \overset{lab}{=} h_l \frac{1}{m}(E, \left|\vec{k}\right|, 0, 0)$, where $h_l = \pm 1$ is the lepton helicity. The $L_{\mu\nu}$ tensor can be exactly calculated in QED. The expression for $L_{\mu\nu}$ is usually decomposed in parts which are symmetric and antisymmetric under exchange of $\mu\nu$ indices

$$L^{\mu\nu} = L^{\mu\nu}_{(S)} + iL^{\mu\nu}_{(A)}, \tag{2.9}$$

where

$$L^{\mu\nu}_{(S)} = 2k'^\mu k^\nu + 2k'^\nu k^\mu + 2(m^2 - k' \cdot k)g^{\mu\nu}, \tag{2.9a}$$

$$L^{\mu\nu}_{(A)} = 2m\epsilon^{\mu\nu\rho\sigma} q_\rho s_\sigma. \tag{2.9b}$$

Here, the $g^{\mu\nu}$ is the symmetric metric tensor and $\epsilon^{\mu\nu\rho\sigma}$ is the antisymmetric Levi-Civita tensor.

The hadronic tensor $W^{\mu\nu}$ contains the information on the internal structure of the nucleon and is defined by

$$W^{\mu\nu} \cong \left\langle P, S \left| j_\mu j_\nu^+ \right| P, S \right\rangle, \tag{2.10}$$

where S stands for the spin four-vector of the nucleon with momentum P and satisfies $S \cdot p = 0$ and $S^2 = -1$. Since the nucleon is at rest so it may be polarised in an arbitrary direction $S \overset{lab}{=} (0, sin\alpha\, cos\beta, sin\alpha\, sin\beta, cos\alpha)$. The β is the azimuthal angle and α is the polar angle as shown in Fig. 2.2. Using the translation, parity and time reversal invariance, the completeness of states and the current conservation, the most general form of the hadronic tensor for DIS reads

$$W^{\mu\nu} = W^{\mu\nu}_{(s)} + iW^{\mu\nu}_{(A)}, \tag{2.11}$$

where

$$W^{\mu\nu}_{(S)} = 2F_1 \left(-g_{\mu\nu} + \frac{q_\mu q_\nu}{2}\right) + \frac{2F_2}{P \cdot q} \left(P_\mu - \frac{P \cdot q}{q^2} q_\mu\right) \left(P_\nu - \frac{P \cdot q}{q^2} q_\nu\right), \tag{2.11a}$$

$$W^{\mu\nu}_{(A)} = \frac{2Mg_1}{P \cdot q} \epsilon_{\mu\nu\lambda\sigma} q^\lambda S^\sigma + \frac{2Mg_2}{(P \cdot q)^2} \epsilon_{\mu\nu\lambda\sigma} q^\lambda \left((P \cdot q)\, S^\sigma - (s \cdot q)\, P^\sigma\right). \tag{2.11b}$$

In addition, the conservation of the lepton current ($q^\mu L_{\mu\nu} = 0$) simplifies the structure of the $W^{\mu\nu}$ tensor (all terms proportional to q_μ, q_ν give zero contribution). The functions F_1, F_2 in Eq. 2.11a and g_1, g_2 in Eq. 2.11b are the structure functions of the nucleon which are determined in experiments and are usually described as functions of x and Q^2.

The differential cross section for the polarised inelastic lepton-nucleon scattering can be written in terms of spin-averaged cross section $\bar{\sigma}$ and the spin-dependent cross section $\Delta\sigma$. The symmetric terms $W^{\mu\nu}_{(S)}$ and $L^{\mu\nu}_{(S)}$ do not depend on the polarisations of the nucleon and the incoming muon. Therefore they contribute to the spin-averaged cross section. Thus the functions F_1 and F_2 are called the unpolarised structure functions. Only the antisymmetric terms $W^{\mu\nu}_{(A)}$ and $L^{\mu\nu}_{(A)}$ depend on polarisations of the initial muon and the nucleon and they make up the spin dependent part of the cross section. Hence the g_1 and g_2 are called the spin dependent structure functions. After the contraction of the $L_{\mu\nu}W^{\mu\nu}$ tensor the formula for the cross section (Eq. 2.7) can be decomposed into a sum of two terms, the first one proportional to $L^{(S)}_{\mu\nu}W^{\mu\nu}_{(S)}$ and the other proportional to $L^{(A)}_{\mu\nu}W^{\mu\nu}_{(A)}$. The interference terms equal to zero due to parity conservation. The differential cross section can be rewritten as

$$\frac{d^3\sigma}{dxdQ^2d\phi} = \frac{d^3\bar{\sigma}}{dxdQ^2d\phi} - \frac{1}{2}h_l \frac{d^3\Delta\sigma}{dxdQ^2d\phi} \tag{2.12}$$

where the first part is independent of the spin orientations of the interacting particles while the second part depends on the relative spin orientation of the target and of the projectile. Therefore to measure the antisymmetric tensor elements, both the beam and the target have to be polarised.

Considering the parallel ($\parallel$) or perpendicular ($\perp$) spin configuration of the nucleon with respect to incoming muon we have

$$\sigma = \bar{\sigma} - \frac{1}{2}h_l\, \Delta\sigma = \bar{\sigma} - \frac{1}{2}h_l(cos\alpha\, \Delta\sigma_\parallel + sin\alpha\, cos\phi\, \Delta\sigma_\perp), \tag{2.13}$$

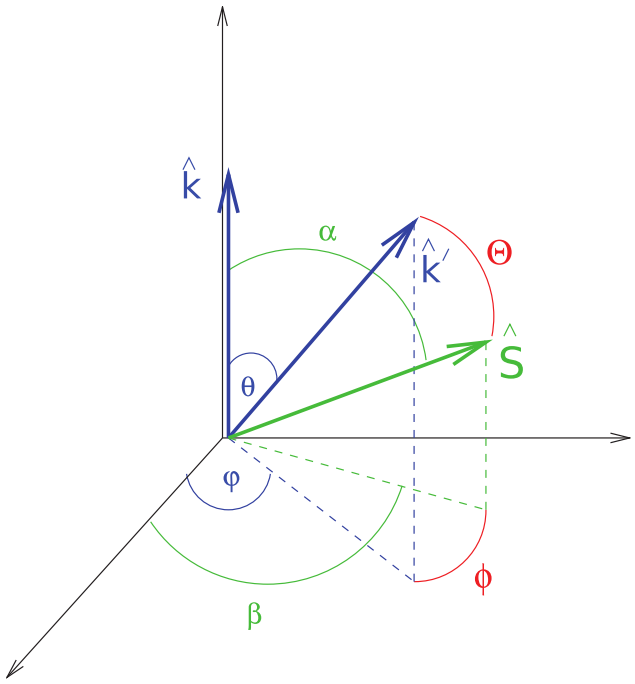

Figure 2.2: Definitions of angles α, β, ϕ used for decomposition of spin-dependent cross section.

where

$$\bar{\sigma} \equiv \frac{d^3\bar{\sigma}}{dxdQ^2d\phi} = \frac{e^4y}{4\pi^2Q^4}\left[\frac{y}{2}(1-\frac{2m^2}{Q^2})F_1 + \frac{1}{2xy}\left(1-y-\frac{\gamma^2y^2}{4}\right)F_2\right], \tag{2.13a}$$

$$\Delta\sigma_{\parallel} \equiv \frac{d^3\Delta\sigma_{\parallel}}{dxdQ^2d\phi} = \frac{e^4y}{4\pi^2Q^4}\left[\left(2-y-\frac{\gamma^2y^2}{2}\right)g_1 - \gamma^2 y g_2\right], \tag{2.13b}$$

$$cos\phi\Delta\sigma_{\perp} \equiv \frac{d^3\Delta\sigma_{\perp}}{dxdQ^2d\phi} = cos\phi\frac{e^4y}{4\pi^2Q^4}\gamma\sqrt{\left(1-y-\frac{\gamma^2y^2}{4}\right)}(yg_1+2g_2). \tag{2.13c}$$

Here $\gamma^2 = \frac{4M^2x^2}{Q^2} = \frac{Q^2}{\nu^2}$ is the kinematic factor, which is very small, $\sim 10^{-3}$, in COMPASS kinematic region. The definitions of angles used in the above equations are presented in Fig. 2.2. The angle α $(0 \leq \alpha \leq \pi)$ is between the incident lepton momentum k and the target spin S while ϕ $(0 \leq \phi \leq 2\pi)$ is the angle between the scattering plane and the plane defined by the target spin and incident lepton momentum. The spin dependent cross sections $\Delta\sigma_{\parallel}$ and $\Delta\sigma_{\perp}$, given by Eq. 2.13b and Eq. 2.13c, refer to the configuration with muon spin parallel ($\parallel$) and perpendicular ($\perp$) to the spin of the nucleon. For the longitudinal target polarisation, the main contribution to $\Delta\sigma_{\parallel}$ is related to the structure function g_1, because the g_2 is suppressed by the small factor γ^2. For the transverse target polarisation both g_1 and g_2 structure functions contribute to $\Delta\sigma_{\perp}$ with similar weights. For a discussion of the presented decomposition and relations between the cross section and structure functions see *e.g.* Ref. [13].

2.1.3 Spin asymmetries of cross sections

In order to determine the structure functions g_1 and g_2, experiments with polarised beam and polarised target are required. To separate the polarised structure functions from the unpolarised functions F_1 and F_2, one measures difference of cross sections with different beam and target polarisations as F_1 and F_2 cancel out in the difference.

In experiments it is more convenient to measure asymmetries than differences of cross sections. The longitudinal double spin asymmetry for the beam ($\rightarrow$) and target ($\Rightarrow$) spins anti-parallel and parallel is

$$A_{LL} = \frac{\sigma^{\rightleftarrows} - \sigma^{\rightrightarrows}}{\sigma^{\rightleftarrows} + \sigma^{\rightrightarrows}} \tag{2.14}$$

and the transverse asymmetry is

$$A_T = \frac{\sigma^{\rightarrow\Downarrow} - \sigma^{\rightarrow\Uparrow}}{\sigma^{\rightarrow\Downarrow} + \sigma^{\rightarrow\Uparrow}}. \tag{2.15}$$

The A_{LL} and A_T asymmetries are measured in COMPASS by reversing the polarisation direction of a longitudinally or transversely polarised target, whereas the beam polarisation is fixed and is defined by the beam kinematics as explained in Sec. 4.2.

The interesting physics quantities are the virtual photon cross section asymmetries

$$A_1 = \frac{\sigma_{1/2} - \sigma_{3/2}}{\sigma_{1/2} + \sigma_{3/2}}, \tag{2.16}$$

$$A_2 = \frac{2\sigma_{TL}}{\sigma_{1/2} + \sigma_{3/2}}, \tag{2.17}$$

where $\sigma_{1/2}$ and $\sigma_{3/2}$ are the virtual photon nucleon cross sections with the projection of the total angular momentum of the photon-nucleon system along the incident lepton direction equal to 1/2 and 3/2, respectively. The σ_{LT} is an interference term between transverse and longitudinal amplitudes . Measurements of A_1 and A_2 allow a determination of the structure functions g_1 and g_2 using the relations

$$A_1 = (g_1 - \gamma^2 g_2)/F_1, \tag{2.18}$$

$$A_2 = \gamma(g_1 + g_2)/F_1. \tag{2.19}$$

The measured lepton asymmetries are related to the virtual photon asymmetries by

$$A_{LL} = D(A_1 + \eta A_2), \tag{2.20}$$

$$A_T = d(A_2 - \xi A_1), \tag{2.21}$$

with the kinematic factors

$$D = \frac{y(1+\gamma^2 y/2)(2-y)}{y^2(1+\gamma^2) + 2(1-y-\gamma^2 y^2/4)(1+R)}, \tag{2.22}$$

$$\eta = \frac{\gamma(1-y-\gamma^2 y^2/4)}{(1+\gamma^2 y/2)(1-y/2)}, \tag{2.23}$$

$$d = \frac{\sqrt{1-y-\gamma^2 y^2/4}}{1-y/2} D, \tag{2.24}$$

$$\xi = \frac{\gamma(1-y/2)}{1+\gamma^2 y/2}. \tag{2.25}$$

The factor D can be regarded as the depolarisation factor of the virtual photon and it describes the fraction of the longitudinal beam polarisation transferred to the virtual photon. The quantity $R = \sigma_L/\sigma_T$ is the ratio of the longitudinal to transverse virtual photon absorption cross sections, which can be expressed in terms

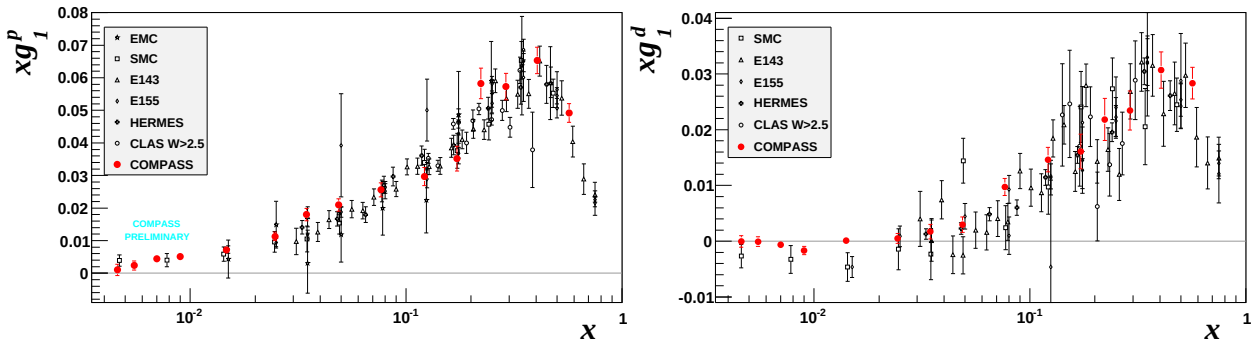

Figure 2.3: The spin dependent structure function $xg_1(x)$ of the proton and the deuteron measured in deep inelastic scattering of electrons/positrons (E143, E155, HERMES, CLAS) and muons (EMC, SMC, COMPASS).

of the structure functions F_1 and F_2 by

$$R = \frac{F_2}{2xF_1}(1+\gamma^2) - 1. \tag{2.26}$$

The factor D vanishes for $y = 0$ and to a good approximation it is equal to unity for $y = 1$. Therefore events with high y are the most sensitive to spin effects measured with longitudinally polarised beam and target. Since g_2 is suppressed by kinematic factor γ one can derive g_1 from a measurement of the longitudinal lepton asymmetry A_{LL} by

$$g_1(x) \approx \frac{F_1(x)}{1+\gamma^2}\frac{A_{LL}(x)}{D(y)}. \tag{2.27}$$

Results from different experiments on the structure function g_1 for the proton and the deuteron are shown in Fig. 2.3. The accuracy of $g_1(x)$ in the kinematic region of low x is clearly improved by a new measurements of the COMPASS collaboration [9, 16, 17].

2.2 Nucleon structure in the framework of QCD

2.2.1 Quark Parton Model

The Quark Parton Model [18, 19] (QPM) describes the nucleon as composed of point-like, almost free (not interacting) and massless partons. The charged partons have spin $1/2$ and they are naturally identified as quarks. The QPM is formulated in the infinite momentum frame where the target nucleon moves with $p_z \to \infty$. The partons are moving collinear with nucleon and their transverse momenta and masses can be neglected. Within the time scale of interaction with the virtual photon partons are assumed not to interact with each other, thus lepton-nucleon scattering is viewed as a scattering of virtual photons off free partons. The cross section for lepton-nucleon interaction can be therefore written as the incoherent sum of cross sections for virtual photon-quark scattering.

Assuming scattering off free massless spin $1/2$ partons inside nucleon, the hadronic tensor $W^{\mu\nu}$ can be

calculated and an expression for the structure functions reads

$$F_1(x) = \frac{1}{2}\sum_f e_f^2 \left[\left(q_f(x)^+ + q_f(x)^-\right) + \left(\bar{q}_f(x)^+ + \bar{q}_f(x)^-\right)\right] = \frac{1}{2}\sum_f e_f^2 \left(q_f(x) + \bar{q}_f(x)\right), \tag{2.28}$$

$$F_2(x) = x\sum_f e_f^2 \left[\left(q_f(x)^+ + q_f(x)^-\right) + \left(\bar{q}_f(x)^+ + \bar{q}_f(x)^-\right)\right] = x\sum_f e_f^2 \left(q_f(x) + \bar{q}_f(x)\right), \tag{2.29}$$

$$g_1(x) = \frac{1}{2}\sum_f e_f^2 \left[\left(q_f(x)^+ - q_f(x)^-\right) + \left(\bar{q}_f(x)^+ - \bar{q}_f(x)^-\right)\right] = \frac{1}{2}\sum_f e_f^2 \left(\Delta q_f(x) + \Delta\bar{q}_f(x)\right), \tag{2.30}$$

$$g_2(x) = 0, \tag{2.31}$$

where the $q_f(x)^{+(-)}$ refers to a quark distribution with its spin parallel (anti-parallel) to that of the target nucleon spin, e_f is the electric charge of a quark of flavour f. The quark distributions are interpreted as the density of probability to find a quark or antiquark with momentum fraction x and given flavor f inside nucleon.

From Eq. 2.28 and Eq. 2.29 we obtain the Callan-Gross relation

$$F_2(x) = 2xF_1(x). \tag{2.32}$$

Applying the above formula to Eq. 2.26 one finds $R(x) \simeq 0$ in the QPM, which expresses the fact that spin $1/2$ quarks can absorb transversely polarised virtual photons only. An important result of the QPM is that the structure functions depend only on x and this prediction is called scaling. This scaling was first pointed out by Bjorken [20], and is experimentally confirmed in kinematic region of $x \sim 0.1$. The scaling violation is discussed in Sec. 2.2.4.

2.2.2 The first moment of g_1 and the spin of the nucleon

The polarised structure function g_1 can be written as

$$g_1(x) = \frac{1}{2}\sum_f e_f^2(\Delta q_f(x) + \Delta\bar{q}_f(x)), \tag{2.33}$$

where $\Delta q_f(x)$ $(\Delta\bar{q}_f(x))$ is the spin dependent probability density of quarks (antiquarks) of flavor f. The first moment of $g_1(x)$ carries information about the quark helicity contribution to the nucleon spin

$$\Gamma_1 = \int_0^1 g_1(x)dx = \frac{1}{2}\sum_f e_f^2 \int_0^1 \left[\Delta q_f(x) + \Delta\bar{q}_f(x)\right] dx. \tag{2.34}$$

Defining $\Delta q_f = \int_0^1 \left[\Delta q_f(x) + \Delta\bar{q}_f(x)\right] dx$, and neglecting contributions from heavy quarks we can write for the proton

$$\begin{aligned}\Gamma_1^p &= \frac{1}{2}\left(\frac{4}{9}\Delta u + \frac{1}{9}\Delta d + \frac{1}{9}\Delta s\right) \\ &= \frac{1}{12}\left(\Delta u - \Delta d\right) + \frac{1}{36}\left(\Delta u + \Delta d - 2\Delta s\right) + \frac{1}{9}\left(\Delta u + \Delta d + \Delta s\right).\end{aligned} \tag{2.35}$$

In the simple parton model the quantity

$$\Delta\Sigma = \Delta u + \Delta d + \Delta s \tag{2.36}$$

gives the helicity contribution of quarks to the nucleon spin.

The three terms in Eq. 2.35 can be related to the expectation values a_i of the proton matrix elements of a SU(3) flavour octet of quark axial-vector currents [21]. They are defined as

$$\left\langle P,S\left|J^i_{5\mu}\right|P,S\right\rangle = Ma_iS_\mu, \qquad i=1\ldots 8 \tag{2.37}$$

with

$$J^i_{5\mu} = \bar{\Psi}\gamma_\mu\gamma_5\frac{\lambda_j}{2}\Psi, \tag{2.38}$$

where λ_j are the Gell-Mann matrices and Ψ is a column vector in flavour space

$$\Psi = \begin{pmatrix} \Psi_u \\ \Psi_d \\ \Psi_s \end{pmatrix}. \tag{2.39}$$

The element a_0 corresponds to the flavour singlet operator

$$J^0_{5\mu} = \bar{\Psi}\gamma_\mu\gamma_5\Psi \tag{2.40}$$

and thus

$$\left\langle P,S\left|J^0_{5\mu}\right|P,S\right\rangle = Ma_0S_\mu. \tag{2.41}$$

Finally one obtains

$$a_3 = \Delta u - \Delta d, \tag{2.42}$$

$$a_8 = \Delta u + \Delta d - 2\Delta s, \tag{2.43}$$

$$a_0 = \Delta u + \Delta d + \Delta s = \Delta\Sigma. \tag{2.44}$$

The octet currents are conserved and therefore a_i $(i=1\ldots 8)$ are independent of Q^2. The singlet current a_0 is not conserved, *i.e.* it depends on Q^2. This is consequence of the axial anomaly [22, 23, 24, 25]. As the result of anomalous contribution coming from gluons through a triangle graph shown in Fig. 2.4, $\partial^\mu J^0_{5\mu} \neq 0$ and therefore the current is not conserved.

The values of two matrix elements a_3 and a_8 are well known from the weak β-decay of the neutron and spin $1/2$ hyperons (*e.g.* $\Lambda \to p$, $\Sigma \to n$, $\Xi \to \Lambda$) in the SU_3 baryon octet. They can be expressed in terms of two parameters F and D which are well measured from aforementioned decays [21, 26, 27]

$$a_3 = F + D \equiv \left|\frac{g_A}{g_V}\right| = 1.2694 \pm 0.0028, \tag{2.45}$$

$$a_8 = 3F - D = 0.585 \pm 0.025, \tag{2.46}$$

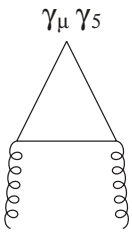

Figure 2.4: Triangle diagram giving rise to the axial anomaly. The gluons couple via the triangle to the axial current and thus contribute to the corresponding proton matrix element.

where g_A and g_V are the weak coupling constants of the neutron β-decay.

Taking into account the Eqs 2.35, 2.42-2.44 we obtain

$$\Gamma_1^p = \frac{1}{12}a_3 + \frac{1}{36}a_8 + \frac{1}{9}a_0. \tag{2.47}$$

Thus knowledge of a_3 and a_8 allows for extraction of a_0 from Γ_1 measurement.

The QCD improved parton model, which will be explained in Sec. 2.2.4, leads to corrections [28, 29, 30] modifying Eq. 2.47 to

$$\Gamma_1^p = \frac{1}{12}\left\{\left(a_3 + \frac{1}{3}a_8\right)E_{NS}(Q^2) + \frac{4}{3}a_0 E_s(Q^2)\right\} \tag{2.48}$$

with

$$E_{NS}(Q^2) = 1 - \frac{\alpha_s}{\pi} - \begin{pmatrix} 3.58 \\ 3.25 \end{pmatrix}\left(\frac{\alpha_s}{\pi}\right)^2 \ldots \tag{2.49}$$

$$E_S(Q^2) = 1 - \begin{pmatrix} 0.333 \\ 0.040 \end{pmatrix}\frac{\alpha_s}{\pi} - \begin{pmatrix} 1.10 \\ -0.07 \end{pmatrix}\left(\frac{\alpha_s}{\pi}\right)^2 \ldots \tag{2.50}$$

where the upper values correspond to the number of flavours $n_f = 3$ and lower ones to $n_f = 4$. The quoted values of coefficients of α_s expansion correspond to the $\overline{MS}$ renormalisation scheme [31]. In general the result depends on the renormalisation scheme.

The first measurement of Γ_1 was performed by the EMC collaboration [3, 4]. The value of a_0 was found to be compatible with zero ($\Delta\Sigma = 0.12 \pm 0.17$). In the naive parton model one would expect $\Delta\Sigma = 1$, while taking into account relativistic effects leads to $\Delta\Sigma \approx 0.6$ [32]. The EMC measurement indicated an unexpectedly small value of a_0 and thus this lead to the "Spin Crisis" of the nucleon, which triggered a lot of theoretical and experimental effort (*e.g.* [5, 33, 34, 8, 35, 36] and references therein). An analysis [9] of recent COMPASS data improves the accuracy for the result on $\Delta\Sigma$

$$\Delta\Sigma(Q^2 = 4\,\text{GeV}^2) = 0.237^{+0.024}_{-0.029} \tag{2.51}$$

and establishes the small contribution of the quarks to the nucleon spin (result obtained from measurement of Γ_1 given in the $\overline{MS}$ scheme).

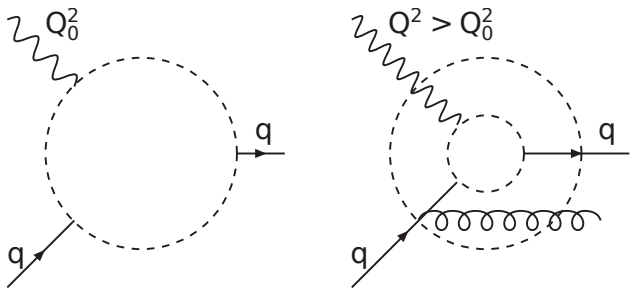

Figure 2.5: Illustration of scaling behaviour in lepton-nucleon scattering. With higher Q^2 the number of visible partons is increasing and the momentum fraction of a single parton decreases.

2.2.3 Bjorken sum rule

Using the isospin invariance the first moment of g_1^n is

$$\Gamma_1^n = -\frac{1}{12}a_3 + \frac{1}{36}a_8 + \frac{1}{9}a_0 \tag{2.52}$$

and

$$\Gamma_1^p - \Gamma_1^n = \frac{1}{6}a_3 \equiv \frac{1}{6}\left|\frac{g_A}{g_V}\right|. \tag{2.53}$$

Eq. 2.53 is the Bjorken sum rule, which was first derived in this form by Bjorken [37, 38]. It describes a relationship between the first moments of g_1^n and g_1^p and the weak coupling constants of the neutron β-decay. This is the fundamental sum rule because it relies only on the isospin invariance, *i.e.* on the SU(2) symmetry between up and down quarks. With the correction introduced in Eq. 2.48 we obtain

$$\Gamma_1^p - \Gamma_1^n = \frac{1}{6}\left|\frac{g_A}{g_V}\right| E_{NS}. \tag{2.54}$$

Beyond the leading order E_{NS} depends on the number of flavours and the renormalisation scheme. Eq. 2.54 is well satisfied by data within 5% [17].

2.2.4 QCD Improved Parton Model

Scaling Violations. Precise measurements of F_2 reveal a weak, logarithmic Q^2-dependence. Fig. 2.6 presents measurements of $F_2^p(Q^2)$ and $F_2^d(Q^2)$ for various values of x obtained by different experiments. Such violation of Bjorken scaling is a signature of quark interactions via gluon exchange. Increasing the Q^2 of the interaction, increases the resolution of the nucleon probing. Therefore at higher Q^2 a nucleon reveals its QCD structure of a compound of quarks and gluons. Quarks can emit bremsstrahlung gluons and gluons can split into $q\bar{q}$ pairs or emit gluons themselves. Then the interaction occurs with a parton that carries fraction z of the parent parton momentum as illustrated on Fig. 2.5. This leads to a smaller observed momentum fraction. The probability that the parent parton resolves increases with higher Q^2, thus leading to lower probability of finding a quark with high x value. Due to the bremsstrahlung gluons one can view the nucleon as compound of three valence quarks in a see of $q\bar{q}$ pairs, hence the $q\bar{q}$ pairs are referred to as "sea-quarks".

In Fig. 2.7 the measurements of spin dependent structure function $g_1(Q^2)$ of proton (deuteron) are presented for various values of x. It is immediately seen that the precision of the results as well as the

covered kinematic range is much smaller compared to the F_2 measurements. Due to this our knowledge of the spin dependent properties of the partons in nucleon is not as precise as in the spin independent case. In particular this affects the precision of ΔG determination from pQCD fits (*cf. infra*).

Q^2 evolution of the parton distributions. Observed scaling violations indicate that the quark and gluon distribution functions are no longer functions of x only but also depend on Q^2: $q(x,Q^2)$ and $g(x,Q^2)$. The Q^2 evolution of parton distributions is determined by the Dokshitzer-Gribov-Lipatov-Altareli-Parisi (DGLAP) equations [39, 40, 41].

The Q^2-dependence of the spin averaged momentum distributions of quarks $q_f = q_f^+ + q_f^-$ of flavour f and a gluons $g = g^+ + g^-$ evolve in DGLAP equations as

$$\frac{dq_f(x,Q^2)}{dlnQ^2} = \frac{\alpha_s(Q^2)}{2\pi}\int_x^1 \frac{dy}{y}\left(q_f(y,Q^2)P_{qq}(z) + g(y,Q^2)P_{qG}(z)\right), \tag{2.55}$$

$$\frac{dg(x,Q^2)}{dlnQ^2} = \frac{\alpha_s(Q^2)}{2\pi}\int_x^1 \frac{dy}{y}\left(\sum_f q_f(y,Q^2)P_{Gq}(z) + g(y,Q^2)P_{GG}(z)\right), \tag{2.56}$$

where $z = {}^x/_y$ and α_s is the running QCD coupling constant. The P_{ij} (splitting functions) are the probabilities to find a parton i that carried a momentum fraction z of the parent parton j of momentum $y > x$. The splitting functions are calculated using Feynman rules for the processes illustrated in Fig. 2.8.

The treatment of the evolution of the structure functions in the polarised case is completely analogous to the unpolarised one. The Q^2 dependence of the spin dependent momentum distributions of quarks $\Delta q_f = q_f^+ - q_f^-$ and gluons $\Delta g = g^+ - g^-$ is described by coupled equations

$$\frac{d\Delta q_f(x,Q^2)}{dlnQ^2} = \frac{\alpha_s(Q^2)}{2\pi}\int_x^1 \frac{dy}{y}\left(\Delta q_f(y,Q^2)\Delta P_{qq}(z) + \Delta g(y,Q^2)\Delta P_{qG}(z)\right), \tag{2.57}$$

$$\frac{d\Delta g(x,Q^2)}{dlnQ^2} = \frac{\alpha_s(Q^2)}{2\pi}\int_x^1 \frac{dy}{y}\left(\sum_f \Delta q_f(y,Q^2)\Delta P_{Gq}(z) + \Delta g(y,Q^2)\Delta P_{GG}(z)\right), \tag{2.58}$$

with the helicity dependent splitting functions $\Delta P_{ij} = P_{ij}^+ - P_{ij}^-$. It is convenient to split the polarised quark distributions in a flavour non-singlet (Δq^{NS}) and a flavour singlet (Δq^S) defined as

$$\Delta q^S(x,Q^2) = \sum_f \Delta q_f(x,Q^2), \tag{2.59}$$

$$\Delta q^{NS}(x,Q^2) = \sum_f \left(\frac{e_f^2}{\langle e^2\rangle} - 1\right)\Delta q_f(x,Q^2), \tag{2.60}$$

where $\langle e^2\rangle = \sum e_i^2 n_f^{-1}$ and n_f is the number of flavours. With these definitions DGLAP equations read for the spin-dependent case

$$\frac{d\Delta q^{NS}(x,Q^2)}{dlnQ^2} = \frac{\alpha_s(Q^2)}{2\pi}\int_x^1 \frac{dy}{y}\Delta q^{NS}(y,Q^2)\Delta P_{qq}^{NS}(z), \tag{2.61}$$

$$\frac{d\Delta q^S(x,Q^2)}{dlnQ^2} = \frac{\alpha_s(Q^2)}{2\pi}\int_x^1 \frac{dy}{y}\left(\Delta q^S(y,Q^2)\Delta P_{qq}^S(z) + 2n_f\Delta g(y,Q^2)\Delta P_{qG}(z)\right), \tag{2.62}$$

$$\frac{d\Delta g(x,Q^2)}{dlnQ^2} = \frac{\alpha_s(Q^2)}{2\pi}\int_x^1 \frac{dy}{y}\left(\Delta q^S(y,Q^2)\Delta P_{Gq}(z) + \Delta g(y,Q^2)\Delta P_{qG}(z)\right). \tag{2.63}$$

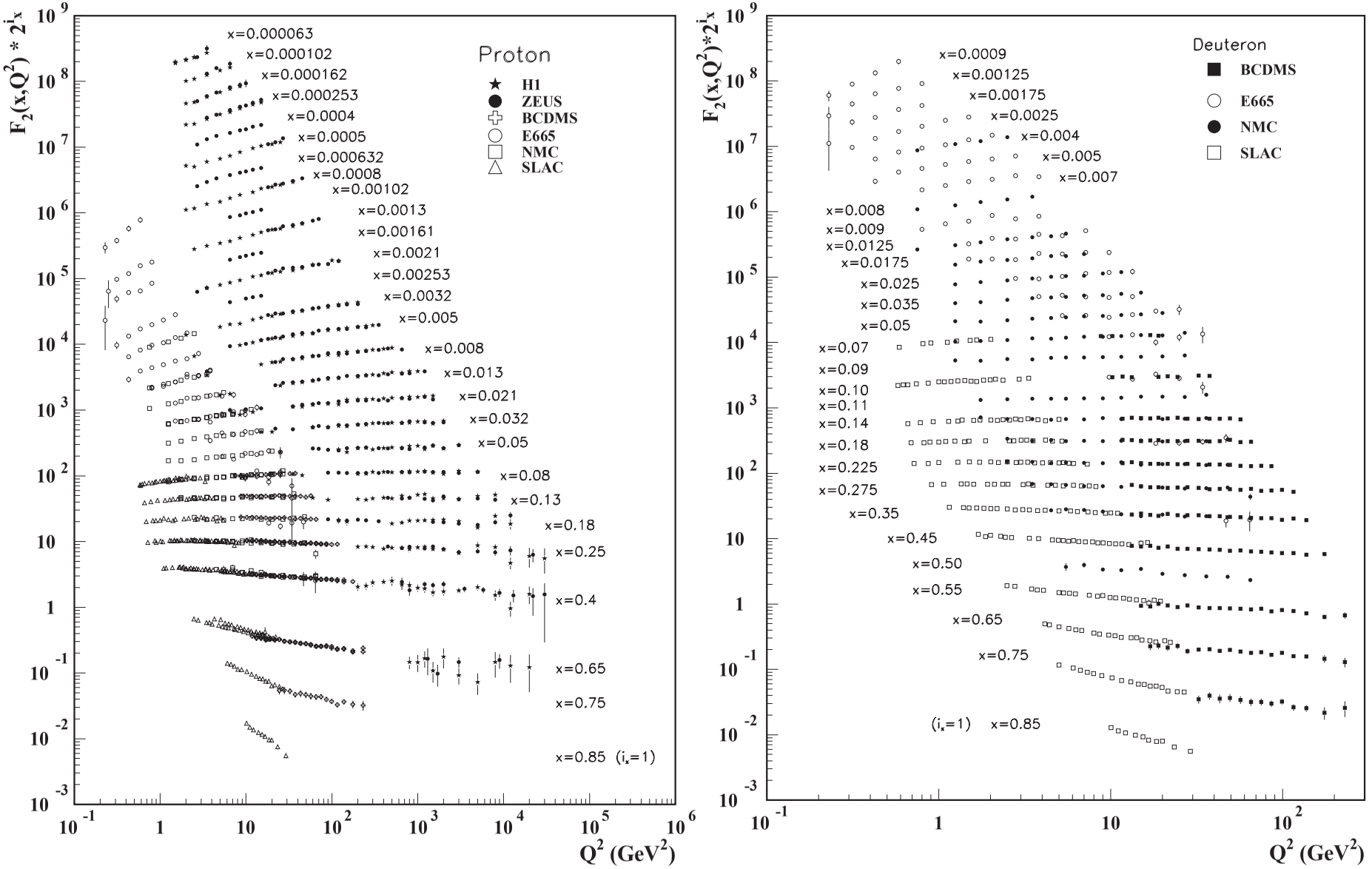

Figure 2.6: The proton (left) and the deuteron (right) structure functions $F_2(x, Q^2)$ measured in scattering of positrons on protons at the e-p collider HERA (ZEUS and H1) and for electrons (SLAC) and muons (BCDMS, E665, NMC) on a fixed target. The figures are from Ref. [27].

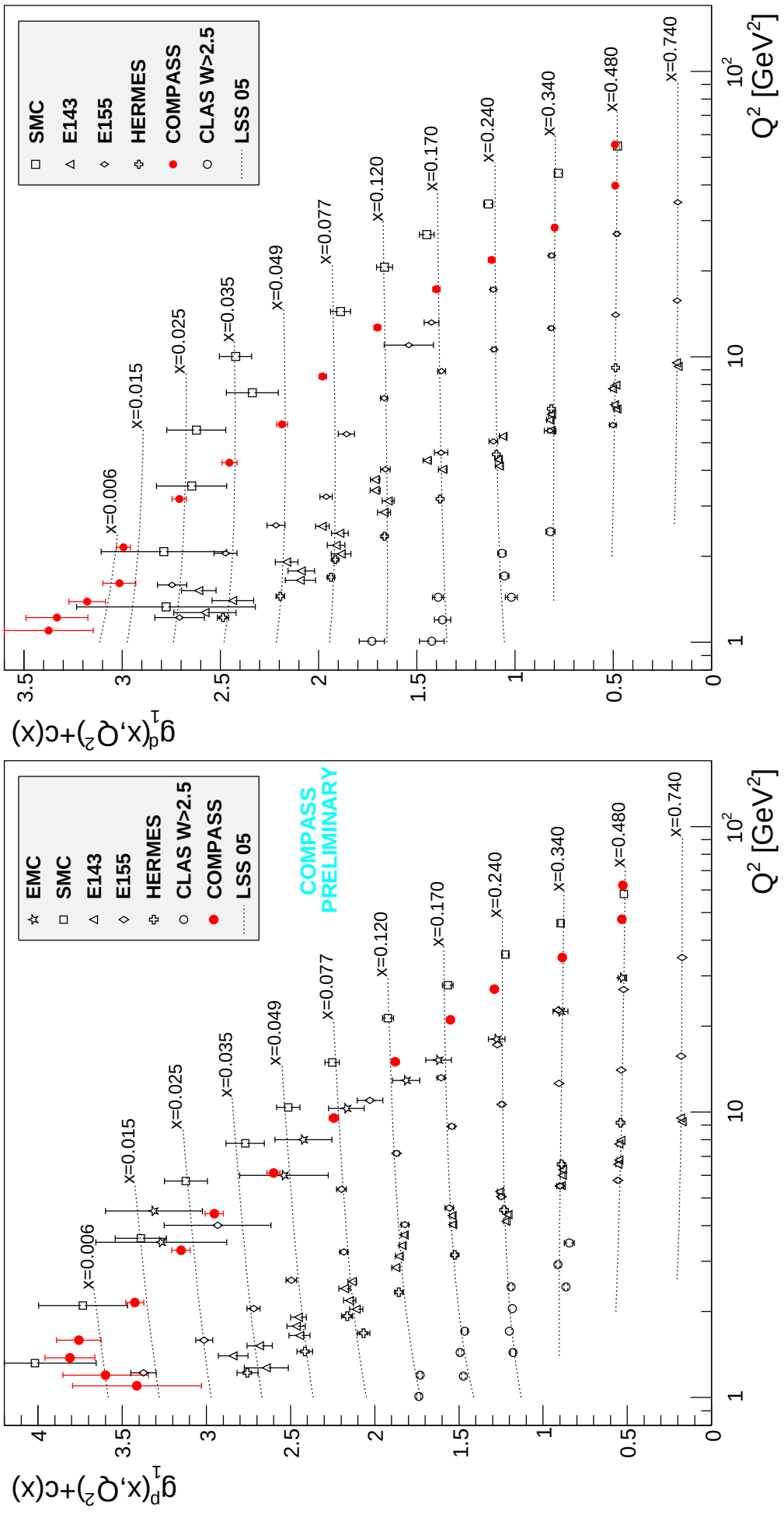

Figure 2.7: The proton (left) and the deuteron (right) spin dependent structure functions $g_1(x, Q^2)$ measured in scattering of electrons/positrons (E143, E155, HERMES, CLAS) and muons (EMC, SMC, COMPASS) on a fixed target. To align points along curves corresponding to a fixed x, LSS05 parametrisations [35] have been used. To increase readability, a constant $c(x) = 0.28(11.6 - i_x)$ is added to g_1 values, where i_x is the number of the x bin.

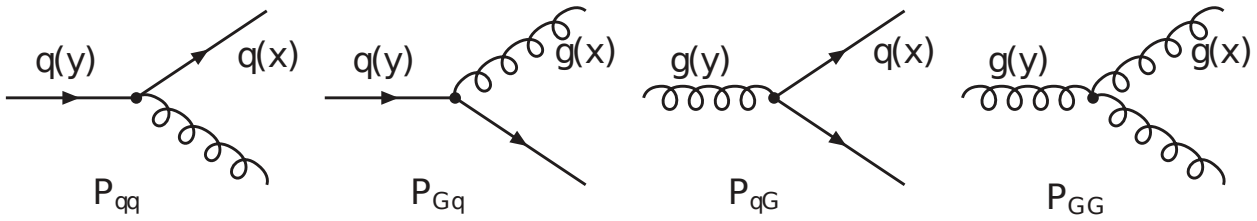

Figure 2.8: Feynman diagrams for the four splitting functions. The splitting function P_{ij} gives the probability that a parton i with momentum fraction x originates from parton j.

As can be seen in above equations the flavour non-singlet combinations evolve independently from the gluons while the singlet and the gluon distributions are coupled.

The structure function g_1 is then given by a convolution of the singlet and non-singlet coefficient functions, ΔC_s, ΔC_{NS}, ΔC_G with the polarised parton distribution functions

$$g_1 = \frac{1}{2}\left\langle e^2 \right\rangle \left\{ \Delta C_{NS} \otimes \Delta q^{NS}(x,Q^2) + \Delta C_S \otimes \Delta q^S(x,Q^2) + 2n_f \Delta C_G \otimes \Delta g(x,Q^2) \right\}. \tag{2.64}$$

The splitting and coefficient functions depend on x and α_s and have been calculated up to next-to-leading order (NLO) in α_s [42, 43, 44]. In the leading order (LO) $\Delta C_G = 0$ and the gluons do not contribute to the g_1. In the NLO the splitting functions and the coefficient functions depend on the factorisation and renormalisation scheme and the interpretation of measurements performed in DIS is scheme dependent. In the gauge invariant so-called Modified-Minimal-Subtraction ($\overline{MS}$) scheme [31] the ΔC_G vanishes and $\Delta g(x,Q^2)$ does not contribute directly to Γ_1. In the Adler-Bardeen (AB) scheme [45] which conserves chirality the ΔC_G is non zero and Γ_1 depends directly on $\Delta g(x,Q^2)$. The first moments of the singlet quark distribution $\Delta\Sigma(Q^2) = \int_0^1 \Delta q^S(x,Q^2)dx$ in the two schemes are related by

$$\Delta\Sigma_{\overline{MS}}(Q^2) = \Delta\Sigma_{AB} - n_f \frac{\alpha_s(Q^2)}{2\pi}\Delta G(Q^2), \tag{2.65}$$

where ΔG is the first moment of the gluons distribution

$$\Delta G(Q^2) = \int_0^1 \Delta g(x,Q^2)dx. \tag{2.66}$$

In $\overline{MS}$ scheme the quark distributions depend on Q^2. In AB scheme the quark distributions are scale independent but the Q^2 dependence appears due to an additional anomalous gluon contribution (an axial anomaly) owing to the triangle graph shown in Fig. 2.4. In this scheme the measured small value of a_0 can be explained by a reduction due to anomalous gluon contribution [24, 25, 23].

The contribution of the gluon spins to the nucleon spin can be estimated using the DGLAP evolution equations and performing the pQCD fits to the measured g_1. The perturbative QCD predicts only the change of parton distribution functions with Q^2 while change with x is not known, thus some functional forms of x-dependence have to be assumed for $\Delta q(x,Q_0^2)$ and $\Delta g(x,Q_0^2)$ at a given Q_0^2. Then using the DGLAP equations it is possible to predict Δq and Δg at any value of Q^2. For each value of g_1 measured at given x and Q^2 the corresponding predicted g_1 is evaluated and χ^2 is calculated including a whole set of measurements. The parameters of assumed x-dependence of $\Delta q(x,Q_0^2)$ and $\Delta g(x,Q_0^2)$ are fitted by χ^2 minimisation. As an example of results obtained from pQCD fits both the spin independent and spin dependent parton distribution

(a)

(b)

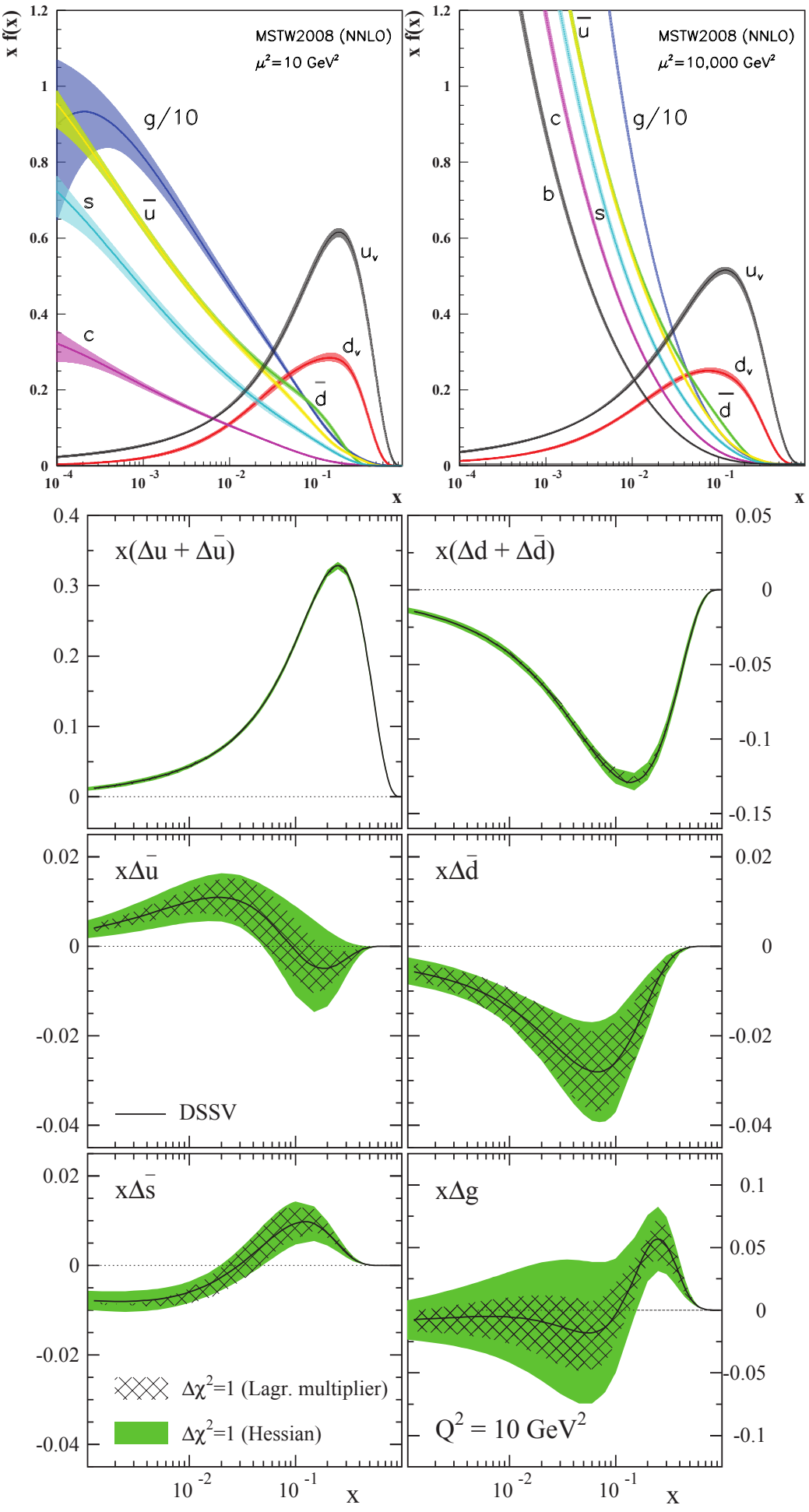

Figure 2.9: The unpolarised MSTW08 PDFs (a) and polarised DSSV PDFs (b). The shaded areas correspond to the uncertainties of the PDF determination. The figures are from Ref. [27] (a) and Ref. [36] (b).

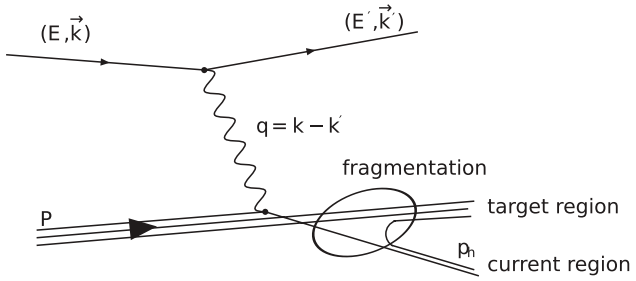

Figure 2.10: Schematic representation of hadron production in DIS.

functions are presented in Fig. 2.9.

The COMPASS collaboration has performed a pQCD analysis of all available measurements of the g_1 structure function which included new COMPASS measurements [9]. Two equal solutions where found: one with positive and and one with negative value of ΔG. The absolute value of the first moment of gluons distribution was found to be in both cases $|\Delta G| \approx 0.2$–0.3. The first moment of the singlet quark distribution derived from the fits to the g_1 data was found to be

$$\Delta\Sigma(Q^2 = 3\,\text{GeV}^2) = 0.30 \pm 0.01(stat.) \pm 0.02(evol.). \tag{2.67}$$

The pQCD fits are performed by several groups of scientists, one of the recent results is by [36]. The value of the first moment of gluons distribution was found to be $\Delta G(Q^2 = 4\,\text{GeV}^2) = -0.096$, unfortunately as the uncertainties due to extrapolation out of the measured x range are hard to estimate the error on this value is not quoted. The truncated first moment of $\Delta g(x)$ in the range $x\epsilon < 0.001,\ 1 >$ was found to be $\Delta G^{[0.001 \to 1]} = 0.13 \pm 0.182$. From those two examples of recent results one can conclude that ΔG is small however the uncertainty of such measurement is sizable.

In order to achieve a good accuracy of the derived gluon distributions, the g_1 structure function has to be known in a wide kinematic range. At present this range is rather limited compared to the range of measurements of unpolarised structure function F_2. As increase of the covered kinematic range will be possible only at a future electron-ion collider, we propose the direct measurement of spin-dependent gluon distribution which will be the main topic of this thesis.

2.3 Fragmentation

In the previous sections we have discussed inclusive DIS experiments, where only the incoming and scattered muons are measured. However, to get more insight into the properties of nucleon's constituents it is very useful to consider semi-inclusive experiments where a hadron is detected in coincidence with the scattered muon. This allows *e.g.* to separate the distributions of quarks of different flavours in the nucleon [46].

Fig. 2.10 illustrates a semi-inclusive scattering of lepton on nucleon. To describe such process a set of two variables is not sufficient, an additional one is needed. The variable that is usually used is the energy fraction of the virtual photon energy carried by the hadron

$$z = \frac{E_h}{\nu}. \tag{2.68}$$

Alternatively, one can use Feynman x

$$x_F = \frac{p_L^{c.m.}}{p_{L,max}^{c.m.}} \approx \frac{2p_L^{c.m.}}{W}, \tag{2.69}$$

where $p_L^{c.m.}$ is the longitudinal momentum of the hadron and $p_{L,max} \simeq W/2$ is the maximum allowed p_L in the virtual photon-nucleon centre of mass system. The region of $x_F < 0$ selects preferably hadrons from the target fragmentation region, which originate from the target remnant. Hadrons which originate from the struck quark are produced mostly at $x_F > 0$.

According to the QCD the quarks are confined *i.e.* they do on exist as unbound states. Thus the struck quark and the target remnant have to form colour neutral final state hadrons. This process of hadronisation cannot be described by perturbative QCD but is parametrised in the form of fragmentation functions. It is assumed, that the factorisation of the hard process and the fragmentation process holds. This means that the hard process can be calculated using perturbative QCD and the soft part, namely the fragmentation, is parametrised independently.

Semi-inclusive scattering in the current region, allows one to obtain an information about the struck quark. The identity and the direction of the leading hadron is correlated with the flavour and the direction of the struck quark. The cross section for the production of a hadron *h* can be written at leading order QCD as

$$\sigma^h(x, Q^2, z) \propto \sum_f e_f^2 q_f(x, Q^2) D_f^h(z, Q^2), \tag{2.70}$$

where $D_f^h(z, Q^2)$ is the fragmentation function parameterising the fragmentation process. The fragmentation function gives the probability density that a struck quark of flavour f, probed at a scale Q^2, fragments into a hadron h carrying a fraction z of the virtual photon energy. One of the most recent parametrisations of fragmentation functions is presented in Ref. [47]. The precision of the fragmentation function determination is of great importance, *e.g.* it is the main contribution to the systematic uncertainty for a recent separation of the spin-dependent quark distributions of different flavours in the nucleon [46].

In this Section we presented the independent fragmentation. For discussion of the string fragmentation *cf.* Sec. 8.1.4.

Chapter 3

Review of direct measurements of gluon polarisation

Direct measurements of the ΔG are based on the selection of pQCD processes where a gluon from nucleon undergoes an interaction. In the lepton-nucleon scattering the interesting process is the Photon Gluon Fusion (PGF), whereas for the proton-proton scattering these are the prompt photon, meson or jet production. The description of these processes along with short overview of existing experimental results is provided in this chapter.

3.1 Photon Gluon Fusion

In the PGF process the interacting virtual photon and the gluon from the nucleon produce a quark-antiquark pair. The process is presented in Fig. 3.1. Two signatures are used to tag such events. The first one is the production of charmed mesons and the second is the production of high transverse momentum hadron pairs. It is worth to note that in the experiments usually the ratio $\Delta G/G(x)$ is extracted in a range of x limited by experimental conditions. To obtain the value of ΔG the known parametrisations of spin averaged gluon distribution function G are used.

3.1.1 Open charm production

Due to the large mass of the charm quark ($m_c = 1.5\,\text{GeV}$) its production via fragmentation of light quarks as well as interactions of virtual photon with intrinsic charm quark in the nucleon are strongly suppressed. Therefore it can be produced only in the hard scattering process. The PGF is the lowest order pQCD pro-

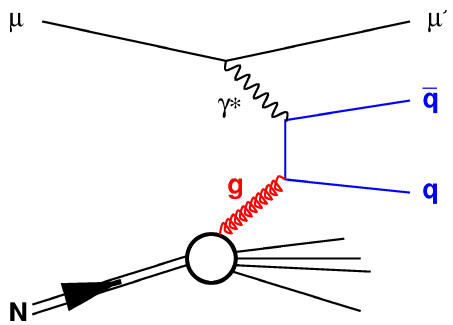

Figure 3.1: Photon Gluon Fusion (PGF)

cess where charmed quarks are produced. Thus selection of charmed mesons in the final state suppresses completely other contributions to the cross section.

The spin dependent cross section asymmetry for the $\gamma N \to c\bar{c}$ process is related to the gluon polarisation in the following way

$$A^{\gamma N \to c\bar{c}} = \frac{\Delta\sigma^{\gamma N \to c\bar{c}}}{\sigma^{\gamma N \to c\bar{c}}} = \frac{\int d\hat{s} \Delta\sigma(\hat{s}) \Delta G(x_G, \hat{s})}{\int d\hat{s} \sigma(\hat{s}) G(x_G, \hat{s})}, \tag{3.1}$$

where $\hat{s}$ is the invariant mass squared of the photon-gluon system which equals to the squared mass of the quark final state: $m^2_{c\bar{c}}$. The $\Delta\sigma(\hat{s})$ and $\sigma(\hat{s})$ are the partonic cross sections that are calculable in the pQCD. The relation of the cross section asymmetry with the counting rate asymmetry, which is the observable measured by the experiment is discussed in Sec. 7.3. In case of the open charm production it can be written as

$$A^{\gamma N \to c\bar{c}} = \frac{1}{P_B P_T f D \frac{S}{S+B}} A^{exp} - A^{BG}, \tag{3.2}$$

where P_B is the beam polarisation, P_T the target polarisation, D the depolarisation factor, and f the dilution factor accounting for the fraction of polarisable nucleons in the target material. The $\frac{S}{S+B}$ is another diluting factor with S and B being the number of signal and background events in the studied open charm sample. The background consists of those non-charm events which passed selections used to obtain the open charm sample. Its asymmetry A^{BG} is assumed to be equal zero. This assumption was verified to be valid within available statistical precision.

The measurement of the gluon polarisation based on tagging of the PGF events via charmed hadrons is for the first time implemented in the COMPASS experiment. This measurement is the main goal of COMPASS. For the description of the experimental setup *cf.* Chapter 4. Two main channels of the open charm production are considered. The first with D^0 meson in the final state identified as a $K\pi$ pair of invariant mass in the mass window around known mass of D^0. The second one is the channel with D^* meson which decays into D^0 and a slow pion. This additional requirement significantly reduces background. For details of the analysis see Refs [10, 48, 49]. The result obtained from the data collected in 2002-2006 years with the polarised deuteron target is

$$\frac{\Delta G}{G} = -0.49 \pm 0.27(stat.) \pm 0.11(syst.) \tag{3.3}$$

at average fraction of nucleon momentum carried by the gluon $< x_G > \approx 0.11$ and at average scale $\mu^2 \approx 13\,\mathrm{GeV}^2$. Recently a preliminary result was obtained including additional channels as well as the data collected in 2007 with the polarised proton target. The extracted gluon polarisation is [50, 51]

$$\frac{\Delta G}{G} = -0.08 \pm 0.21(stat.) \pm 0.03(syst.). \tag{3.4}$$

3.1.2 High transverse momentum hadron pairs

For the interactions of virtual photon with gluon the lowest order pQCD (LO pQCD) process is the PGF. A selection of high p_T hadron pairs will result in a sample of events produced by perturbative processes, where mostly light quarks (u, d, s) and gluons are involved. Thus in addition to the PGF two other processes contribute to the cross section in the LO pQCD. These are the Leading Process (LP) and QCD-Compton (QCDC) process. The diagrams for the three LO processes are shown in Fig. 3.2. As all three processes

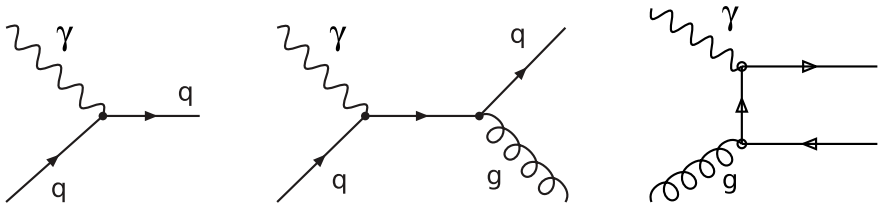

Figure 3.2: Diagrams of the LO pQCD processes. Leading Process (left), QCD-Compton (centre), Photon Gluon Fusion (right)

contribute to the cross section the expression for the cross section spin asymmetry is following

$$A^{\gamma N \to hhX} = \hat{a}_{LL}^{PGF} \frac{\Delta G}{G} R^{PGF} + \hat{a}_{LL}^{QCDC} \frac{\Delta q}{q} R^{QCDC} + \hat{a}_{LL}^{LP} \frac{\Delta q}{q} R^{LP}, \tag{3.5}$$

where $\hat{a}_{LL}^{i}$ are the partonic cross section asymmetries for given process, R^{i} is the fraction of process i, and Δq (q) are the spin dependent (spin averaged) quark distributions.

Most of the events with light quark production originate from the leading process. However hadrons produced in the LP have small transverse momenta. Therefore selecting events with high p_T hadron pairs significantly suppresses the contribution of LP events to the analysed sample. Because their suppression is not perfect and the QCDC events are only weakly affected by this selection, the knowledge of the processes fractions is required. It is obtained from Monte Carlo (MC) simulations.

For more detailed discussion of $\Delta G/G$ extraction from the measured cross section asymmetries for high p_T hadron pair events *cf.* Chapter 7.

HERMES (DESY).

HERMES is an experiment at DESY laboratory by the HERA accelerator. The HERA was shut down in 2007, but the analysis of collected data is still ongoing. HERMES studies scattering of polarised electrons (positrons) with 27.5 GeV energy on polarised gaseous target injected inside the accelerator beam pipe. The electron beam is naturally polarised in the accelerator due to Sokolov-Ternov effect [52]. The resulting spin orientation is perpendicular to the accelerator plane. Thus to obtain a longitudinal configuration, the the spin is rotated before the interaction point using magnet systems called spin rotators. Achieved average polarisation is $55 \pm 2\%$. For the determination of the gluon polarisation a hydrogen target was used with average polarisation of $86 \pm 4\%$.

HERMES is equipped with a forward spectrometer based on a dipole magnet of $\int Bdl = 1.3$ Tm. Particle identification relies on a set of detectors including the RICH and the calorimeter. A description of the detector setup can be found in Ref. [53].

The sample of events used for the $\Delta G/G$ extraction consisted of at least two oppositely charged hadrons of momentum larger than 4.5 GeV. The transverse momentum of the fastest hadron with regards to the beam axis was required to be larger than 1.5 GeV, while for the second hadron the requirement was > 0.8 GeV. In addition, to suppress the contribution of resonances, the invariant mass of the hadron pair was required to be larger than 1 GeV.

As the bulk of the selected events has $Q^2 \approx 0$, the transverse momenta are approximately equal to the transverse momenta calculated with regards to the direction of virtual photon. The fractions of processes were estimated using the PYTHIA [54] event generator. In the analysis the contribution of LP was assumed

to be negligible, this assumption was verified using the LEPTO [55] event generator. The contributions from resolved photon processes to the asymmetries were neglected. The result of the analysis

$$\frac{\Delta G}{G} = 0.41 \pm 0.18(stat.) \pm 0.03(exp.syst.) \tag{3.6}$$

with $< x_G >= 0.17$ and the scale μ^2 given by the average $\sum p_T^2$ equal to $2.1\,\text{GeV}^2$. For more details on the HERMES analysis see Ref. [56].

Recently HERMES presented a new result on $\Delta G/G$ [57, 58]. It is based on the measurement of the inclusive hadron production asymmetry. The target was the deuteron and the events selected for the analysis had at least one high p_T hadron of $1.05 < p_T < 2.5\,\text{GeV}$. The preliminary result of this analysis is

$$\frac{\Delta G}{G} = 0.071 \pm 0.034^{+0.127}_{-0.105} \tag{3.7}$$

with the average x_G equal to 0.22 and μ^2 scale of $1.35\,\text{GeV}^2$.

SMC (CERN).

The SMC experiment studied interactions of $190\,\text{GeV}$ polarised muon beam with polarised proton and deuteron targets. It was situated at CERN by the SPS accelerator in the same experimental hall as COMPASS which is SMC's successor. The muon beam line and the polarised target were essentially the same as at COMPASS. However, it is worth to emphasise that the beam intensity at COMPASS is about five times larger than for the SMC. Also in the SMC for the measurement on polarised deuterons a deuterated buthanol target was used instead of ^{6}LiD. For a more complete description of the SMC experimental setup see Ref. [59].

In the SMC experiment the gluon polarisation was extracted from a sample of events with high p_T hadron pairs (p_{T1}, $p_{T2} > 0.7\,\text{GeV}$, $\sum p_T^2 > 2.5\,\text{GeV}^2$) for $Q^2 > 1\,\text{GeV}^2$. To select the current fragmentation region following cuts were used: $x_F > 0.1$ and $z > 0.1$.

In addition a second method of selection was developed that was based on Neural Networks (NN). In this method the input to the NN contained: x, Q^2, y, tracks multiplicity and variables describing the two hadrons with the highest p_T (p_T, p_L, z, charge, azimuthal angle ϕ) and the selection cut was set on the output of the NN. It was shown that using the NN a better purity of selected sample can be achieved while retaining the same efficiency.

The final result of the SMC analysis [12] is

$$\frac{\Delta G}{G} = -0.20 \pm 0.28(stat.) \pm 0.1(syst.). \tag{3.8}$$

The average x_G is 0.07 and μ^2 scale at which the nucleon structure was probed is $3\,\text{GeV}^2$.

COMPASS (CERN).

At COMPASS two complementary analyses of the high p_T hadron pairs channel are performed. The analysis at $Q^2 > 1\,\text{GeV}^2$ kinematic region is the topic of this thesis. It is discussed in the following chapters. The second analysis is performed for the $Q^2 < 1\,\text{GeV}^2$ kinematic region.

The high p_T sample selection for $Q^2 < 1\,\text{GeV}^2$ is based on a set of cuts. First, at least two hadron tracks are required to be reconstructed in the primary vertex. Then to suppress the contribution from the the LP

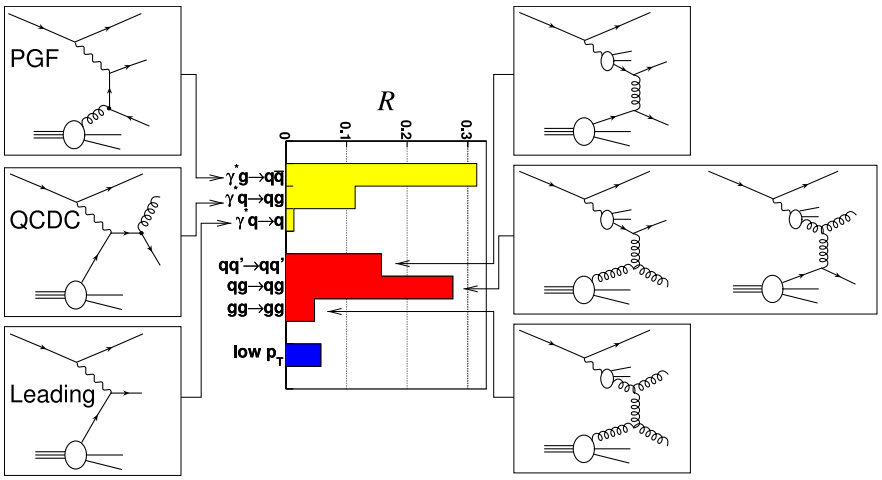

Figure 3.3: Relative contributions R of the dominant PYTHIA processes to the MC sample of high p_T events at $Q^2 < 1$ GeV^2. Left: point-like photon processes, right: resolved photon processes. Longitudinal photons, as well as minor resolved photon contributions, are not shown.

and ensure factorisation we require p_T of the two fastest hadrons to be > 0.7 GeV and their $\sum p_T^2$ to be > 2.5 GeV^2. To remove regions with low sensitivity to ΔG and regions with large radiative corrections the events with $0.35 < y < 0.9$ are selected. Finally to ensure that only events from current fragmentation region are selected and to remove ρ resonance additional cuts are imposed: $x_F > 0$ and $M_{inv} > 1.5$ GeV.

In the region of $Q^2 < 1$ GeV^2 there is an additional contribution of resolved photon processes. In Fig. 3.3 the fractions of contributing processes are presented. They were estimated using a MC simulation with the PYTHIA event generator. Three processes are treated as a signal: the PGF and two resolved photon processes that probe gluons in the nucleon: $qg \to qg$, $gg \to gg$. The LP and so called "low p_T" sample, which consists of non-perturbative processes are neglected as they contribute only small fraction of events. The expression that decomposes the cross-section asymmetry into contributions from aforementioned processes can be written as

$$\begin{aligned} A_{||}/D &= \underline{R_{PGF}\left\langle \frac{a_{LL}^{PGF}}{D} \right\rangle \frac{\Delta G}{G}} + R_{QCDC}\left\langle \frac{a_{LL}^{QCDC}}{D} \right\rangle A_1 + \\ &+ R_{qq\to qq}\left\langle \frac{a_{LL}^{qq\to qq}}{D} \right\rangle \frac{\Delta q}{q}\frac{\Delta q^\gamma}{q^\gamma} + R_{gq\to gq}\left\langle \frac{a_{LL}^{gq\to gq}}{D} \right\rangle \frac{\Delta q}{q}\frac{\Delta G^\gamma}{G^\gamma} \\ &+ \underline{R_{qg\to qg}\left\langle \frac{a_{LL}^{qg\to qg}}{D} \right\rangle \frac{\Delta G}{G}\frac{\Delta q^\gamma}{q^\gamma}} + \underline{R_{gg\to gg}\left\langle \frac{a_{LL}^{gg\to gg}}{D} \right\rangle \frac{\Delta G}{G}\frac{\Delta G^\gamma}{G^\gamma}}, \end{aligned} \tag{3.9}$$

where R_i is the fraction of process i, a_{LL}^i is a partonic cross section asymmetry [60], q, Δq are the parton distributions in the nucleon, q^γ, G^γ are unpolarised PDFs in the photon and Δq^γ, ΔG^γ are polarised PDFs in the photon. The cross section spin asymmetry A_1 is taken from parametrisation to global data. Terms in Eq. 3.9 that contribute to the signal are underlined.

The parton distributions in the nucleon were taken from fits to world data [5, 6, 61, 62], similarly to the unpolarised PDFs in the photon [63]. For polarised PDFs in the photon there are no measurements available. We can treat those PDFs as a sum of a non-perturbative (VMD) term and a perturbative (point-like) term. The point-like PDFs are fully calculable but for the VMD part we can only consider the minimal and the maximal scenarios [64]. Uncertainty coming from this is taken into account in the systematic error.

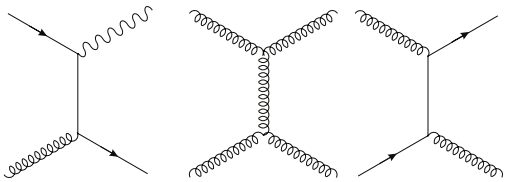

Figure 3.4: Selected lowest-order Feynman diagrams for elementary processes with gluons in the initial state in p − p collisions: quark-gluon Compton process with prompt photon production (left), gluon-gluon (centre) and gluon-quark (right) scattering for jet production.

In order to estimate the systematic error associated with PYTHIA generator, $\Delta G/G$ was extracted for different values of most important parameters describing: the parton fragmentation, the primordial transverse momentum of partons within the nucleon and the photon, the renormalisation and factorisation scales, and the parton showers.

Using the data collected in 2002-2003 years the obtained value of gluon polarisation is

$$\frac{\Delta G}{G} = 0.024 \pm 0.089(stat.) \pm 0.057(syst.) \qquad \text{at} \qquad x_g \approx 0.095^{+0.08}_{-0.04}. \tag{3.10}$$

The scale at which measurement is made was estimated to be $3\,\text{GeV}^2$. This result was published [11]. The analysis of combined data from years 2002-2004 provides us with a more precise preliminary result [65]

$$\frac{\Delta G}{G} = 0.016 \pm 0.058(stat.) \pm 0.055(syst.). \tag{3.11}$$

This value was presented at several conferences.

3.2 Proton-proton scattering

Studies of the polarised proton-proton scattering are performed at Brookhaven laboratory (USA) by experiments at the RHIC accelerator. The measurements are performed by the two experiments STAR and PHENIX with colliding polarised proton beams at the centre-of-mass energy $\sqrt{s} = 200\,\text{GeV}$. The data were collected in years 2002-2006 and 2009. In 2009 apart from the data collected at $\sqrt{s} = 200\,\text{GeV}$ also the first collisions at the centre-of-mass energy $\sqrt{s} = 500\,\text{GeV}$ were recorded. The data from 2009 still remain to be analysed.

Extraction of the gluon polarisation in the proton-proton interactions is performed using the processes presented in Fig. 3.4. The leftmost diagram presents a prompt photon production while the two others show the jet production processes. The main advantage of the studies performed with *pp* interactions is that they provide a large number of events with gluon interactions, a disadvantage is a sizable background. As an example, for the prompt photon channel the background comes mostly from the decay of $\pi^0 \to \gamma\gamma$, while for the jet channels from the quark-quark interactions.

The protons are polarised at the polarised proton source. After passing the 3-step acceleration they are injected and then accelerated in the two rings of the RHIC. The proton spin orientations inside the rings are usually vertical. However, before the interaction the spins are rotated to the longitudinal orientation. To overcome the protons depolarisation during the acceleration dedicated superconducting magnets called *Siberian Snakes* where installed along the accelerator ring. The magnetic field in the *Snakes* flips the protons spins leading to compensation of the depolarisation effects. The maximum polarisation of the proton beam

has been improved over the years, from 30% in 2003 to 65% in 2006.

The STAR is a detector which is optimised for the charged particles tracking and identification. It is also well suited for the jet reconstruction. The PHENIX specialises in the lepton and photon registration and has an excellent capability to detect π^0's in the mid-rapidity region. A discussion of the STAR and PHENIX detectors can be found in Refs [66] and [67].

For a selected final state the observable measured in the experiment is the cross section asymmetry for parallel (σ^{++}) and anti-parallel (σ^{+-}) directions of the two proton beams polarisations

$$A_{LL}^{exp} = \frac{1}{P_1 P_2} \frac{\sigma^{++} - \sigma^{+-}}{\sigma^{++} + \sigma^{+-}}, \tag{3.12}$$

where P_1 and P_2 are the beams polarisations.

The A_{LL}^i cross section asymmetry for a given partonic reaction *i* can be expressed in the LO pQCD as

$$A_{LL}^i = \frac{\Delta f_1^i}{f_1^i} \frac{\Delta f_2^i}{f_2^i} \hat{a}_{LL}^i. \tag{3.13}$$

The $\Delta f^i / f^i$ factors are the ratios of the spin dependent to spin averaged parton density functions. When in the process there is a gluon interaction, as in Fig. 3.4, then corresponding $\Delta f/f$ equals to $\Delta G/G$. The parton density functions are obtained from the QCD fits to the results of DIS experiments (*cf.* Sec. 2.2.4). The partonic cross section asymmetry $\hat{a}_{LL}^i$ can be calculated for each process in pQCD.

The experimental asymmetry, A_{LL}^{exp}, is a sum of all A_{LL}^i, for reactions leading to a given final hadronic state. The asymmetries in the sum should be taken with weights corresponding to a fraction of a given reaction in the studied sample. Disentangling the $\Delta G/G$ from this sum is a complex and difficult task. Therefore another method was elaborated. Different scenarios of $\Delta G(x)$ distribution are assumed and the corresponding expected experimental double spin asymmetries for a production of a given final state are calculated. They are then compared to the data.

In Fig. 3.5 selected results of the measured A_{LL} asymmetries as a function of p_T from PHENIX and STAR are compared to various theoretical predictions. The curves correspond to theoretical predictions obtained for different parametrisations of $\Delta G(x)$ resulting in different values of the first moment $\Delta G (\equiv \int_0^1 \Delta G(x) dx)$. Clearly the proton-proton data disfavour scenarios with high values of the first moment of $\Delta G(x)$. For more detailed analysis of the measurements see Refs [68] and [69].

The comparison of the result of this thesis with various fixed target results and results from RHIC is discussed in Chapter 11.

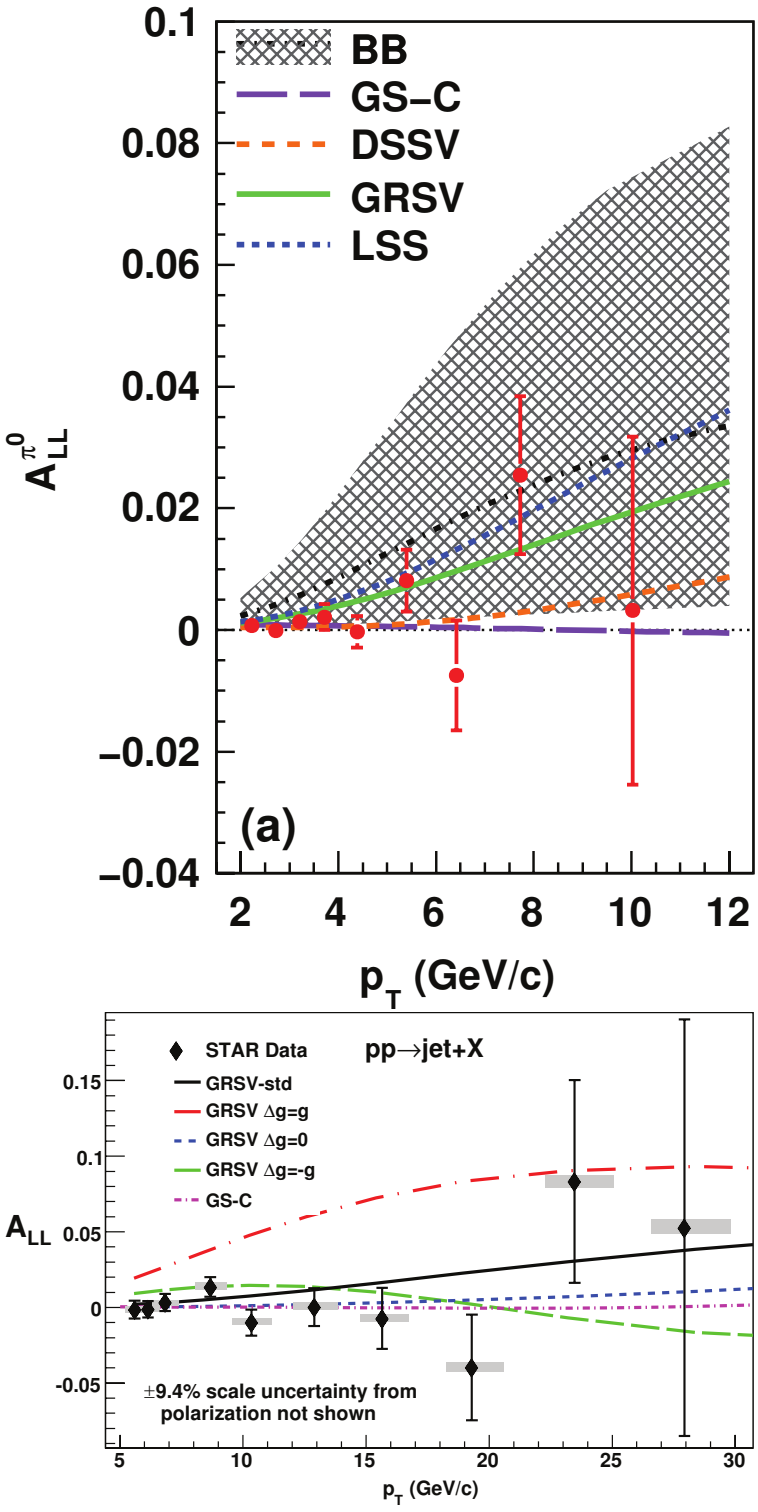

Figure 3.5: Measurements of the A_{LL} cross section asymmetry at RHIC. Top diagram presents results obtained with a sample of π^0 (from $pp \rightarrow \pi^0 X$) at the PHENIX experiment. Bottom diagram presents the results from the STAR experiment obtained from an inclusive jets sample. The curves present theoretical predictions with different assumed distributions of $\Delta G(x)$.

Chapter 4

COMPASS experiment

4.1 Introduction

The COMPASS experiment [70, 71] at the Super Proton Synchrotron (SPS) accelerator at CERN was approved in 1998. First test runs were recorded in 2001 with a partial setup while the physics data taking started in 2002.

The COMPASS is a fixed target experiment with two physics programs. The muon program focuses on the spin structure of the nucleon which is studied using interactions of polarised muon beam with polarised deuteron or proton targets. The main goal of this program is the determination of polarisation of gluons in the nucleon. It is also the topic of this thesis. Among other topics of the muon program there are: inclusive and semi-inclusive asymmetries, asymmetries in the production of vector mesons, the Collins and Sivers asymmetries. For the hadron program a broad selection of hadron beams and target materials is used. The goal of this program are the studies of the Primakoff reaction, charmed hadron spectroscopy and a search for exotic states *e.g.* glueballs or hybrids.

Data taking with muon beam took place in 2002-2004 and 2006-2007 years. After the first year of data taking the spectrometer was equipped with additional detectors. In 2005 a major upgrade of the experimental setup was performed; the superconducting target magnet was replaced, readout electronics of the RICH detector were refurbished and new detectors were introduced to cover increased acceptance of target magnet. The interactions of muons with nucleons were studied on the deuteron and in 2007 on the proton targets. Beam time for the hadron program was dedicated for a short pilot run in 2004 and for full data taking in 2008 and 2009.

Since the determination of the gluon polarisation is the topic of this thesis the description of the spectrometer will be restricted to the muon setup. Detailed description of the COMPASS experiment for both experimental programs is presented in Refs [71, 72, 70].

In Sec. 4.2 the muon beam used by COMPASS is described followed by description of the polarised target in Sec. 4.3. The COMPASS spectrometer is the topic of Sec. 4.4 whereas the Trigger system is covered in Sec. 4.5. Sec. 4.6 presents the Data Acquisition system (DAQ) along with on-line and off-line analysis tools.

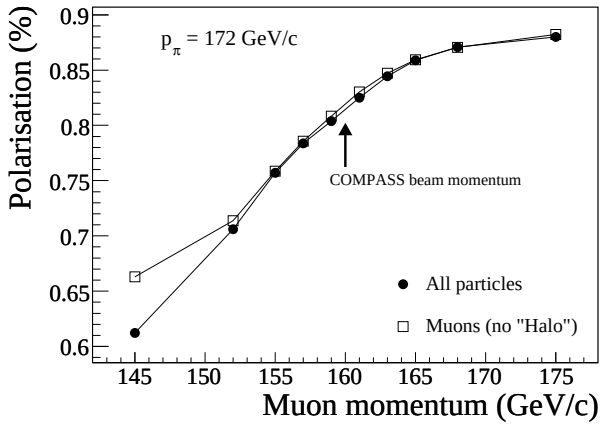

Figure 4.1: The muon beam polarisation (absolute value) as a function of the central muon momentum, assuming a central hadron momentum of 172 GeV.

4.2 Muon beam

The COMPASS experiment is located at the M2 beam line [73] of the SPS accelerator. In SPS the protons are accelerated to an energy of 400 GeV and then they are extracted to collide with a beryllium target to produce secondary hadrons, mostly pions. The accelerator cycle has a duration of 16.8 s with 4.8 s of extraction (the so called spill). The intensity of the proton beam is of the order of 10^{13} protons per spill.

After the production target a section of magnets enables to select hadrons of desired momentum and charge. It is followed by 600 m decay channel where $\sim 10\%$ of pions decay into muons ($\pi \rightarrow \mu + \nu_\mu$). Remaining hadrons are stopped using 9.9 m beryllium absorber. After the hadron absorber a set of magnets is used to select muons momenta and to steer the beam into the experimental hall. At the Bend 6 magnet the Beam Momentum Station is situated, which is used to determine the momentum of the beam particle on the event-by-event basis. Detailed discussion of the beam momentum reconstruction is presented in Chapter 5. Apart from the dipole and quadrupole magnets the beam line consist of scrapers and magnetic collimators that are used to reduce unwanted muon halo at the experiment. Finally a section of dipoles and quadrupoles focuses the beam on the target to the size of $\sigma \simeq 7$ mm for the Gaussian core with a divergence of 1 mrad. For the typical production target of 50 cm length and μ^+ beam of 160 GeV the intensity of $2 \times 10^8\, \mu^+/spill$ can be achieved.

The muon beam is naturally polarised due to the parity violating decay of the pion. In the rest frame of the decaying pion the muon polarisation is 100%. In the laboratory frame the polarisation is a function of the ratio of the pion to muon energies [59]

$$P_{\mu^\pm} \approx \mp \frac{m_\pi^2 + \left(1 - 2\frac{E_\pi}{E_\mu}\right) m_\mu^2}{m_\pi^2 - m_\mu^2}. \tag{4.1}$$

The sign of the polarisation, *i.e.* the spin orientation with respect to the muon direction, depends on the muon charge. In COMPASS the ratio $\frac{E_\pi}{E_\mu} = \frac{177\,\text{GeV}}{160\,\text{GeV}}$ was selected resulting in a μ^+ polarisation of -76% with a relative error of 5%. In 2004 the ratio was changed to $\frac{E_\pi}{E_\mu} = \frac{172\,\text{GeV}}{160\,\text{GeV}}$ resulting in -80% of μ^+ polarisation. The polarisation of the muon beam was measured at the M2 beam line in the SMC experiment. The results of the MC simulations were found to be in good agreement with measurements [73, 74, 75]. Therefore in COMPASS the simulated values are used. In Fig. 4.1 the polarisation is presented as a function of momentum

for the 2004 setting.

4.3 Polarised target

In order to obtain a high polarisation of target material and keep it in so called "frozen spin" mode, where the polarisation decay is very slow, the target has to be put into a high magnetic field and a very low temperature. In COMPASS this is achieved using a superconducting solenoid magnet capable of producing a highly homogeneous filed of 2.5 Tesla and an efficient ^{3}He/^{4}He dilution refrigerator that allows to achieve temperatures down to 50 mK (Fig. 4.2). In 2002-2004 years a target magnet with acceptance of ± 70 mrad, inherited from the SMC experiment, was used. During the upgrade of 2005 the magnet was replaced with a new one of acceptance ± 180 mrad. In addition to the solenoid magnet a 0.5 T dipole magnet is present. It is used to rotate periodically the target spin by 180°, because such procedure allows to cancel effects of acceptance as described in Chapter 7. The dipole magnet also enables for measurements with transversely polarised target.

The target material is placed in two cylindrical cells, each 60 cm long and with diameter of 3 cm, located one after another along the beam (Fig. 4.2). The large length of the cells is required to provide a sufficient luminosity. Division of the target into two cells enables a simultaneous measurement for the two spin configurations and makes the measurement of spin asymmetry independent from the beam flux determination.

As the target material the deuterated lithium ^{6}LiD was used. The ^{6}Li nucleus can be approximately considered as a loosely bound ^{4}He + D system, so each ^{6}LiD molecule in the COMPASS polarised target can be considered as consisting of the two polarised deuterons and the unpolarised helium nucleus [76]. In 2007 the data were taken on an ammonia NH_3 target in order to measure interactions with polarised protons.

Due to the small magnetic moment of nucleon it is impractical to polarise it using the statistical method based on the Zeeman effect. In strong magnetic field (2.5 T) and low temperature (0.5 K) the expected polarisation for the deuteron is ~ 0.001. On the other hand the electrons due to their high magnetic moment are polarised up to 0.998. To achieve a high level of the nucleon polarisation the Dynamic Nuclear Polarisation (DNP) [77] is used. The principle of DNP relies on an induced transfer of the high electron polarisation to the nucleons. It is achieved by irradiating the target material with Micro Wave (MW) radiation of a characteristic energy needed for simultaneous spin flip of the proton and the electron. As this energy depends on the spin of the final e-p system (0 or 1) by selecting a proper MW frequency the required orientation of the nucleon spin with respect to the direction of magnetic field can be chosen. The electrons relax to the lower energy state within milliseconds due to their high magnetic moment. The small magnetic moment of the nucleon causes that a spontaneous spin flip has a low probability. This leads to a buildup of the polarisation of the nucleons and a relaxation time of ~ 1000 hours. Using the DNP in COMPASS for ^{6}LiD target material the polarisation of $\sim 50\%$ is achieved. Typical buildup of the polarisation is presented in Fig. 4.3. The idea behind the DNP method is illustrated in Fig. 4.4.

4.4 Spectrometer

Products of Deep Inelastic Scattering (DIS) of muons on nucleons are measured in a two stage spectrometer. The first part is the Large Angle Spectrometer (LAS). It is located directly after the polarised target and

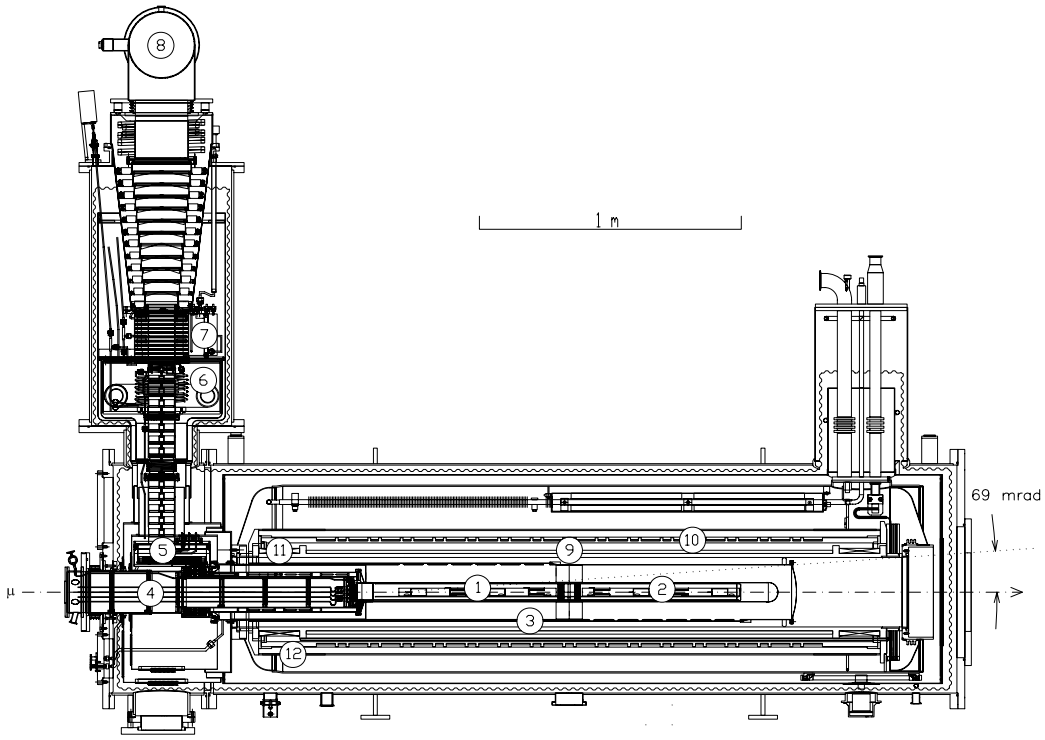

Figure 4.2: Side view of the COMPASS polarised target: (1) upstream target cell and (2) downstream target cell inside mixing chamber, (3) microwave cavity, (4) target holder, (5) still (3He evaporator), (6) 4He evaporator, (7) 4He liquid/gas phase separator, (8) 3He pumping port, (9) solenoid coil, (10) correction coils, (11) end compensation coil, (12) dipole coil. The muon beam enters from the left. The two halves of the microwave cavity are separated by a thin microwave stopper.

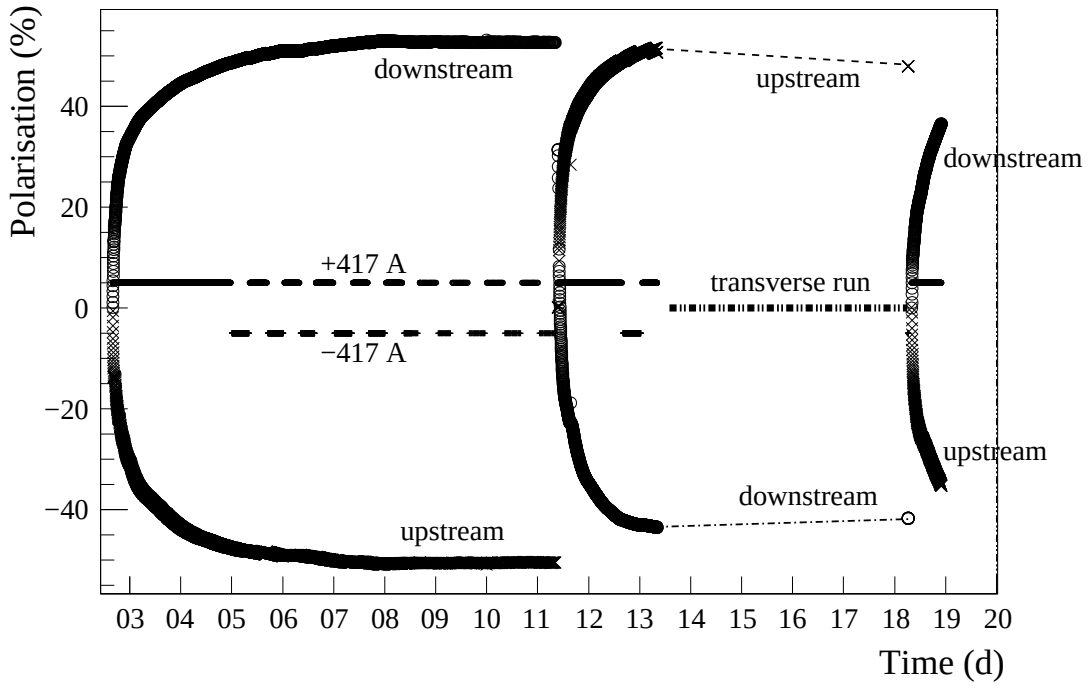

Figure 4.3: Typical average polarisations in the upstream and downstream target cells during 20 days of the 2004 run. After day 11, the polarisations in the target cells are reversed by changing the microwave frequencies. Data are taken in transverse mode from day 13 to day 18 and a new field reversal by microwaves is performed at the end of the period. The current of ± 417 A corresponds to an axial field of 2.5 T.

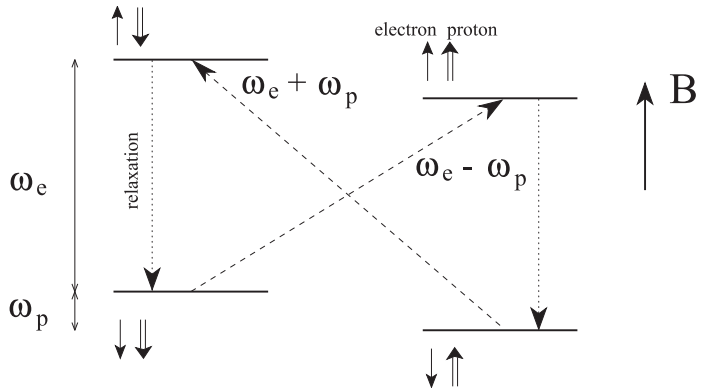

Figure 4.4: Energy levels for an e-p state in a strong magnetic field B. Arrows indicate direction of the proton $\Uparrow$ and electron $\uparrow$ spins; ω_p and ω_e are Lamor frequencies of the proton and electron, respectively. Figure comes from Ref. [78].

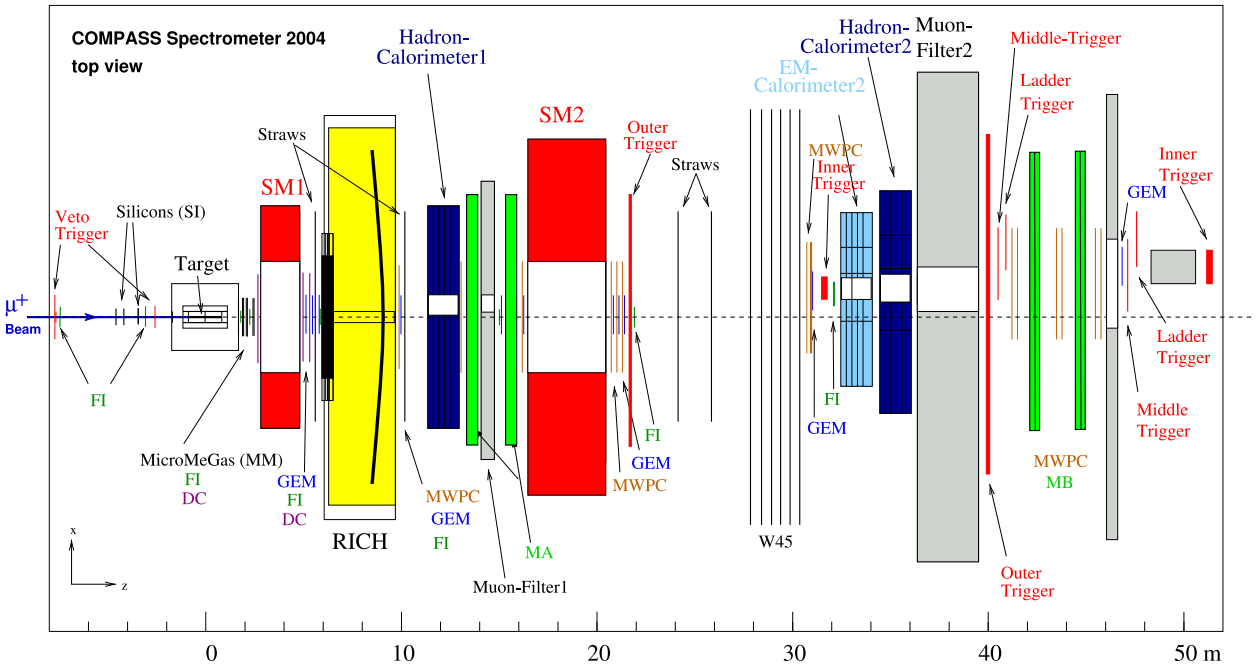

Figure 4.5: Compass 2004 muon setup top view (for detector names, see text).

covers an acceptance of ± 70 mrad (± 180 mrad since 2006). The LAS is equipped with the bending magnet SM1 of bending power 1 Tm. The inner ± 30 mrad is covered by the Small Angle Spectrometer (SAS) which is placed downstream of LAS (Fig. 4.5). The SM2 is the bending magnet of SAS with a bending power of 4.4 Tm.

In the region upstream of the target the Beam Telescope (BT) is located. In order to measure precisely the position and direction of incoming beam particles it is composed of Scintillating Fibres (FI) and Silicon micro-strip (SI) stations. Those detectors have good spatial resolution and can cope with high counting rates. In addition the FI detectors have a high resistance to radiation damages. A precise measurement of beam time, provided by the FI stations, is essential for its momentum determination as described in Chapter 5, whereas the knowledge of the spatial beam parameters is needed for the reconstruction of interaction vertex and scattering angle of the muon.

Both LAS and SAS are composed of several types of detectors:

- Very Small Area Trackers:

They are used for tracking of particles close to the beam axis and have to withstand similar conditions as the BT detectors. Also here the Scintillating Fibre (FI) stations are used.

- Small Area Trackers:
  Those detectors are dedicated for tracking of particles up to 40 cm from the beam axis. Two novel micro-pattern gaseous detector types are used for this purpose: GEM - Gas Electron Multiplier (GM) and MicroMeGas - Micromesh Gaseous Structure (MM). Their main characteristics is a separation of gas amplification area from the readout part. They can stand a high flux of incoming particles and introduce minimal amount of material into the beam. To avoid damages in the very high intensity region of the beam the high voltage can be switched off in the central part of the detectors, which is the case during the standard data taking. However the central parts are used for low intensity studies and the detector alignment.

- Large Area Trackers
  For outer parts of the spectrometer the granularity of the detectors can be much lower as the particle flux is significantly decreased. However good spatial resolution is still desired which led to the selection of drift detectors to be used in COMPASS. In LAS the Saclay Drift Chambers (DC) and Straw Tubes (ST) are used while for SAS the large drift chambers (W45) together with the Straw Tubes (ST) are used. In addition both spectrometers are equipped with Multiwire Proportional Chambers (MWPC).

- Calorimeters
  Since 2006 both LAS and SAS contain a hadronic and an electromagnetic calorimeter, HCAL1, ECAL1 and HCAL2, ECAL2 respectively. Until then ECAL1 hasn't been constructed yet and ECAL2 was only partially equipped with the readout electronics. Hadronic calorimeters are used for the discrimination between hadrons and muons and are a vital part of the trigger system. The electromagnetic calorimeters are used for detection of electrons and photons.

- Muon Filters
  The muon identification is performed by two detector systems, the Muon Wall detectors. These detectors, MA and MB, are located at the end of LAS and SAS, respectively. They consist of two sections of planes (MA - proportional chambers and MB - drift chambers) accompanied by hadron absorbers (60 cm of iron in the case of MA and 2.4 m of concrete in case of MB).

- RICH
  In the original design of the COMPASS experiment two Ring Image Cerenkov detectors were foreseen. Currently only LAS is equipped with RICH detector. It allows measurement of particle velocity which combined with momentum measurement performed in magnetic spectrometers provides the particle identification. Pions, kaons and protons can be identified for momenta greater than $2, 8, 18$ GeV respectively. The separation is possible for momenta up to 50 GeV.

- Trigger Hodoscopes
  Throughout the spectrometer dedicated trigger elements are placed which are designed to detect scattered muons. More detailed discussion of the trigger system is presented in the next section.

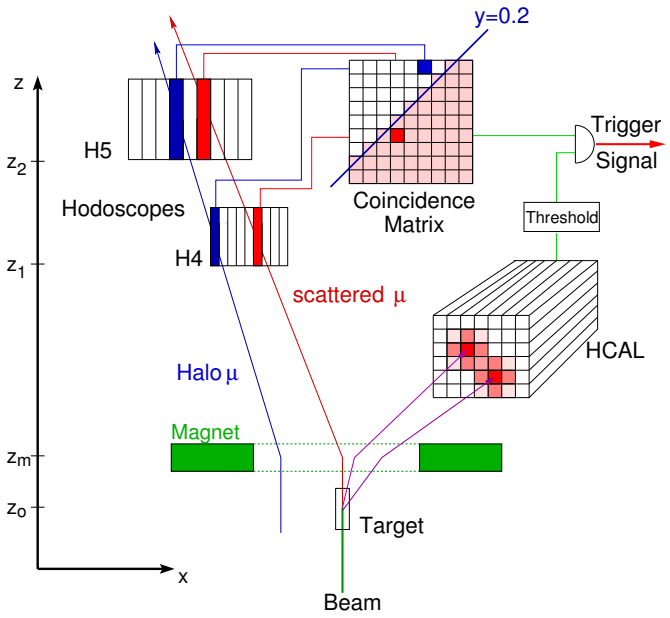

Figure 4.6: Concept of the trigger for quasi-real photo-production with high energy loss. The scattered muon leads to a coincidence in the activated area of the coincidence matrix while the halo muon fails. In addition, a minimum hadron energy can be required in the calorimeter.

4.5 Trigger system

The COMPASS Data Acquisition system (DAQ) is able to collect about 40k events per spill. In order to write to tapes only interesting events and to limit the data flux to a level that DAQ can handle, a trigger system detecting scattered muons was designed [79]. It also provides the timing for an event which is required for hit correlations and drift time calculations. As muons are scattered at non-zero angles a set of scintillator hodoscopes separated by distance ΔZ is used to detect them. Hits from the upstream hodoscopes are combined with hits from the downstream hodoscopes using time correlation. The correlation is performed by a coincidence matrix, which is an electronic chip that takes 32 rows and 32 columns of input signals. The rows correspond to channels of one hodoscope while columns to the other. Each matrix pixel implements a tight time window that suppresses random coincidences. In addition the pixels can be programmed do accept or reject the coincidences. The matrix patterns are determined from the known geometry and the desired acceptance in y. A schematic presentation of the coincidence evaluation by a coincidence matrix is presented in Fig. 4.6.

The hodoscopes are shielded by absorbers to filter out hadron and electron contamination. Due to broad physics program of COMPASS the scattered muons are detected in a wide kinematic range, $Q^2 \in (10^{-3}-10^2)$, $x \in (10^{-5}-1)$. As the flux of the particles varies significantly between different kinematic regions the granularity of various hodoscope planes has to be different as well. To cope with such requirements sets of different hodoscopes were introduced:

- IT - Inner Trigger: photo-production region with very small energy loss y of the scattered muon.
- LT - Ladder Trigger: photo-production region with large scattered muon energy loss y.
- MT - Middle Trigger: DIS region with small to moderate four-momentum transfers Q^2.

- OT - Outer Trigger: DIS region with moderate to large four-momentum transfers Q^2.

To increase the purity of triggers two additional requirements were made. The first one is no signal in Veto counters. The Veto detectors are installed upstream of the target and have holes in the centre that correspond to the size of the beam in that area. Beam particles that go through the target do not give signal in the Veto counters as opposed to the beam halo muons which travel at a distance from the target. The second condition, applied to certain triggers, is the requirement of an energy deposit in the hadronic calorimeters above a $6\,$GeV threshold. This criterion reduces contamination from radiative events, μe scattering and low energy halo tracks. The idea behind COMPASS trigger is presented in Fig. 4.6.

The Q^2 range which is available with mentioned triggers is limited by the SM2 acceptance for scattered muons. Since 2003 also a pure Calorimetric Trigger (CT) was introduced, when for an event to be recorded it is just enough if an energy deposit in the calorimeters exceeds $8 - 18\,$GeV. This extends the Q^2 range to events with scattered muon out of the acceptance of the hodoscope triggers.

Thus we have three types of triggers:

- Inclusive triggers - the triggers that require only coincidence of hits in scintillating hodoscopes (OT, incMT),
- Semi-inclusive triggers - the triggers that require additional energy deposit in the hadronic calorimeters apart from coincidence of hits in scintillating hodoscopes (IT, LT, MT),
- Pure calorimetric trigger - trigger based solely on the information from hadronic calorimeters (CT).

In Fig. 4.7 the kinematic regions covered by the different triggers as well as the relative contributions of the three trigger types are presented.

Additional triggers exist for calibration, efficiency and alignment studies:
- Beam Trigger - a beam particle is detected in first FI station,
- Veto Trigger - a beam halo particle is detected in Veto detectors,
- Random Trigger - the data acquisition is started randomly.

Events recorded with these triggers usually contain small number of particles which makes the reconstruction and interpretation simpler.

4.6 Data acquisition and analysis chain

The processing of experimental data can be divided into the off-line and on-line parts. The on-line part is responsible for filtering, recording and monitoring of the data in real time. The off-line part is responsible for reconstruction, physics analysis and also for simulations of the data using underlying physics models and a model of the experimental setup.

4.6.1 On-line analysis

The analog signals coming from about $200\,$k detector channels are digitised, as close to the detector as possible, on the front-end boards. Then they are concentrated into a few high bandwidth streams in the readout drivers. Two systems are used as the readout drivers in COMPASS [70]: the CATCH and the GeSiCA.

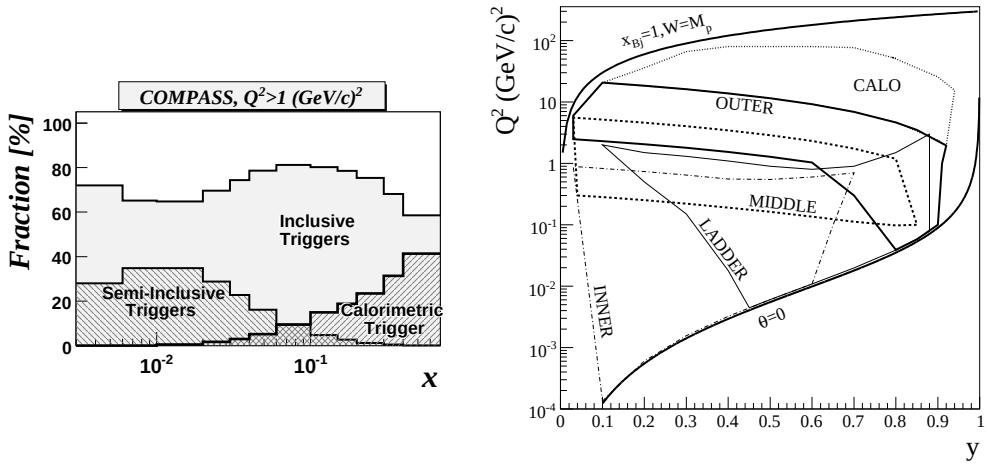

Figure 4.7: Left panel shows the fraction of inclusive, semi-inclusive, and calorimetric triggers as a function of x. Right panel presents the kinematical coverage in y and Q^2 for the COMPASS trigger subsystems. The two lines, $x_{Bj} = 1; W = M_p$ and $\theta = 0$ show the kinematic limits of elastic scattering and forward scattering, respectively.

From the CATCH/GeSiCA cards the data are transferred via optic links to spill buffers that are located in the Readout Buffer computers (ROBs). From the ROBs the data are transferred using a gigabit Ethernet network to the Event Builder computers where information from all detectors is combined into an event. Complete events are transferred to the Central Data Recording (CDR) at CERN where they are copied to tapes for long term storage (Fig. 4.8). The data acquisition (DAQ) software is based on DATE framework [80] developed for the ALICE experiment at the LHC accelerator.

In order to increase the maximum trigger rate that could be handled by DAQ an On-line Filter was introduced in year 2004. The time correlation between hits in BT detectors is used to reject events where a beam cannot be reconstructed. For semi-inclusive triggers also the correlation between beam time and calorimeter time is checked [81]. In 2002-2008 COMPASS collected $\sim 1\,$PB of raw data.

In order to ensure a correct performance of the DAQ and the detectors a constant monitoring during the data taking is required. For this purpose several tools are used:

- MurphyTV - allows for monitoring of readout errors that are returned by readout drivers.
- COOOL (Compass Object Oriented On Line) [82] - performs quick decoding of raw data and allows to create histograms of hit positions, time spectra *etc.*. This provides a monitoring of detector performance by comparison to reference histograms.
- DCS (Detector Control System) [83] - monitors all available parameters of various spectrometer elements *e.g.* temperatures, voltages, currents, NMR readings, gas flows. The implementation of safety "interlocks" in DCS prevents a detector damage due to abnormal operating conditions. Apart from monitoring it enables for interactive setting of detectors parameters.

4.6.2 Off-line analysis

The main part of the off-line data analysis is performed by the CORAL program [84]. It is responsible for decoding of the raw detector information into measured quantities (absolute hit positions, energy deposits in calorimeters, *etc.*). Then the reconstruction of charged particle tracks, interaction and decay vertices

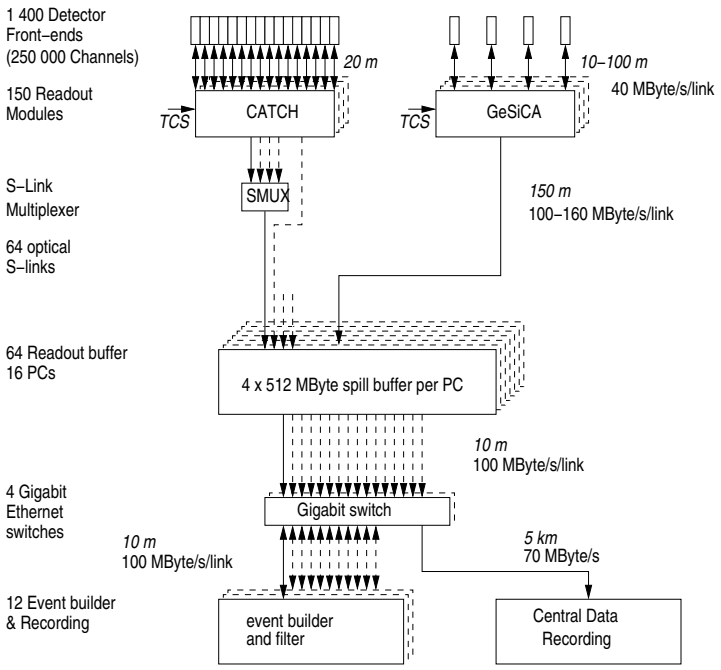

Figure 4.8: General architecture of the DAQ system. Digitised data from the detector front-ends are combined on the readout modules named CATCH and GeSiCA close to the detectors. The storage of the data during the spill and the event building is performed locally. The data are recorded at the CERN computer centre.

as well as calorimeter clusters is performed. For charged tracks, including beam tracks, the momentum is determined using bending in magnetic field. Finally also the RICH identification of particles is performed. In principle CORAL can be used also as a tool for physics analysis, but because the time needed to process the raw data is not negligible a higher level tool was developed for this purpose. CORAL remains the main tool for various calibration purposes and most notably for the detector alignment.

PHAST [85] operates with the Data Summary Tapes (DST). The DSTs contain all essential information about reconstructed events omitting the raw detector response. This provides significant size reduction (~ 10 times) that directly translates to the significant reduction of computational time. PHAST provides a versatile tool for event filtration and analysis of events in terms of desired physics quantities.

The DSTs are created using CORAL reconstruction in a process called production. As the time required for events reconstruction, using available computational resources, is comparable to the time spent on collecting them, the process has to be centralised. The production is performed on lxplus computing farm at CERN by a dedicated team of physicists. When producing the data collected during one week the versions of both the software as well as the calibration constants are being frozen. This ensures that the events from one period are reconstructed with the same conditions. Moreover as the relevant information is stored it can be used to study the impact of future improvements to the software or the calibration constants. The resulting DSTs are then copied to outside computing centres, *e.g.* Interdisciplinary Centre for Mathematical and Computational Modelling of Warsaw University [86], where the final physics analysis is performed.

The second part of the off-line analysis focuses not on direct analysis of the recorded data but rather on the Monte Carlo (MC) simulations of the data using a selected physics model and a model of the spectrometer. The MC simulations performed in the scope of this thesis are presented in Chapter 8.

Chapter 5

Reconstruction of the beam momentum

The momentum spread of the muon beam defined by the beam optics is about 5%. The precise determination of the beam particle momentum vector on event-by-event basis is a crucial ingredient to the correct estimation of the kinematic variables in the virtual photon-nucleon interactions, such as x and Q^2.

In the COMPASS experiment the measurement of the beam momentum vector is performed using the Beam Momentum Station (BMS) and the Beam Telescope (BT), both located upstream of the COMPASS target. The setups of BMS and BT are described in Sec. 5.1 and Sec. 4.4, respectively. In Sec. 5.2 the principle of the measurement is explained followed by a description of the used algorithm (Secs 5.3 and 5.4). The efficiency of the procedure is presented in Secs 5.5 and 5.6.

For a more detailed discussion of the beam momentum reconstruction at COMPASS see Refs [87, 88].

5.1 Beam Momentum Station

The BMS is located $\sim 100\,\text{m}$ upstream of the COMPASS target. Presently it consists of six planes measuring vertical coordinate, three before and three after the Bend 6 dipole magnet of the M2 beam line (Fig. 5.1). The incoming muons are bent in YZ plane enabling an accurate momentum estimation. Two types of detectors were used in the BMS:

- In 2002 the BMS had two planes before (BMS01/02) and two after (BMS03/04) Bend 6. These planes were built for the EMC experiment in 1970-ties. They consist of 64 scintillator elements of 5 mm pitch and 20 mm thickness. The slabs are oriented horizontally so that they are measuring the position of beam impact in vertical direction. They provide an excellent time resolution of 0.3 ns [70]. To obtain an equal occupancy of all channels the slabs exposed to higher beam intensity are divided into several parts as shown in Fig. 5.1 [87, 70].

- In 2003 a degrading performance and lack of spare parts of the ageing electronics of BMS01-04 stations lead to the decision that two new stations will be built. The upstream telescope was supplemented with the new BMS05 station halfway between the BMS01 and BMS02 stations. The plane consists of 4 double-layers of scintillating fibres each of 2 mm in diameter as shown in Fig. 5.2. Each readout channel collects the signals from two adjacent columns of the scintillating fibres. This results in effective 64 channels with a pitch of 2.5 mm and a very good spatial resolution [89]. However, the time resolution of 500 ps is worse compared to the BMS01-04 stations, which limits the impact of this plane on momentum reconstruction.

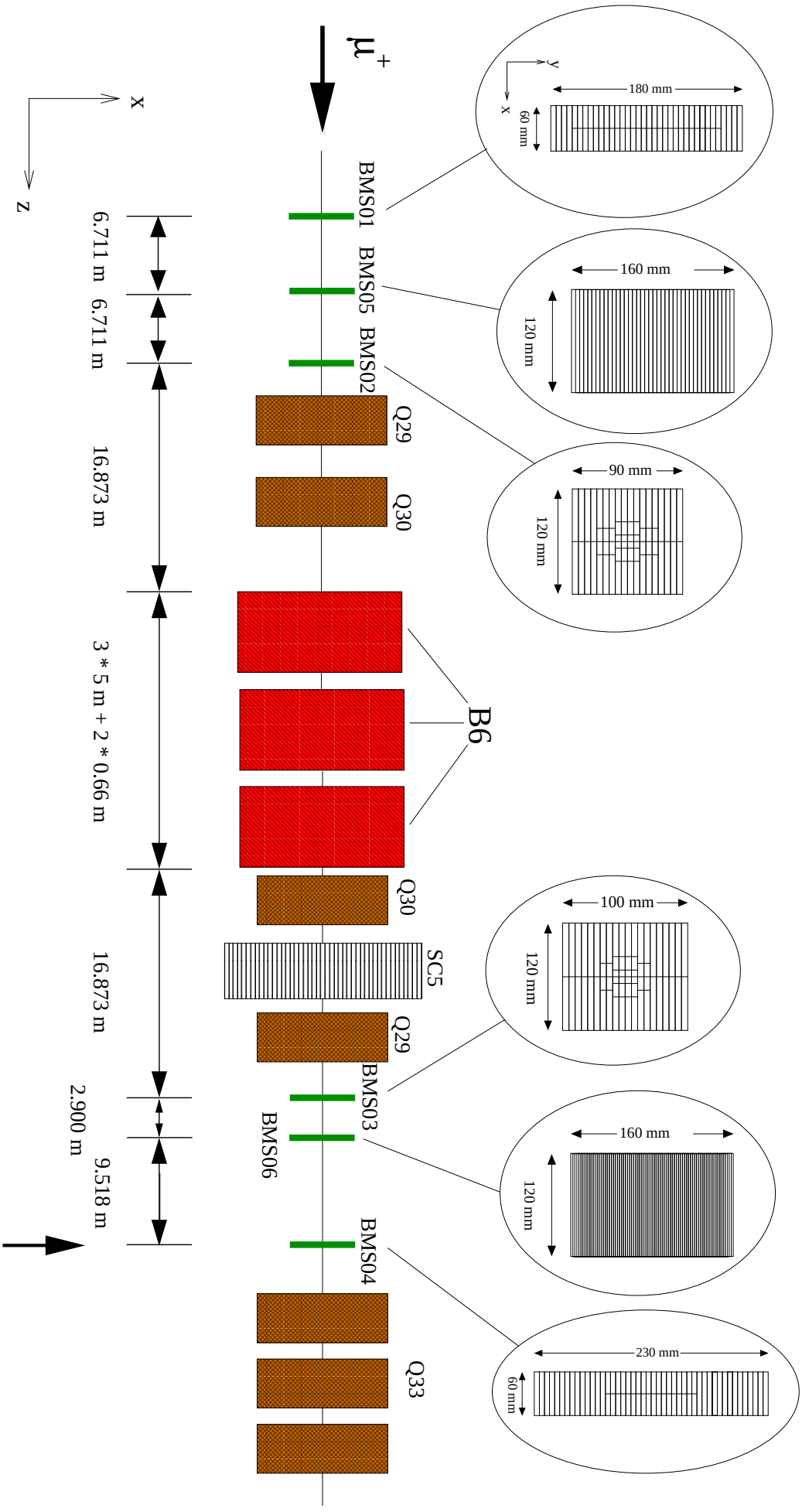

Figure 5.1: The schematic view of the Beam Momentum Station (BMS) setup. The green elements are the BMS detector planes. Their dimensions and division into channels is presented. The setup is positioned on two sides of the Bend 6 magnet group (B6). Elements marked with "Q" are the quadrupole magnets while the SC5 is a scraper. (The plot is not up to scale). Figure comes from Ref. [87].

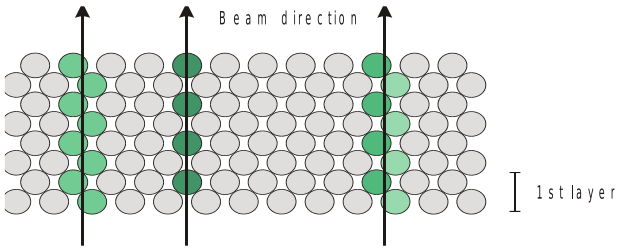

Figure 5.2: A schematic view of the BMS05/06 planes. The plane consists of 4 double-layers of scintillating fibres. The odd and even sub-layers are offset by 1/2 of the pitch. In case of BMS05 the columns are grouped by 2 to form channels. For BMS06 each column corresponds to one detector channel. Figure comes from Ref. [89].

- In 2004 the new BMS06 station was introduced between the BMS03 and BMS04 planes. It was produced using the same technology as the BMS05 but the readout is performed for individual columns which results in a pitch of 1.25 mm and 128 channels. As the same multi-anode photomultiplier technology was used for the readout as in the BMS05, it suffers from the same suboptimal time resolution.

After installation of the BMS05 and while the BMS06 plane was still prepared, a solution was found that enabled refurbishing of the readout electronics of the BMS01-04. This lead to an improvement of their performance [89]. In consequence the impact of the newly built planes became limited.

5.2 Principle of the measurement

Both the information about the momentum of a beam particle and its direction are needed to obtain the kinematics of event. The momentum is measured by the BMS and the direction by the BT. Matching this information is not a trivial task as the stations are set ~ 100 m apart and the beam particle travelling between them goes through several bending and focusing magnets. Thus the main criteria used to obtain a Beam Candidate is the time correlation of the hits in the considered detectors.

In order to determine the momentum, positions of hits in at least three planes, two on one side, and one on the other side of Bend 6, are needed. Three points in space are sufficient to provide a flight direction and a bending angle. Hits from other planes can be used for the compatibility test by means of χ^2, as the system will be then over-constrained. We primarily consider only events with three or four hits in the BMS01-04 planes, as the BMS05 and BMS06 are implemented as “rescue” planes (see Sec. 5.4). In order to minimise the computational time the momentum and the χ^2 are parametrised as a function of three or four measurements. The parametrisation is based on a MC simulation of the beam with a given momentum profile, travelling through the field of the bending magnet and surrounding quadrupoles. The simulated tracks are used to calculate hits in the hodoscope planes. To simplify the problem only combinations with at most four hits are considered, thus beam tracks are represented in four dimensional space.

Principle Component Analysis (PCA) is used to further reduce the complexity. The goal of the PCA is to compute the most meaningful basis to re-express the input data set. The new basis is assumed to be a linear combination of the old one while principal components are assumed to be the ones that have the largest variance. The latter assumption holds in case the precision of the measurement is high. New basis is constructed to be orthogonal. Obtaining the new basis where the components are orthogonal and associated to directions with the largest variance is achieved by the diagonalisation of the covariance matrix [90, 91].

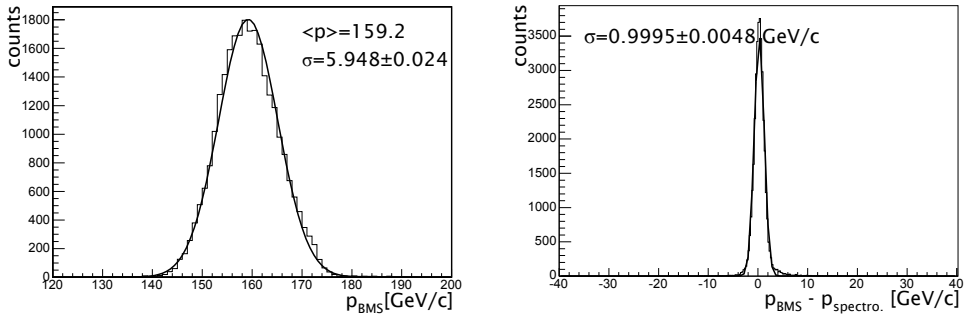

(a) (b)

Figure 5.3: The beam momentum spectrum as measured by the BMS for events with one beam track (a). The difference between momentum measured in the BMS and in the spectrometer (b). The curves represent Gaussian fits, obtained value of σ is quoted on the plots.

Finally the beam track momentum is parametrised as a function of track parameters in the new basis. The parameters of the functional form are determined by minimisation of χ^2 for a large sample of MC beam tracks [92, 93, 87]. The procedure produces a parametrisation of the form

$$p = < p > + f_p(\overrightarrow{g}), \qquad \chi^2 = f_{\chi^2}(\overrightarrow{g}), \tag{5.1}$$

where $< p >$ is the average momentum at which the simulation was done, $\overrightarrow{g} = (Y_1^{'}, Y_2^{'}, Y_3^{'}, Y_4^{'})$ is the vector of the coordinates $Y_i^{'}$ of the track in the new basis (linear combinations of the Y_j hit positions), f_p parametrises the deviation of the momentum from the mean value as a function of hits positions, while f_{χ^2} parametrises the χ^2. Such approximation gives an accuracy of the momentum reconstruction of about 0.7 GeV.

In Fig. 5.3a the obtained momentum spectrum for events with one beam candidate is shown. To test the reconstruction accuracy and to verify that no bias is introduced the momentum determined in the BMS was compared with the momentum measured for the same track in the spectrometer. The result is presented in Fig. 5.3b and it is clearly seen that the two measurements are in good agreement. Assuming the relative resolution of momentum measurement in the spectrometer to be $\sigma(p)/p = 0.5\%$ [70] the resolution of the BMS measurement is ~ 0.6 GeV.

5.3 Reconstruction of BMS tracks

The following description of the BMS track reconstruction is applied primarily only to the BMS01-04 hits. As described in the next section, the BMS05-06 planes are treated as “rescue” planes and in this case the algorithm is the same as for 3-hit BMS01-04 tracks.

In order to reduce the combinatorial background a loose time window around the trigger time is applied to the BMS hits. It is adjusted to include all hits that have been associated to a beam track. As seen in Fig. 5.4 selecting a $\pm 10\, ns$ window will not remove good events while reducing significantly the combinatorial background. For selected hits all possible 4-hit combinations are considered. To remove fake combinations a time correlation between the hits is required. The cut on the time difference between the hits in subsequent planes is set to 3σ of the distribution of correlated hits, shown in Fig. 5.5. If more than one combination of

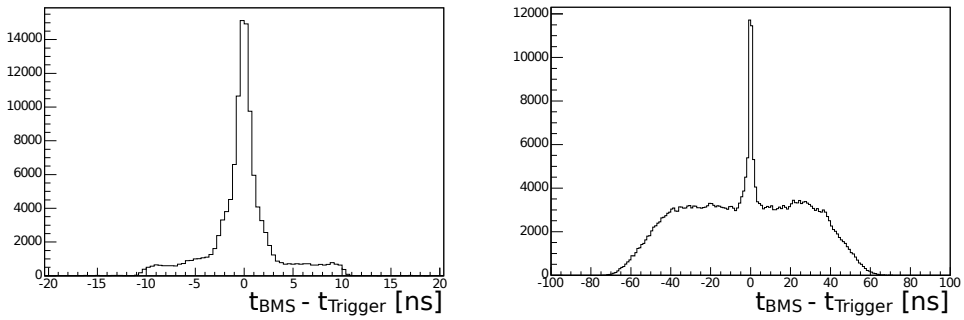

(a) Associated BMS hits (b) Unassociated BMS hits

Figure 5.4: Figures present the distributions of time difference between the BMS hits and the trigger time. Plot (a) consists of BMS hits that are associated to reconstructed Beam Candidates for unambiguous events. It is seen that it is contained in the ± 10 ns region. Plot (b) contains all BMS hits, where large combinatorial background is seen spreading up to ± 70 ns.

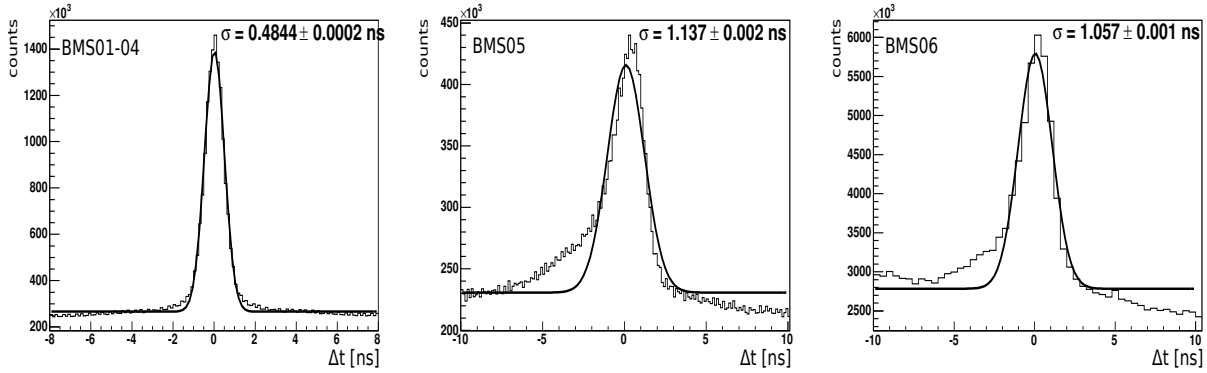

Figure 5.5: Distribution of hit time differences Δt between hits in BMS01-04 planes (left), all pair combinations are considered. The middle (right) figure presents distribution of hit time differences Δt between hits in BMS01-04 planes and BMS05 (BMS06) plane. The curves represent Gaussian fits, obtained value of σ is quoted on the plots.

time-correlated hits is found, it is required that they do not share more than one hit. In such a case the combination with the best time correlation is selected. The hits that were not used for the 4-hit track candidates are combined into 3-hit track candidates using the same criteria as for the previous class of tracks.

The BMS track candidates are then correlated with tracks reconstructed in the BT to obtain a Beam Candidate with a measured momentum vector. The track reconstruction in the BT is performed by the standard CORAL tracking package TRAFDIC [94]. BMS track candidates and BT tracks are required to have small time difference (less than 3σ of the distribution of time correlation of BMS and BT tracks - Fig. 5.6a). Finally all beam candidates have to be correlated with the trigger within a 3σ window around the trigger time (Fig. 5.6b). Ambiguities are resolved at this stage using the back-propagation procedure explained below.

For a Beam Candidate we can use momentum determined in the BMS, direction measured in the BT and the description of the beam transport known from the MC to check the compatibility of BMS and BT data. Using transport equations a back propagation algorithm of the BT track to the position of BMS planes is performed. Then the probability of the hypothesis that BMS hits correspond to the extrapolated track is calculated [88]. If several BMS tracks are combined to a BT track or vice versa, the combination with the highest probability is selected (Fig. 5.7). The events where the probability for the best beam candidate is

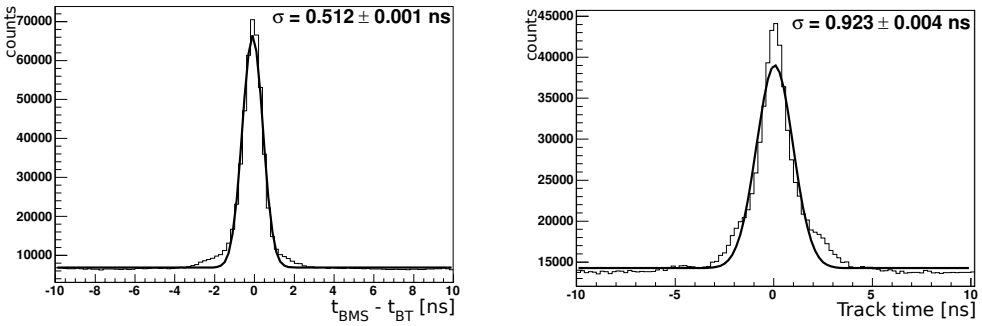

(a) (b)

Figure 5.6: The time difference between the BMS and BT tracks for unambiguous events (a). Beam track mean time (b). Zero corresponds to the trigger time. The curves represent Gaussian fits, obtained value if σ is quoted on the plots.

below 0.005 are flagged. Thus such events can be discarded later during the physics analysis.

In Fig. 5.8 the differences between measured and extrapolated positions in BMS planes for unambiguous events are presented showing a very good correlation. For the planes upstream of the B6 bending magnet the spread is about two times larger as compared to the downstream planes. The B6 magnet causes large vertical dispersion in the transport equation as a function of track momentum. Thus, for the back-propagated track it results in an additional contribution to the uncertainty of Y coordinate in the upstream planes. The offsets of the distributions from zero are caused by a misalignment of BMS planes with regards to the spectrometer as well as beam steering (*cf.* the discussion of global transformations of the spectrometer in Sec. 6.4). The offsets are evaluated on year-by-year basis and then included in the χ^2 calculation.

As the result of this procedure we could get three possibilities:

- No Beam Candidate is found and the event is rejected. To suppress such events rescue algorithms were developed which are presented in the next section.
- There is exactly one Beam Candidate found.
- There are more than one Beam Candidates found. All the candidates are used as an input for the vertex fit.

5.4 Rescue algorithms

In order to reduce the fraction of events with no beam candidate found when only the information from the BMS01-04 planes was used, two rescue procedures were developed.

First one involves BMS05 and BMS06 planes. All hits in BMS01-04 that were not associated to 4 or 3-hit track candidates are checked for the time correlation with BMS05 hits. As the time resolution of the scintillating fibre planes is worse compared to that of BMS01-04, a wider time window is applied. Accepted BMS track candidates are matched with the BT tracks. If the procedure fails then in the same manner BMS06 is utilised.

As a last resort the back-propagation rescue algorithm is used. Two hits in BMS01-04 planes and a direction obtained from the BT track are used to form a Beam Candidate. The momentum can be determined

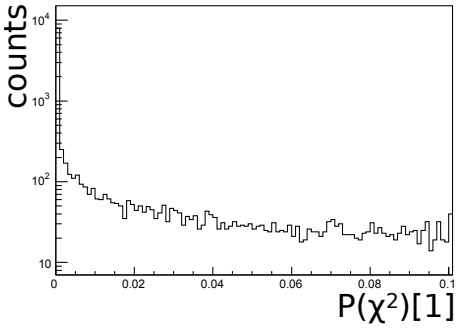

Figure 5.7: Probability distribution for the correlation between the measured Y coordinates in BMS planes and extrapolated ones for beam track candidates.

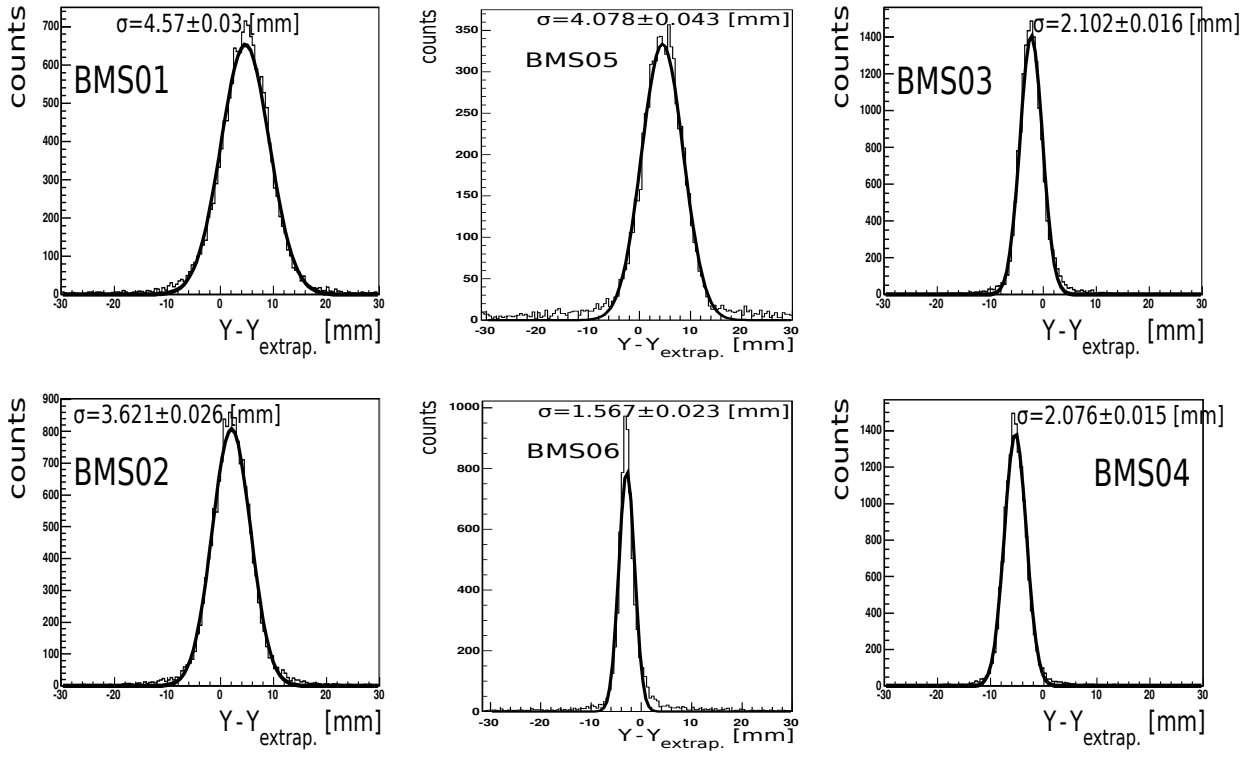

Figure 5.8: Results of the back-propagation procedure. The differences between the Y coordinates as measured in a given BMS plane and obtained using extrapolation of BT tracks. Top row presents the BMS planes located upstream of the B6 magnet (left - most upstream plane). Bottom row presents the BMS planes located downstream of the B6 magnet (right - most downstream plane). The curves represent Gaussian fits, obtained value if σ is quoted on the plots.

Plane	BMS01	BMS02	BMS03	BMS04	BMS05	BMS06
Efficiency	94.7%	93.1%	93.7%	90.1%	93.8%	90.6%

Table 5.1: The efficiency of the BMS01-06 planes extracted from the 2004 data with nominal beam intensity and standard physics triggers.

	0 BC	1 BC	>1 BC
Random trigger events	6.7%	89.9%	3.3%
Physics trigger events	11.8%	69.2%	19.0%

Table 5.2: The fraction of events with one, more then one and without a reconstructed Beam Candidate (BC) for the 2004 data.

if time and spatial χ^2 cuts are satisfied and at least one hit is present upstream of the Bend 6 magnet. Efficiency of this method was tested on unambiguous Beam Candidates where two hits were artificially removed [88].

5.5 Determination of BMS efficiency

An efficiency for a BMS plane, for example let us consider plane number 1, can be defined as $\varepsilon_1 = \frac{N(1,2,3,4,5,6)}{N(2,3,4,5,6)}$, where $N(1,2,3,4,5,6)$ is the number of events for which all planes fired and $N(2,3,4,5,6)$ is the number of events where at least all planes besides the plane 1 fired. For the purpose of efficiency determination a plane is considered as fired if it has a hit within a time window around the trigger time. The window was set to be $\pm 2\sigma$ of the BMS plane time resolution. Similarly, the efficiency of other planes are defined. Results obtained from the 2004 data with nominal beam intensity are presented for all BMS planes in Table 5.1.

To estimate the efficiency of the whole beam reconstruction algorithm we must select events that contained a beam particle. Moreover selected beam particles should have travelled through the involved detectors, *i.e.* the BMS and the BT. Events where the trigger was caused by a halo muon would artificially reduce the efficiency as such muons most probably do not cross all active areas of the BMS. Therefore a sample of random trigger events was used with beam track reconstructed in FI detectors downstream of the target [88]. The beam track was required to pass through both target cells, which ensures that in the considered event there was a beam track in the geometrical acceptance of the BMS planes. A random trigger was used because in case of physics trigger the sample of events with beam track detected and reconstructed in the spectrometer is suppressed; the physics triggers are designed to select events where the beam muon has interacted in the target. Also the beam trigger cannot be used because the Beam Telescope (SciFI station FI01 X and Y planes) is a part of this trigger and this would introduce a bias to the estimation of efficiency. In Table 5.2 the beam momentum reconstruction efficiency for the 2004 data is presented. For comparison the efficiency calculated for physics triggers is also shown. The beam momentum reconstruction efficiency is estimated to be 93.3% based on random trigger events. In 3.3% of events more than one Beam Candidates were found. For nominal data taking the algorithm is able to reconstruct the beam momentum in 88.2% of events.

BMS planes used	0 BC	1 BC	>1 BC	Improvement
BMS01-04	6.9%	89.7%	3.3%	N/A
BMS01-05	6.7%	89.9%	3.3%	0.2±0.2%
BMS01-06	6.7%	89.9%	3.3%	0.0±0.2%

Table 5.3: The fraction of events with one, more then one and without a reconstructed Beam Candidate (BC) for three cases: BMS01-04 is used, BMS05 is also considered, all six BMS planes are utilised. The impact of BMS05 is already quite small and addition of the BMS06 plane does not provide further improvement.

5.6 The impact of the BMS06

Implementation of the BMS06 plane in the reconstruction algorithm, as well as tuning of the cuts used in the selection of good BMS hits for the 2004 data were responsibilities of the author. Due to a poor time resolution of this station a decision was made that it should be used in the same way as the BMS05.

In order to check if the implementation of the BMS06 in the algorithm of beam momentum reconstruction is working properly it was compared to the results obtained with BMS05 plane. Reconstruction of the beam momentum was performed twice with the same data sample. Once with only BMS03-05 planes included into the algorithm and for the second time with only BMS01-02 and BMS06. In the first case the BMS05 is the only active plane upstream of B6 magnet thus it will always have to be used to obtain a Beam Candidate. In the second case the BMS06 is the only plane downstream of B6 magnet and will always be used to obtain a Beam Candidate. For the considered data sample 3984 Beam Candidates were reconstructed with BMS05 hit and 4071 Beam Candidates were obtained when using BMS06. Thus we can conclude that both rescue planes give compatible results.

In Table 5.3 the impact of the BMS06 plane for the 2004 data is presented. Currently information provided by the BMS06 is almost not used in the reconstruction. There are two reasons that make the BMS06 redundant: the implementation of the plane only as a rescue one and the very good efficiency of BMS01-05 stations. However, it is fully implemented in the reconstruction algorithm and it can be used in case of a failure of one of the old planes without interruption of the data taking.

5.7 Conclusions on the beam momentum reconstruction.

A detailed description of the beam momentum reconstruction algorithm was presented along with discussion of fine tuning of its parameters for the 2004 data. The achieved efficiency of the beam momentum reconstruction is 93% for the 2004 data with uncertainty on the reconstructed momentum of $\sim 0.6\,\mathrm{GeV}$. In order to improve the redundancy of the BMS setup the new BMS06 plane was introduced into the algorithm. Finally as the BMS05 plane was produced using the same technology as BMS06, it was tested that the reconstruction using the BMS06 plane gives results comparable to the case where BMS05 was used.

Chapter 6

Alignment of the COMPASS spectrometer

An alignment of detectors can be divided into two stages. In the first one detectors are physically positioned with a precision of $\sim 1\,\text{mm}$ based on measurements performed by the surveyors. In the second stage, the positions of detectors are determined using reconstructed tracks of charged particles and each detector plane is aligned to a fraction of the detector resolution. This is a difficult task as the spectrometer includes more than 300 detector planes and for each plane at least 3 degrees of freedom have to be tuned. In addition, detectors have different sizes (from $4 \times 4\,\text{cm}^2$ up to $4 \times 5\,\text{m}^2$) and resolutions (from $10\,\mu\text{m}$ to $10\,\text{cm}$). To make the situation more complex the magnetic fringe fields affect detectors measurements which calls for alignment in the presence of magnetic fields.

The knowledge of positions of tracking detectors, up to the best possible precision, is crucial for the efficient track reconstruction as well as for the vertex reconstruction and is important for precise determination of event kinematic variables.

The following chapter will focus on the offline part of the detectors alignment. Sec. 6.1 describes the parameters that are optimised in the alignment procedure. Secs 6.2, 6.3 and 6.4 describe the principle of alignment method. In Sec. 6.5 the alignment procedure is presented and Sec. 6.6 describes how alignment quality can be quantified.

The author was responsible for alignment of the COMPASS spectrometer for almost two years: June 2005 - December 2006 and June-July 2008. In Sec. 6.7 some of the results are presented. For a detailed discussion of detector alignment at COMPASS see also Refs [95] and [96].

6.1 Alignment parameters

6.1.1 Coordinate systems

The main COMPASS coordinate system is the following:

- Z axis - along the beam direction,
- Y axis - vertical directed from bottom to top,
- X axis - defined in such a way that the system is right-handed.

With each detector a local coordinate system is defined:

- Z axis - the same as in the main coordinate system,
- U axis - in the detector plane and perpendicular to strips/wires,
- V axis - defined in such a way that the system is right-handed.

6.1.2 Parameters

The position of each detector can be described by a set of parameters. For alignment purposes following set was chosen:

- δu, the transverse detector offset perpendicular to the detector wires,
- $\delta\theta$, the rotational detector offset in a plane perpendicular to the beam axis,
- δz, the longitudinal detector offset along the beam axis.

The transverse offset of a detector along the wires (δv) cannot be directly taken into account since the detector does not give any information about the position along this direction. However if a detector station consists of at least two planes with a non zero angle between the measured directions then the δv can be determined.

A pitch of the detector is a distance between adjacent wires, strips or pads. It may happen that a pitch of a detector is different from the design value. To adjust the pitch value a δp parameter was introduced. A value $(1 + \delta p)$ is used as a scaling factor for the detector pitch. The δp parameter is strongly correlated with the δz offset along the beam axis. Actually if all the tracks were straight and originated from the same point, then a strict relation would hold: $\delta p = \delta z/z$. Even if these assumptions are not fulfilled still the δp parameter can be used to partially correct for the misalignment in Z.

There are at least two additional parameters that could be used: $\delta\theta_u$, $\delta\theta_v$ which describe the rotational offsets out of the plane perpendicular to the beam axis. However the internal representation of detectors in COMPASS tracking software (CORAL) assumes that the detectors are perpendicular to the beam. This makes such parameters unusable in our case. Still if misalignments in θ_u and θ_v are small, their effect on the tracking would be of second order with respect to other parameters.

6.2 Principle of alignment

Measured hits in detectors are used to reconstruct tracks of charged particles. The difference ΔS between position of hits as measured by detectors and expected from the track model can be expressed as a function of three independent sets of parameters

$$\Delta S_j(u_j, \alpha^t, \alpha^a_j) \tag{6.1}$$

with u_j being hit position in the j-th detector, the track parameters α^t (*e.g.* in case of absence of magnetic fields the track is approximated by a straight line), and alignment parameters α^a_j of the j-th detector. There is a set of track parameters α^t for each considered track. However the alignment parameters α^a are common to all tracks.

To obtain corrected detectors positions a minimisation of a global χ^2 of all considered tracks is performed. The χ^2 is defined as

$$\chi^2 = \sum_{i=1}^{n_{track}} \sum_{j=1}^{n_{det}} \frac{[\Delta S_{ij}(u_{ij}, \alpha_i^t, \alpha_j^a)]^2}{\sigma_j^2} \tag{6.2}$$

where n_{track} is the number of used tracks, n_{det} is the number of detectors contributing to the track i, u_{ij} is a hit position of the i-th track as measured by the j-th detector, σ_j is the detector resolution, α_i^t are parameters of the track i and α_j^a are alignment parameters of the detector j. If the dependence of ΔS on the parameters α^t and α^a is linear the minimisation of the χ^2 can be performed analytically. We write

$$\Delta S_{ij} = \Delta S_{ij}^0 + \sum_k \frac{\partial \Delta S_{ij}}{\partial \alpha_k} \alpha_k, \tag{6.3}$$

where the sum extends over all tracking and alignment parameters and ΔS_{ij}^0 is the value of ΔS_{ij} when all parameters are set to zero. In order to perform the minimisation, all partial derivatives with respect to the parameters are requested to be zero. Thus we obtain

$$\frac{1}{2}\frac{\partial \chi^2}{\partial \alpha_m} = \sum_i \sum_j \frac{1}{\sigma_j^2} \frac{\partial \Delta S_{ij}}{\partial \alpha_m} \left(\Delta S_{ij}^0 + \sum_k \frac{\partial \Delta S_{ij}}{\partial \alpha_k} \alpha_k \right) = 0, \tag{6.4}$$

where m goes over all tracking and alignment parameters. This results in following matrix equation

$$\begin{pmatrix} \sum_i \sum_j \frac{1}{\sigma_j^2} \frac{\partial \Delta S_{ij}}{\partial \alpha_1} \frac{\partial \Delta S_{ij}}{\partial \alpha_1} & \cdots & \sum_i \sum_j \frac{1}{\sigma_j^2} \frac{\partial \Delta S_{ij}}{\partial \alpha_1} \frac{\partial \Delta S_{ij}}{\partial \alpha_m} & \cdots \\ \vdots & \ddots & \vdots & \\ \sum_i \sum_j \frac{1}{\sigma_j^2} \frac{\partial \Delta S_{ij}}{\partial \alpha_m} \frac{\partial \Delta S_{ij}}{\partial \alpha_1} & \cdots & \sum_i \sum_j \frac{1}{\sigma_j^2} \frac{\partial \Delta S_{ij}}{\partial \alpha_m} \frac{\partial \Delta S_{ij}}{\partial \alpha_m} & \\ \vdots & & & \ddots \end{pmatrix} \begin{pmatrix} \alpha_1 \\ \vdots \\ \alpha_m \\ \vdots \end{pmatrix} = - \begin{pmatrix} \sum_i \sum_j \frac{1}{\sigma_j^2} \frac{\partial \Delta S_{ij}}{\partial \alpha_1} \Delta S_{ij}^0 \\ \vdots \\ \sum_i \sum_j \frac{1}{\sigma_j^2} \frac{\partial \Delta S_{ij}}{\partial \alpha_m} \Delta S_{ij}^0 \\ \vdots \end{pmatrix}. \tag{6.5}$$

It is easily seen that only a few terms are non zero thus the equation can be rewritten as follows

$$\left(\begin{array}{c|c|c|c} \sum_i C_i & \cdots & G_i & \cdots \\ \hline \vdots & \ddots & 0 & 0 \\ \hline G_i^T & 0 & \Gamma_i & 0 \\ \hline \vdots & 0 & 0 & \ddots \end{array}\right) \left(\begin{array}{c} \alpha_a \\ \hline \vdots \\ \hline \alpha_i^t \\ \hline \vdots \end{array}\right) = \left(\begin{array}{c} \sum_i b_i \\ \hline \vdots \\ \hline \beta_i \\ \hline \vdots \end{array}\right). \tag{6.6}$$

In this equation the matrices C_i, Γ_i, G_i and the vectors b_i and β_i contain contributions from the i-th track. C_i are symmetric matrices of dimension n_{det} while b_i is a vector of with size n_{det} and both contain partial derivatives of ΔS with respect to the alignment parameters α^a. The Γ_i are symmetric matrices of size ν equal to the number of parameters per track (size of α_i^t vector). The β_i are vectors of size ν. Both Γ_i and β_i include only derivatives of ΔS with respect to track parameters α^t. The G_i is a matrix with a row number of n_{det} and a column number of ν and includes mixed terms of type $(\partial \Delta S_{ij}/\partial \alpha_j^a)(\partial \Delta S_{ij}/\partial \alpha_i^t)$.

Solution of this equation requires inversion of the matrix. The time needed for a matrix inversion grows as n^3 where n is its size. Inversion of a symmetric 10000×10000 matrix requires ~ 1 hour of computation on 2.6 GHz CPU and ~ 200 MB of memory for single precision representation [97]. Such size of the matrix is easily achieved using 2500 tracks (described by 4 parameters each) and about 1000 alignment parameters

which are used in COMPASS to describe ~ 300 detector planes (3 parameters each). During alignment of the COMPASS spectrometer often much larger samples have to be used to obtain reliable results as a lot of detectors have none or very small overlap in terms of tracks crossing their active areas. Apart from computational constrains the direct inversion of very large matrices suffers from numerical divergences which can become a limiting factor.

Fortunately the matrix in Eq. 6.6 is sparse and has a special structure. It can be shown [97] that the alignment parameters can be obtained from the equation

$$\alpha_a = (C')^{-1} b', \tag{6.7}$$

where

$$C' = \Sigma_i C_i - \Sigma_i G_i \Gamma_i^{-1} G_i^T, \qquad b' = \Sigma_i b_i - \Sigma_i G_i \Gamma_i^{-1} \beta_i. \tag{6.8}$$

Thus instead of inversion of the full matrix we have to invert Γ_i matrices one-by-one and then perform inversion of the C' matrix. Size of the C' matrix is equal to the number of alignment parameters. The inversion of C' becomes feasible because its size is much smaller than the size of the full matrix and is independent of the number of tracks. The matrix inversion which is the core of the alignment program is performed by a "Millepede" routine which was written by Volker Blobel, the co-author of Ref. [97].

6.3 ΔS function and its derivatives

6.3.1 Alignment with straight tracks

Alignment procedure requires determination of ΔS function (Eq. 6.1) and its derivatives. As stated before the ΔS depends on alignment parameters and on an assumed track model. In the simplest case, when the magnetic fields are turned off, the tracks can be approximated by straight lines. Alignment runs taken with SM1 and SM2 magnets switched off are used as a first step of the COMPASS alignment procedure. The position of the track at z_j position of detector j is described by

$$x_j = x_0 + t_{x0}(z_j - z_0), \qquad y_j = y_0 + t_{y0}(z_j - z_0). \tag{6.9}$$

Here x_0, y_0 and z_0 are the track coordinates in the reference plane, usually chosen as the most upstream plane containing a hit associated to the track. The $t_{x0} = \frac{dx}{dz}$, $t_{y0} = \frac{dy}{dz}$ are the tangents of the track angles with respect to the beam axis at the position z_0.

ΔS can be expressed in terms of the track model and alignment parameters

$$\begin{aligned} \Delta S_j = (1+\delta p)\{&cos(\theta+\delta\theta)\{x_0 + t_{x0}(z_j + \delta z - z_0] \\ &+ sin(\theta+\delta\theta)[y_0 + t_{y0}(z_j+\delta z - z_0)]\} - (u_j + \delta u), \end{aligned} \tag{6.10}$$

where θ is the angle between the U and X axes.

The partial derivatives over track parameters are

$$\frac{\partial \Delta S}{\partial x_0} = cos\theta, \qquad \frac{\partial \Delta S}{\partial y_0} = sin\theta, \qquad \frac{\partial \Delta S}{\partial t_{x0}} = cos\theta(z_j - z_0), \qquad \frac{\partial \Delta S}{\partial t_{y0}} = sin\theta(z_j - z_0). \tag{6.11}$$

And the partial derivatives over the alignment parameters are expressed as

$$\frac{\partial \Delta S}{\partial \delta u} = -1, \qquad \frac{\partial \Delta S}{\partial \delta z} = t_{x0}cos\theta + t_{y0}sin\theta, \qquad \frac{\partial \Delta S}{\partial \delta \theta} = -x_j sin\theta + y_j cos\theta, \qquad \frac{\partial \Delta S}{\partial \delta p} = x_j cos\theta + y_j sin\theta. \tag{6.12}$$

6.3.2 Alignment in the presence of magnetic field

Fringe fields of SM1 and SM2 magnets affect nearby detectors. In case of drift detectors there is a Lorenz force $q\overrightarrow{v} \times \overrightarrow{B}$ acting on the drift electrons inside the detector. The deflection causes the electrons to be registered by a different readout channel compared to the field-off case. This can be viewed as an effective movement of the detector in the presence of magnetic filed and is discussed in more detail in Sec. 6.7. The second effect originates from magnetised support structures of certain detectors. When the magnetic field is switched on after alignment run, their position can change due to a movement of the supports. Due to the mentioned effects, the alignment with magnetic field-on is essential for the COMPASS experiment.

In case of magnetic field-on the tracks are no longer straight. This calls for a more sophisticated track model to perform the minimisation. Such a model is based on the representation of tracks used in CORAL reconstruction program. In this model a track can be described by its parameters in the j-th detector as reconstructed by CORAL (x_j^0, y_j^0, t_{xj}, t_{yj}) corrected by linear deviations

$$x_j = x_j^0 + \delta x_0 + \delta t_{x0}(z_j - z_0), \qquad y_j = y_j^0 + \delta y_0 + \delta t_{y0}(z_j - z_0). \tag{6.13}$$

Here δx_0, δt_{x0}, δy_0, δt_{y0} are small corrections to the CORAL parameters. In such approach we are taking an advantage of CORAL to describe bent tracks properly, while the linear corrections of the initial CORAL track parameters allow to perform the iterative minimisation. It means that the model parameters can be updated without a need to perform a new tracking procedure. In the framework of this model we obtain an expression for ΔS

$$\begin{aligned}\Delta S_j = (1+\delta p)\{&cos(\theta+\delta\theta)\{x_j^0 + t_{xj}\delta z + \delta x_0 + \delta t_{x0}(z_j + \delta z - z_0] \\ &+ sin(\theta+\delta\theta)[y_j^0 + t_{yj}\delta z + \delta y_0 + \delta t_{y0}(z_j + \delta z - z_0)]\} - (u_j + \delta u).\end{aligned} \tag{6.14}$$

When compared with straight tracks (Eq. 6.10) we see that the track parameters have been modified by δx_0, δt_{x0}, δy_0, δt_{y0} but the derivatives stay unchanged. Concerning derivatives over alignment parameters the only change to Eqs 6.12 is that t_{x0} and t_{y0} should be replaced by t_{xj} and t_{yj}.

6.4 Constraints

The procedure described above is used for a relative alignment, where positions of detectors relative to each other will be constrained by the requirement for minimal χ^2. However global transformations of the

spectrometer, like simultaneous rotations or translations of all detectors, will not affect the χ^2. In order to prevent introduction of global transformations some constraints have to be introduced into the alignment procedure. This is done by introducing a reference system by fixing the alignment parameters of some detectors in the spectrometer. Usually the GM04 and GM10(09) are used. Those detectors are far enough from SM1 and SM2 magnets not to be affected by their fringe fields. They also provide a good compromise between the size (the constraining detector should cover as wide area as possible) and the resolution (as high as possible resolution is desired). The positions of these detectors should be easily obtainable from high precision surveyors measurements, which is indeed the case for GM04 and GM10(09).

6.5 The alignment procedure

During the data taking special runs for alignment purposes are recorded. Usually a set of two runs is taken: one with magnetic fields of SM1 and SM2 magnets turned off and the other with the nominal magnetic fields. Runs are taken with low intensity of the beam: about $10^6\,\mu$/spill. Special types of triggers are used for these runs in order to illuminate Large Angle Trackers with beam and halo tracks resulting in ~ 15k triggers per spill. Initial positions of the detectors are taken from measurements performed by surveyors. These measurements are performed for markers on the detector frame, so called fiducial marks, and an achieved precision is up to $300\,\mu m$. From obtained fiducial marks positions the position of the centre of active area of the detector has to be calculated. Quite often it is not feasible to measure the required four points on the detector frame. Coupled with imprecise knowledge of the detectors internal structure and human errors this leads to a degradation of the precision. Hence it is assumed that a position of a detector is known with precision of ~ 1 mm. For the rotation angle θ and the pitch usually the nominal values are taken.

The procedure consists of three steps. In the first one the alignment is performed using field-off runs. This ensures no misalignment between parts of the spectrometer upstream and downstream of the magnets and assures that there will be no momentum bias. In the next step the alignment is performed using field-on data, either from a special alignment run or a standard run used for physics analysis. The later one ensures the same conditions for detectors as during data taking and takes into account dependence of detectors response to fringe fields of SM1 and SM2 magnets. In the second step usually a data sample with standard triggers is used. In this case the beam tracks interact mostly in the target and are associated to a primary vertex. The relative alignment of detectors upstream and downstream of the target is not performed in this step. This is done in the third step using a special selection of "off-time" tracks. By including tracks that do not coincide in time with the trigger we increase the amount of pile-up beam muons in the sample. The probability that a pile-up particle interacts in the target is low and therefore the approximation of the tracks with straight lines in the target area is valid. At this step during χ^2 minimisation the alignment parameters of detectors downstream of the target are fixed. This means that we are adjusting position of the Beam Telescope (which is upstream of the target) with regards to the rest of the spectrometer.

Each step is divided into three phases:

1. In the first one the data sample is reconstructed by the CORAL program using a description of the spectrometer stored in *detectors.dat* file. As an output, a ROOT [98] tree containing information about reconstructed tracks, hits and clusters is created.

2. In the second phase the information from the tree is used as an input for χ^2 minimisation performed by the Millepede. As a result a set of alignment parameters for each detector is obtained.

3. In the last phase the positions stored in *detectors.dat* file are updated using results from the second phase.

As described in Sec. 6.2 we assumed that ΔS depends linearly on the alignment parameters and on the track parameters. In general it does not have to be true. However, the method still works well provided the corrections are small. If they are not small enough, it is possible to perform an iterative procedure; the updated alignment parameters are used to reconstruct the tracks again and perform a new alignment. The number of iterations depends on the size of the needed correction relative to the detector resolution. On average it is enough to perform three iterations for the procedure to converge.

6.6 Quality criteria

An evaluation of the alignment quality is based on two sets of criteria: absolute and relative ones.

6.6.1 Absolute criteria

Absolute criteria are defined as those where the value of considered observable is known for the perfectly aligned spectrometer. Such criteria can be either global, *e.g.* χ^2/ndf of the tracks, reconstructed invariant masses of particles like K^0, D^0, J/Ψ, or they can be defined per detector plane. Global criteria characterise quality of alignment of the spectrometer as a whole. They are very important as different parts of the spectrometer could be misaligned despite all the local criteria being satisfied.

There are four distributions that are used as local criteria for each detector plane:

- The distribution of residuum $\Delta u = u_{cluster} - u_{track}$, the difference between the position of a hit cluster and a reconstructed track. The mean value of Δu is sensitive to a possible transverse displacement δu. The quality of alignment is indicated both by the position of the centre of this distribution and its shape. Unusual shape could indicate a misalignment, though it can be often attributed to problems in the detector itself or to an error in its calibration constants.

- Δu as function of u. The slope of the correlation is sensitive to misalignment of pitch parameter and to some extent to δz offset.

- Δu as function of v. The slope is sensitive to rotational offset $\delta\theta$.

- Δu as function of θ. The slope is mostly sensitive to δz offset. However, as δz is highly correlated with δp it is also sensitive to misalignment of pitch, similarly to Δu versus u.

6.6.2 Relative criteria

As it was mentioned in previous section the local criteria are not sufficient to monitor alignment quality. On the other hand the absolute global criteria like the masses can be extracted precisely only using large statistics, which makes them not useful for constant monitoring of the alignment. Thus other global criteria were defined:

- Number of all reconstructed tracks per event,
- Ratio of the numbers of tracks reconstructed in the LAS and the SAS,
- Number of reconstructed vertices per event,
- Number of tracks associated to vertex,
- Fraction of events with reconstructed primary vertex.

Few words of explanation about the first two relative criteria is in order. For example, in case if there is misalignment of spectrometer zones before and after SM2 magnet, a particle can be reconstructed as two tracks, one in the LAS and the other in the SAS, instead of one long track. The correction of the misalignment will lead to a decrease of the number of reconstructed tracks. Thus, in case of perfectly aligned spectrometer the number of all reconstructed tracks will not be maximal, we rather expect that ratio of numbers of tracks in the LAS and the SAS will be close to 1.

One more set of variables is used for relative criteria, although not for constant monitoring of alignment quality. These are the widths of reconstructed particle mass distributions, *e.g.* $K^0, D^0, J/\Psi$. As for the criteria listed above, the expected values of the widths are not known even for perfectly aligned spectrometer. Thus these can be used mainly to compare between different descriptions of spectrometer geometry. The evaluation using global criteria is performed on data collected during standard physics runs. The special alignment runs are not used for this purpose.

6.7 Results

6.7.1 Convergence of alignment procedure

In Fig. 6.1 the convergence of the procedure is presented. Three detectors were artificially misaligned: FI07 was transversely shifted by 1σ, GM05 pitch was enlarged by 1% and MM03 was rotated by 1°. Then four iterations of the alignment were performed. One can see in the plots that small misalignments are corrected immediately. However, the procedure is not able to correct for a large misalignment in one iteration. Performing a few iterations enables the alignment to converge.

6.7.2 Impact of magnetic fields

As stated in Sec. 6.3.2 the alignment with magnetic fields is essential for the COMPASS setup. This originates from the fact that some of the detectors are affected by the fringe fields of SM1 and SM2 magnets. This phenomenon is illustrated in Fig. 6.2. White histogram represents the distribution of residuals Δu for GM01X and GM02X planes. It is obtained from an alignment run with magnets turned off. On can see that detectors are correctly aligned - mean values of the residuals are centred at zero. Shaded histogram corresponds to the data taken during a physics run a few minutes after the alignment run. A clear discrepancy is observed between the mean values of residual distributions. The “movement” in case of GM01X is five times larger than the detector resolution. The effect is not visible in Y projections because it is only present in bending plane of the magnets. The GM01-03 stations are located close to the SM1 magnet and are exposed to its

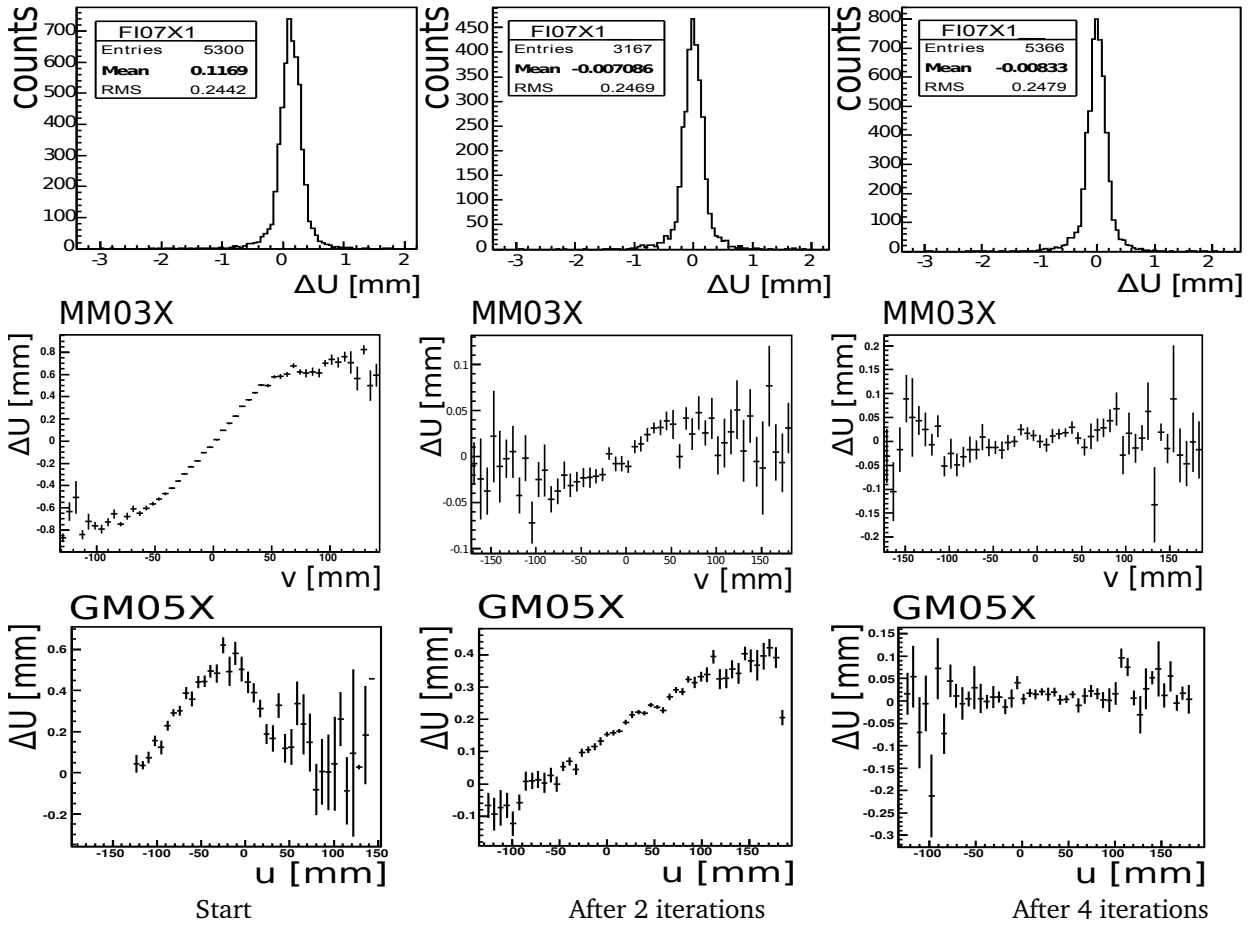

Figure 6.1: The convergence of alignment procedure. Top row shows distributions of residuals for FI07X detector with initial misalignment of 1σ of its resolution. The middle row shows the residuals as a function of the position v perpendicular to the measured direction of MM03X detector. The initial misalignment of the detector's angle θ was 1°. The bottom row presents the residuals as a function of position u along the measured direction of the GM05X detector. The initial misalignment of detector's pitch p was 1%. The columns present the results for the initial conditions (left), after 2 iterations of alignment procedure (middle) and after 4 iterations (right).

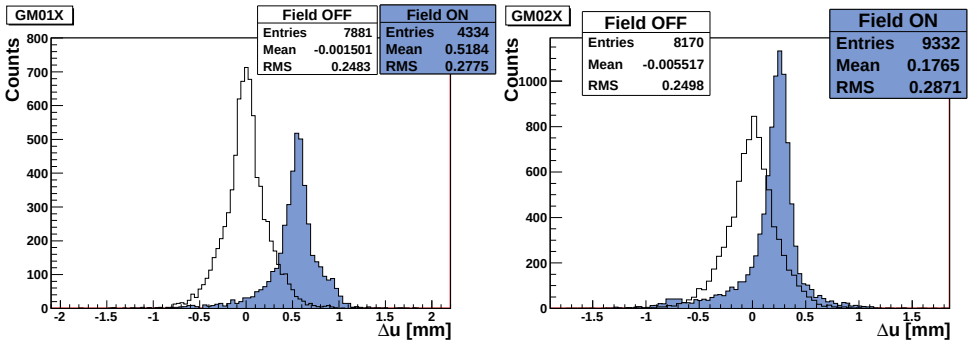

Figure 6.2: The residuals Δu for detector planes GM01X (left) and GM02X (right). Empty histograms present residuals obtained on data collected with magnets switched OFF. The residuals are centred at zero indicating proper alignment. The shaded histograms present residuals obtained from data collected with magnets switched ON using the same geometry description as for the FIELD OFF case. A clear offset from zero is visible.

Criterion	Corrected - Previous	σ	t
$<\chi^2>$: all tracks	-0.8720	0.0044	198.18
$<\chi^2>$: LAS	-0.9570	0.0030	319.00
$<\chi^2>$: SAS	-1.0710	0.0077	139.09
$<\chi^2>$: μ'	-0.9820	0.0049	200.41
# Tracks / Event	72.60	13.16	5.52
% Events with PV	0.020	0.117	0.17
% Events with μ'	0.050	0.034	1.47
# Sec. vert. / Event	0.694	0.243	2.86
# Tracks in PV	0.017	0.004	4.25

Table 6.1: Change of relative criteria values for event reconstruction using proper geometry description compared to reconstruction using geometry description from previous week of data taking. It is seen that all the criteria have improved. Moreover the improvement for all but one is statistically significant.

large fringe field. As explained in Sec. 6.3.2 the trajectories of the drift electrons are deflected which causes wrong determination of the impact point of ionising particle that traversed the detector.

6.7.3 Alignment sensitivity

During the data taking usually once per week a one day "Machine Development" (MD) takes place. During the MD technicians perform the accelerator maintenance. Detector experts in the experiment usually take advantage of that time to perform repairs or upgrades of detectors. Often it results in a movement of detectors and thus requires a new alignment. Table 6.1 shows a comparison of tracking performances for the data taken *after* a MD with two different *detectors.dat*, where one was obtained using the data collected *before* the MD and the second one *after* the MD. The criteria used for the performance evaluation can be grouped into two sets. First one consist of average track χ^2's for different track sub-samples. We expect to observe a decrease of χ^2 with improved alignment. The second set contains: fraction of events with reconstructed PV, average number of tracks associated to PV, fraction of events with reconstructed scattered muon, average number of secondary vertices per event. For the criteria in the second set we expect to observe an increase with improved alignment. Indeed, all of the criteria indicate a better performance of the track reconstruction with new alignment.

The values of the considered criteria vary significantly on the event-by-event basis. Thus as an estimate of uncertainty of their comparison a t-test is used (Chapter 12 of Ref. [99]). For each criterion a variable $t =< X_A - X_B > /\sigma(X_A - X_B)$ is calculated, with X_i being the values of the criterion X for the two samples. The values of $t > 1$ indicate a significant difference between the samples. As the error we take the σ of the distribution of differences between mean values extracted from several sub-samples.

6.7.4 Global alignment

As explained in Sec. 6.4 the alignment procedure provides the relative alignment of detector planes. In order to cope with possible shifts and rotations of the whole spectrometer additional position constraints (pivot points) are used. The position of the pivot points is crucial as even small bias in their position will lead to a global movement of the spectrometer. Such an effect is presented in Fig. 6.3. The alignment was performed with fixed parameters of GM04 and GM10 detectors. The new positions of detectors were compared to positions obtained from surveyors measurements. All detectors with available results of survey

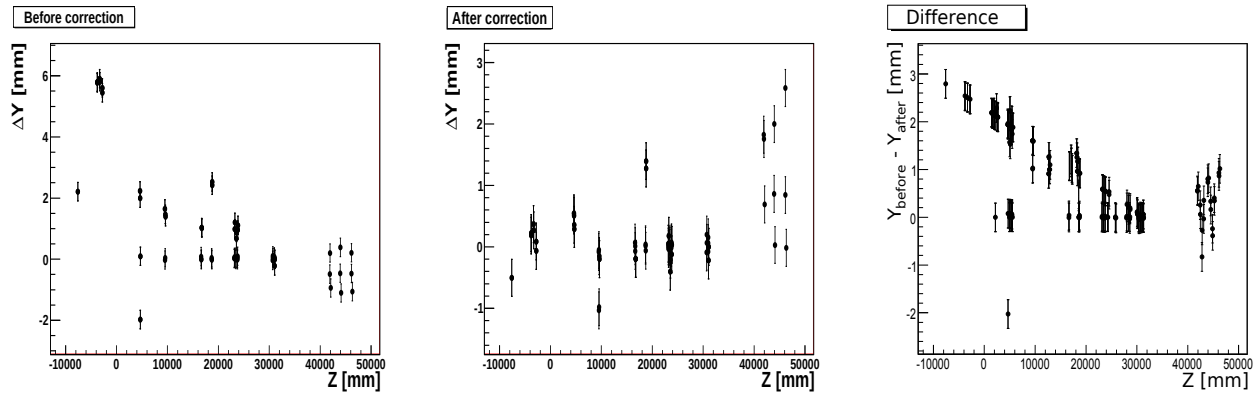

(a) Wrong position of GM04 (b) Correct position of GM04 (c) Difference

Figure 6.3: The difference between surveyors measurements of detectors positions along Y coordinate and the Y position determined by alignment as a function of detectors placement along the beam axis Z (Figs. (a) and (b)). Plot (a) illustrates results of alignment with erroneously determined position of GM04 detector used as *pivot point* in the alignment. Plot (b) presents the results of alignment after the position of the GM04 detector was corrected. Plot (c) presents the difference between positions obtained from the alignment procedure before and after the correction.

measurements were taken into account. The plot shows the difference between position obtained from the alignment and from the survey as a function of Z position of detector (Figs 6.3a and 6.3b). The error bars correspond to the resolution of surveyors measurement.

In Fig. 6.3a the points are grouped along two lines, one is along the Z axis and the second one is at an angle with regards to the Z axis. The points that lay along the Z axis correspond to detectors that do not measure the Y coordinate thus their Y position was not changed by the alignment procedure. The points grouped along a line at an angle to the Z axis indicate a global rotation of the spectrometer.

The problem was traced and found to be due to an error in the calculation of the position GM04 detector‘s centre (the GM04 detector was used as a *pivot point* in the alignment procedure and is located at $Z = 960\,\text{cm}$). Also the centres of SI detectors were determined erroneously. After the correction of their position the alignment procedure was repeated from scratch. The result is presented in Fig. 6.3b with the spectrometer rotation not present. The Fig. 6.3c displays the difference between the results of the alignment procedure performed twice (before and after the correction). It contains more points as values for the detectors without surveyor measurements are also plotted. A consistent rotation of obtained spectrometer geometry is observed.

Chapter 7

Data analysis

In this chapter details of the data analysis are given. First the theoretical basis of evaluation of gluon polarisation, $\Delta G/G$, is discussed. It is followed by a review of external information needed for $\Delta G/G$. Then the different methods of cross section asymmetry and $\Delta G/G$ extraction are detailed. The last part of this chapter is dedicated to description of the events selection.

7.1 Gluon polarisation from high p_T hadron pairs

7.1.1 Motivation for selection of high p_T events

As it was shown in Sec. 2.2.4 the uncertainty of determination of the ΔG from QCD evolution of g_1 structure function is currently very large. This is due to the fact that only limited range of x and Q^2 is covered by present experiments with polarised beams and targets. In order to determine the gluon spin contribution to the nucleon spin a direct measurement is required. To perform such a measurement a probe that has access to gluons is needed. In DIS experiments the Photon Gluon Fusion (PGF, $\gamma g \to q\bar{q}$) process can be used as a such probe. In the PGF a virtual photon interacts with a gluon from the nucleon with production of a quark-antiquark pair (Fig. 7.1a). As the PGF is the lowest order pQCD process where lepton interacts with gluon from the nucleon we will be calling it (and all other processes of the same order) as LO pQCD. With a polarised beam and a polarised target one gets an access to the spin dependent gluon distribution functions via the measurement of the double spin asymmetry.

To tag such events in the COMPASS experiment we use two complementary channels. First one is the open charm production with the D meson in the final state. Because the contribution of the charmed quarks in the nucleon is expected to be small, then in LO pQCD the only process contributing to the charm pro-

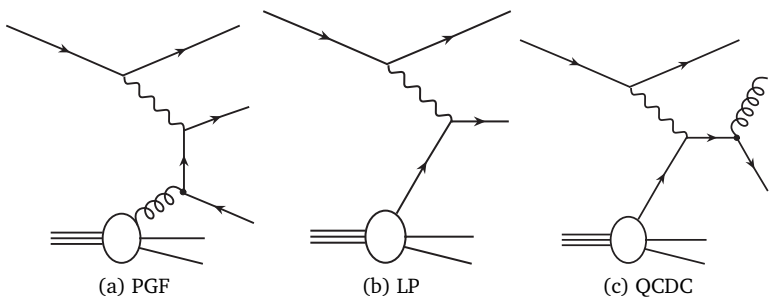

(a) PGF (b) LP (c) QCDC

Figure 7.1: PGF and background processes.

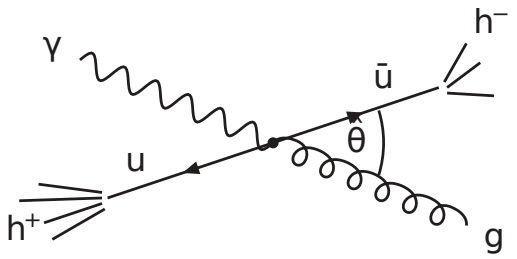

Figure 7.2: The PGF process in the centre-of-mass system of gluon and photon.

duction is the PGF. By selecting charmed mesons we obtain a signal free from physics background. The disadvantages of this channel are a limited statistics, due to a strong suppression of this channel by the large mass of charmed quark, and a large combinatorial background. The method and the obtained results are described in detail in Refs [10, 49]. The second method is based on a selection of a pair of hadrons with high transverse momenta. The high p_T channel data were divided into two kinematic regions, $Q^2 < 1\,\text{GeV}^2$ and $Q^2 > 1\,\text{GeV}^2$. The division originates from the limited regions of applicability of various MC generators which are essential for this analysis, as described in Chapter 8. The results and the details of the analysis covering low Q^2 region are presented in Refs [11, 100], while $Q^2 > 1\,\text{GeV}^2$ region is considered in this thesis.

In contrast to the open charm channel, in this analysis we consider mainly production of light quarks (u, d, s), hence the statistics is much larger. The drawback for this channel is the contribution from background processes which have to be considered as well. The background to the PGF comes from the Leading Process (LP, $\gamma q \to q$), the QCD Compton (QCDC, $\gamma q \to qg$) (see Figs 7.1b and 7.1c) as well as from Resolved Photon Processes which are studied in more detail in Sec. 10.7. The LP in the inclusive case contributes to $\sim 80\%$ of events, therefore it has to be strongly suppressed by our event selection.

The PGF process in the photon-gluon centre-of-mass system is shown in Fig. 7.2. In this system the produced quarks are emitted back-to-back. After the Lorentz boost to the laboratory system they can still have large transverse momenta with respect to the virtual photon direction [101]. Another contribution to the transverse momenta of produced quarks come from the intrinsic transverse momentum k_T of partons. The distribution of transverse momentum of quarks in the nucleon can be described by a Gaussian distribution with a mean value $\langle k_T \rangle \approx 440\,\text{MeV}$. The outgoing quark carries a fraction x of struck parton momentum, thus on average it gets the transverse momentum $\langle k_T \rangle \cdot x < 400\,\text{MeV}$. As described in Sec. 2.3, due to the confinement the quarks are not observed as free particles. During the process of fragmentation they are "dressed" into hadrons. The transverse momentum of a hadron, with respect to the produced quark direction, obtained in the fragmentation is of the same order as $k_T; < p_T^{frag} > \approx 360\,\text{MeV}$. Adding both in quadrature leads to a value of $570\,\text{MeV}$. Requiring two hadrons with larger transverse momentum will suppress contribution from LP as k_T and fragmentation are the only sources of transverse momentum in this case. The QCDC process is not suppressed by such requirement, as due to the gluon emitted in the final state the produced hadrons can acquire transverse momentum besides contributions from intrinsic partons k_T and from the fragmentation. The detail description of event selection is presented in Sec. 7.4.

7.1.2 Extraction of $\Delta G/G$

As the background processes cannot be eliminated from the event sample the measured double spin asymmetry will contain contributions from all of them

$$A_{LL}^{p_T} = \frac{\Delta\sigma}{\sigma} = \frac{\Delta\sigma^{PGF} + \Delta\sigma^{QCDC} + \Delta\sigma^{LP}}{\sigma^{PGF} + \sigma^{QCDC} + \sigma^{LP}}. \tag{7.1}$$

Assuming factorisation of the cross section into *hard* and *soft* parts, the cross sections for the contributing processes can be expressed as

$$\begin{array}{rclcrcl} \sigma^{PGF} & = & G \otimes \hat{\sigma}^{PGF} \otimes H & , & \Delta\sigma^{PGF} & = & \Delta G \otimes \Delta\hat{\sigma}^{PGF} \otimes H \quad , \\ \sigma^{QCDC} & = & \sum\limits_f e_f^2 q_f \otimes \hat{\sigma}^{QCDC} \otimes H & , & \Delta\sigma^{QCDC} & = & \sum\limits_f e_f^2 \Delta q_f \otimes \Delta\hat{\sigma}^{QCDC} \otimes H \quad , \\ \sigma^{LP} & = & \sum\limits_f e_f^2 q_f \otimes \hat{\sigma}^{LP} \otimes H & , & \Delta\sigma^{LP} & = & \sum\limits_f e_f^2 \Delta q_f \otimes \Delta\hat{\sigma}^{LP} \otimes H \quad . \end{array} \tag{7.2}$$

Here $\hat{\sigma}^i$ and $\Delta\hat{\sigma}^i$ are the spin averaged and spin dependent partonic cross sections describing interaction of virtual photon with the struck parton (bottom vertex of Feynman diagrams in Fig. 7.1), the sum $\sum_f$ is over all contributing quarks and antiquarks, and H is the fragmentation function for given process into observed final state (*cf.* Sec. 2.3), which is assumed to be spin independent as long as the polarisation of the final hadronic state is not studied. For simplicity the dependence of the fragmentation function H on the initial partonic state is not shown explicitly.

Let us rewrite the polarised cross section for the PGF process in the following form

$$\Delta\sigma^{PGF} = \frac{\Delta G \otimes \Delta\hat{\sigma}^{PGF} \otimes H}{G \otimes \hat{\sigma}^{PGF} \otimes H} \cdot G \otimes \hat{\sigma}^{PGF} \otimes H = \frac{\frac{\Delta G}{G} G \otimes \frac{\Delta\hat{\sigma}^{PGF}}{\sigma^{PGF}} \sigma^{PGF} \otimes H}{G \otimes \hat{\sigma}^{PGF} \otimes H} \cdot \sigma^{PGF}. \tag{7.3}$$

Thus leading to

$$\Delta\sigma^{PGF} = \left\langle \frac{\Delta G}{G} \hat{a}_{LL}^{PGF} \right\rangle \sigma^{PGF}, \tag{7.4}$$

where $\hat{a}_{LL}^{PGF} = \Delta\hat{\sigma}^{PGF}/\sigma^{PGF}$ is the partonic cross section spin asymmetry, also referred to as the analysing power, and the average of a quantity X is defined as

$$< X >= \frac{\int_{sample} X(x) G(x) \hat{\sigma}^{PGF}(x,z) H(z) dx dz}{\int_{sample} G(x) \hat{\sigma}^{PGF}(x,z) H(z) dx dz}. \tag{7.5}$$

The average $\left\langle \frac{\Delta G}{G} \hat{a}_{LL}^{PGF} \right\rangle$ can be decomposed into a product of average values

$$\left\langle \frac{\Delta G}{G} \hat{a}_{LL}^{PGF} \right\rangle = \frac{\int \frac{\Delta G}{G} \hat{a}_{LL}^{PGF} G \hat{\sigma}^{PGF} H}{\int G \hat{\sigma}^{PGF} H} = \frac{\int \frac{\Delta G}{G} \hat{a}_{LL}^{PGF} G \hat{\sigma}^{PGF} H}{\int \hat{a}_{LL}^{PGF} G \hat{\sigma}^{PGF} H} \frac{\int \hat{a}_{LL}^{PGF} G \hat{\sigma}^{PGF} H}{\int G \hat{\sigma}^{PGF} H} = \left\langle \frac{\Delta G}{G} \right\rangle_{a_{LL}} \left\langle \hat{a}_{LL}^{PGF} \right\rangle, \tag{7.6}$$

where the average $\left\langle \frac{\Delta G}{G} \right\rangle_{a_{LL}}$ contains $\hat{a}_{LL}^{PGF}$ in the weight.

Now we will assume that $\Delta G/G(x)$ is a linear function of x. Although the shape of this distribution is not known, it is a good approximation provided the result is obtained in narrow bins of x. With this assumption the average $\left\langle \frac{\Delta G}{G} \right\rangle_{a_{LL}}$ can be approximated [102] by value of $\Delta G/G$ at average x, $\langle \Delta G/G \rangle_{a_{LL}} \approx \Delta G/G(\bar{x}_G)$, thus leading to

$$\Delta\sigma^{PGF} \approx \frac{\Delta G}{G}(\bar{x}_G) \left\langle \hat{a}_{LL}^{PGF} \right\rangle \sigma^{PGF}. \tag{7.7}$$

The same procedure applied to QCDC and LP leads to

$$\Delta\sigma^{QCDC} \approx A_1^{LO}(\bar{x}_C) \left\langle \hat{a}_{LL}^{QCDC} \right\rangle \sigma^{QCDC}, \tag{7.8}$$

$$\Delta\sigma^{LP} \approx A_1^{LO}(\bar{x}) \left\langle \hat{a}_{LL}^{LP} \right\rangle \sigma^{LP}, \tag{7.9}$$

where

$$A_1^{LO} \equiv \frac{\sum_f e_f^2 \Delta q_f}{\sum_f e_f^2 q_f}. \tag{7.10}$$

Putting Eqs 7.7-7.9 into Eq. 7.1 we obtain

$$A_{LL}^{p_T}(x) = R_{PGF} \left\langle \hat{a}_{LL}^{PGF} \right\rangle \frac{\Delta G}{G}(\bar{x}_G) + R_{QCDC} \left\langle \hat{a}_{LL}^{QCDC} \right\rangle A_1^{LO}(\bar{x}_C) + R_{LP} \left\langle \hat{a}_{LL}^{LP} \right\rangle A_1^{LO}(\bar{x}), \tag{7.11}$$

where $R_i = \sigma^i/\sigma$ is a fraction of the process i in the sample. Fractions R_i are estimated using a MC simulation. The $x_i = (\hat{s} + Q^2)/2M\nu$ is the fraction of nucleon momentum carried by the struck parton; a gluon in case of PGF (x_G) and a quark in case of QCDC (x_C), with $\hat{s}$ being the invariant mass of the system virtual boson - interacting parton. The partonic asymmetries $\hat{a}_{LL}^i$ are calculated in LO pQCD. For A_1^{LO} there are two possibilities to estimate it. As it is expressed in terms of polarised and unpolarised quark distributions (PDFs) existing parametrisations of the world data could be used. The other option is to use directly the measured inclusive asymmetry A_1. The second option was selected in this thesis because for the determination of PDFs assumptions on the shape of ΔG and G as a function of x are needed and this could lead to a bias of extracted $\Delta G/G$.

Previous *high* p_T analyses [12, 103, 104] had done further assumptions. First, it was assumed that the measured inclusive asymmetry $A_{LL}^{inc} \approx A_1 D$ contains only the LP contribution. With such assumption we obtain A_1 as (*cf.* Eqs 2.18, 2.28 and 2.30)

$$A_1 \approx \frac{\sum_f e_f^2 \Delta q_f}{\sum_f e_f^2 q_f} \equiv A_1^{LO}. \tag{7.12}$$

Thus the equation for $A_{LL}^{p_T}$ can be rewritten as

$$A_{LL}^{p_T}(x) \approx R_{PGF} \left\langle \hat{a}_{LL}^{PGF} \right\rangle \frac{\Delta G}{G}(\bar{x}_G) + R_{QCDC} \left\langle \hat{a}_{LL}^{QCDC} \right\rangle A_1(\bar{x}_C) + R_{LP} \left\langle \hat{a}_{LL}^{LP} \right\rangle A_1(\bar{x}). \tag{7.13}$$

To obtain a value of $\Delta G/G$ the mean values of $A_{LL}^{p_T}$, R_i, $\hat{a}_{LL}^i$ and A_1 are put into Eq. 7.13. Results of such an analysis performed at COMPASS are presented in Ref. [104].

However, we know from MC simulations that for the inclusive sample $R_{LP} \neq 1$ and all three processes contribute to the inclusive asymmetry A_{LL}^{inc}. To cope with this a new method of analysis was developed. The inclusive asymmetry can be decomposed in a similar way as $A_{LL}^{p_T}$ in Eq. 7.11

$$\begin{aligned} A_1(x)D \approx & A_{LL}^{inc}(x) \\ = & R_{PGF}^{inc} \left\langle \hat{a}_{LL}^{inc,PGF} \right\rangle \frac{\Delta G}{G}(\bar{x}_G) + R_{QCDC}^{inc} \left\langle \hat{a}_{LL}^{inc,QCDC} \right\rangle A_1^{LO}(\bar{x}_C) + R_{LP}^{inc} \left\langle \hat{a}_{LL}^{inc,LP} \right\rangle A_1^{LO}(\bar{x}). \end{aligned} \tag{7.14}$$

The expressions for $\hat{a}_{LL}$'s are the same as in $A_{LL}^{p_T}$ case, however to emphasise the fact that the kinematic phase space is different they are presented with *inc* index. In general y, x, x_G and x_C in the inclusive and

high p_T samples could be different. However, it was checked with the MC that the average values of x_i are very similar for the two samples. Therefore, for the further analysis a plausible assumption was made that they are the same for the two samples, which simplifies significantly the analysis. Let us rewrite Eq. 7.14 taking advantage of the fact that $D = \hat{a}_{LL}^{inc,LP}$ and introduce the equation for A_1 measured at $\bar{x} = \bar{x}_C$

$$A_1(x) = A_1^{LO}(\bar{x})R_{LP}^{inc} + A_1^{LO}(\bar{x}_C)R_{QCDC}^{inc}\frac{\left\langle \hat{a}_{LL}^{inc,QCDC} \right\rangle}{D} + \frac{\Delta G}{G}(\bar{x}_G)R_{PGF}^{inc}\frac{\left\langle \hat{a}_{LL}^{inc,PGF} \right\rangle}{D}, \tag{7.15}$$

$$A_1(x_C) = A_1^{LO}(\bar{x}_C)R_{LP}^{inc} + A_1^{LO}(\bar{x}_C^{'})R_{QCDC}^{inc}\frac{\left\langle \hat{a}_{LL}^{inc,QCDC} \right\rangle}{D} + \frac{\Delta G}{G}(\bar{x}_G^{'})R_{PGF}^{inc}\frac{\left\langle \hat{a}_{LL}^{inc,PGF} \right\rangle}{D}, \tag{7.16}$$

with $x_C^{'}$ and $x_G^{'}$ being fractions of nucleon momentum carried by the struck parton for sample measured at $\bar{x} = \bar{x}_C$.

Therefore we have a set of 3 equations (7.11, 7.15, 7.16) and three unknowns: $\Delta G/G$, $A_1^{LO}(x)$ and $A_1^{LO}(x_C)$. After combining the equations and neglecting small terms (the fractions R_{PGF} and R_{QCDC} are much smaller for the inclusive sample than for the high p_T sample) the formula for $A_{LL}^{p_T}$ reads

$$\begin{aligned} A_{LL}^{p_T}(x) = {} & R_{PGF}\left\langle \hat{a}_{LL}^{PGF} \right\rangle \frac{\Delta G}{G}(\bar{x}_G) \\ & + \frac{R_{LP}}{R_{LP}^{inc}} D \left(A_1(\bar{x}) - A_1(\bar{x}_C)\frac{\left\langle \hat{a}_{LL}^{inc,QCDC} \right\rangle}{D}\frac{R_{QCDC}^{inc}}{R_{LP}^{inc}} - R_{PGF}^{inc}\frac{\left\langle \hat{a}_{LL}^{inc,PGF} \right\rangle}{D}\frac{\Delta G}{G}(\bar{x}_G) \right) \\ & + \frac{R_{QCDC}}{R_{LP}^{inc}}\left\langle \hat{a}_{LL}^{QCDC} \right\rangle \left(A_1(\bar{x}_C) - A_1(\bar{x}_C^{'})\frac{\left\langle \hat{a}_{LL}^{inc,QCDC} \right\rangle}{D}\frac{R_{QCDC}^{inc}}{R_{LP}^{inc}} - R_{PGF}^{inc}\frac{\left\langle \hat{a}_{LL}^{inc,PGF} \right\rangle}{D}\frac{\Delta G}{G}(\bar{x}_G^{'}) \right). \end{aligned} \tag{7.17}$$

Because the terms $\Delta G/G$ are present in Eq. 7.17 at two different x_G values (denoted as x_G and $x_G^{'}$), the extraction of $\Delta G/G$ requires a new definition of average x_G at which the measurement is performed

$$x_G^{av} = \frac{\alpha_1 x_G - \alpha_2 x_G^{'}}{\lambda}, \tag{7.18}$$

where

$$\alpha_1 = \left\langle \hat{a}_{LL}^{PGF} \right\rangle R_{PGF} - \left\langle \hat{a}_{LL}^{inc,PGF} \right\rangle R_{LP}\frac{R_{PGF}^{inc}}{R_{LP}^{inc}}, \qquad \alpha_2 = \left\langle \hat{a}_{LL}^{inc,PGF} \right\rangle R_{QCDC}\frac{R_{PGF}^{inc}}{R_{LP}^{inc}}\frac{\left\langle \hat{a}_{LL}^{QCDC} \right\rangle}{D}, \tag{7.19}$$

$$\lambda = \alpha_1 - \alpha_2. \tag{7.20}$$

The final formula for the gluon polarisation reads now

$$\Delta G/G(x_G^{av}) = \frac{A_{LL}^{p_T}(\bar{x}) + A^{corr}}{\lambda}, \tag{7.21}$$

$$A^{corr} = -A_1(\bar{x})D\frac{R_{LP}}{R_{LP}^{inc}} - A_1(\bar{x}_C)\beta_1 + A_1(\bar{x}_C^{'})\beta_2, \tag{7.22}$$

where

$$\beta_1 = \frac{1}{R_{LP}^{inc}} \left(\left\langle \hat{a}_{LL}^{QCDC} \right\rangle R_{QCDC} - \left\langle \hat{a}_{LL}^{inc,QCDC} \right\rangle R_{QCDC}^{inc} \frac{R_{LP}}{R_{LP}^{inc}} \right), \tag{7.23}$$

$$\beta_2 = \left\langle \hat{a}_{LL}^{inc,QCDC} \right\rangle \frac{R_{QCDC}^{inc}}{R_{LP}^{inc}} \frac{R_{QCDC}}{R_{LP}^{inc}} \frac{\left\langle \hat{a}_{LL}^{QCDC} \right\rangle}{D}. \tag{7.24}$$

In the following the $\bar{x}_C^{'}$ is assumed to be equal to $\bar{x}_C$. Possible impact of $\bar{x}_C^{'}$ being different from $\bar{x}_C$ is taken into account in the systematic error estimation.

In order to reduce the statistical uncertainty a weighted estimator for $\Delta G/G$ is used. A value of $\Delta G/G$ is calculated on the event-by-event basis and a weight is applied (*cf.* Secs 7.3.5 and 9.2). All the input variables like $\hat{a}_{LL}$ or R are estimated using Neural Networks. In order not to introduce a bias in $\Delta G/G$ extraction one has to take into account the fact that the average x and y are different for inclusive and *high* p_T samples. In case of a proposed weighted method of $\Delta G/G$ extraction this requirement is automatically fulfilled because the fractions and analysing powers are estimated on the event-by-event basis.

7.2 Inputs to the asymmetry

7.2.1 Beam and target polarisation

The beam polarisation P_b is calculated for the measured beam momentum on the event-by-event basis using a parametrisation, as discussed in Sec. 4.2. In Fig. 4.1 the dependence of the beam polarisation on its momentum is presented for year 2004. The relative uncertainty of the beam polarisation is 5% [70].

The target polarisation P_t is measured by the NMR coils (*cf.* Sec. 4.3) several times per run, which typically takes 30-60 minutes, and then averaged to obtain a single polarisation value for a given run. The relative precision of the target polarisation measurement is 5% [70].

7.2.2 Dilution factor

The dilution factor f is introduced to quantify the fraction of interactions that occurred in the polarisable material. The naive expectation in case of the COMPASS polarised deuteron target would be that the dilution factor f equals to 0.5, because four out of eight nucleons in the ^{6}LiD system are polarisable (*cf.* Sec. 4.3). However besides ^{6}LiD there are also other materials in the target cells. These are mainly ^{3}He and ^{4}He used for the cooling of the target material, but also C, F, Ni and Cu from the NMR coils. All these materials have to be included in the computation of the dilution factor. Apart from the number of nucleons bound in nuclei of a given type also the corresponding cross sections enter the dilution factor. Therefore f depends on the event kinematics. The dilution factor is defined as

$$f_{bare}(x, Q^2) = \frac{n_d \sigma_d(x, Q^2)}{n_d \sigma_d(x, Q^2) + \sum_A n_A \sigma_A(x, Q^2)}, \tag{7.25}$$

where n_i corresponds to number of nuclei of type i inside the target, σ_d and σ_A are the unpolarised cross sections for the muon-deuteron and muon-nucleus scattering respectively. The above expression can be

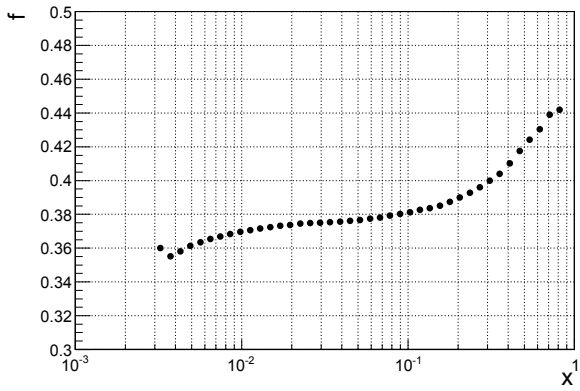

Figure 7.3: The dependence of the effective dilution factor f used for this analysis on x kinematic variable.

rewritten in following form

$$f_{bare} = \frac{n_d}{n_d + \sum_A n_A \frac{\sigma_A}{\sigma_d}}. \tag{7.26}$$

The ratio σ_A/σ_d is approximately proportional to the ratio of unpolarised structure function F_2^A/F_2^d. The dilution factor is computed using a parametrisation of the cross section ratios measured by NMC and EMC experiments and the composition of the material inside the COMPASS target [105]. The dilution factor defined in Eq. 7.26 is multiplied by factor $C \approx 1.9$ which takes into account:

- purity of the material used for the ^{6}LiD production,
- the ^{6}Li nucleus can be treated as α particle plus quasi-free *p* and *n* thus we take into account:
  - probability that the quasi-free *p* and *n* in ^{6}Li are aligned with respect to each other (when they can be treated as the deuteron) [76],
  - correction to such deuteron originating from a fact that it can be in D-state where nucleons can be anti-aligned with respect to the deuteron spin *cf.* Sec. 7.2.4.

In addition the factor Cf_{bare} is multiplied by the factor ρ to take into account the unpolarised radiative corrections. These corrections were calculated using the TERAD program [106]. The radiative corrections are discussed in more detail in Sec. 10.6. Final effective dilution factor is defined therefore as

$$f = \rho C f_{bare}. \tag{7.27}$$

The effective dilution factor for this analysis is shown in Fig. 7.3. The relative uncertainty of the dilution factor in COMPASS kinematics was estimated to be $\sim 2\%$.

7.2.3 Depolarisation factor

The depolarisation factor describes the transfer of the polarisation from the incoming muon to the virtual photon and is given by [107]

$$D = \frac{y\left[\left(1+\gamma^2 y/2\right)(2-y) - 2y^2 m_\mu^2/Q^2\right]}{y^2\left(1-2m_\mu^2/Q^2\right)(1+\gamma^2) + 2\,(1+R)\,(1-y-\gamma^2 y^2/4)}. \tag{7.28}$$

In contrast to Eq. 2.22 the mass of the muon is not neglected here. The depolarisation factor D is to a good approximation directly proportional to y. Therefore events with large values of y are more sensitive to spin effects. The average value of D is $\langle D \rangle = 0.63$ in 2002, $\langle D \rangle = 0.65$ in 2003 and $\langle D \rangle = 0.64$ in 2004.

7.2.4 Deuteron D wave correction

When presenting measurements performed on a deuteron target it is customary to do it in terms of an *average nucleon N*. The cross section for such *average nucleon* is defined as $\sigma_N = (\sigma_p + \sigma_n)/2$. To translate spin dependent measurements performed on the deuteron to such an average nucleon one has take care that the spins of the constituent proton and neutron are aligned with the deuteron spin.

When the deuteron is in the S state its constituent proton and neutron spins are indeed aligned with the deuteron spin. However in case of the D state three configurations of the proton and neutron spin projections are possible: both are aligned with the deuteron spin, both are anti-aligned with deuteron spin and the neutron and proton spin projections have opposite directions thus one is anti-aligned to the deuteron spin.

As shown in Ref. [108] after taking into account the probabilities of each configuration one will obtain the following expression for the deuteron cross section asymmetry

$$A_{||}^d = (1 - 1.5\omega_d) A_{||}^N, \tag{7.29}$$

with $\omega_d \approx 6\%$ being the probability of the D state. The D state correction $(1 - 1.5\omega_d)$ directly transfers to $\Delta G/G$ as seen in Eq. 7.11. The final results for $\Delta G/G$ in this thesis will be presented for the *average nucleon*.

7.3 Extraction of the asymmetry

7.3.1 Numbers of events and the cross section

In this section the relation between the numbers of collected events and cross section asymmetry is given. Also the weighted mean estimator of the asymmetry is discussed.

The total number of observed interactions N of the muon beam in the target is a product of the total cross section σ and the integrated luminosity $\mathcal{L}$. In a fixed target experiment the luminosity is defined by an integrated beam flux ϕ and the density of the nucleons n in the target (the scattering centres). Thus we can express N as follows

$$N = \int a\phi n \left(\frac{d^2\sigma}{dx dQ^2} \right) d\vec{\xi}, \tag{7.30}$$

where $\vec{\xi}$ denotes all integration variables like: Q^2, x, time t, position of the interaction point $\vec{v}$, *etc.* In Eq. 7.30 the total spectrometer acceptance a was taken into account, which is a probability that an interaction which occurred in the target volume has been observed and reconstructed. Time-dependent variations of the spectrometer acceptance and of the target position (position of the target affects the number of the scattering centres illuminated by the beam) can lead to false asymmetries. These are discussed in Sec. 10.1.3.

The beam and the target material are polarised and therefore Eq. 7.30 should be expressed in terms of the helicities of the beam and target. To simplify the formula the differential cross section $d^2\sigma/dxdQ^2$

will be denoted by σ. Since the deuteron has spin one, 3 states with spin projections $+1,\ 0$ and -1 on the reference axis have to be considered. The arrows $\phi^{\uparrow}, (\phi^{\downarrow})$, $n^{\uparrow}(n^{\downarrow})$ indicate the orientation of the spin of the beam and the target relative to the beam direction: parallel (anti-parallel), with n^0 being the projection 0. As only the relative spin orientation between the beam and the nucleon matters the following expressions hold: $\sigma^{\uparrow\uparrow} = \sigma^{\downarrow\downarrow}$, $\sigma^{\uparrow\downarrow} = \sigma^{\downarrow\uparrow}$, $\sigma^{\uparrow 0} = \sigma^{\downarrow 0}$. Thus we can write

$$N = \int d\vec{\xi} a \left[(\phi^{\uparrow} n^{\uparrow} + \phi^{\downarrow} n^{\downarrow})\sigma^{\uparrow\uparrow} + (\phi^{\uparrow} n^{\downarrow} + \phi^{\downarrow} n^{\uparrow})\sigma^{\uparrow\downarrow} + (\phi^{\uparrow} + \phi^{\downarrow}) n^0 \sigma^{\uparrow 0} + (\phi^{\uparrow} + \phi^{\downarrow}) \sum_i n_i \bar{\sigma_i} \right], \tag{7.31}$$

where $\bar{\sigma}$ is a spin average cross section $\bar{\sigma} = (\sigma^{\uparrow\downarrow} + \sigma^{\uparrow\uparrow})/2$ and the $\sum_i n_i \bar{\sigma_i}$ is a sum over all elements in the target other than the deuteron. Most of these elements are not polarised and for them the spin averaged cross section is used. We can now introduce the beam and the deuteron target polarisations

$$P_b = \frac{\phi^{\uparrow} - \phi^{\downarrow}}{\phi}; \quad P_t = \frac{n^{\uparrow} - n^{\downarrow}}{n} \tag{7.32}$$

and define the measured asymmetry as

$$A = (\sigma^{\uparrow\downarrow} - \sigma^{\uparrow\uparrow})/(\sigma^{\uparrow\downarrow} + \sigma^{\uparrow\uparrow}), \tag{7.33}$$

where $\phi = \phi^{\uparrow} + \phi^{\downarrow}$ is the total muon flux and $n = n^{\uparrow} + n^{\downarrow} + n^0$ is the total density of scattering centres. Using the above definitions we can rewrite Eq. 7.31 in the following form

$$N = \int d\vec{\xi} a \left[\phi n \bar{\sigma} - \phi n \bar{\sigma} P_b P_t A + \phi \sum_i n_i \bar{\sigma} \right]. \tag{7.34}$$

Taking into account the dilution and depolarisation factors we come to the final form of Eq. 7.31

$$N = \int d\vec{\xi} a \phi n \bar{\sigma} \left[1 - f D P_b P_t A \right]. \tag{7.35}$$

7.3.2 The first order method

In COMPASS it is not practical to use directly Eq. 7.35 to extract the cross section asymmetry, because the incoming muon flux is known with the precision of $\sim 10\%$ which would translate to a large uncertainty on the derived asymmetry. Instead a counting rate asymmetry is defined as

$$A_N = \frac{N^{\uparrow\downarrow} - N^{\uparrow\uparrow}}{N^{\uparrow\downarrow} + N^{\uparrow\uparrow}} = \frac{N_u - N_d}{N_u + N_d}, \tag{7.36}$$

where N_u, N_d are the number of events observed in upstream and downstream target cells respectively. Here upstream cell has nucleons polarised anti-parallel to the beam $(P_b P_t < 0)$ while for downstream one it is opposite $(P_b P_t > 0)$. The flux is secured to be the same for both target cells by selecting events with the extrapolated beam trajectory crossing the full length of the target. Furthermore by considering small intervals in x, Q^2 the convolution in Eq. 7.35 can be approximated by a product which allows for cancellation

of the beam flux and the cross section. The expression for the counting rate asymmetry becomes [109]

$$A_N = \frac{r - 1 - wA(rP_u - P_d)}{r + 1 - wA(rP_u + P_d)}, \tag{7.37}$$

where $r = a_u n_u / a_d n_d$ and $w = fDP_b$. As usually the $wA \ll 0.1$ and $P_u \approx -P_d$, then with an assumption that the difference between the acceptances is small ($r \approx 1$), the term $wA(rP_u + P_b)$ in the denominator can be neglected. This leads to a linear dependence of A on the counting rate asymmetry. For this reason this method is called the first order method. The obtained expression for A is following

$$A = \frac{1}{w} A_N - \frac{1}{w} \left(\frac{r-1}{r+1} \right). \tag{7.38}$$

The acceptances and the density of scattering centres are not the same for the two target cells. Hence $r \neq 1$, which means that A_N is an estimator of A which is biased by the term $(r-1)/(r+1)$, which is called the apparatus asymmetry. In order to eliminate this bias the polarisations in the target cells are reversed periodically. Figs 7.4 a) and b) illustrate the spin configurations before and after reversal. The unprimed notation ($N^{\uparrow\downarrow},\ N^{\uparrow\uparrow}$) belongs to configuration a), the primed notation ($N'^{\uparrow\downarrow},\ N'^{\uparrow\uparrow}$) to configuration b) in Fig. 7.4. The counting rate asymmetry after the field reversal is defined as

$$A'_N = \frac{N'^{\uparrow\downarrow} - N'^{\uparrow\uparrow}}{N'^{\uparrow\downarrow} + N'^{\uparrow\uparrow}} = \frac{N'_d - N'_u}{N'_d + N'_u} = -\frac{N'_u - N'_d}{N'_u + N'_d} = -\frac{r' - 1 - wA(r'P'_u - P'_d)}{r' + 1 - wA(r'P'_u + P'_d)}. \tag{7.39}$$

Then data collected with two configurations of target spin orientations are combined

$$\frac{A_N + A'_N}{2} = \frac{1}{2} \left[\frac{r - 1 - wA(rP_u - P_d)}{r+1} - \frac{r' - 1 - wA(r'P'_u - P'_d)}{r'+1} \right]. \tag{7.40}$$

The spin orientation of nucleons in upstream (downstream) cell is defined to be parallel (anti-parallel) to the beam direction, similarly after the polarisation reversal the orientation in upstream (downstream) cell is anti-parallel (parallel). Thus we can use the absolute values of the polarisations

$$\begin{aligned} |P_b|\,|P_u| &= -P_b P_u, \quad |P_b|\,|P'_u| = -P_b P'_u, \\ |P_b|\,|P_d| &= P_b P_d, \qquad |P_b|\,|P'_d| = P_b P'_d. \end{aligned} \tag{7.41}$$

Hence we obtain

$$\frac{A_N + A'_N}{2} = \frac{1}{2} \left[\frac{r-1}{r+1} - \frac{r'-1}{r'+1} + \langle w \rangle A \left(\frac{r\,|P_u| + |P_d|}{r+1} + \frac{r'\,|P'_u| + |P'_d|}{r'+1} \right) \right], \tag{7.42}$$

where $\langle w \rangle$ is defined as $\langle w \rangle = \langle f \rangle \langle D \rangle \langle |P_b| \rangle$ with $\langle f \rangle$ and $\langle D \rangle$ being average values of f and D in the $(x,\, Q^2)$ bin and $\langle |P_b| \rangle$ is the average of the absolute value of the beam polarisation. Using the average target polarisation

$$\langle P_t \rangle = \frac{1}{2} \left[\frac{r\,|P_u| + |P_d|}{r+1} + \frac{r'\,|P'_u| + |P'_d|}{r'+1} \right], \tag{7.43}$$

we obtain following expression for the cross section asymmetry and its statistical error

$$A = \frac{1}{\langle w \rangle \langle P_t \rangle} \left(\frac{A_N + A'_N}{2} \right) - \underbrace{\frac{1}{2 \langle w \rangle \langle P_t \rangle} \left(\frac{r-1}{r+1} - \frac{r'-1}{r'+1} \right)}_{A_{false}} \tag{7.44}$$

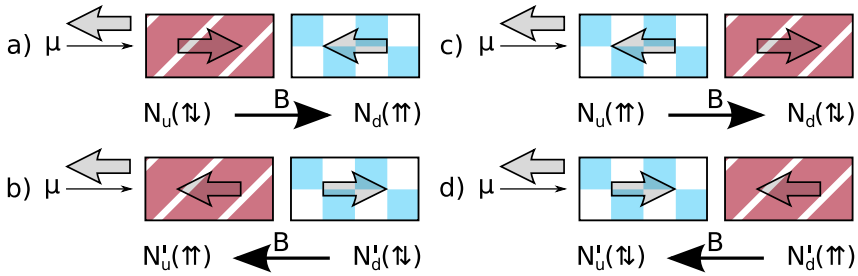

Figure 7.4: Target spin configurations for the asymmetry calculation. The top row illustrates the configuration before the solenoid field reversal while the bottom row after. Figures a) and b) present the positive Micro Wave setting with the upstream cell positively polarised (striped pattern), *i.e.* the spins are oriented along the magnetic field. For the negative Micro Wave setting (c) and d)) the upstream target cell is negatively polarised (checkboard pattern), i.e. the spins are anti-aligned with the field. See text for details.

$$\sigma(A) \cong \frac{1}{2\langle w\rangle\langle P_t\rangle}\sqrt{\frac{1}{N_u+N_d}+\frac{1}{N'_u+N'_d}}. \tag{7.45}$$

The statistical error for the asymmetry is determined assuming that $r \approx 1$ and the number of collected events is large ($\sigma(N_i) = \sqrt{N_i}$).

The false asymmetry A_{false} vanishes provided the ratio r is stable in time ($r = r'$). Another remark is that the r is "hidden" in the definition of $\langle P_t\rangle$, therefore it has to be known for the correct asymmetry extraction. Determination of r with high precision is difficult and therefore a *second order* method of asymmetry extraction was developed.

In Sec. 10.1.3.1 we discuss false asymmetries that arise from sensitivity of the spectrometer's acceptance to the direction of the solenoid field. Such effects can be suppressed by reversing direction of the target nucleons spins with respect to the magnetic field and combining data collected in the two configurations. The second configuration is illustrated on Figs 7.4 a) and b). For more detailed discussion of the *Micro Wave reversal* procedure *cf.* Sec. 10.1.3.1.

7.3.3 The second order method

In this section a second order method of asymmetry extraction is introduced. We start from the expression for the total numbers of events collected in the two target cells for the two spin configurations.

$$N_u = \int d\vec{\xi} a_u \phi n_u \overline{\sigma}(1 - P_b P_u f_u D A) = \int d\vec{\xi}\alpha_u(1-\beta_u A), \tag{7.46}$$

$$N_d = \int d\vec{\xi} a_d \phi n_d \overline{\sigma}(1 - P_b P_d f_d D A) = \int d\vec{\xi}\alpha_d(1-\beta_d A), \tag{7.47}$$

$$N'_u = \int d\vec{\xi} a'_u \phi n'_u \overline{\sigma}(1 - P_b P'_u f'_u D A) = \int d\vec{\xi}\alpha'_u(1-\beta'_u A), \tag{7.48}$$

$$N'_d = \int d\vec{\xi} a'_d \phi n'_d \overline{\sigma}(1 - P_b P'_d f'_d D A) = \int d\vec{\xi}\alpha'_d(1-\beta'_d A), \tag{7.49}$$

where $\alpha_i \equiv a_i \phi n_i \overline{\sigma}$ and $\beta_i \equiv P_b P_i f_i D$ and the $\vec{\xi}$ denotes, as in Eq. 7.30, all variables (x, Q^2, $\overrightarrow{v}$ etc.) involved in the integration. The above integrals are equivalent to [110]

$$N_i = \langle a_i\rangle(1 - \langle\beta_i\rangle) A \int \phi n_i \overline{\sigma} d\vec{\xi}, \tag{7.50}$$

with the average acceptance

$$\langle a_i \rangle = \frac{\int a_i \phi n_i \overline{\sigma} d\vec{\xi}}{\int \phi n_i \overline{\sigma} d\vec{\xi}} \tag{7.51}$$

and the average β

$$\langle \beta_i \rangle = \frac{\int \beta_i \alpha_i d\vec{\xi}}{\int \alpha_i d\vec{\xi}} \overset{N_i \, large}{\approx} \frac{\sum_{j=1}^{N_i} \beta_i^j}{N_i}, \tag{7.52}$$

where β_i^j is the value of β_i for event j with $j = 1 \ldots N_i$.

In the first order method we have defined the counting rate asymmetry. This time the interesting quantity will be the double ratio of the counting rates

$$\delta \equiv \frac{N_u N_d'}{N_d N_u'} = \frac{\langle a_u \rangle \langle a_d' \rangle}{\langle a_u' \rangle \langle a_d \rangle} \frac{\int \phi n_u \overline{\sigma} d\vec{\xi} \int \phi n_d' \overline{\sigma} d\vec{\xi} \left(1 - \langle \beta_u \rangle A\right) \left(1 - \langle \beta_d' \rangle A\right)}{\int \phi n_u' \overline{\sigma} d\vec{\xi} \int \phi n_d \overline{\sigma} d\vec{\xi} \left(1 - \langle \beta_u' \rangle A\right) \left(1 - \langle \beta_d \rangle A\right)}. \tag{7.53}$$

Assuming that the target position does not change between the spin reversals we obtain

$$\frac{\int \phi n_u \overline{\sigma} d\vec{\xi} \int \phi n_d' \overline{\sigma} d\vec{\xi}}{\int \phi n_u' \overline{\sigma} d\vec{\xi} \int \phi n_d \overline{\sigma} d\vec{\xi}} = 1. \tag{7.54}$$

In addition we assume that the ratio of acceptances is equal to 1

$$\frac{\langle a_u \rangle \langle a_d' \rangle}{\langle a_u' \rangle \langle a_d \rangle} = 1. \tag{7.55}$$

This leads to a second order equation for the asymmetry A

$$aA^2 + bA + c = 0 \tag{7.56}$$

with $a = \delta \langle \beta_u' \rangle \langle \beta_d \rangle - \langle \beta_u \rangle \langle \beta_d' \rangle$, $b = -\delta \left(\langle \beta_u' \rangle + \langle \beta_d \rangle \right) + \left(\langle \beta_u \rangle + \langle \beta_d' \rangle \right)$ and $c = \delta - 1$.
If $a \neq 0$, $A = \frac{\pm\sqrt{b^2 - 4ac} - b}{2a}$ and for $a = 0$, $A = -\frac{c}{b}$.

The error of asymmetry is given by

$$\sigma(A) = \frac{1}{\langle \beta \rangle \sqrt{N_{tot}}}, \tag{7.57}$$

where we assumed that $\frac{N_{tot}}{4} \equiv N_u \approx N_d \approx N_u' \approx N_d'$ and $< \beta > \equiv < \beta_u > \approx < \beta_d' > \approx - < \beta_u' > \approx - < \beta_d >$. One of the solutions of Eq. 7.56 yields $A \gg 1$ which is non-physical, thus it is rejected. An important observation is that in case of the second order method the asymmetry does not depend on r in contrast to the first order method.

7.3.4 The second order weighted method

In both the first order method and the second order method only mean values of $\langle f \rangle$, $\langle D \rangle$, $\langle P_b \rangle$ and $\langle P_t \rangle$ were considered. This is not an optimal solution as far as the statistical uncertainty is concerned. An estimator that gives the smallest variance is the weighted mean. In this section a method of asymmetry extraction based on such estimator is presented.

In this approach the values of f, D, P_b and P_t are calculated on the event-by-event basis and then they are used in a weight. To introduce the weight into the second order method a few modifications of the

formalism are necessary. Here, we define p_i

$$p_i = \int w N_i d\vec{\xi} = \int \phi n_i \overline{\sigma} d\vec{\xi} \left\langle a_i \right\rangle_w \left(1 - A \left\langle \beta_i \right\rangle_w\right), \tag{7.58}$$

where

$$\left\langle a_i \right\rangle_w = \frac{\int a_i w \phi n_i \overline{\sigma} d\vec{\xi}}{\int w \phi n_i \overline{\sigma} d\vec{\xi}}, \tag{7.59}$$

$$\left\langle \beta_i \right\rangle_w = \frac{\int \beta_i w \phi n_i \overline{\sigma} d\vec{\xi}}{\int w \phi n_i \overline{\sigma} d\vec{\xi}} \overset{N_i \, large}{\approx} \frac{\sum_{j=1}^{N_i} w_j \beta_i^j}{\sum_{j=1}^{N_i} w_j} \tag{7.60}$$

with β_i^j being the value of β_i for event j. Then the double ratio δ from Eq. 7.53 is redefined as

$$\delta = \frac{p_u p'_d}{p'_u p_d}. \tag{7.61}$$

Using similar assumptions as in the previous section we obtain the equation: $aA^2 + bA + c = 0$
with $a = \delta \left\langle \beta'_u \right\rangle_w \left\langle \beta_d \right\rangle_w - \left\langle \beta_u \right\rangle_w \left\langle \beta'_d \right\rangle_w$, $b = -\delta \left(\left\langle \beta'_u \right\rangle_w + \left\langle \beta_d \right\rangle_w\right) + \left(\left\langle \beta_u \right\rangle_w + \left\langle \beta'_d \right\rangle_w\right)$, $c = \delta - 1$. With the assumptions that $\frac{N_{tot}}{4} \equiv N_u \approx N_d \approx N'_u \approx N'_d$ and $< \beta > \equiv < \beta_u > \approx < \beta'_d > \approx - < \beta'_u > \approx - < \beta_d >$ the statistical error of the asymmetry is following

$$\sigma(A) = \sqrt{\frac{\langle w^2 \rangle}{\langle w\beta \rangle^2} \frac{1}{N_{tot}}}. \tag{7.62}$$

The optimal weight, which gives the smallest statistical error $\sigma(A) = \sqrt{\frac{1}{\langle \beta^2 \rangle N_{tot}}}$ is $w = \beta = fDP_bP_t$. The error for this estimator is reduced by factor $\sqrt{\langle \beta^2 \rangle / \langle \beta \rangle^2}$ compared to the one for the non-weighted second order method.

However, such weight is not optimal as far as the systematic error is concerned. This is due to a fact that the mean value of the weight should be the same before and after the spin reversal. If this is not the case then the false asymmetries appear. Indeed in COMPASS case the P_t is often different between the spin reversals. The data are sometimes collected when the polarised target is not yet in the "frozen spin" mode but it is still being polarised. Thus we choose the weight $w = fDP_b$ and for the target polarisation we use its mean value $\langle P_t \rangle$.

Detailed discussion of the second order method of asymmetry extraction as well as its uncertainties is given in Refs [110, 111].

7.3.5 Extraction of the asymmetry in presence of known background asymmetry

According to Eq. 7.21 the measured cross section asymmetry can be decomposed into two terms

$$A_{LL}^{p_T} = \lambda \frac{\Delta G}{G} - A_{corr}. \tag{7.63}$$

Then number of observed events can be expressed as

$$N_i = \int d\vec{\xi} a_i \phi n_i \overline{\sigma} \left[1 - P_b P_i f_i D \left(\lambda \frac{\Delta G}{G} - A_i^{corr}\right)\right] = \int d\vec{\xi} \alpha_i \left[C_i - \beta_i \frac{\Delta G}{G}\right], \tag{7.64}$$

where $\beta_i = P_b P_i f_i D\lambda$ and $C_i = P_b P_i f_i D A_i^{corr}$. For the second order weighted method we define

$$p_i = \int w N_i d\vec{\xi} = \int \phi n_i \overline{\sigma} d\vec{\xi} \langle a_i \rangle_w \left(\langle C_i \rangle_w - \frac{\Delta G}{G} \langle \beta_i \rangle_w \right), \tag{7.65}$$

with $\langle \beta_i \rangle_w$ redefined as

$$\langle \beta_i \rangle_w = \frac{\sum_j^{N_i} w_i \beta_i}{\sum_j^{N_i} w_j} \tag{7.66}$$

and $\langle C_i \rangle_w$ defined as

$$\langle C_i \rangle_w = 1 + \frac{\sum_j^{N_i} w_i C_i}{\sum_j^{N_i} w_i}. \tag{7.67}$$

The expression for $\langle a_i \rangle$ remains the same as in Sec. 7.3.4. Following the formalism described in the previous section we arrive at a second order equation for $\Delta G/G$

$$a \left(\frac{\Delta G}{G} \right)^2 + b \frac{\Delta G}{G} + c = 0, \tag{7.68}$$

where

$$\begin{aligned} a =& \delta \langle \beta'_u \rangle_w \langle \beta_d \rangle_w - \langle \beta_u \rangle_w \langle \beta'_d \rangle_w , \\ b =& -\delta \left(\langle C_d \rangle_w \langle \beta'_u \rangle_w + \langle C'_u \rangle_w \langle \beta_d \rangle_w \right) + \left(\langle C'_d \rangle_w \langle \beta_u \rangle_w + \langle C_u \rangle_w \langle \beta'_d \rangle_w \right), \\ c =& \delta \langle C'_u \rangle_w \langle C_d \rangle_w - \langle C_u \rangle_w \langle C'_d \rangle_w . \end{aligned} \tag{7.69}$$

In such approach the $\Delta G/G$ value is extracted directly without an intermediate step of evaluation of the $A_{LL}^{p_T}$ cross section asymmetry. This method was used in this analysis to evaluate $\Delta G/G$. For the statistical and systematic errors the optimal weight in the COMPASS case is $w = fDP_b\lambda$. The values of f, D, P_b, λ and A^{corr} have to be known on the event-by-event basis. The parametrisation of P_b, f, D were discussed in sections 7.2.1, 7.2.2, 7.2.3. The values of λ and A^{corr} were parametrised using artificial neural networks as explained in Sec. 9.2.

To compare the statistical error of the new method, where $\Delta G/G$ is extracted directly, with the old method, where the weighted average of $A_{LL}^{p_T}$ was used, let us assume $A_{corr} = 0$, $R_{LP}^{inc} = 1$ and $R_{PGF}^{inc} = R_{QCDC}^{inc} = 0$ (both assumptions were used *e.g.* in Ref. [104] although they are not fully justified). If we redefine $\lambda = \hat{a}_{LL}^{PGF} R_{PGF} \equiv \gamma$ then Eq. 7.63 can be rewritten as

$$A_{LL}^{p_T} = \gamma \frac{\Delta G}{G}. \tag{7.70}$$

For the old method we would extract $\Delta G/G$ as $\Delta G/G(< x >) =< A_{LL}^{pT} > / < \gamma >$ while in the new method it will be $\Delta G/G(< x >) =< A_{LL}^{pT}/\gamma >$. With the same assumptions as in Sec. 7.3.4 ($\frac{N_{tot}}{4} \equiv N_u \approx N_d \approx N'_u \approx N'_d$, $< \beta > \equiv < \beta_u > \approx < \beta'_d > \approx - < \beta'_u > \approx - < \beta_d >$ and $w = \beta$) it easy to show that

$$\sigma^2(\frac{\Delta G}{G})_{old} = \frac{1}{< \gamma >^2 < \beta^2 > N_{tot}}, \tag{7.71}$$

$$\sigma^2(\frac{\Delta G}{G})_{new} = \frac{1}{< \gamma^2 >< \beta^2 > N_{tot}}. \tag{7.72}$$

Thus the statistical error is reduced by the factor $\sqrt{\langle\gamma^2\rangle / \langle\gamma\rangle^2}$ when extracting directly the $\Delta G/G$ compared to the old method. Moreover the new method treats properly contributions of the three LO processes to the $A_{LL}^{p_T}$ and A_{LL}^{inc} asymmetries.

7.4 Selection of events

This analysis includes the data taken with the COMPASS spectrometer in the years 2002, 2003 and 2004. The data used in the analysis have been selected using the data quality criteria (Sec. 7.4.1), the topological and kinematic cuts (Secs 7.4.2, 7.4.4 and 7.4.3), the hadron identification and high p_T selection cuts (Secs 7.4.5 and 7.4.6).

7.4.1 Data quality and grouping.

The selection of runs for the analysis is based on general criteria, like minimum number of spills per run, maximum number of detector planes that were marked by a shift crew as having problems, *etc*. Such information is stored during the data taking in the electronic logbook and then is used for the data quality studies. Further analysis is performed by looking on the data itself. On the spill-by-spill basis it is required that certain observables have stable values, otherwise a spill is marked as problematic. These observables are for example: number of primary vertices, number of tracks per event, number of K^0particles per event, number of tracks per vertex [49]. For each data production (*cf.* Sec. 4.6.2) a list of bad spills is produced and those spills are discarded from the analysis. Such data selection is used in general for all analyses of the COMPASS data. Appendix A.2 gives an overview of the run statistics.

Data taking in COMPASS is divided in periods that usually span a week. Such division is natural because usually once per week the accelerator undergoes the machine development. During that time no data are taken and moreover maintenance of the spectrometer is carried out. To avoid systematic effects due to different spectrometer conditions the periods are treated separately. The value of the $\Delta G/G$ is extracted for every period and then a weighted mean is used as the final result.

Within one period of data taking every eight hours a reversal of the solenoid magnetic field is performed. There are two possible ways to combine such data in the analysis:

- The global configurations (Fig. 7.5a)
  All the runs from the considered data taking period are treated together. The runs that belong to $\Leftarrow\Rightarrow$ setting are combined and used to calculate weights β_u and β_d from Eq. 7.69. Similarly runs from $\Rightarrow\Leftarrow$ configuration are combined to extract $\beta_u^{'}$ and $\beta_d^{'}$. Global configuration has the advantage of utilisation of larger statistics thus requirement of the 2nd order method that N is large can be safely assumed to be fulfilled.

- The consecutive configurations (Fig. 7.5b)
  The period is split into sets of groups of runs. Each group is composed from two consecutive subgroups: one that corresponds to one solenoid field direction and the following subgroup that corresponds to opposite one. Within one group the data are treated as for the global configuration, *i.e.* runs that belong to the same configuration are combined. The weighted average over all groups is calculated

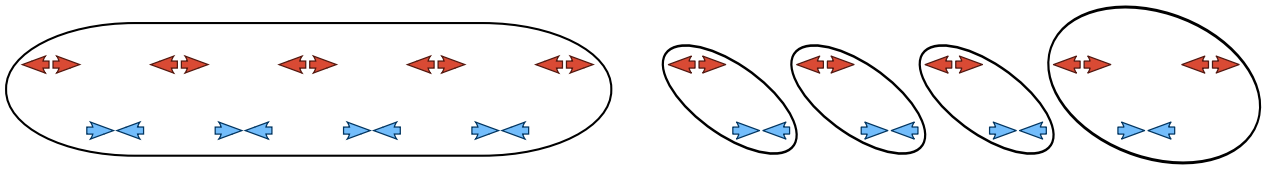

(a) Global configuration (b) Consecutive configuration

Figure 7.5: Global (a) and consecutive (b) configurations for the asymmetry calculation.

to obtain the result for the complete period. During the data quality evaluation it is also checked that the spectrometer conditions in subsequent solenoid current configurations were similar. For some subgroup pairs the spectrometer behaviour was found to differ between the first and the second configuration. In such case the first (second) configuration is added to the previous (subsequent) group of runs if conditions during considered runs were similar. Thus there are cases when set of three groups are combined.

The advantage of the consecutive configurations is that only runs that are close in time are combined. As the performance of the COMPASS spectrometer is not fully stable *e.g.* due to temperature variations over one week of data taking, usage of the consecutive configuration reduces impact of random false asymmetries induced by such instabilities.

The latter type of grouping is used by analyses that have large quantities of data *e.g.* A_1^d, the former one in the opposite case. To obtain the final result from high p_T sample the global configurations were used, while the consecutive ones were considered for systematic studies.

7.4.2 Topology selection

Selected events are required to have a reconstructed interaction point (primary vertex) containing a reconstructed track of beam muon μ, a reconstructed track of scattered muon μ' and at least two additional outgoing tracks - hadron candidates. The primary vertex is identified using BestPrimaryVertex() function provided by PHAST [85].

7.4.3 Vertex cuts

For extraction of $\Delta G/G$ only the events that occurred in the polarised material are relevant. To ensure this the primary vertex is required to be located within one of the target cells. Such requirement is ensured by a series of cuts:

- The value of Z coordinate of the reconstructed primary vertex is contained in one of the target cells $Z_{PV} \epsilon (-100, -40) \cup (-30, 30)$. The two target cells are clearly seen in Fig. 7.6 (left) as well as the gap between them.

- In the plane perpendicular to the beam direction the primary vertex is required to be within a radius of $R_{PV} < 1.3\,\text{cm}$ from the target centre. Taking into account that the target cell has a radius of $(1.50 \pm 0.05)\,\text{cm}$ [70] such a limit is rather conservative. The radial cut was selected taking into account that the position of the target with respect to the spectrometer is known with a precision of

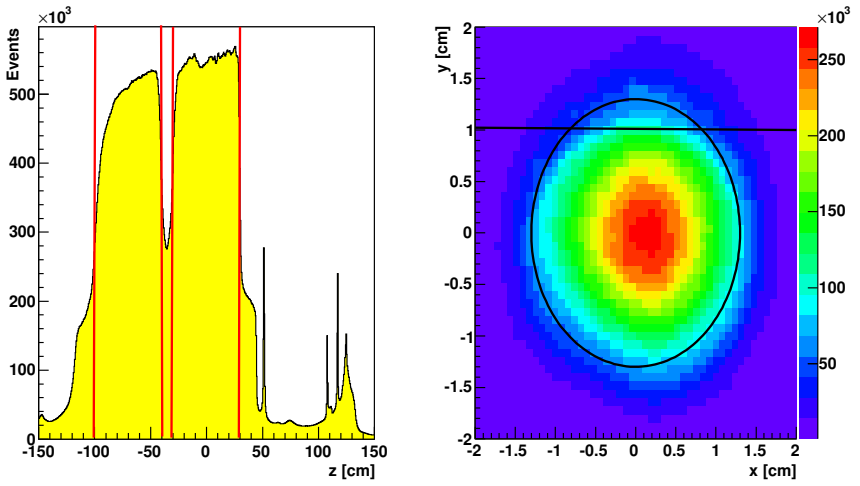

Figure 7.6: The longitudinal vertex distribution (left) with the cuts along Z coordinate ($-100\,\text{cm} < Z < -40\,\text{cm}$ and $-30\,\text{cm} < Z < 30\,\text{cm}$) and the transverse vertex distribution (right) with cuts on $Y > 1\,\text{cm}$ and $R < 1.3\,\text{cm}$.

$\sim 0.05\,\text{cm}$, the target could move between weeks of the data taking by $\sim 0.05\,\text{cm}$ and it also moves during the field reversal by $\sim 0.06\,\text{cm}$.

- Because the target cells are not fully filled at the top, it is required for Y coordinate of the primary vertex to be $Y_{PV} < 1\,\text{cm}$.

- The target volume is not perfectly aligned with the beam axis. A certain tilt is present and it is year dependent. It is taken into account while applying above mentioned cuts.

The cuts are illustrated in Fig. 7.6.

The extrapolation of incoming muon μ track is required to cross both target cells. The cells are defined with the same cuts as in primary vertex case. Such requirement ensures that both parts of the target are exposed to the same beam flux and that it will then cancel out in asymmetry calculations.

These cuts are applied using two PHAST functions CrossCells() and InTarget().

7.4.4 Cuts on muon kinematic variables

The beam energy is selected with the cut $140 < E_\mu < 180\,\text{GeV}$. Then the cut $y < 0.9$ removes events that are expected to have large radiative corrections. This cut also removes μ' with low momentum. Such μ' could originate from a pion decay and not from the primary vertex. The additional cut $y > 0.1$ removes events with poorly reconstructed scattered muon and events with a beam halo muon misidentified as μ'. Events with the low values of y have low values of the depolarisation factor D and their impact on $A_{LL}^{p_T}$ is highly reduced. In order to select events from perturbative regime the Q^2 is required to be above $1\,\text{GeV}^2$.

In order to prevent fake triggers a reconstructed scattered muon is required to have associated hits in both stations that gave a trigger (*e.g.* HO03 and HO04). In case of pure calorimetric trigger it is required that none of "muon" triggers had fired. The pure calorimetric trigger extends the kinematic coverage to high Q^2 region where muon is scattered at large angle and does not go through muon identification setup.

7.4.5 Particle identification

As explained in Sec. 7.4.4 the scattered muon is required to have associated hits in certain trigger hodoscope planes. As the hodoscope planes are shielded by absorbers one can be fairly certain that track that corresponds to the trigger is a muon. This is not the case for the Calorimetric Trigger (CT) where the muon is scattered at large angle and is not in the acceptance of the hodoscope planes, thus μ' is also required to have passed an amount of material accounting to a sufficient number of radiation lengths ($> 50X_0$). The scattered muon is selected using the PHAST function iMuPrim().

The two particles with the highest values of p_T associated to the primary vertex, besides μ and μ', are considered hadron candidates. They must fulfil the following requirements:

- Exclusion of muon track candidates.
  There is a small probability for a pile-up muon to be included in the primary vertex and therefore being considered a hadron candidate. To remove such events an information from hadron calorimeters and muon filters is utilised. If the energy measurement by hadron calorimeters is available, the hadron is required to have $E_{cal}/p \geq 0.3$, where E_{cal} is the energy deposit in the calorimeters associated to the hadron candidate track of momentum p. If no measurement of energy is available from calorimeters the hadron candidate is rejected if it goes through the Muon Filter 2 (position of last cluster $z > 40\,\text{m}$).

- Good quality of the track reconstruction.
  First, the χ^2/ndf for the fitted track has to be smaller then 20. Then it is verified that the track was not reconstructed only within the fringe field of SM1 magnet by requiring the last cluster to be located behind SM1 ($z > 300\,\text{cm}$).

- Track does not go through the body of the target solenoid magnet.
  The tracks are extrapolated to the entrance of the solenoid and then the distance between the track and the Z axis should be less than the radius of the solenoid aperture ($14.9\,\text{cm}$).

7.4.6 Cuts on hadronic kinematic variables

The following cuts are applied to the leading (highest transverse momentum p_{T1}) and the sub-leading (p_{T2}) hadrons in order to enhance the sample with events originating from PGF:

- $p_{T1} > 0.7\,\text{GeV}$ and $p_{T2} > 0.7\,\text{GeV}$. This requirement constitutes the high p_T cut.

Additional cuts are used to clean up the sample:

- $x_F > 0$; ensure that events originate from the current fragmentation,

- $z_1 + z_2 < 0.95$; rejects events from exclusive production of a pair of hadrons,

- invariant mass of the two hadrons (assuming pion masses) is above the resonance region ($m(h1,\, h2) > 1.5\,\text{GeV}^2$); removes events for which the virtual photon fluctuates to a vector meson such as a ρ, moreover this cut suppresses pairs of hadrons with a small difference in the azimuth angle [104] and enriches the selected sample with PGF events.

- $x > 0$, $x < 1$; ensures that only events where reconstructed kinematics is physical are considered.

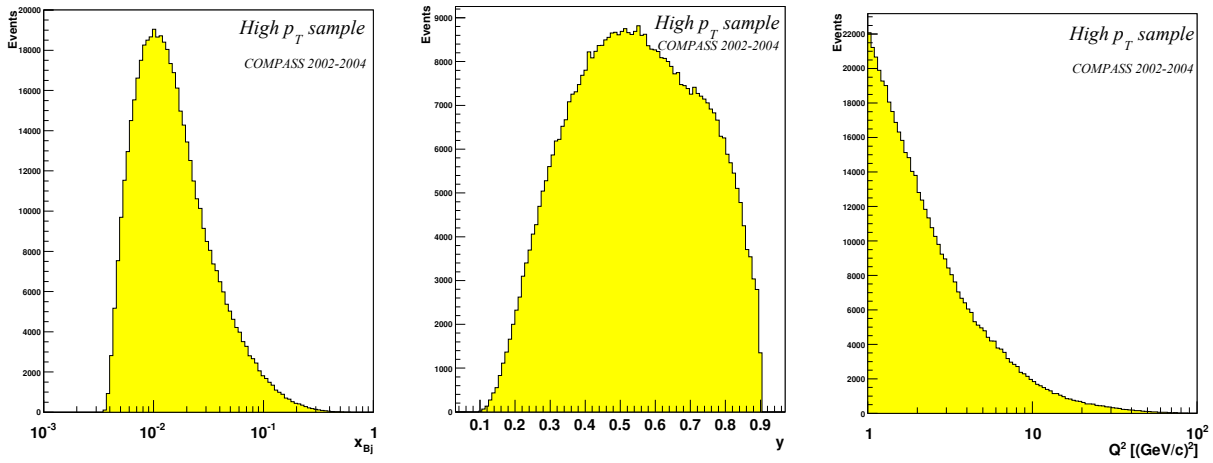

Figure 7.7: The distributions of inclusive variables x, y, Q^2 for the *high* p_T data sample.

The impact of the additional hadron quality cuts as well as particle identification cuts is presented in Table 7.1. In this table, the event *candidates* are events that pass the cuts defined in Secs 7.4.1, 7.4.2, 7.4.3, 7.4.4 and pass the *high* p_T cut. "Hadron ID" refers to events that passed muon exclusion cuts from Sec. 7.4.5. "Track quality" corresponds to the events that passed the quality requirements and the solenoid aperture cut form Sec. 7.4.5.

The distributions of the kinematic variables Q^2, y, x are shown in Fig. 7.7. The distributions of $p, p_T, \sum p_T^2$ and z variables for leading and sub-leading hadrons are presented in Fig. 7.8.

	Number of events that passed each cut				
Cuts	2002	2003	2004	All years	%
Event candidate	89111	309893	524862	923866	100.0
Invariant mass	59711	208055	350989	618755	67.0
Hadron ID	52363	180965	301698	535026	57.9
$x_F > 0$	51325	176426	294970	522721	56.6
$z_{12} < 0.95$	49962	172431	288732	511125	55.3
Track quality	49585	170943	286685	507213	54.9

Table 7.1: Summary of the hadron cuts.

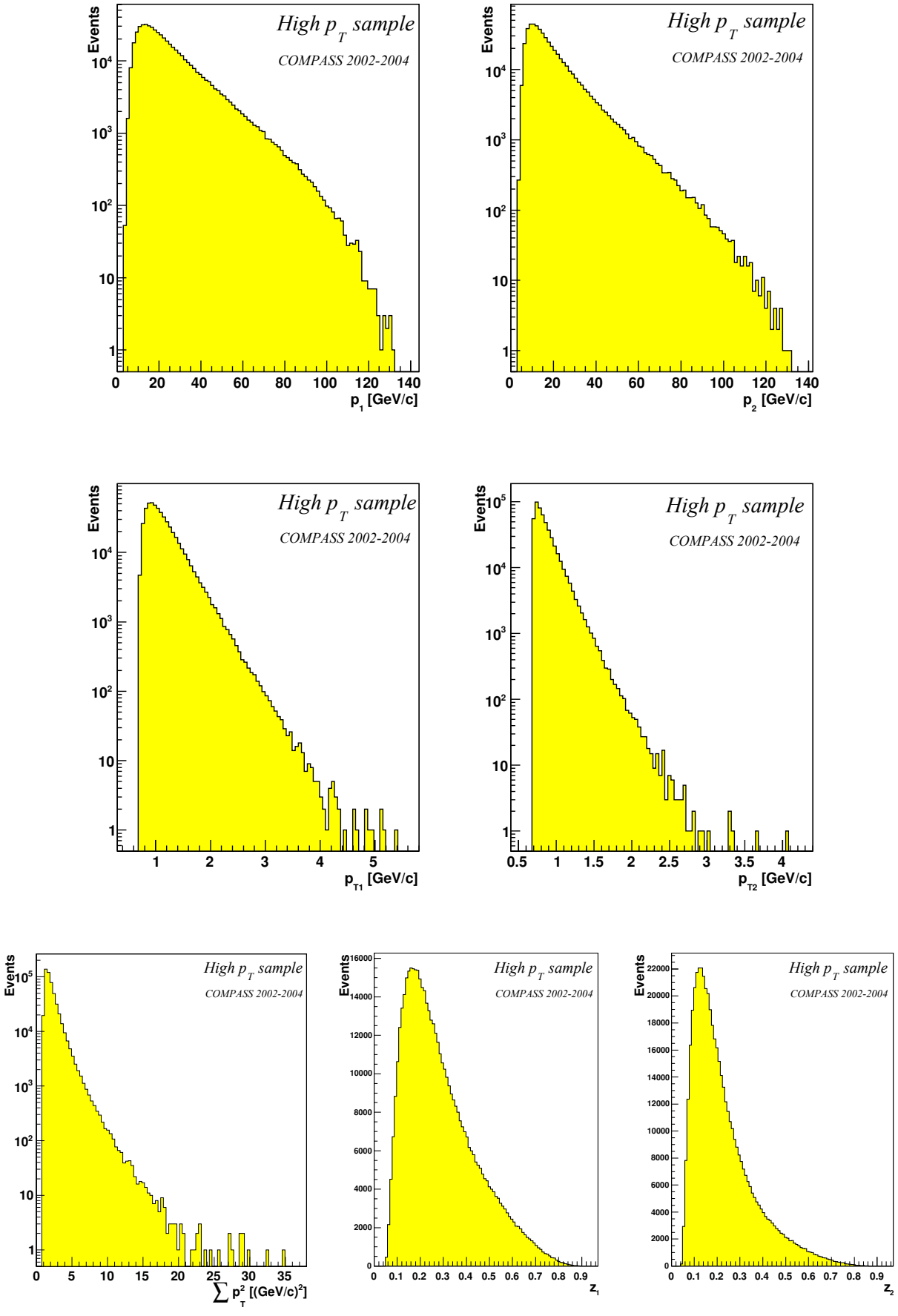

Figure 7.8: The distributions of hadron variables p_1 , p_2, p_{T1}, p_{T2}, Σp_T^2, z_1, z_2 for the *high* p_T data sample.

Chapter 8

Monte Carlo simulations

In this chapter details of Monte Carlo simulations are presented. First the physics event generator LEPTO [55] is described, followed by the discussion of the simulation of experimental conditions. The adjustments made to LEPTO steering parameters are described and finally the comparison with experimental data is shown.

In Sec. 7.1.2 it was discussed that in order to obtain the gluon polarisation from the measured asymmetry certain characteristics, unobservable in the experiment, have to be known on the event-by-event basis. In this analysis they were parametrised using Neural Networks based on Monte Carlo (MC) simulations. This is the reason why a good description of the experimental data by MC is crucial. In order to compute weights needed for extraction of $\Delta G/G$ we need the information from the two MC samples: the *high* p_T sample and the inclusive one. Both samples should be restricted to the DIS region, defined by $Q^2 > 1\,\text{GeV}^2$. The LEPTO is the event generator used to describe the DIS data. Another widely used generator is PYTHIA [54]. However PYTHIA cannot be used for the analysis of $Q^2 > 1\,\text{GeV}^2$ data, since there are problems in the description of the processes fractions in this case, even though the total cross section is reproduced properly, as explained in Ref. [104].

The first step in the Monte Carlo studies was the simulation of experimental conditions to reproduce the particles distributions observed for the data. The simulations were therefore checked extensively by comparing the distributions of normalised data and MC for variables describing the scattered muon and both selected hadrons. With enough confidence that LEPTO describes our data correctly we can treat it as a model for the underlying physics processes. In the second step MC simulations are used to extract essential physics quantities. This step is described in Chapter 9.

8.1 LEPTO generator

In presented analysis the muon-nucleon interactions were generated using LEPTO 6.5 program. LEPTO generator is based on the leading order electroweak cross sections and includes the QCD corrections using exact first order matrix elements for the PGF and QCDC processes. It has an option to include also higher order corrections simulated in terms of the leading $\log Q^2$ parton cascade approach. The fragmentation of produced partons into observable hadrons is performed with the LUND string hadronisation model.

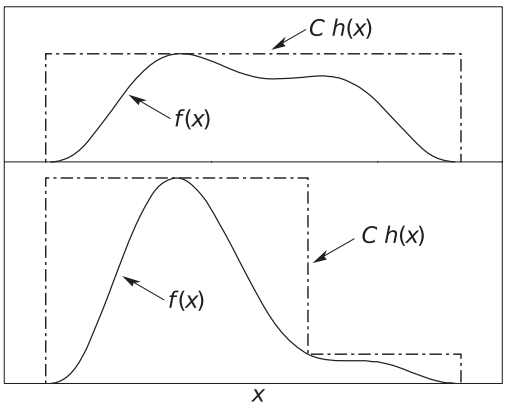

Figure 8.1: Illustration of the acceptance-rejection method. Random points are chosen inside the upper bounding figure ($C \cdot h(x)$), and rejected if the ordinate exceeds $f(x)$. The lower figure illustrates a method to increase the efficiency by selecting an "envelope" that closer follows the variation of $f(x)$. The figure is from Ref. [27].

8.1.1 Simulation procedure

In the LEPTO generator the procedure used to simulate the event kinematics for a chosen process is based on the known measured cross sections. For neutral current interactions a phase space point has to be generated, usually in the $(x,\ Q^2)$ plane, with a probability proportional to the known cross section.

It is done in two steps. First the cross section dependence for each variable $(x,\ Q^2)$ is parametrised independently as a simple functional form. Such function f must "envelop" the cross section, $f(\chi) > d\sigma/d\chi$ (Fig. 8.1). It should be also chosen so that its cumulative distribution function is analytically invertible. Then a univocal χ value can be obtained that follows $f(\chi)$ distribution

$$\chi = F^{-1}(u), \tag{8.1}$$

where F^{-1} is an inverse of cumulative distribution of function $f(\chi)$, χ represents one of the $x,\ Q^2$ variables and u is a random number obtained from the uniform distribution. Regions where f overestimates the cross-section are treated using the rejection technique. Then another random number v is generated from uniform distribution. If $v \cdot f(\chi) < d\sigma/d\chi$ the point is accepted. Otherwise the procedure is repeated [27, 55].

8.1.2 Cross section parametrisation

For the considered Q^2 region the pure γ exchange dominates the cross section which can be described as

$$\frac{d^2\sigma}{dxdQ^2} = \frac{2\pi\alpha^2}{xQ^2}(1 + (1-y)^2)F_2(x,\ Q^2), \tag{8.2}$$

where the structure function F_2 is parametrised in terms of the $q(x, Q^2)$, $\bar{q}(x, Q^2)$ and $g(x, Q^2)$ parton density functions (PDFs). The best PDFs were selected by requiring consistency of the parametrisations of the F_2 structure function with the results of the F_2 measurements by the NMC experiment [112]. Such agreement is important as the region of x and Q^2 covered in this measurement is very similar to the one of the NMC. There is an additional restriction for PDF selection to be considered; the PDF has to be usable down to $Q^2 = 1\,\text{GeV}^2$. The "MRST04 LO 3 flavours" [113] parametrisation was selected for further simulations. The "MRST family" of PDFs describes the data most precisely from available LO PQCD parametrisations and the

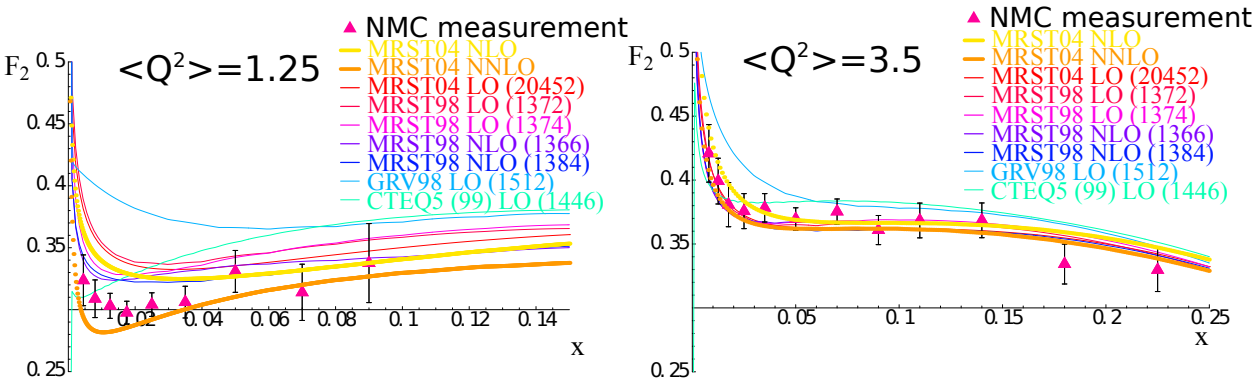

Figure 8.2: Comparison of F_2 parametrised using different PDF sets with the NMC measurement. The comparison is shown for two Q^2 bins: $\langle Q^2 \rangle = 1.25\,\mathrm{GeV}^2$ (left) and $\langle Q^2 \rangle = 3.5\,\mathrm{GeV}^2$ (right). The GRV98 LO [62] and CTEQ5 LO [114] parametrisations do not describe NMC data while the agreement for MRST "family" of PDF sets is reasonable.

MRST04 is the most recent one. The LO parametrisation had to be selected as LEPTO generator is using LO approximation. The difference between NLO and LO parametrisations in the considered region is anyhow small. Moreover the visible effects of NNLO corrections are partially taken into account in the simulations via Parton Shower mechanism. Results of the comparison are presented in Fig. 8.2.

8.1.3 First order QCD processes

The leading order parton level process is $\gamma q \to q$. At first order of QCD the QCDC process $\gamma q \to qg$ and the PGF process $\gamma g \to q\bar{q}$ have to be included in the matrix element. The first order matrix elements have soft and collinear divergences that in the full calculations are partly cancelled by virtual corrections while the rest is absorbed in the parton density functions. Such cancellation is not possible in MC calculation, thus to avoid those singularities cut-offs are introduced. In the presented analysis the "$z\hat{s}$ cut-off" scheme was used (it is the default option for LEPTO generator). It has two cut-off parameters: the fraction z_q of parton energy with respect to the virtual photon and the invariant mass of the partonic subsystem $\hat{s}$, to regulate separately the divergences with respect to the incoming parton direction and for the two produced partons, respectively. The cut-offs are implemented as $z_{q,min} < z_q < 1 - z_{q,min}$ and $\hat{s} > \hat{s}_{min}$. It was checked if our experimental data can be used to determine the parameters ($z_{q,min}$, $\hat{s}_{min}$) of the cutoffs. Unfortunately none of the considered hadronic observables (p_L, p_T, z, θ, ϕ) is sensitive to the cutoff selection. Hence the default values are used as they were selected by the authors of LEPTO based on more suitable data.

To decide on the event-by-event basis which process type should be generated a probability for each event type is calculated as a function of kinematic variables x and Q^2. The measured cross section contains all processes from all orders of QCD perturbative expansion. Thus when considering only three processes and neglecting higher order corrections the probabilities for them should add up to one. Hence the LP events probability P_{LP} is defined by $P_{LP} = 1 - P_{QCDC} - P_{PGF}$, where P_{QCDC} and P_{PGF} are the first order QCD processes probabilities. They are defined as the ratio of the cross section obtained from the first order matrix element and the overall differential cross section. As explained previously the calculations of the matrix element integral depend on the cutoff selection, therefore the simulated fractions of processes are sensitive to the values of cutoffs.

For the factorisation scale, which appears in the parton densities, and for the renormalisation scale, which

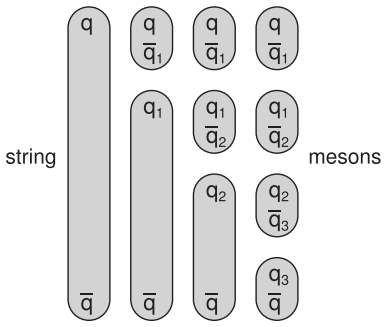

Figure 8.3: Iterative string fragmentation into hadrons. The string breaking continues as long as enough energy for the production of new $q\bar{q}$ pairs is available.

appears in expressions depending on the strong coupling constant α_s, the Q^2 was selected. This choice of the scale is a default one in LEPTO. The uncertainty related to the Q^2 scale selection is taken into account in the determination of systematic uncertainty.

8.1.4 Hadronisation

The hadronisation of produced partons into observable hadrons is based on the LUND model as implemented in JETSET package [115]. In this model a colour triplet string is stretched between the products of the reaction. This system hadronises by the production of quark-antiquark or quark-diquark pairs from the energy of the colour field, leading to production of hadrons.

Fig. 8.3 illustrates the string breaking of the colour flux between q and $\bar{q}$ with the creation of the new $q_1\bar{q}_1$-pair, such that a meson $q\bar{q}_1$ can be formed followed by the scaled down version of the string between $\bar{q}$ and q_1 and the further creation of new $q_i\bar{q}_i$ pairs is an iterative procedure until the last two hadrons are formed. Classically the two quarks of the $q_i\bar{q}_i$-pair must be produced at a certain distance so that the field energy between them can be used to produce the mass. Quantum mechanically the quarks may be created at the same point with local flavour conservation and then tunnelled out to the classically allowed region. For $q_i\bar{q}_i$-pairs generated in a tunnelling process the production probability is

$$exp\left(-\frac{\pi m_T^2}{\kappa}\right) = exp\left(-\frac{\pi m^2}{\kappa}\right) exp\left(-\frac{\pi k_T^2}{\kappa}\right) \tag{8.3}$$

with the mass m of the produced quark (antiquark) and its transverse momentum k_T relative to the string. The string constant κ, representing the energy per unit length of the colour flux tube, is known phenomenologically to be $\kappa \approx 1$GeV/fm.

Since the string is assumed to have no transverse excitations, the k_T is locally compensated between the quark and antiquark of the pair. This leads to a flavour independent Gaussian spectrum for the p_T of the produced hadrons (*i.e.* the $q_i\bar{q}_j$-pairs) with a width $\sigma(p_T) \approx 0.36\,$GeV (parameter PARJ(21) in JETSET [115]). In practise there are non-Gaussian tails to this shape which are modelled by a second broader Gaussian that is added to the first one. The width of the second Gaussian is given by the parameter PARJ(24) (=2, default value) and the fraction of this admixture by PARJ(23) (=0.01, default value). The tunnelling picture also implies a suppression of heavy quark production, $u : d : s : c \approx 1 : 1 : 0.3 : 10^{-11}$ [116].

In JETSET the hadronisation process is governed by so called LUND symmetric fragmentation function based on Eq. 8.3. It defines the probability for the fraction z of the available energy taken by a newly created

hadron as

$$f(z) = z^{-1}(1-z)^a e^{-bm_T^2/z}, \tag{8.4}$$

where $m_T^2 = m^2 + p_T^2$ and m is the mass of the hadron. The parameters a and b were obtained from fits to e^+e^- data and are usually assumed to be the same in the DIS region. However in studies carried out by HERMES and SMC experiments it was shown that the modification of those parameters is needed for better description of the experimental data [117, 103]. Also in the analysis presented here these parameters were adjusted to obtain a correct description of the experimental results. This is described in more detail in Sec. 8.3.

Let us describe the nucleon remnant treatment starting from the LP. When the struck parton is a valence quark the string is attached to the nucleon remnant which is a diquark. The string is split according to the LUND fragmentation function f (Eq. 8.4).

In case of a struck sea quark (antiquark) the remaining system consists of three valence quarks and a corresponding sea antiquark (quark). The partner of the struck parton gets assigned a fraction of the nucleon longitudinal momentum according to the Altareli-Parisi splitting function $P(g \to q\bar{q})$ (*cf.* Sec. 2.2.4). The valence quarks are randomly divided into a quark and a diquark. The split of the remnant involves sharing of the momentum between the quark and the diquark according to the LUND fragmentation function f (Eq. 8.4). Two strings are formed: one between the single valence quark and the sea antiquark, the second between the diquark and the sea quark.

In case of the PGF process a very similar scenario occurs, also in this case the nucleon remnant is split into a quark and diquark. They form two strings with the antiquark and quark, respectively, produced in the fusion process.

For the QCDC process the string is stretched from the scattered quark via gluon to the target remnant (for detailed description of multiparton system fragmentation see Ref. [116] Sec. 12.2.4).

8.1.5 Parton shower

In order to take into account higher order QCD effects in LEPTO the parton shower (PS) approach [118] is used. In DIS the struck parton can emit a gluon either before or after the boson vertex thus leading to initial or final state parton showers (Fig. 8.4). In such approach any higher orders in α_s can be simulated, but only in the leading $\log Q^2$ approximation. The shower evolution is governed by the Sudakov form factor. The inclusion of the PS into the MC simulation dramatically improves the description of the data. Especially the p_T distributions are affected as presented in Fig. 8.8. In part this is expected as the parameters of the fragmentation function were tuned in the presence of the PS. For the case without PS the fragmentation parameters should be adjusted to take into account the additional parton emissions not simulated explicitly because the default settings are obtained with PS.

8.2 Selection of MC samples

For the *high* p_T MC sample the same selection of events as for the experimental data is used (see Sec. 7.4). To economise the computational time the high p_T sample is generated with additional pre-cuts applied at the generator level: p_T of two hadrons $> 0.6\,\text{GeV}$ and $\theta_h < 250\,\text{mrad}$.

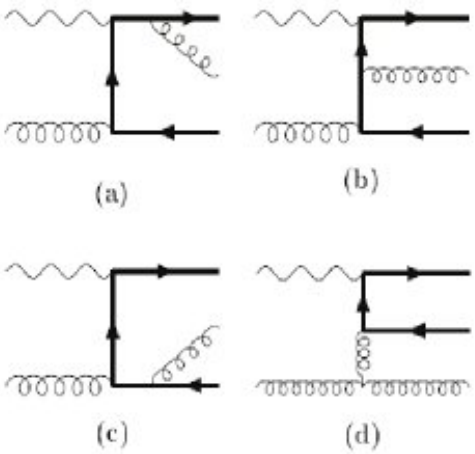

Figure 8.4: Selected Feynman diagrams of the PGF process with gluon emissions treated by Parton Shower mechanism. Figures (a-c) present final state showers while figure (d) shows a initial state one.

For the inclusive sample the selection is as follows. Selected events are required to have a primary vertex containing a reconstructed beam muon μ and a reconstructed scattered muon μ'. In order to prevent fake triggers a reconstructed scattered muon is required to have associated hits in both hodoscope stations that gave a trigger as in high p_T case. In case of semi-inclusive triggers a presence of a hadron track originating from the interaction point is required in addition. The beam energy is required to be in the interval between 140 and 180 GeV. In order to select events from perturbative regime it is required that $Q^2 > 1\,\text{GeV}^2$. In addition as described for high p_T selection a cut $0.1 < y < 0.9$ is applied. Also the same vertex cuts are used as for the data.

8.3 Simulation of experimental conditions

The LEPTO generator is responsible for the simulation of an underlying physics process on the partonic level and the hadronisation of produced partons. The experimental setup and response of the spectrometer for the passage of the produced particles is simulated by the COMGEANT program [119]. COMGEANT is based on GEANT 3 package [120] and is responsible for description of material located in the experimental hall, interactions of particles produced by LEPTO with that material, description of the magnetic fields and the passage of charged particles through them, and finally description of the COMPASS spectrometer detectors and simulation of their response. The "hits" generated by COMGEANT are then processed by the CORAL reconstruction program in the same way as the experimental data. This ensures that any tracking inefficiencies of the data are taken into account in the MC simulations. The reconstructed MC events can be analysed in the same way as experimental data with an additional benefit of available full information about the generated events.

8.3.1 Verification of the apparatus description

In order to obtain a good description of the experimental data a proper simulation of our apparatus was examined. For this purpose mainly the agreement between the real and simulated data for muon variables in the inclusive sample was considered.

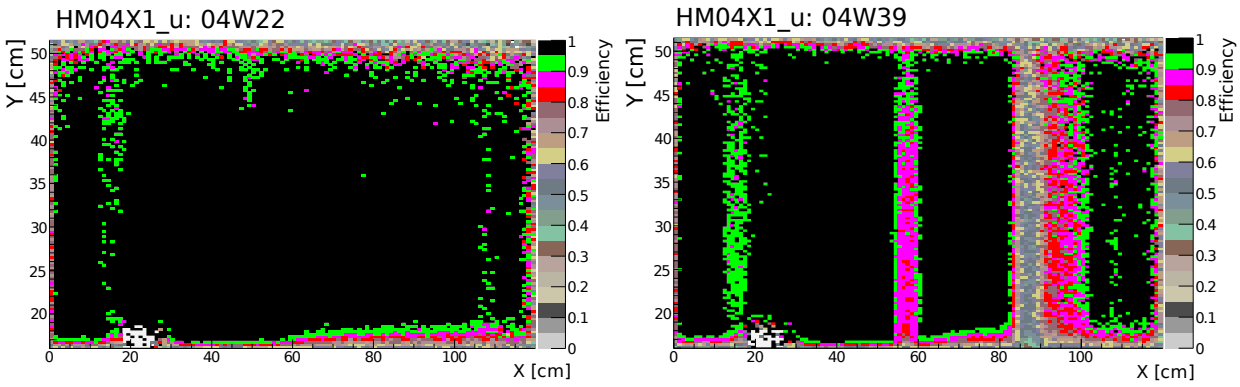

Figure 8.5: Efficiency of one of the trigger hodoscope planes during two periods of data taking. For period 04W39 less efficient slabs are clearly visible.

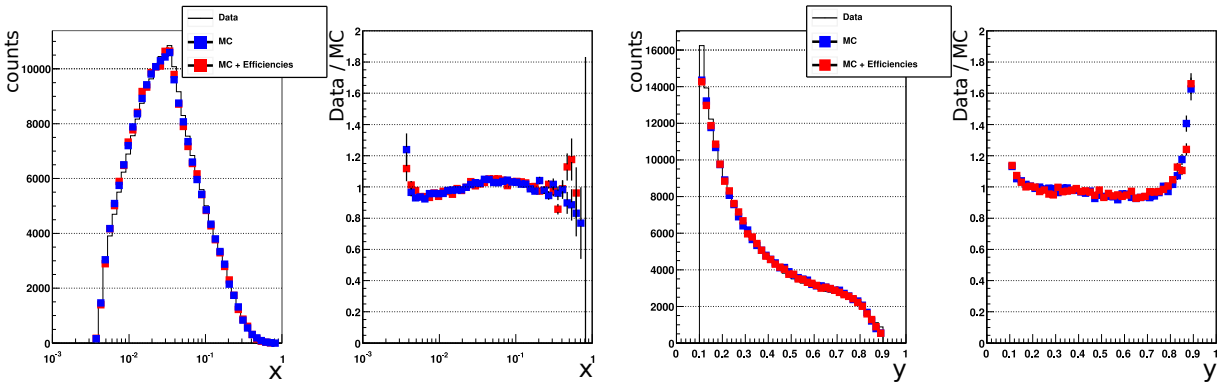

Figure 8.6: Impact on the data description by the MC simulations of trigger hodoscope inefficiencies. The data vs. MC comparison is presented for x and y kinematic variables for inclusive sample (2004).

Incoming beam particles used by the generator were extracted from data. For each year of data taking one set of beam tracks was created. To describe properly the beam the data obtained with the random trigger were used. This ensures that the beam profile is not biased by trigger acceptance as most of the beam tracks will not interact in the target. Beam tracks are reconstructed by the Beam Telescope and the BMS with possibility of bridging with a spectrometer track. To extract halo tracks the time gates in the reconstruction are enlarged. This enables to reconstruct the "off time" tracks. Tracks that are reconstructed in the spectrometer and can be identified as a muons, excluding all that are identified as beam, are extracted as halo tracks. The impact of the proper description of the beam position on the inclusive kinematic variables was studied and have been found to be negligible in case of $Q^2 > 1\,\mathrm{GeV}^2$ samples. As a next step the efficiencies of the trigger hodoscope planes were extracted for years 2003 and 2004 from the experimental data and were included in the COMGEANT. Also here the impact on distributions of the kinematic variables was found to be small. As an example, the 2D efficiency map of one of the trigger planes and its evolution during one year of data taking is presented in Fig. 8.5. The impact on the kinematic variables is shown in Fig. 8.6. The fact that those two effects do not have a big impact on data description by MC simulations, in spite of the fact that both beam position and efficiencies of hodoscope planes have been found to vary with time, allows us to use only one MC simulation per year.

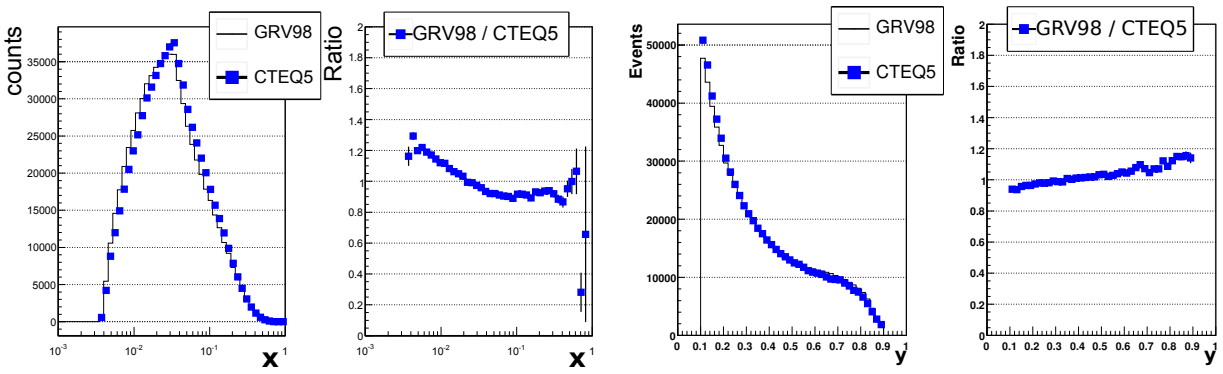

Figure 8.7: Comparison of two MC simulations with two different selections of the PDFs. The comparison is presented for x and y kinematic variables.

8.3.2 Adjustment of the generator parameters

With a gained confidence that the apparatus is described well to our best knowledge, tuning of generator parameters was performed. The Fig. 8.7 presents the agreement between two MC simulations with different selection of the PDF parametrisation. It is seen that the choice of PDFs has strong influence on the shape of kinematic variables distribution for simulated events. Thus it will have a significant impact on agreement between the data and MC. As explained in Sec. 8.1.2 the PDFs were selected based on the comparison with the F_2 measurement by the NMC experiment.

With a satisfactory description of the inclusive variables distributions studies of the agreement between the data and the simulation for the high p_T sample were performed. To obtain a good description of the experimental data Parton Shower in LEPTO had to be enabled. Especially the description of hadrons transverse momenta has improved as presented in Fig. 8.8. This poses a theoretical dilemma, as with the PS one simulates higher order effects whereas the formula for the $\Delta G/G$ is derived in LO. The impact of this is taken into account for the estimation of the systematic uncertainty.

To improve the agreement between data and MC for hadronic variables the parametrisation of fragmentation in the LEPTO generator has been tuned. The parameters a (PARJ 41) and b (PARJ 42) of the LUND fragmentation function (Eq. 8.4) were adjusted in such a way that the description of the p_L, p_T and z of the leading hadron is optimal. A broad spectrum of parameter values was scanned in order to check sensitivity of hadronic observables to these parameters. The final set of parameters was selected based on the best agreement of the full MC simulation with the experimental data. To improve further the agreement for high values of transverse momenta the distribution of the transverse momenta from the fragmentation process was adjusted. Three parameters are available: PARJ 21 - the width of the Gaussian core, PARJ 23 - the width of a second Gaussian modelling the non Gaussian tails, PARJ 24 - height of second Gaussian as a fraction of the core height. The obtained values are given in Table 8.1. For detailed discussion of the adjustment of the JETSET fragmentation parameters see Ref. [104].

	PARJ 21	PARJ 23	PARJ 24	PARJ 41	PARJ 42
Default	0.36	0.01	2.0	0.3	0.58
COMPASS	0.3	0.02	3.5	0.6	0.1

Table 8.1: Default and COMPASS tuned values of LEPTO fragmentation parameters.

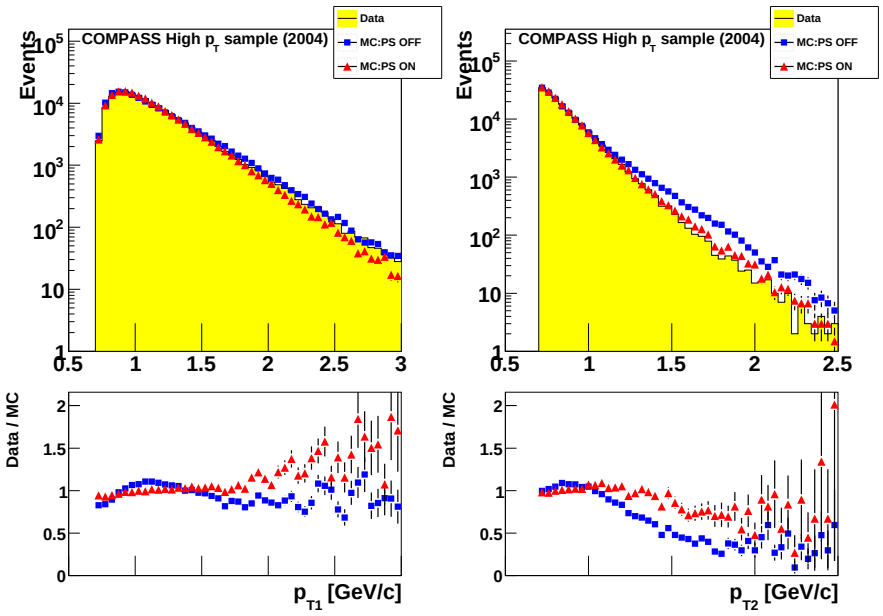

Figure 8.8: Comparison between the data and the MC simulations for the high-p_T sample (2004): red triangles - PS on, blue squares - PS off. The distributions and ratios Data/MC for hadron transverse momenta are shown.

	Final MC	Mean from 4 MC's	RMS from 4 MC's
$< a_{LL}^{LP} >$	0.633	0.628	0.030
$< a_{LL}^{QCDC} >$	0.495	0.474	0.018
$< a_{LL}^{PGF} >$	-0.363	-0.376	0.012
R^{LP}	0.399	0.394	0.066
R^{QCDC}	0.292	0.309	0.044
R^{PGF}	0.309	0.296	0.025

Table 8.2: Dependence of $< a_{LL}$'s $>$ and process fractions on MC settings. Presented are values for "Final" MC sample and averaged ones over the four MC samples.

8.3.3 Comparison with the data

In Fig. 8.9 the comparison between the data and the MC simulation for the inclusive sample is presented for kinematic variables x, Q^2 and y. In Fig. 8.10 and 8.11 the agreement for the high p_T sample is illustrated for the MC with default (red triangles) and COMPASS tuning (blue squares). Fig. 8.10 shows distributions of variables x, Q^2, y, while Fig. 8.11 those for hadronic ones: momenta and transverse momenta of the leading and next to leading hadrons. Distributions were normalised to the number of events in the data sample.

MC is used to train neural networks in order to parametrise several characteristics of our samples. It is important to know how those characteristics are affected by different tunings of the MC. In order to estimate systematic effects associated with this, four MC samples were prepared:

1. default fragmentation parameters, PS off;
2. default fragmentation parameters, PS on;
3. COMPASS fragmentation tuning, PS off;
4. COMPASS fragmentation tuning, PS on.

The dependence of considered variables (a_{LL}^{LP}, a_{LL}^{QCDC}, a_{LL}^{PGF}, R^{LP}, R^{QCDC}, R^{PGF}) on the MC settings

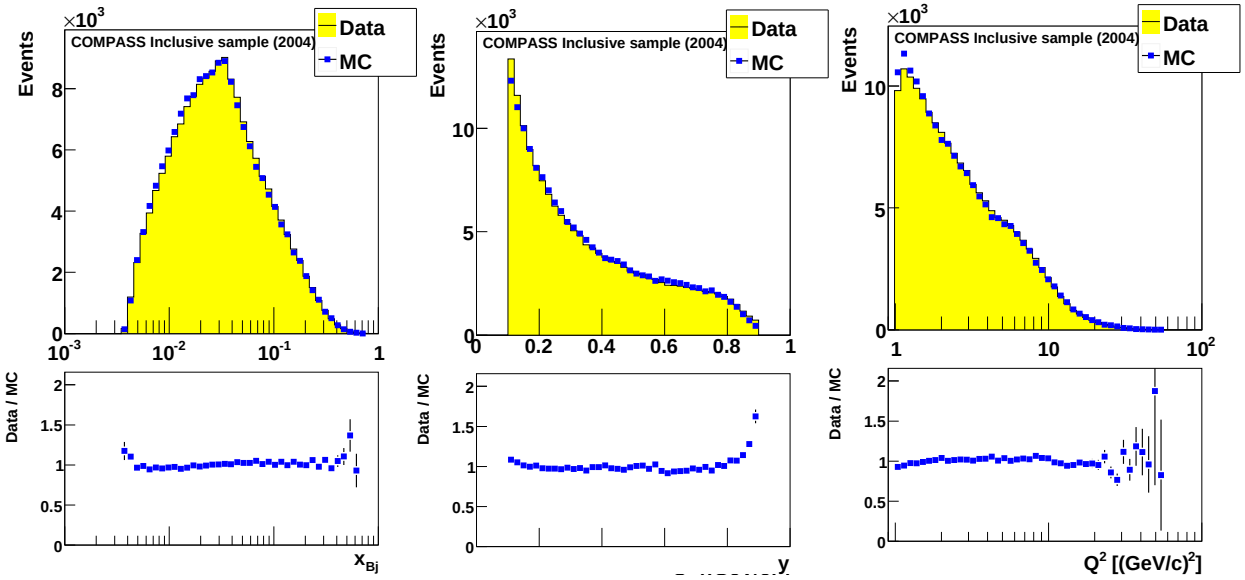

Figure 8.9: Comparison between the data and the MC simulation for the inclusive sample (2004). The distributions and the ratios Data/MC are shown as functions of x_{Bj}, Q^2 and y.

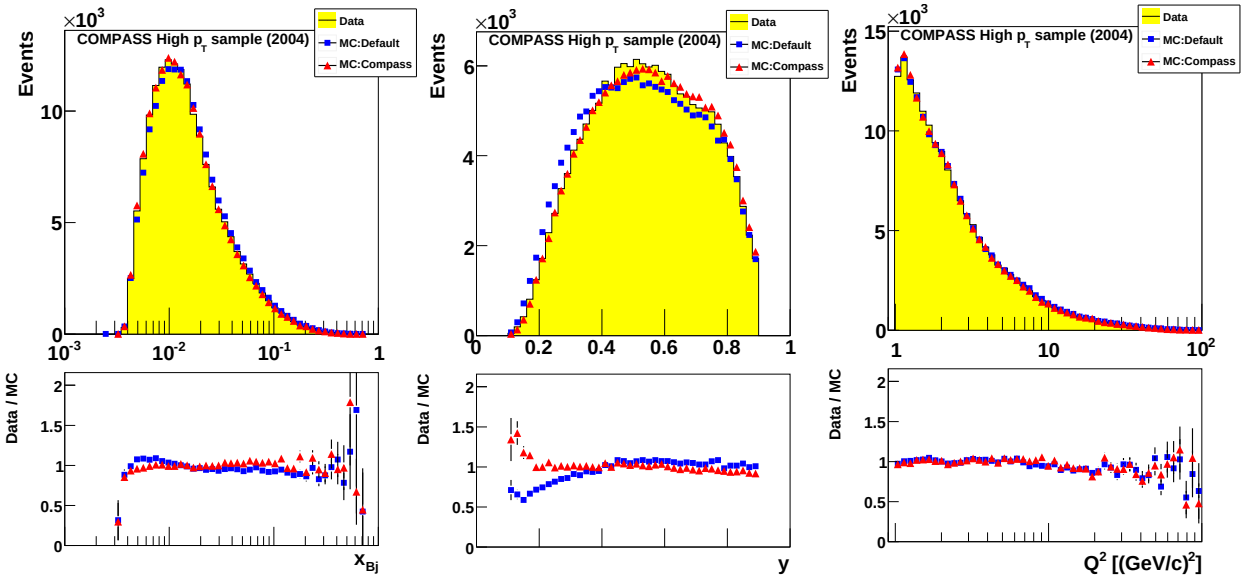

Figure 8.10: Comparison between the data and the MC simulations for the high-p_T sample (2004): red triangles - COMPASS tuning, blue squares - default parameters. The distributions and ratios Data/MC are shown for inclusive variables x_{Bj}, Q^2, y.

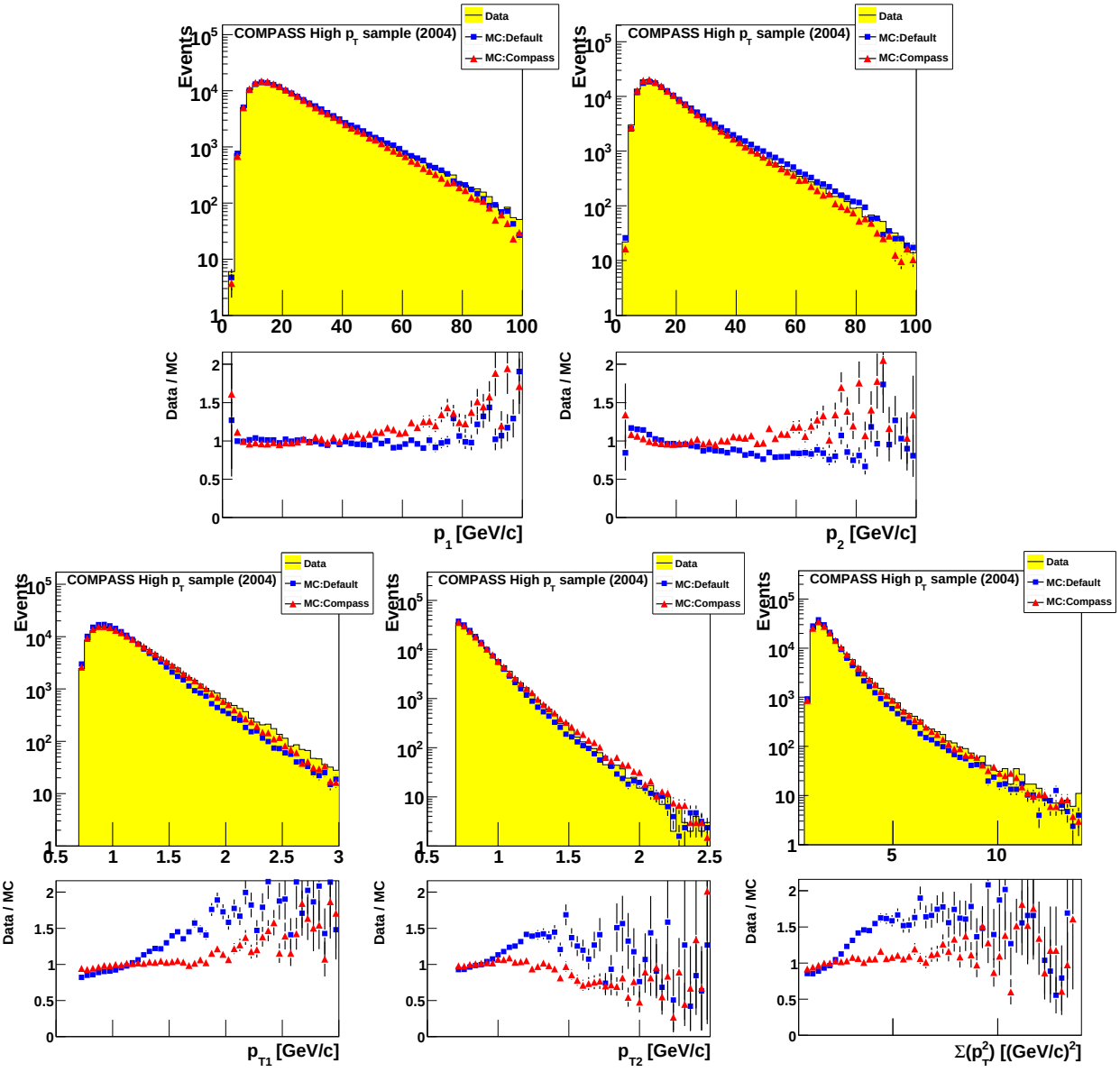

Figure 8.11: Comparison between the data and the MC simulations for the high-p_T sample (2004): red triangles - COMPASS tuning, blue squares - default tuning. The distributions and ratios Data/MC are shown for hadronic variables p_1, p_2, p_{T1}, p_{T2} and $\Sigma(p_T^2)$.

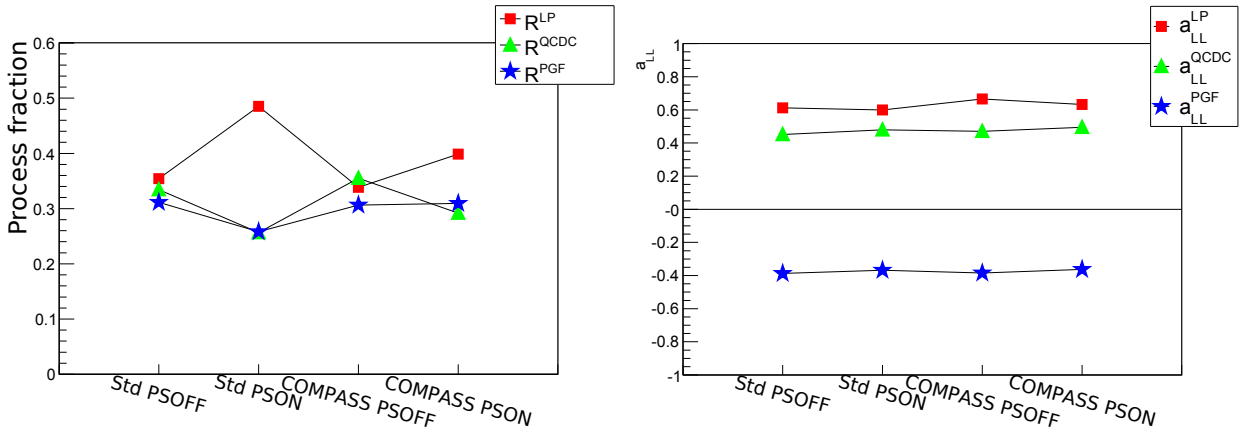

Figure 8.12: The dependence of fractions R^i (left plot) and $< a_{LL}$'s $>$ (right plot) for LO, QCDC and PGF processes on the MC settings.

is presented in Table 8.2 and in Fig. 8.12. Studies of systematic uncertainty due to generator parameters setting are described in more detail in Sec. 10.5.

The final settings for the MC simulations that gave the best description of data consist of:

1. Usage of the beam profile extracted from experimental data.
2. Parametrisation of trigger hodoscopes efficiencies.
3. Usage of MRST04 LO parametrisation of the PDFs.
4. Inclusion of Parton Shower mechanism.
5. Modification of the fragmentation parameter values as defined in Table 8.1.

Due to the performed tuning of the LEPTO parameters a satisfactory description of experimental data by MC, both for the inclusive and high p_T samples, was obtained. Therefore with a confidence we can use the MC to parametrise fractions of processes and their a_{LL}'s.

Chapter 9

Neural networks approach

As already explained in Sec. 7.1.2, in order to extract the polarisation of gluons in the nucleon parametrisations of several quantities as a function of measured variables are needed. Such parametrisations were obtained using neural networks. In the following section the basic terminology is introduced and the type of neural networks that was used in the analysis is described in more detail. In Sec. 9.2 the details of the training procedure as well as the results of the parametrisations are discussed. Secs 9.3 and 9.4 discuss the parametrisation of the momentum fraction carried by the gluon x_G and the scale μ^2.

9.1 Neural networks

Artificial neural networks (NN) are one of the modern methods of data analysis. They are based on the way the human brain works and their main characteristic is an ability to learn. Although neural networks are a greatly simplified model of the brain they are capable *e.g.* of modelling an object of unknown characteristics - parametrisation, dividing a set of objects into several groups based on their characteristics - classification, and many more. In fact the classification is one of the most popular tasks where neural networks are used; for image recognition, speech recognition, separation of signal from background.

In this chapter the focus will be on one type of neural networks, a multilayer perceptron (MLP). This type of neural network is frequently used for classification or parametrisation tasks and it was used also in the presented analysis. The MLP is a neural network without a feedback, the signal is propagated throughout the network in one direction. In Fig. 9.1 a schematic diagram of a MLP is presented. The neural network, similarly to the brain, is composed of neurons and their connections. In the MLP the neurons are organised in several layers, with neurons connected only to the previous and the next layers. The input signal is introduced through the input layer by setting the state of the neurons from which it is composed. For a network with N_0 inputs this will be denoted as u_i where $i = 1, \ldots, N_0$. Then the signal, through the connections between the neurons, is propagated to the output layer. It is worth to say that at least one hidden layer is needed for the MLP to be able to parametrise the exclusive OR (XOR) logic function. However, already two hidden layers are sufficient to enable the network to cope with any parametrisation problem [121].

The neuron is a building block of the neural network, it has input connections that have different weights and its state is a function of the weighted input signals. The output can be connected to several other neurons. A model of the neuron that is commonly used has been introduced by McCulloch and Pitts in 1943

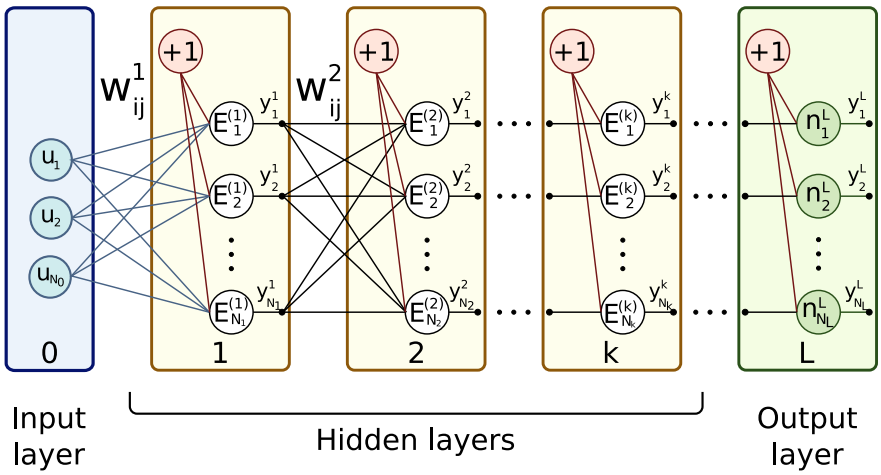

Figure 9.1: Multilayer perceptron. The "+1" inputs for each layers are the *bias terms* and allow for adjustment of the activation threshold.

[122]. We will consider an MLP with L layers, each consisting of N_k neurons where $k = 1, 2, \ldots, L$. The state of a neuron i from a layer k ($E_i^{(k)}$) is defined as

$$y_i^{(k)} = f\left(s_i^{(k)}\right), \tag{9.1}$$

where

$$s_i^{(k)} = \sum_{j=0}^{N_{k-1}} w_{ij}^{(k)} x_j^{(k)}, \qquad f(x) = \begin{cases} 1 \; when & x \geqslant 0 \\ 0 \; when & x < 0 \end{cases}. \tag{9.2}$$

The x_j are the input signals of the neuron $E_i^{(k)}$ which are connected to the neurons from the layer $k-1$ in the following way

$$x_i^{(k)} = \begin{cases} u_i & for\ i > 0,\ k = 1 \\ y_i^{(k-1)} & for\ i > 0,\ k = 2, \ldots, L \\ +1 & for\ i = 0,\ k = 1, \ldots, L \end{cases}. \tag{9.3}$$

The w_{ij} are the weights of the connections with input neurons. Such a neuron is presented schematically in Fig. 9.2. The weights $w_{i0}^{(k)}$ are called bias terms and have a meaning of a threshold value for the neurons activation. This is easily seen by rewriting Eq. 9.2 as follows

$$y_i^{(k)} = \begin{cases} 1 & when\ \hat{s}_i^{(k)} + w_{i0}^{(k)} \geq 0, \\ 0 & when\ \hat{s}_i^{(k)} + w_{i0}^{(k)} < 0, \end{cases} \tag{9.4}$$

where $\hat{s}_i^{(k)} = \sum_{j=1}^{N_{k-1}} w_{ij}^{(k)} x_j^{(k)}$.

In most applications of MLP the original Heaviside activation function $f(x)$ is replaced with a continuous sigmoid function like $f(x) = 1/(1 + exp(-\beta x));\ \beta > 0$, or a hyperbolic tangent $f(x) = tgh(\alpha x/2) = (1 - exp(-\alpha x))/(1 + exp(-\alpha x));\ \alpha > 0$. Different activation functions are presented in Fig. 9.3. By selection of an activation function the sensitivity of the neural network to the outliers in the input data can be adjusted. In the presented analysis the unipolar sigmoid function was used. One exception is the activation function of the neurons in the output layer, which for the parametrisation tasks is chosen as a simple linear function

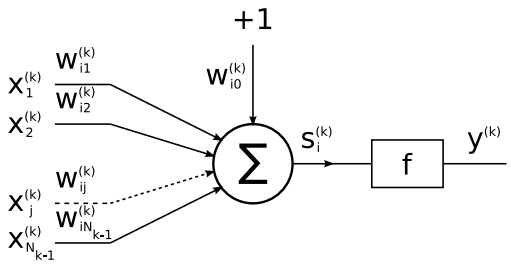

Figure 9.2: Schematic representation of a neuron $E_i^{(k)}$.

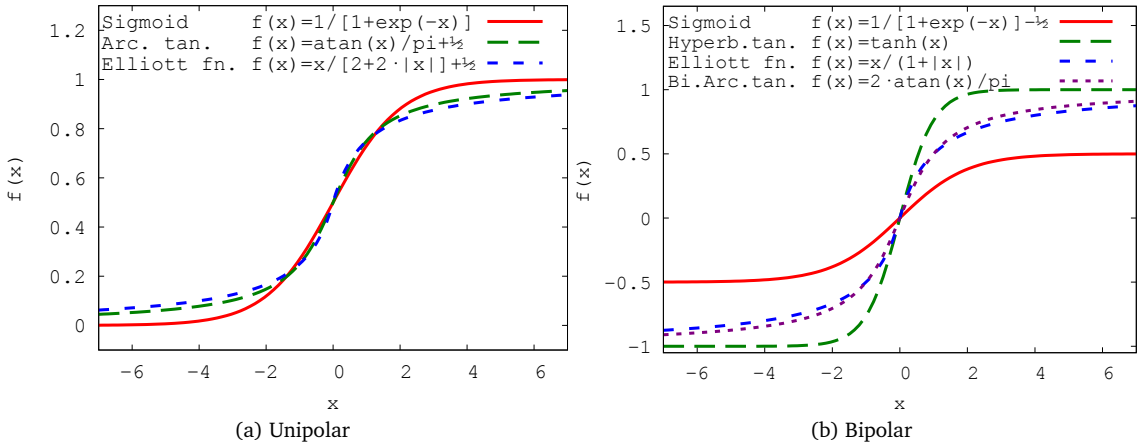

(a) Unipolar (b) Bipolar

Figure 9.3: Neuron activation functions.

$f(x) = x$. This assures that the output is proportional to the input signals.

The ability of the neural network to learn is realised by the weights that are assigned to the connections between neurons. Values of the weights are adjusted during the training procedure. In the presented work the supervised training technique is used. It is an iterative procedure where for each iteration step n the values of weights are adjusted. To determine the weights corrections a training data set is needed where the expected output $d_i(n)$ of neural network for step n is known for each input vector. During the training the response of the neural network is compared to the expected one and an error is calculated, usually as the Mean Squares Error (MSE)

$$Q(n) = \sum_{i=1}^{N_L} \left(d_i(n) - y_i^{(L)}(n) \right)^2, \tag{9.5}$$

where L denotes the output layer. In the presented analysis the MSE function was always used, although in some other applications an asymmetric error function can be better suited, *e.g.*
$Q(n) = \sum_{i=1}^{N_L} \left[a \left(d_i(n) - y_i^{(L)}(n) \right) \right]^2 / \left[a \left(d_i(n) - y_i^{(L)}(n) \right) + 1 \right]$, where a is a scaling factor.

In the course of the training procedure, the weights are adjusted in order to minimise the error. The minimisation is based on the steepest gradient algorithm

$$w_{ij}^{(k)}(n+1) = w_{ij}^{(k)}(n) - \eta \frac{\partial Q(n)}{\partial w_{ij}^{(k)}(n)}, \tag{9.6}$$

where the constant $\eta > 0$ stands for the step size. Let us consider

$$\frac{\partial Q(n)}{\partial w_{ij}^{(k)}(n)} = \frac{\partial Q(n)}{\partial s_i^{(k)}(n)} \frac{\partial s_i^{(k)}(n)}{\partial w_{ij}^{(k)}(n)} = \frac{\partial Q(n)}{\partial s_i^{(k)}(n)} x_j^{(k)}(n) = -2\delta_i^{(k)}(n) x_j^{(k)}(n); \qquad \delta_i^{(k)}(n) = -\frac{1}{2} \frac{\partial Q(n)}{\partial s_i^{(k)}(n)}. \tag{9.7}$$

Thus we obtain the following equation for the weight after adjustment

$$w_{ij}^{(k)}(n+1) = w_{ij}^{(k)}(n) + 2\eta\delta_i^{(k)}(n)x_j^{(k)}(n). \tag{9.8}$$

In case of the MSE function $\delta_i^{(k)}(n)$ becomes

$$\delta_i^{(k)}(n) = \varepsilon_i^{(k)}(n)f'(s_i^{(k)}(n)); \qquad \varepsilon_i^{(k)}(n) = \begin{cases} d_i(n) - y_i^{(L)}(n) & \text{for } k = L \\ \sum_{m=1}^{N_{k+1}} \delta_m^{(k+1)}(n)w_{mi}^{(k+1)} & \text{for } k = 1, \ldots, L-1 \end{cases}, \tag{9.9}$$

with f' being the derivative of f. In this algorithm the errors are calculated starting from the output layer and then propagated towards the input layer. Such an algorithm of weights adjustment is called "error back-propagation". During the training the step size starts from being fairly large, then it is decreased when we are approaching the minimum in the error space. In order to speed up the convergence it is common to introduce a momentum term

$$w_{ij}^{(k)}(n+1) = w_{ij}^{(k)}(n) + 2\eta\varepsilon_i^{(k)}(n)f'(s_i^{(k)}(n))x_j^{(k)}(n) + \alpha\left[w_{ij}^{(k)}(n) - w_{ij}^{(k)}(n-1)\right], \tag{9.10}$$

where the parameter $\alpha\epsilon(0,1)$.

The data set on which the neural network is trained is randomly divided into two parts: the "training set" and the "testing set". The network is trained using the "training set" while the "testing set" is used to monitor the training procedure. When the network errors obtained from the two sets diverge too much, the training is stopped. This prevents situations where the neural network would learn the contents of the "training set" by heart instead of finding more general patterns. For more detailed description of neural networks see Ref. [123] and references therein.

It is possible that after training the neural network will end up in a local minimum in the error space. In order to minimise such a possibility a dynamic structure of the network is used. During the procedure additional neurons can be introduced or neurons that are not used can be removed. In case the modified network structure leads to a smaller error the modification is retained, otherwise the previous structure is used for further training. Attempts to modify the network structure are repeated periodically while the modification's position is selected randomly. Such procedure allows the network to search for a global minimum in case a local minimum is found.

The NN's used in this thesis were prepared using the NetMaker package [124]. The package was implemented for COMPASS and ICARUS neutrino experiment. The program is written in the C#[1] language and optimised for working with large data sets. It provides a graphical interface for a network preparation and for controlling the learning process. After the process is finalised, a file containing the description of the structure of the network, including all the weights, is prepared. It is a text file written in an XML[2] standard. A special C++ class, that simulates the neural network based on the XML file, was prepared and added to the PHAST package. The class allows to run during the analysis the neural network obtained with the NetMaker, and estimate the values of required kinematic variables and a_{LL}'s on the event-by-event basis.

[1] C# (C sharp) is an object-oriented programming language developed by Microsoft and based on C++ syntax.

[2] XML - the Extensible Markup Language is a general-purpose markup language. It provides a set of rules based on markups according to which an information, *e.g.* a structure of network, is described.

9.2 Parametrisations

In the proposed method of $\Delta G/G$ extraction from the measured asymmetry the knowledge of the fractions of the contributing processes (R_{PGF}, R_{QCDC}, R_{LP}, R^{inc}_{PGF}, R^{inc}_{QCDC}, R^{inc}_{LP}) and the values of the a_{LL}'s (a^{PGF}_{LL}, a^{QCDC}_{LL}, $a^{inc,PGF}_{LL}$, $a^{inc,QCDC}_{LL}$) as well as $x_C\,(x^{inc}_C)$ and $x_G\,(x^{inc}_G)$ is required on the event-by-event basis. For that purpose neural networks are used as a tool to obtain a parametrisation of required quantities as a function of measured variables. Several neural networks are needed, because each of the a_{LL}'s and the x variables is parametrised independently. The processes fractions were parametrised by the two neural networks, one for the inclusive and one for the high p_T sample.

The neural networks are trained in a mode where their output has an interpretation of the expectation value X of parametrised quantity as a function of the considered input parameters. Technically this means that the error function used in the training is a standard Mean Squares Error function (MSE) and that the neuron(s) of the last (output) layer has(ve) a linear activation function, resulting in the response proportional to the sum of the amplitudes of the input signals.

In the inclusive case the Bjorken scaling variable x and Q^2 are selected as the input variables. In case of the high p_T sample in addition the transverse and longitudinal momenta of the hadron pair (p_{T1}, p_{T2}, p_{L1}, p_{L2}) are used. The input variables are first normalised so that their mean value and variance in the training sample correspond to a normal distribution. This ensures that all signals from the input neurons are of the same magnitude and that importance of neither of the input variables is not enhanced artificially.

For the a_{LL}'s and the x variables the parametrisations are based on neural networks with one output neuron. Results of the training are presented in Fig. 9.4. The output of the neural networks, *i.e.* the parametrised value of the considered quantity, is plotted as a function of the input value. In the implementation of the $\Delta G/G$ extraction a_{LL}/D is used instead of a_{LL}, where D is the depolarisation factor. Therefore the NN is trained to parametrise directly a_{LL}/D. Obtained correlations between the parametrised and the true values are in general $\sim 60\%$. An exception is the correlation for the a_{LL} of the QCDC process which is significantly lower and which is not understood currently. However in order not to introduce a bias, it is sufficient that the mean value of the a_{LL} is reproduced correctly.

To illustrate this statement let us consider the unweighted method which can be treated as weighted method where all events have the same weight. In such case we could build the weight from the averaged values of a_{LL}'s over the whole sample, *i.e.* we would use a parametrisation that gives poor correlation while reproducing mean value correctly. As the unweighted method does not introduce a bias, we can assume that this is also the case for weighted method even for non-prefect correlation of a_{LL}'s parametrisation, provided that the mean values are reproduced.

The fractions R of the three processes sum up to unity. With this constraint it is sufficient to use two variables (dimensions) to parametrise them. Relations between the two parametrisation variables o_1 and o_2 and the processes fractions are following

$$R_{PGF} = 1 - o_1 - 1/\sqrt{3}o_2, \qquad R_{QCDC} = o_1 - 1/\sqrt{3}o_2, \qquad R_{LP} = 2/\sqrt{3}o_2. \tag{9.11}$$

Thus for the parametrisation a neural network with two output neurons (o_1 and o_2) is used. Table 9.1 gives the expected values of neural network outputs (so called training flags). The resulting neural net-

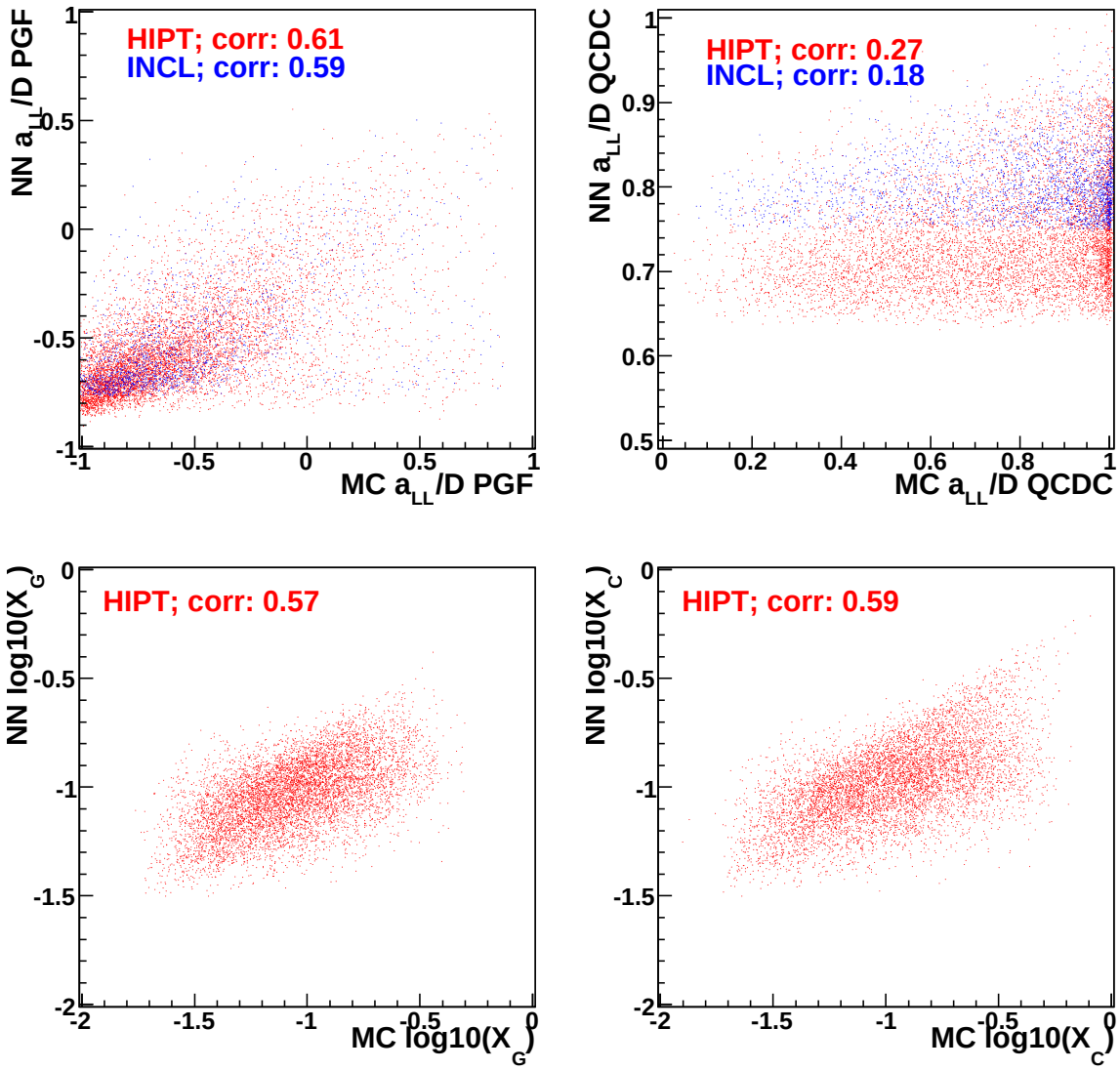

Figure 9.4: Output of neural networks for a_{LL}'s and x's. See text for details.

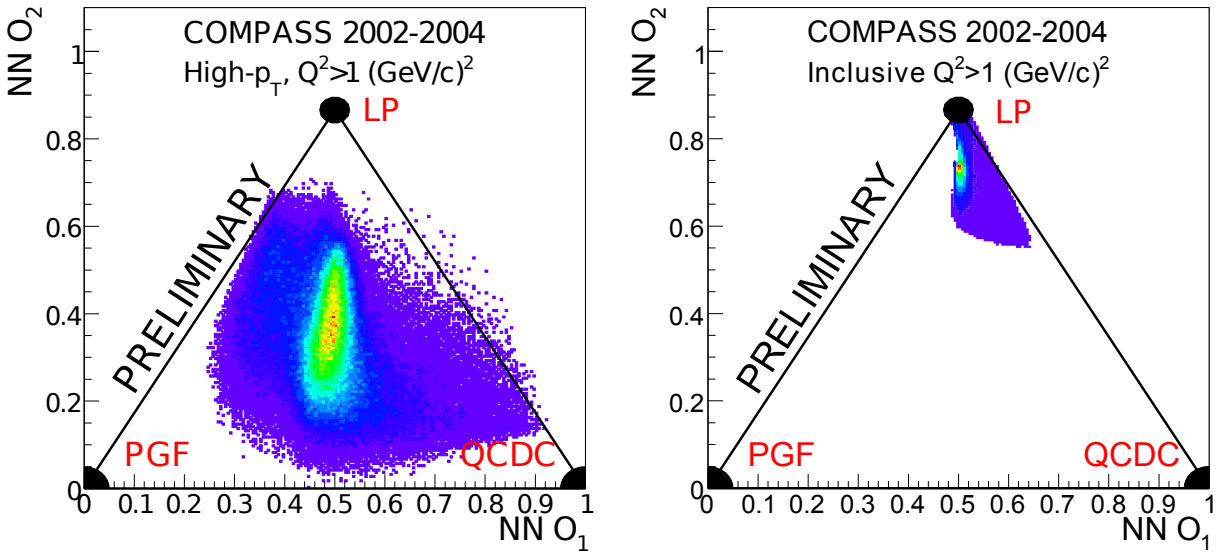

Figure 9.5: Two dimensional output of neural networks for estimation that a given event originated as PGF, QCDC, or LP. Left - high p_T sample, right - inclusive sample.

work outputs obtained for the high p_T and inclusive MC samples are presented as two-dimensional plots in Fig. 9.5. The triangles enclose the region where all R fractions are positive. Each triangle apex represents the situation when the fraction of indicated process is equal to 100%. The distances from the triangle sides are proportional to the fractions of 3 processes (0 for the distance equal to 0 and 100% for distance equal to the triangles height as defined in Eqs 9.11).

We know that for the inclusive sample $\sim 80\%$ of the events originates from the LP while the remaining 20% is divided to a good approximation evenly between QCDC and PGF. As consequence of this the NN returns on average large values of o_2, which correspond to high probability for an event to originate from LP, and values of o_1 that are ~ 0.5 which reflects the similar PGF and QCDC fractions. To explain why the NN output is being grouped in one corner of the output space and that no events are clearly identified as the PGF we have to consider that R's have a weak sensitivity to the input variables x and Q^2. If the R fractions would not depend on x and Q^2 then the neural network would simply return for each event the average values of R in the considered sample. On the "triangle plot" for the inclusive sample it would correspond to a single point[3] at $o_1 \approx 0.5$ and $o_2 \approx 0.7$. Fortunately the R fractions exhibit an x, Q^2 dependence although a weak one. This is seen as the elongated shape on the plot of 2D output of the NN. The visible "wing" on the right-hand side corresponds to a quite small fraction of events. In this region the average fraction of the QCDC is high and the events have high x values. For high x region the gluon distribution goes to zero, thus the PGF events are strongly suppressed. Still for the considered input variables $(x,\, Q^2)$ no sharp cut can be found that defines a region where only one process occurs. Therefore NN will only be able to reproduce average values of the fractions as a function of x and Q^2.

For the high p_T case the situation is different. The addition of hadronic input variables improves the sensitivity, while the high p_T cuts increase the PGF and QCDC fractions to a level where all R's are $\approx 1/3$. The increased sensitivity is visible as the elongated shape of the two-dimensional output along the o_2 axis. This shows that the neural network is able to distinguish between the LP and the remaining two processes. However dependence of the cross-sections for the QCDC and PGF in the considered variables are similar which leads to smaller discriminating power between these two processes; in most cases the neural network returns $R_{PGF} \approx R_{QCDC}$.

Although the discrimination between the three competing processes is not perfect it improves significantly statistical accuracy of $\Delta G/G$ compared to the usage of average values of R's and a_{LL}'s (*cf.* Sec. 7.3.5). The resulting statistical precision will be presented in Chapter 11, after the discussion of the systematic uncertainties which contain also a contribution from the neural networks studies.

9.3 The gluon momentum fraction x_G

The gluon polarisation is determined for a kinematic region covered by the selected sample and corresponds to a given fraction of a nucleon momentum carried by gluons, $x_G \equiv \xi$, defined as [125]

$$\xi = x(\frac{\hat{s}}{Q^2} + 1). \tag{9.12}$$

[3]Using equations 9.11 this corresponds to $R_{PGF} = R_{QCDC} \approx 0.095$ and $R_{LP} \approx 0.81$.

process	expected o_1	expected o_2
PGF	0	0
QCDC	1	0
LP	0.5	$\sqrt{3}/2$

Table 9.1: Neural network training flags for estimation of the fractions R of different processes.

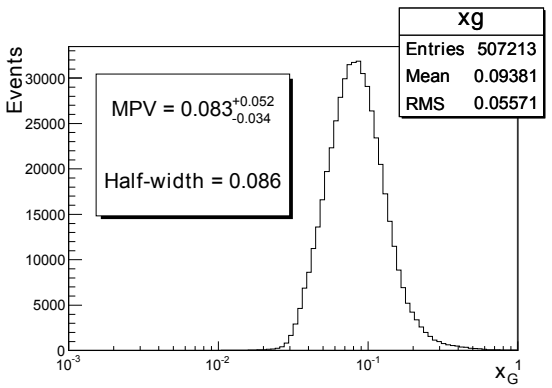

Figure 9.6: The distribution of x_G^{av} for selected data sample, estimated using LEPTO MC and NN parametrisation.

The ξ has a meaning of a fraction of a nucleon momentum carried by a struck parton also for LP and QCDC events. The quantity $\hat{s}$ is the Mandelstam variable for the hard process and is known for simulated PGF and QCDC events but cannot be directly determined from data. Therefore based on MC simulations a NN parametrisation is built as a function of measured observables. The procedure of obtaining such parametrisation is described in previous section.

As explained in Sec. 7.1.2 for the extraction method introduced in this thesis the value of $\Delta G/G$ is probed at an average x_G^{av}. The x_G^{av} is defined in Eq. 7.18. To estimate the value of x_G^{av} at which the $\Delta G/G$ is measured the NN parametrisation of x_G described *supra* is used. For each event of the selected data sample the x_G, $x_G^{'}$ and the α_1, α_2, λ weights are obtained from NN parametrisation and thus we obtain x_G^{av} on event-by-event basis. In Fig. 9.6 the distribution of the x_G^{av} is shown, with mean value $< x_G^{av} >= 0.094$ and RMS = 0.056. However as the distribution is asymmetric (note that the x_G^{av} axis has a logarithmic scale) we will instead quote the $< x_G >$ as the value corresponding to the maximum of the x_G^{av} distribution (MPV - most probable value) and the asymmetric error is taken as distribution width at half-height. Thus we obtain

$$< x_G >= 0.083^{+0.052}_{-0.034}. \tag{9.13}$$

9.4 Scale μ^2

Another important information is the scale at which the gluon distribution is probed. For the considered kinematic regime the relevant scale is $\mu^2 = Q^2$. The average Q^2 for the selected sample is $< Q^2 >= 3\,\text{GeV}^2$. The scale dependence of the MC was studied by previous analyses and was found to be small in the kinematic region covered by COMPASS [103, 104].

In the weighted method of the $\Delta G/G$ extraction different Q^2 regions contribute with different weights. Therefore for estimation of the scale at which the gluon polarisation is probed in presented analysis a weighted average of Q^2 is used. The weight is $fDP_B\lambda$ as described in Sec. 7.3.5. The resulting average scale of the presented $\Delta G/G$ measurement is

$$< \mu^2 >= 1.94\,\text{GeV}^2. \tag{9.14}$$

Chapter 10

Systematic uncertainties

In this chapter details of the analysis of systematic errors are discussed. There are two main origins of the systematic errors for the performed $\Delta G/G$ extraction: experimental effects and Monte Carlo simulations.

The experimental systematic uncertainties are described in Sec. 10.1, with the main contribution due to false asymmetries. In Sec. 10.2 the contribution due to A_1 asymmetry parametrisation is discussed, followed by estimation of the non-pion contamination of the selected sample and its effect on $\Delta G/G$ extraction (Sec. 10.3). Sec. 10.4 is dedicated to analysis of systematic uncertainties related to the Neural Networks used in this thesis. The estimation of the systematic uncertainties due to the Monte Carlo simulations is explained in Sec. 10.5. Discussion of possible effects due to Radiative Corrections and Resolved Photon processes is presented in Secs 10.6 and 10.7, respectively. Finally the contribution to the systematic error due to simplifications used in derivation of the formula for $\Delta G/G$ extraction is given in Sec. 10.8. The summary of the systematic uncertainties is presented in Sec. 10.9.

10.1 Experimental systematic uncertainties

To obtain a result that is not dominated by systematic uncertainties, the systematic effects should be controlled with a precision much better than the statistical precision of the considered result. One of the main systematic effects that affect an asymmetry measurement are the false asymmetries. The precision of measured asymmetry depends on the size of the data sample used. Therefore to increase the precision of false asymmetries determination a larger sample was selected. It was obtained by removing the cuts on p_T of the leading hadrons as well as the cut on Σz (*cf.* the standard selection in Sec. 7.4.6) and it will be called *"all* p_T*"* sample. To insure that estimation of systematic effects obtained with this sample is relevant for the *high* p_T sample, events from both samples should have similar distributions of measured momenta and angles. It was checked to be the case for this analysis. As an example the comparison of distributions of average θ angle for the two leading hadrons for the two samples is shown in Fig. 10.1. The agreement between the two samples is reasonable, in contrast to the low Q^2 analysis where a cut on the θ angle of the hadrons was essential [126].

In the $\Delta G/G$ extraction method used in this analysis the event weight is introduced, which reflects a sensitivity of a given event to the gluon distributions. There is no intermediate step of asymmetry extraction as it was done in the previous analyses. By loosening cuts one will mainly introduce events originating from the LP, but the statistical error of the $\Delta G/G$ obtained from such weighted method for the *all* p_T sample

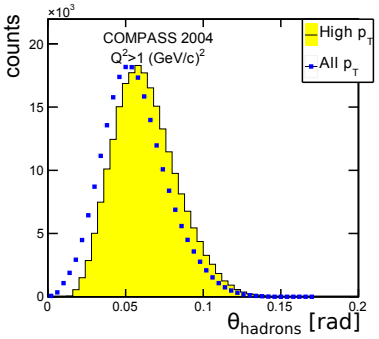

Figure 10.1: The average θ angle of the leading hadron pair for the *high* p_T (yellow histogram) and *all* p_T (blue points) samples.

will not decrease significantly. Thus, the experimental systematic effects should be studied directly for the asymmetries rather than for the value of $\Delta G/G$. Furthermore by performing the study on the asymmetries we decouple from the systematic effects from the MC simulations. In the study of experimental uncertainties the following quantities were considered:

- $A_1^{p_T} = A_{LL}^{p_T}/D$; the A_1 asymmetry for the *high* p_T sample,
- $A_1^{2h} = A_{LL}^{2h}/D$; the A_1 asymmetry for the *all* p_T sample.

10.1.1 Validation of the sign of the asymmetries

A possible concern may arise if an asymmetry is extracted with a correct sign. In order to verify that the asymmetries have the correct signs the fact that the measured A_1^d is positive for high values of x [9] is utilised. The A_1^{2h} is actually very similar to A_1^d in COMPASS as for the majority of events there are at least two outgoing hadrons from the interaction point. In order to access high values of x the A_1^{2h} was extracted for the pure calorimeter trigger events only at an average $x \approx 0.11$. The values obtained for the two MW configurations are $A_{1,MW+}^{2h} = 0.076 \pm 0.015$ and $A_{1,MW-}^{2h} = 0.092 \pm 0.014$. Thus the correctness of the sign of the asymmetries is confirmed.

10.1.2 Global versus consecutive configuration

In Sec. 7.4.1 the difference between the extraction of asymmetry using global or consecutive configurations was discussed. As the 2nd order method can introduce a bias in case the used data sample is too small, the global configuration was selected for the evaluation of the $\Delta G/G$. However, to check if it does not introduce a bias, results obtained from the global and consecutive configurations for *all* p_T sample are compared: $A_{1,C}^{2h} \equiv A_C = 0.00700 \pm 0.00205,\ A_{1,G}^{2h} \equiv A_G = 0.00750 \pm 0.00175$.

To check the compatibility of the two sets one has to consider their difference and take into account correlation between the two samples for the error calculation. As periods without matching counterparts are excluded from the consecutive set, it is a subset of the global sample. Therefore an approximate expression for error of difference between sample and its sub-sample was used $\sigma(A_C - A_G) = \sqrt{\sigma^2(A_C) - \sigma^2(A_G)}$ [127]. The difference between the asymmetries obtained from the two configurations, $A_G - A_C = 0.0005 \pm 0.00107$, is compatible with zero.

10.1.3 False asymmetries

A false asymmetry does not depend on the orientation of the target spins and may result from changes of spectrometer acceptance and/or changes of the density of the target material exposed to the beam. Such asymmetry was defined in Sec. 7.3.2. Let us rewrite Eq. 7.44

$$A_{meas} \equiv \frac{1}{2\langle w\rangle\langle P_t\rangle}\left(A_N + A_N^{'}\right) = A_{LL} + \frac{1}{2\langle w\rangle\langle P_t\rangle}\left(\frac{r-1}{r+1} - \frac{r'-1}{r'+1}\right) = A_{LL} + A_{false}. \tag{10.1}$$

As seen from this formula the false asymmetry vanishes when the ratio $r = a_u n_u / a_d n_d$ is stable in time ($r = r'$).

False asymmetries could be of two types: reproducible false asymmetry and random false asymmetry.

10.1.3.1 Reproducible false asymmetry

This asymmetry is caused by changes of the ratio r during the solenoid field reversal. It was measured that COMPASS target moves vertically by $600\,\mu m$ during the change of the solenoid field. This results in a change of the number of nucleons exposed to the beam especially as the target cells filling with the target material is not perfectly uniform. Also the performance of a part of the detectors is affected by the direction of the solenoid field which can cause changes in the spectrometer acceptance. Such asymmetries can be suppressed by combining data collected with different MW polarisations. As explained in Sec. 4.3 the two target cells are polarised using the MW radiation with a different frequency for each cell. This results in one cell being polarised parallel to the magnetic field and the second cell anti-parallel. By exchange of the applied MW frequencies one obtains an opposite configuration (Fig. 7.4).

Let us consider the expression for the experimental asymmetry for the positive MW setting, *i.e.* with positive polarisation of the upstream cell with respect to the magnetic field,

$$A_+ \equiv A_{LL} + A_{rep} = \frac{1}{2\langle w\rangle\langle P_t\rangle}\left(\frac{N_u - N_d}{N_u + N_d} - \frac{N'_u - N'_d}{N'_u + N'_d}\right). \tag{10.2}$$

For the negative MW setting the upstream cell has a negative polarisation. Thus with the same direction of the solenoid field as for the positive setting we obtain an opposite spin configuration of the muon-nucleon system. As the cross-section asymmetry A_{LL} is defined as $A_{LL} = \frac{\sigma^{\rightleftarrows} - \sigma^{\rightrightarrows}}{\sigma^{\rightleftarrows} + \sigma^{\rightrightarrows}}$ the equation for A_- asymmetry should consider difference between downstream and upstream counting rates as opposed to A_+. The reproducible asymmetry does not depend on the spin direction but on the setting of the magnetic field so it is not affected by the MW reversal. Thus for the negative MW polarisation the reproducible asymmetry contributes to the measured asymmetry with a negative sign;

$$A_- \equiv A_{LL} - A_{rep} = -\frac{1}{2\langle w\rangle\langle P_t\rangle}\left(\frac{N_u - N_d}{N_u + N_d} - \frac{N'_u - N'_d}{N'_u + N'_d}\right). \tag{10.3}$$

Measurements of both A_+ and A_- enable to decouple A_{LL} and A_{rep};

$$A_{LL} = \frac{1}{2}\left(A_+ + A_-\right),\ A_{rep} = \frac{1}{2}\left(A_+ - A_-\right). \tag{10.4}$$

As the amount of data taken at each of the two MW settings was not always equal, the error of obtained

asymmetry would be dominated by the smaller sample. For that reason a weighted mean is used to determine A_{LL} at the cost that A_{rep} does not cancel completely.

MW asymmetry. In Fig. 10.2 the values of A_1^{2h} asymmetry for the three analysed years are presented. Each point corresponds to a week of data taking, with data collected for the opposite MW settings clearly separated. No significant difference between the two settings is observed.

However to estimate the size and possible non-cancellation of A_{rep} the asymmetry extraction was performed for both the *all* p_T and *high* p_T data samples. The values of $A_1 = A_{LL}/D$ and $A_{1,rep} = A_{rep}/D$ for the two samples are summarised in Table 10.1. The average reproducible false asymmetry for the *high* p_T sample is compatible with zero at $2.5\,\sigma$ level while for the *all* p_T sample the compatibility is within $2.1\,\sigma$. Although the obtained reproducible asymmetry is compatible with zero within 3 sigma a thorough investigation of possible causes of such asymmetry was performed. The results of this investigation are presented in following paragraphs.

For a weighted average of $A_{1,MW+}^{2h}$ and $A_{1,MW-}^{2h}$ a part of $A_{1,rep}^{2h}$ contribution (A_R^{2h}) will remain. In our case the remaining part is compatible with zero within the statistical uncertainty

$$A_R^{2h} = A_{1,rep}^{2h} \frac{\sigma\left(A_{1,MW-}^{2h}\right) - \sigma\left(A_{1,MW+}^{2h}\right)}{\sigma\left(A_{1,MW-}^{2h}\right) + \sigma\left(A_{1,MW+}^{2h}\right)} = 0.000110 \pm 0.000052. \tag{10.5}$$

However this only tests the bias introduced by usage of the weighted average. Therefore for the estimate of the contribution from the $A_{1,rep}$ to the systematic error of $\Delta G/G$ measurement a conservative value of 0.001 based on previous studies [96, 65, 100] was used for $\sigma(A_{1,rep}^{2h})$.

False asymmetries in the data samples without physics asymmetry. As explained at the beginning of Sec. 10.1.3, the false asymmetries arise when the ratio r is not constant in time. One way to quantify the systematic effect due to such instability is to decouple it from the physics asymmetry. This is achieved by combining data in such a way that physics asymmetry does not contribute; asymmetry is calculated between the data sets collected with the same spin configuration. Two such false asymmetries are considered: asymmetry for data collected during periods with the same sign of the solenoid magnetic field and asymmetry within one target cell.

Field reversal asymmetry. In the double ratio method of the asymmetry extraction it is assumed that the ratio of the spectrometer acceptance for the two target cells and the numbers of nucleons in the target cells are constant over the solenoid field reversals (Eqs 7.54, 7.55). To verify that this is the case an asymmetry is constructed in such a way that no physics asymmetry is present and only the false asymmetries appear. The data for each target cell are treated separately. The target cell is divided into two halves and each half gets artificially attributed a different sign of the nucleon spins orientation (Fig. 10.3). Therefore the physics asymmetry is expected to cancel out and any observed asymmetry will be a false one. Moreover the obtained false asymmetries should cancel out when combining data collected with opposite MW settings. Thus such asymmetry allows to test the conjecture that A_{rep} cancels out by simple verification that observed asymmetry is compatible with zero. This is in contrast to the A_1 asymmetry which has positive values for high x region, thus it is not trivial to use it for such a test.

	all p_T	*high* p_T
MW+	0.0111 ± 0.0025	-0.032 ± 0.022
MW-	0.0037 ± 0.0026	0.052 ± 0.023
$A_{1,rep}$	0.0038 ± 0.0018	-0.040 ± 0.016
A_1	0.0075 ± 0.0018	0.008 ± 0.016

Table 10.1: Two top rows contain the values of A_1 asymmetry obtained from data collected with each of the MW settings (MW+ or MW-). Row three and four contain the values of the asymmetries $A_{1,rep}$ and A_1. The first column corresponds to the *all* p_T data sample used for the systematic studies, while the second column contains values for the *high* p_T data sample (used for the final result).

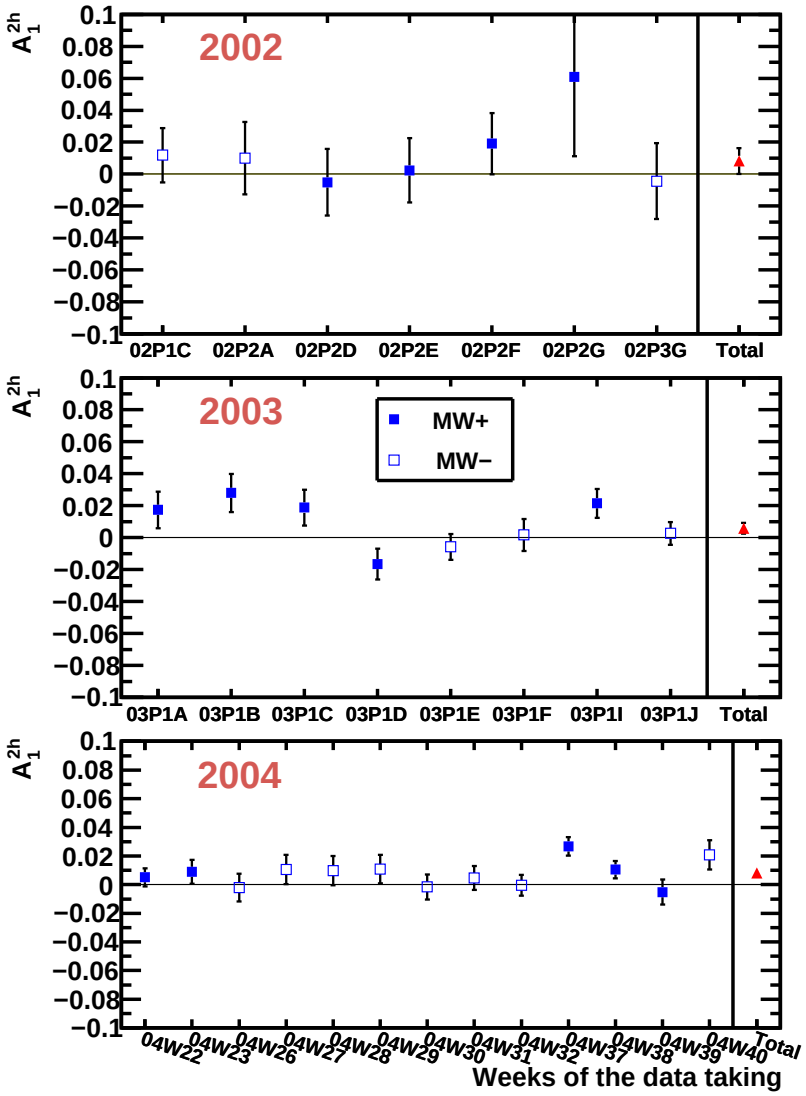

Figure 10.2: Values of the A_1^{2h} asymmetry as a function of the week of data taking presented separately for each year. The full (empty) squares correspond to the data collected with positive (negative) MW setting. Red triangles are the averages over full year.

The results for the asymmetries between the two halves of the upstream and downstream cells are given in Fig. 10.4. Neither significant false asymmetry is observed, nor correlation with the MW configurations. The results are stable through the data taking within the statistical fluctuations. The weighted average over all periods values are $A^{2h}_{1,upstream} = -0.00054 \pm 0.00263$, $A^{2h}_{1,downstream} = -0.00058 \pm 0.00248$. The obtained asymmetries are compatible with zero within the statistical uncertainties. It has to be kept in mind that this method is sensitive to the variations of the ratio r over a range limited to the size of one cell. If the study were performed over the whole target the obtained false asymmetry might be larger. Also by artificially dividing our sample we tend to be more sensitive to statistical fluctuations.

False asymmetries in presence of physics asymmetry Although the observed false asymmetry is consistent with zero, one may consider a hypothesis that several false asymmetries would exist but they average out when combining all the data. To check this the data were divided in several ways. Then the asymmetries calculated for different sub-samples were compared. The following asymmetries were considered:

Day-night asymmetry. The temperature in the experimental hall varies with time (Fig. 10.5). Apart from global trends (warmer and colder periods), a day-night effect is clearly visible. Due to the temperature changes the dimensions and positions of the detectors vary, which was observed in the alignment procedure. This may lead to a variation of the performance of the spectrometer and thus to changes of acceptance. To quantify this effect an asymmetry is calculated using the data divided into groups according to the temperature in the experimental hall. It was observed that the temperature is the highest around 7pm and the lowest around 6am. Therefore the data were divided into two groups: from midnight to noon ("night") and from noon to midnight ("day"). The results are presented in Fig. 10.6 and the two asymmetries are found to be compatible within errors. Thus we conclude that no variation of the spectrometer performance due to temperature changes is observed. However, even if a non-zero asymmetry would exist, its effect would be minimised because the solenoid field was reversed odd number of times per day.

Trigger-by-trigger asymmetries. Different triggers cover different kinematic regions and different angles of the scattered muon and thus they select muons reconstructed in different types of tracking detectors. *E.g.* for the LT the μ' is reconstructed mainly from hits in the GEM and MicroMega detectors, while for the OT the μ' is reconstructed in the large drift chambers and proportional chambers. If there would be a significant difference in performance of different types of tracking detectors, the triggers would be affected differently. To quantify the effect the asymmetry is calculated separately for each trigger with only events that had the corresponding trigger bit set being included in the calculation. The resulting asymmetries are summarised in Table 10.2. They are consistent within the statistical uncertainties.

Inner - outer asymmetry. To check the effect of the target material inhomogeneity as well as the effect of the target movement on the asymmetry, the data were divided into two samples based on the distance R of the interaction point from the beam axis. Two regions are considered, the inner ($R < 0.8\,$cm) and the full ($R < 1.3\,$cm) ones. The outer ($0.8\,\text{cm} < R < 1.3\,\text{cm}$) region, after selections to ensure the same beam muon flux for the two target cells, has insufficient statistics. Thus the full sample which contains both the inner as well as the outer regions has to be used. Using the approximate formula for the error of the difference

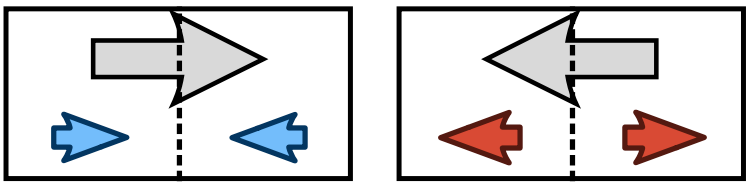

Figure 10.3: Spin configuration used for the calculation of the field reversal asymmetry. The large grey arrows denote the actual spin orientation of target nucleons. The two target cells are artificially divided into halves. Each half gets attributed a different spin orientation as denoted by small coloured arrows.

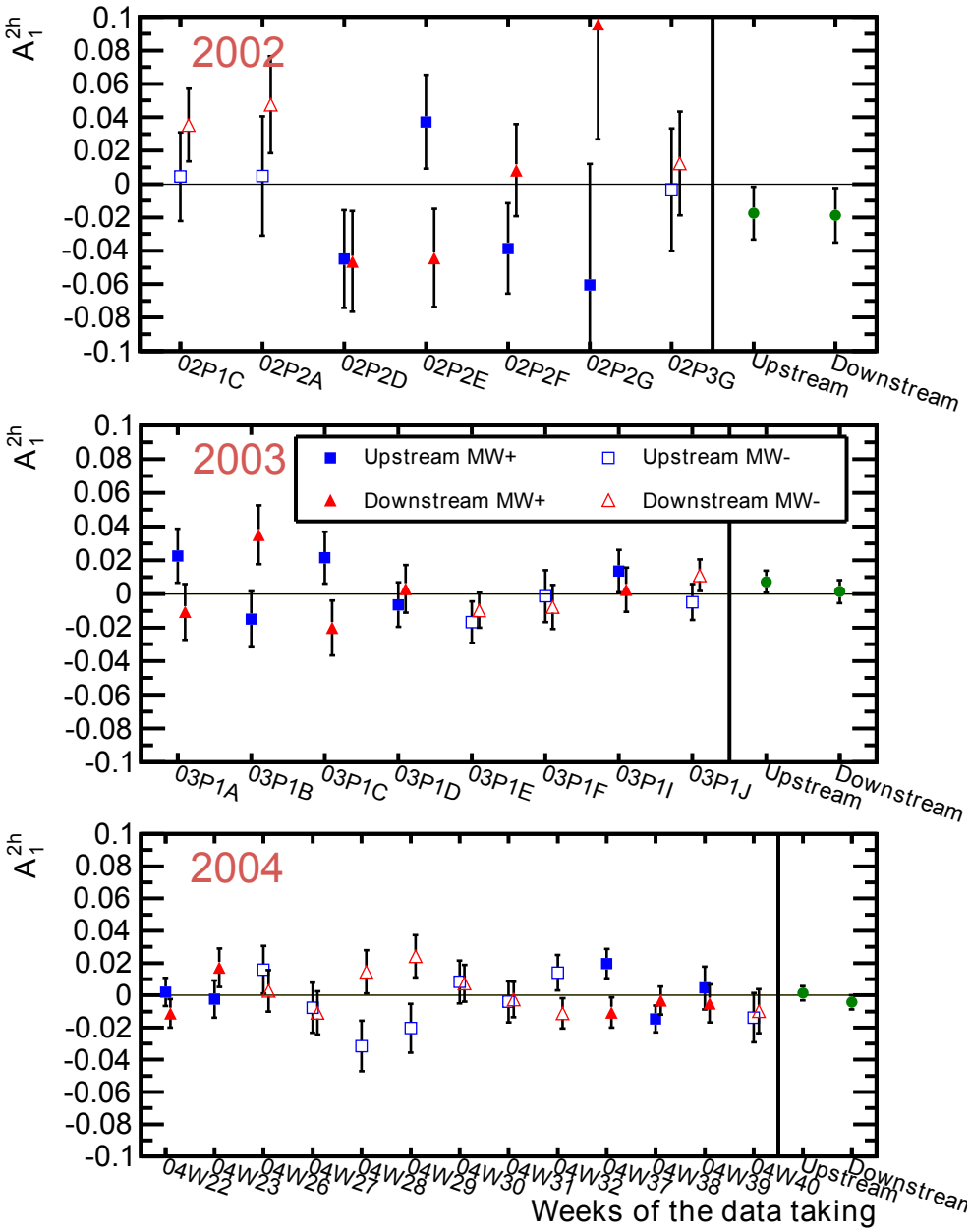

Figure 10.4: Values of the field reversal false asymmetry shown for the three analysed years as a function of week of data taking. The blue squares correspond to the upstream cell while the red triangles to the downstream one. The full (empty) squares/triangles are based on data taken for positive (negative) MW setting. The green circles are averages over one whole year for upstream and downstream cells separately.

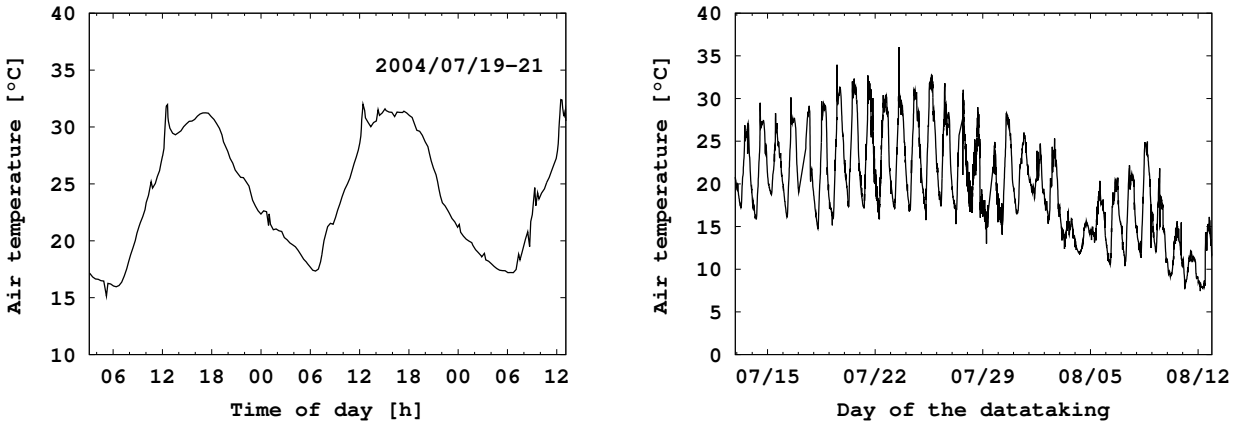

(a) Small scale temperature variation

(b) Large scale temperature variation

Figure 10.5: Variation of the temperature in the experimental hall in the scale of few days (a) or a month (b).

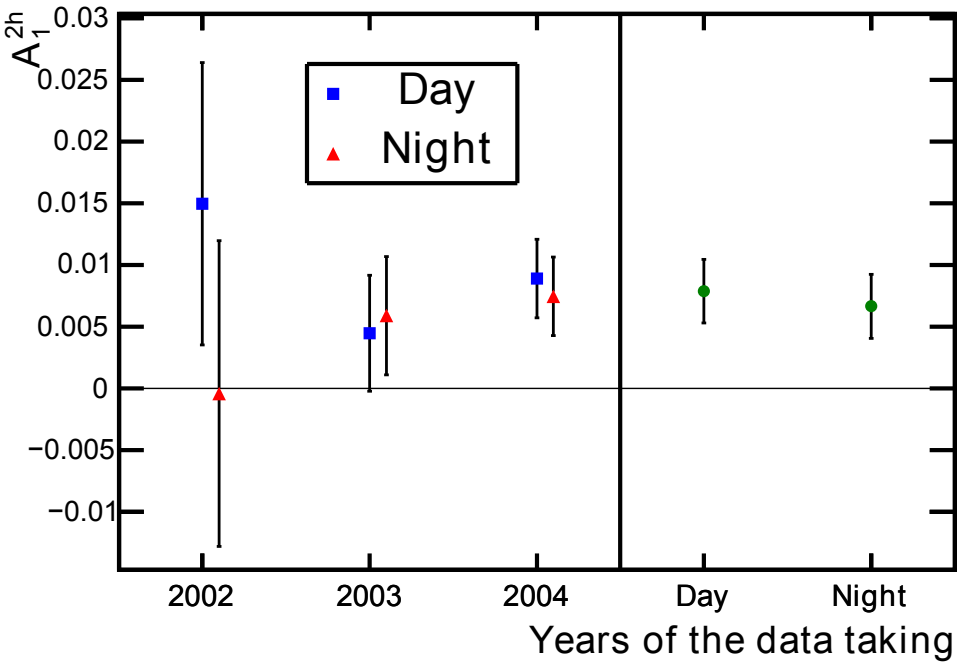

Figure 10.6: Values of the A_1^{2h} asymmetry calculated for data collected during the day (blue squares) and night (red triangles) shown for the three analysed years. The green circles are averages over all years for the day and night data samples separately.

Trigger	LT	MT	incMT	OT	CT
A_1^{2h}	0.0094	-0.0005	-0.0019	0.0079	0.0071
$\sigma(A_1^{2h})$	0.0046	0.0029	0.0038	0.0025	0.0023
$\langle x \rangle$	0.014	0.014	0.014	0.022	0.023

Table 10.2: Values of A_1^{2h} for the main triggers contributing to the analysed data sample. Last row contains average value of the x variable for each sub-sample.

between sample and its sub-sample [127], one obtains $A_{1,full}^{2h} - A_{1,inner}^{2h} = 0.0004 \pm 0.0017$. The result is compatible with zero within statistical uncertainty and we conclude that no false asymmetry between the two regions of the target is observed.

Left-right and top-bottom scattered muon asymmetries. The COMPASS spectrometer is not left-right symmetric due to the spectrometer magnets. It is also not fully top-bottom symmetric. Furthermore for some detectors the high voltage is supplied from several power supplies as well as the readout is performed in groups of channels. Such fragmentation of the power supply and the readout could lead to a different behaviour of a certain region of the spectrometer in case hardware problems would occur. The effect is expected to be negligible as the tracking planes in the spectrometer offer a high level of redundancy. Furthermore, runs with serious problems during data taking are excluded from the analysis. However, to quantify a possible effect the two false asymmetries related to the detection of scattered muon are considered:

- left-right
  The asymmetry is calculated for events where the scattered muon goes to the left (right) part of the spectrometer, *i.e.* with positive (negative) values of the X coordinate. The obtained asymmetries are following $A_{left\,\mu'} = 0.0087 \pm 0.0024$, $A_{right\,\mu'} = 0.0062 \pm 0.0027$.
- top-bottom
  Similarly to the left-right case the two asymmetries are calculated for the scattered muon going to the top (bottom) half of the spectrometer, *i.e.* with positive (negative) values of the Y coordinate $A_{top\,\mu'} = 0.0064 \pm 0.0025$, $A_{bottom\,\mu'} = 0.0087 \pm 0.0026$.

As the values of the considered asymmetries are compatible within the statistical uncertainties we conclude that a false asymmetry related to the detection of scattered muon is not observed.

Top-bottom hadron asymmetry. Significant false asymmetry is observed as a function of the ϕ azimuthal angle of the leading hadron in p_T. The ϕ angle is measured in the laboratory system relative to the Y axis, thus $\phi = 0$ corresponds to the "top" direction. The A_1^{2h} asymmetry is presented in Fig. 10.7 for the two MW settings. For an assumed flat distribution one obtains the total $\chi^2/NDF = 136/31$ with the probability $\sim 10^{-15}$. Such false asymmetry was already observed at COMPASS for the $\Delta G/G$ extraction from the high p_T pairs channel at $Q^2 < 1\,\text{GeV}^2$. As shown in that analysis the same effect can be reproduced in a MC simulation and is caused by an interference of the fringe fields of the solenoid and the SM1 magnets. It leads to a different illumination of the spectrometer for different solenoid field directions. For a perfectly top-bottom symmetric spectrometer such asymmetry should cancel out completely after integrating over the ϕ angle. In experimental conditions such requirement is not always met as the detectors are not perfectly centred on the beam axis. However, as it was already shown, by combining the data collected with the two MW configurations the false asymmetry cancels to a level better then 0.001 for A_1^{2h}.

10.1.3.2 Random false asymmetries

Such asymmetries can be caused by random changes of the performance of experiment. For example a set of detectors having lower efficiency during a period of time would affect differently the acceptance of the spectrometer for events coming from the two target cells. Such variation of acceptance could cause a false

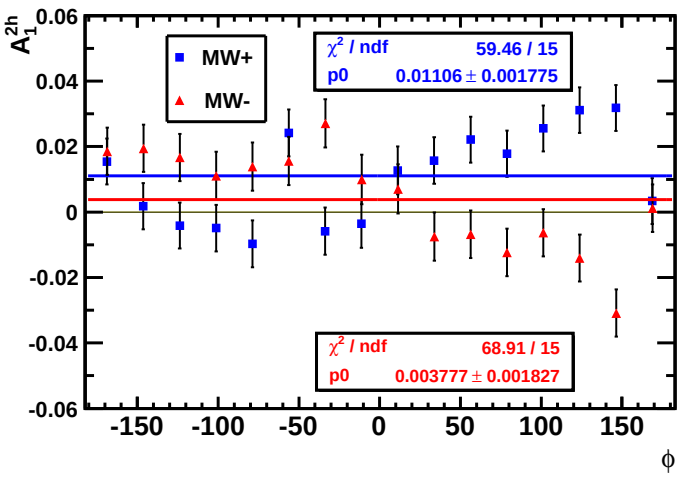

Figure 10.7: Values of the A_1^{2h} asymmetry as a function of leading hadron's ϕ angle. The blue squares (red triangles) correspond to data collected with positive (negative) MW setting. The lines correspond to a test of a hypothesis about linear behaviour of the A_1^{2h} asymmetry as a function of ϕ. In the boxes the obtained χ^2 is presented.

asymmetry. As the occurrence of such variations is random they should average out when combining data taken with large number of field rotations. This assumption is checked using the pulls method described *infra*.

A special case would be an asymmetry caused *e.g.* by a continuous degradation of the spectrometer performance. However, in order to assess that this effect does not produce a bias, it is sufficient to show that the non-cancellation of the reproducible false asymmetry is small and that the random false asymmetries average out.

Pulls method for the estimate of random false asymmetries. The upper limit for the random false asymmetries is obtained in a standard approach used in different COMPASS analyses. It is called the pulls method. As explained in Sec. 7.4.1 for the global configuration the data are divided into groups of runs called "periods", each corresponding to one week of data taking. For each period the value of $\Delta G/G$ is extracted and the weighted mean over all periods is taken as the final result. To test stability of the spectrometer between the periods we will compare A_1^{2h} values obtained for each of them. As each period corresponds to only one MW setting the A_{rep} false asymmetry has to be removed from the obtained values of asymmetry: $A_1^{2h} = A_{1,MW+}^{2h} - A_{rep}^{2h}$, $A_1^{2h} = A_{1,MW-}^{2h} + A_{rep}^{2h}$. Using these values we obtain the distribution of pulls P_i, defined as

$$P_i = \frac{A_{1,i}^{2h} - \left\langle A_1^{2h} \right\rangle}{\sigma(A_{1,i}^{2h})}, \tag{10.6}$$

where i runs over all periods.

In the absence of false asymmetries the distribution of pulls should be Gaussian with the mean value equal to zero and the RMS equal to 1. Random fluctuations of the spectrometer efficiency would enlarge the RMS. The limit for the systematic error due to such false asymmetries can be derived as follows. The dispersion of the results taking into account statistical fluctuations and possible systematic effects is $\sigma_{MAX}^2 = \sigma_{SYS}^2 + \sigma_{STAT}^2$, where σ_{STAT} is expected to be equal to 1. Let us define $\sigma_{MAX} = \rho + 2\delta\rho$, where ρ denotes the RMS of the pulls distribution and $\delta\rho$ its uncertainty.

Then $\sigma_{SYS} = \sqrt{(\rho + 2\delta\rho)^2 - 1^2}$. Thus the contribution to the systematic error of A_1^{2h} is $\sigma(A_{1,random}^{2h}) =$

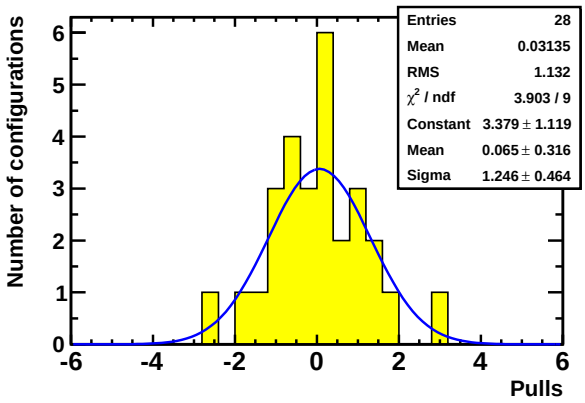

Figure 10.8: Pulls distribution for A_1^{2h} asymmetry. The curve is a fitted Gaussian.

$\sigma_{SYS} \cdot \sigma(A_1^{2h}) = \sigma_{SYS} \cdot 0.0018$. The distribution of pulls is presented in Fig. 10.8. The RMS value of the distribution is estimated from a Gaussian fit to be $\rho = 1.246 \pm 0.464$ and the evaluated contribution to the systematic error is $\sigma(A_{1,random}^{2h}) = 0.0035$.

10.1.3.3 Total systematic error due to false asymmetries

At this point all the contributions to the systematic error connected to the false asymmetries can be combined. The two types of the false asymmetries under considerations were the reproducible and random asymmetries. The contribution from the former was estimated to be $\sigma(A_{1,rep}^{2h}) = 0.001$ and letter to $\sigma(A_{1,random}^{2h}) = 0.0035$. In order to express the systematic error due to false asymmetries in terms of $\sigma(\Delta G/G)$ we should note that the obtained statistical error of $\Delta G/G$ is larger than the error of $A_1^{p_T}$ calculated for the same data sample (comparing Eqs 7.62 and 7.72 it is seen that the statistical error is increased by factor $\sim 1/\left\langle \lambda^2 \right\rangle^2$, where $\lambda < 1$). This factor in our case is $\sigma(\Delta G/G)/\sigma(A_1^{p_T}) \approx 5.2$. Thus it seams reasonable to assume that the systematic error obtained from the *all* p_T sample should be multiplied by the same factor.

Finally the total systematic error due to the false asymmetries reads

$$\sigma(\Delta G/G)_{false} = \sqrt{\sigma^2(A_{1,random}^{2h}) + \sigma^2(A_{1,rep}^{2h})} \cdot \sigma(\Delta G/G)/\sigma(A_1^{p_T}) = 0.019. \tag{10.7}$$

10.1.4 Contributions to the systematic error from f, P_b and P_t

As stated in Sec. 7.2 the error of the beam, P_b, and the target polarisation, P_t, is 5% and it is 2% for the dilution factor, $\sigma(f)$. Because an estimation of the correlation factors is not straightforward, it is assumed that the systematic errors $\sigma(\Delta G/G)_f$, $\sigma(\Delta G/G)_{P_b}$ and $\sigma(\Delta G/G)_{P_t}$ are proportional to the errors given above. It is an overestimation because a part of the formula used for the $\Delta G/G$ extraction, that relates to A_1^d, should not be affected strongly by these uncertainties. It is due to the fact that A_1^d is extracted from the world data, not only the COMPASS ones. The total contribution to the systematic error due to uncertainties of P_b, P_t and f is

$$\sigma(\Delta G/G)_{f,P_b,P_t} = 0.006. \tag{10.8}$$

A_1^d parametrisation	$\Delta G/G$
#1	0.077 ± 0.094
#2	0.078 ± 0.094
#3	0.090 ± 0.094
#4	0.088 ± 0.094

Table 10.3: Results for $\Delta G/G$ using various A_1^d parametrisation.

10.2 Systematic error related to the A_1^d parametrisation

In order to estimate the systematic effect due to used A_1^d, four parametrisation of this asymmetry are used. These are:

1. fit to the world data for all Q^2 [128],
2. fit to the world data for $Q^2 > 1\,\text{GeV}^2$,
3. fit to the COMPASS data only for $Q^2 > 1\,\text{GeV}^2$,
4. simple fit: $A_1^d = x_{Bj}^{1.24}$.

Obtained results for the $\Delta G/G$ with the four parametrisation are presented in Table 10.3. The RMS of these results is used as an estimate of the uncertainty connected with the A_1^d parametrisation. The estimated error is $\sigma(\Delta G/G)_{A_1} = 0.007$. For the final $\Delta G/G$ result the published fit to the world data [128] is used.

10.3 Non-pion contribution

In our data sample, there are about 30% of events where a non-pion particle is selected. However, the agreement between the MC simulations and the experimental data for multiplicities of different hadrons in the final state was not tested. And thus the adjustment of the fragmentation parameters did not take those observables into account. To test the impact of events with non-pion particle in the final state on $\Delta G/G$ extraction, such events were removed in two ways using information from the RICH (Ring Image Cerenkov detector, *cf.* Sec. 4.4). For the first sample only events with positively identified pions were accepted. For the second one events with positively identified kaons or protons were removed. The obtained results in both cases are in agreement with $\Delta G/G$ from the whole sample. Note however, that a difference by 30% in the number of events between pure pion and full samples allows a statistical fluctuation of $\Delta G/G$ larger than $0.5\,\sigma$. Therefore, the described test is a weak one.

10.4 Neural Network stability

As shown in Sec. 9.2 ten different neural networks (NN's) are used in the analysis. The most crucial is the one that determines the probabilities for an event to originate from each of the three LO processes. Therefore most of the systematic studies were done for this particular neural network.

First, it has to be verified that the output of the NN behaves as expected. For this purpose the NN was tested on a MC sample that was not used during the training procedure. The data set was divided in bins of R_{PGF}, R_{QCDC} and R_{LP} as obtained from NN. In each bin and for each process p, the average fraction R_p is

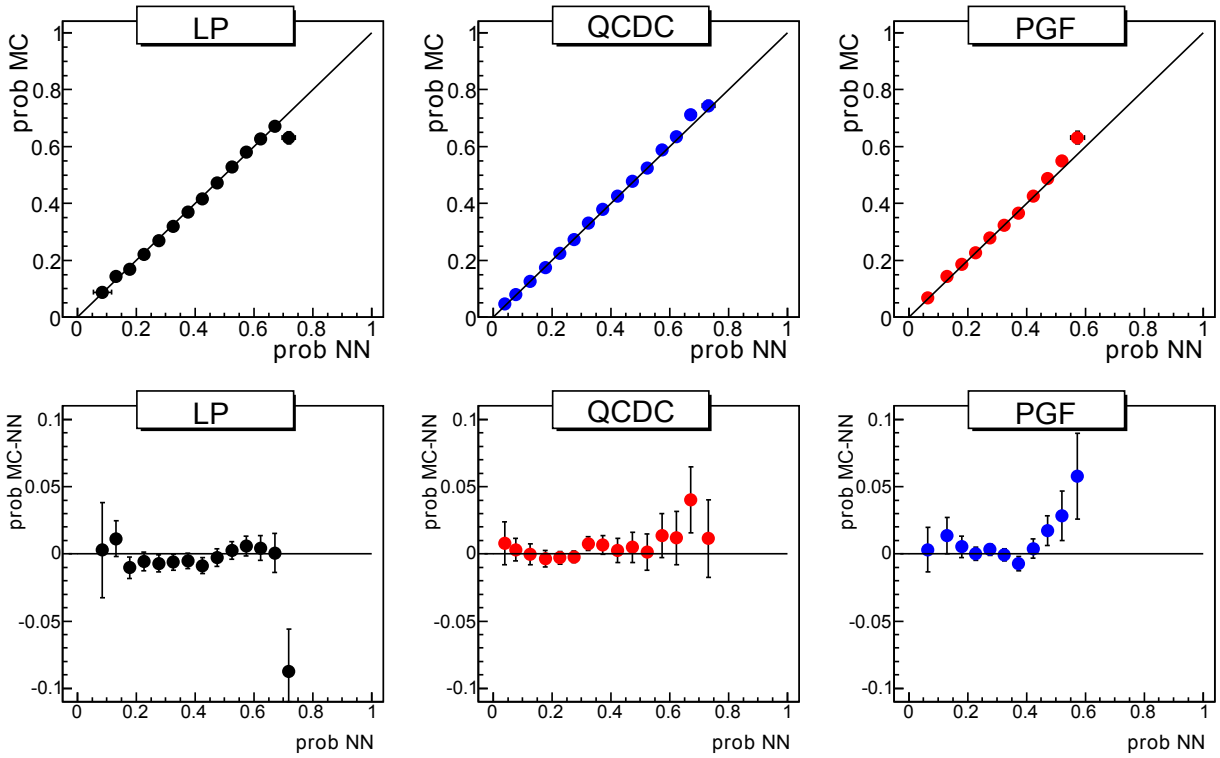

Figure 10.9: NN and MC comparison for R_{PGF}, R_{QCDC}, R_{LP} in bins of NN parametrisation.

computed according to the complete information available for generated events. For a correctly trained NN one expects that the fractions obtained directly from the MC will be equal to the ones obtained from the NN. The results are presented in Fig. 10.9. In the top part, the process fractions obtained from MC are shown as a function of NN response, while in the bottom part their difference is presented. The results are in good agreement. Although for the LP a deviation is observed for the last point with R_{LP} about 2.8 sigma away from the expected value, it has no significant impact as this bin contains only 0.5% of the events. Also for this process there are seven consecutive points below the expected value by about 0.005. A probability for such occurrence is within 3 σ for Gaussian distribution thus this is not significant. To quantify the effect of a possible NN bias on $\Delta G/G$, the fractions R_{LP} and R_{PGF} where artificially distorted

$$R_{LP,bias} = R_{LP} + 0.04\,(0.5 - R_{LP})\,,\ R_{PGF,bias} = R_{PGF} - 0.04\,(0.5 - R_{LP})\,. \tag{10.9}$$

The resulting change of $\Delta G/G$ is 0.023 ± 0.012, where the error was calculated using simplified formula $\sqrt{\left|\sigma\left(\Delta G/G\right)^2_{no\,bias} - \sigma\left(\Delta G/G\right)^2_{bias}\right|}$, which gives the lower limit for allowed statistical fluctuations. As the resulting change of $\Delta G/G$ is consistent with zero, we don't use the above result for further systematic error estimate.

A similar test is presented in Fig. 10.10. It shows a comparison of probabilities obtained from the NN and the MC as a function of the sum of p_T^2 values of the two hadrons. The results from the NN and the MC are in agreement. Note that, for this comparison the binning is done in $\sum p_T^2$, thus MC points can be obtained without any NN training. Moreover the plot presents how the agreement between NN and MC depends on the kinematics of the event. This makes this test to be complementary to the previous one.

Similar tests (but not so detailed) have been done for all other NN's used in the analysis for estimation

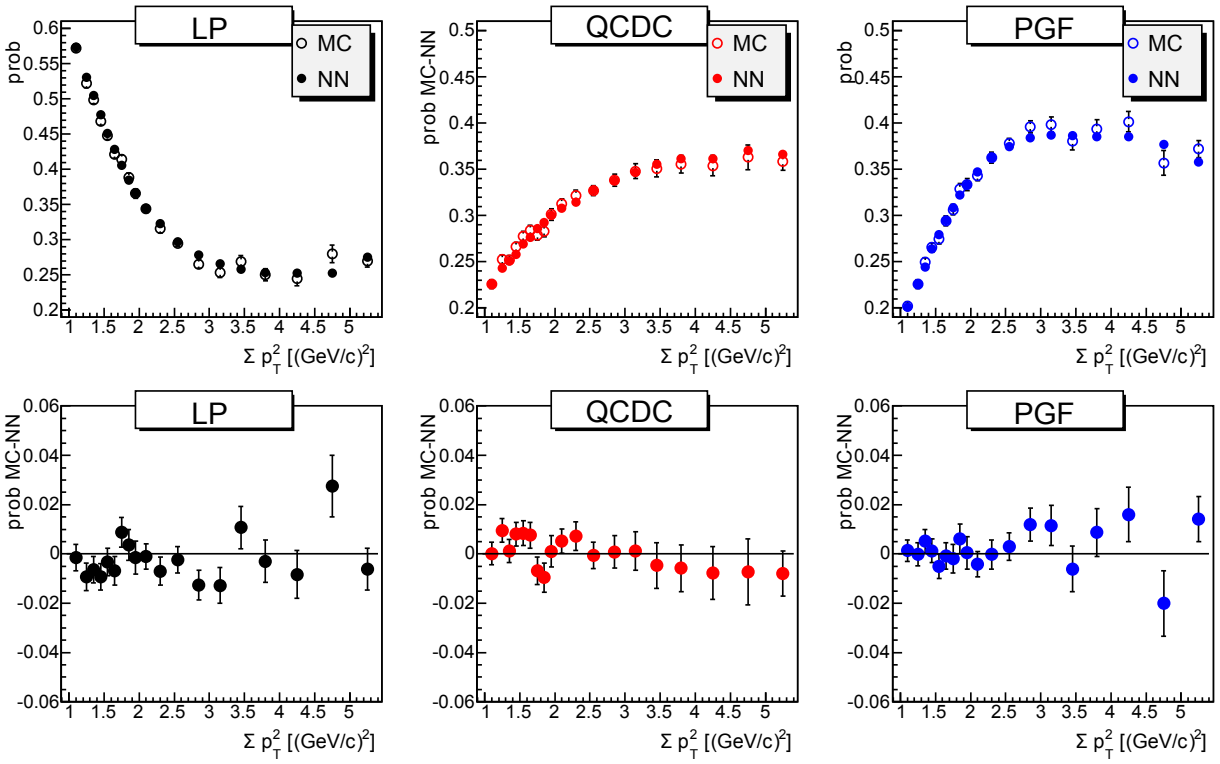

Figure 10.10: NN and MC comparison for R_{PGF}, R_{QCDC}, R_{LP} as a function of $\sum p_T^2$.

NN	$\Delta G/G$	$\sigma(\Delta G/G)$
Fixed NN #1	0.1337	0.0843
Fixed NN #2	0.1350	0.0847
Fixed NN #3	0.1365	0.0832
Fixed NN #4	0.1403	0.0839
Fixed NN #5	0.1392	0.0846
Fixed NN #6	0.1339	0.0838
Dynamic NN	0.1451	0.0853

Table 10.4: $\Delta G/G$ results obtained using NN's trained in various configurations.

of a_{LL} and x values (*cf.* Sec.9.2). In all cases, the NN output corresponds to the expectation value of the considered variable in the MC.

In the training procedure a NN with dynamic structure was used. To quantify what is the effect of different structures on the stability of obtained result a set of NN's with varying structure was tested. They differed by the number of neurons in the two hidden layers. To have a more strict control over the structure the tested NN's were not allowed to dynamically adjust during the training procedure. These NN's were then used for $\Delta G/G$ extraction. The results are summarised in Table 10.4.

All the NN's with the fixed structure give similar $\Delta G/G$ results. Their RMS is about 0.002. However, their mean is below the dynamic NN result by about 0.009. It is conjectured that it is due to the fixed internal structure, which was used for these tests, as it increases the probability that the NN training ends in a local minimum. Using dynamic structure decreases this probability, but never eliminates it. For a more conservative estimate of the error connected to the NN stability, $\sigma(\Delta G/G)_{NN}$, we use the value 0.009 (deviation from the dynamic NN result) instead of 0.002 (RMS). Note that this test was performed in an early stage of the analysis, when the final MC sample and data selection cuts where not finalised. Therefore

the quoted value given for $\Delta G/G$ differs from the final one (*cf.* Chapter 11).

10.5 Systematic errors due to the MC

To obtain a satisfactory description of the experimental data it was necessary to include the Parton Shower (PS) model into the MC simulations as well as to adjust values of parameters controlling the fragmentation process (*cf.* Sec. 8.3.2). To estimate a possible systematic effect on $\Delta G/G$ four different MC simulations were considered:

1. PS enabled, default parameters of the fragmentation,
2. PS enabled, COMPASS parameters of the fragmentation,
3. PS disabled, default parameters of the fragmentation,
4. PS disabled, COMPASS parameters of the fragmentation.

For each of these MC samples we performed three different analyses to extract $\Delta G/G$. The first analysis used MC events without further changes. In the second one the events from kinematic regions with a poor description of the data by the MC were discarded. In the third analysis the MC events were re-weighted to obtain a perfect description of the data. The rejection of the problematic regions as well as the weight determination was performed with a help of a dedicated NN.

The NN used to determine the problematic regions was trained to distinguish between the data and the MC events based on 6D input vector $(x,\, Q^2,\, p_{T,1},\, p_{T,2},\, p_1,\, p_2)$. The network was trained to return 1 for MC events and 0 for events originating from data. As the network was working in the mode where it returns a probability P (for a given event to originate from MC), it should return 0.5 if it is not able to distinguish between the data and MC. Thus the kinematic regions of data where the result differs significantly from 0.5 are considered as poorly described by the MC simulation.

The probability can be easily translated into the data over MC ratio $r = (1-P)/P$. We define regions that are properly described by the MC as those for which the ratio r obtained from the NN falls into the range $[0.66,\, 1.5]$. Events for which the ratio lies outside of this region were not included for $\Delta G/G$ determination by the second method.

For the third method the same output of the NN was used as discussed above. However, this time, instead of applying cuts, a weight equal to r was applied to each MC event, so that the data over MC ratio after re-weighting is constant and equal to 1. The weight was applied to the events during the training of the standard NN's used for $\Delta G/G$ extraction (parametrisation of R_{PGF}, a_{LL}^{PGF}, *etc.*). Although for this method all events were used, due to the re-weighting procedure the obtained R's, a_{LL}'s and x's are different from the ones used for extraction of the final result.

From these studies we obtained 12 values of $\Delta G/G$ which are summarised in Table 10.5. In the first column, the version of the MC for the three analyses is indicated ("rejection" denotes the second while "weighted" the third analysis). In the second and the third columns the values and errors for $\Delta G/G$ are given, respectively. As presented in Sec. 8.3.2 and 8.3.3, the agreement with the data is poor for some of the considered MC samples, in particular the ones without Parton Shower. Therefore, for the estimate of the systematic error, instead of the difference between the maximum and minimum value of $\Delta G/G$, it is safer

MC's		$\Delta G/G$	$\sigma(\Delta G/G)$
standard	COMPASS, PS ON	0.0867	0.0935
	COMPASS, PS OFF	0.0744	0.0775
	default, PS ON	0.1114	0.0805
	default, PS OFF	0.1129	0.0711
rejection	COMPASS, PS ON	0.0997	0.0953
	COMPASS, PS OFF	0.0598	0.0798
	default, PS ON	0.0751	0.0930
	default, PS OFF	0.0861	0.0826
weighted	COMPASS, PS ON	0.0737	0.0915
	COMPASS, PS OFF	0.0750	0.0787
	default, PS ON	0.1099	0.0801
	default, PS OFF	0.0980	0.0704
RMS:		0.0176	

Table 10.5: Results for $\Delta G/G$ obtained with various settings of the MC generator. See text for details.

to use their RMS (last raw in Table 10.5). However, as we tend to observe values of both $\Delta G/G$ and $A_1^{p_T}$ that are consistent with zero, the RMS could underestimate the error. As seen in Eq. 7.11 relatively small values of $A_1^{p_T}$ and A_1^d will lead to small $\Delta G/G$ values without much sensitivity to the estimated fractions of processes. To be on the safe side the systematic error connected to the MC simulations is extracted using the following formula

$$\sigma(\Delta G/G)_{MC} = \frac{RMS(\Delta G/G)}{\Delta G/G} \cdot (\Delta G/G + \sigma(\Delta G/G)) = 0.037. \tag{10.10}$$

Here the results for the "COMPASS, PS ON" case were used for the values of $\Delta G/G$ and $\sigma(\Delta G/G)$.

10.6 Radiative corrections

The differential cross section for lepton-nucleon scattering defined in Eq. 2.7 is the cross section for one photon exchange. However, there are also contributions to the measured cross section from other electroweak processes which cannot be discarded on event-by-event basis (Fig. 10.11). As these additional processes account for a large fraction of the measured cross section, especially at low x and high y regions, a radiative corrections (RC) procedure was devised to subtract them. The measured differential cross section is multiplied by a correction factor calculated theoretically which accounts for such processes [129].

Radiative corrections for the data are taken into account in the dilution factor calculation (*cf.* Sec. 7.2.2). For the MC simulations a working implementation of the RADGEN program in LEPTO generator is currently not available. In order to estimate an upper limit for the effect due to the RC, tables of RC weights were used. Corrections for inclusive and semi-inclusive events were prepared for the dilution factor calculation and were parametrised as functions of variables x and y. Two MC samples were studied: the inclusive and the semi-inclusive ones. Studying the effect of RC on *high* p_T sample is not possible due to lack of RC calculations for such sample. The study performed for the semi-inclusive case can be viewed as an upper limit for the effect on the *high* p_T sample. For selected two hadrons with high transverse momentum the available phase space is limited as the two hadrons will take away on average more energy than a single hadron. Furthermore by cutting on p_T we will cut the hadron angular distributions. Thus it is conjectured that the RC for the *high* p_T sample will be smaller than for the semi-inclusive sample.

	R_{PGF}	R_{LP}	R_{QCDC}	$\langle a_{LL}^{PGF} \rangle$	$\langle a_{LL}^{LP} \rangle$	$\left\langle a_{LL}^{QCDC} \right\rangle$
Inclusive	0.07	0.83	0.10	-0.27	0.40	0.38
Inclusive + RC	0.07	0.83	0.10	-0.26	0.39	0.37
Semi-inclusive	0.06	0.85	0.09	-0.27	0.38	0.35
Semi-inclusive + RC	0.06	0.85	0.09	-0.27	0.38	0.35

Table 10.6: The effect of the radiative corrections in the inclusive and semi-inclusive MC samples for fractions of the processes and a_{LL}'s.

Radiative correction weights were applied on event-by-event basis. It was observed that for the semi-inclusive sample the RC effect on the distributions of kinematic variables x, y, Q^2 can be neglected while for the inclusive case the distributions change significantly (Fig. 10.12). To quantify their impact on the $\Delta G/G$ extraction, the process fractions and average values of a_{LL}'s were extracted using RC weighted events. Their comparison with the values obtained from the unweighted MC (Table 10.6) leads to a conclusion that effect due to RC is small for the considered quantities.

10.7 Resolved photon

Apart from the three LO processes also *resolved photon* processes could contribute to the cross-section. In such processes the photon fluctuates into a hadronic state and one of the produced partons interacts with the nucleon (Fig. 10.13). A contribution of such processes was found to be significant, of the order of 50%, in the low Q^2 *high* p_T analysis [11].

Because the PYTHIA (the generator used in the low Q^2 study) is not applicable for simulations in the kinematic region of current analysis [104], the RAPGAP [130] generator was used to estimate the contribution of the resolved photon processes to our sample. As opposed to the PYTHIA the RAPGAP does not allow to generate simultaneously events originating from the three LO processes and the resolved photon ones. They have to be generated separately and then weighted with the obtained cross-sections. Unfortunately the parton distribution functions of the photon are poorly known which leads to a variation of obtained cross-section by few orders of magnitude depending on the selection of PDFs. Thus to estimate the resolved photon contribution a fitting procedure was developed.

First, it was verified that for the *high* p_T sample the RAPGAP gives comparable results to the LEPTO

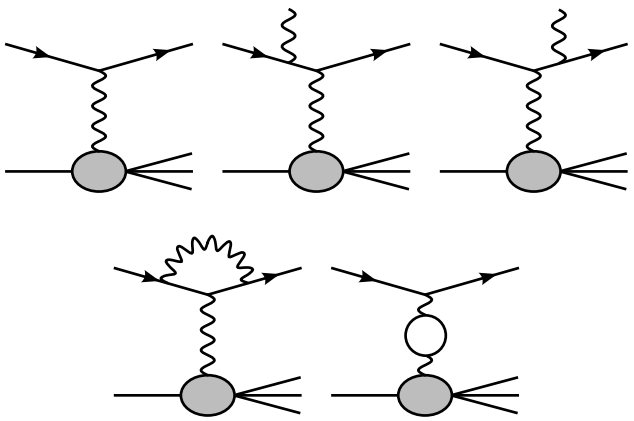

Figure 10.11: Feynman diagrams for the deep inelastic scattering in the one photon exchange approximation and the lowest order radiative processes that were considered in the calculations.

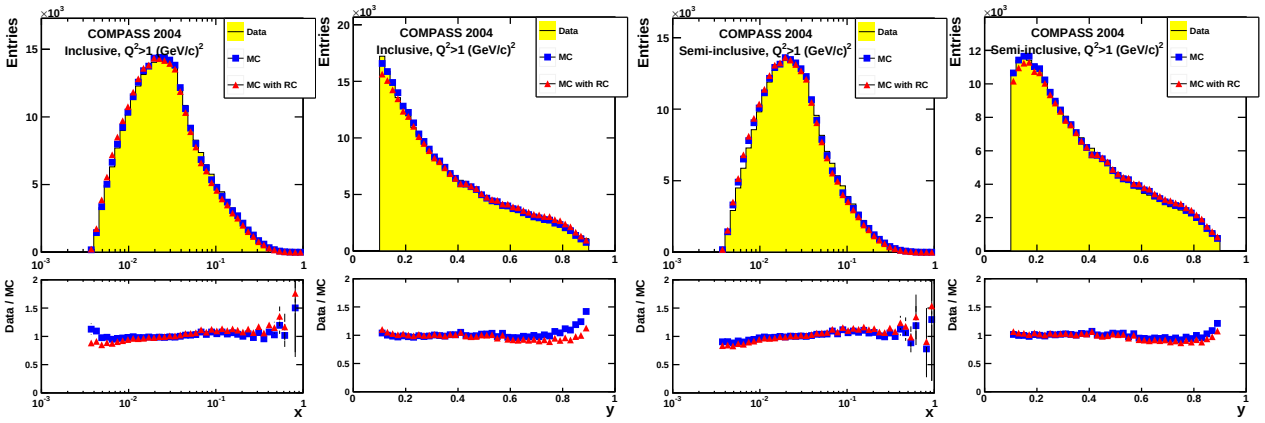

(a) Inclusive sample (b) Semi-inclusive sample

Figure 10.12: The distributions of kinematic variables x and y for inclusive (a) and semi-inclusive (b) samples. The distribution of real data events (yellow histogram) is compared to the results of MC simulations. The blue squares correspond to events generated by LEPTO while red triangles present the distribution of LEPTO events weighted with Radiative Corrections tables.

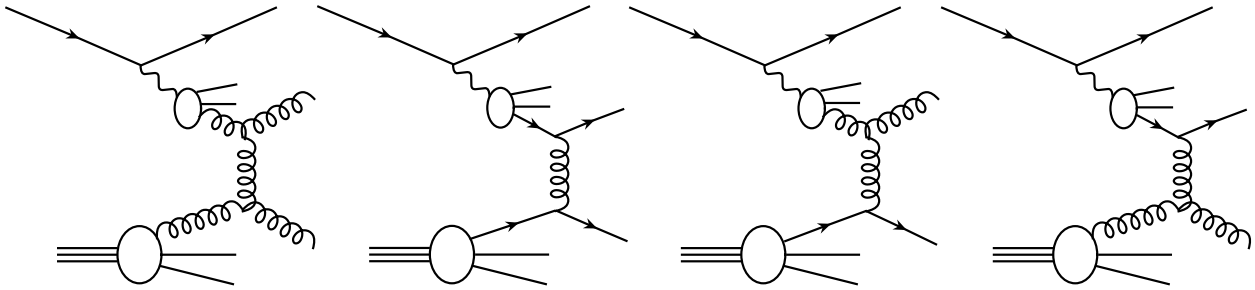

Figure 10.13: Diagrams of resolved photon processes.

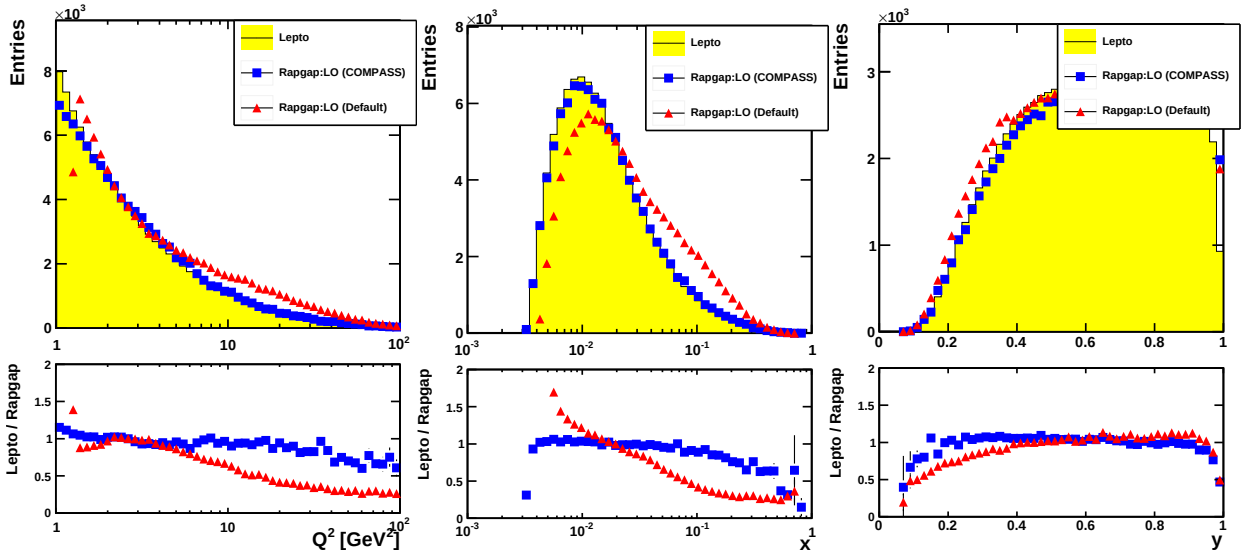

Figure 10.14: Comparison of kinematic distributions of events generated by the LEPTO with distributions of events originating from LO processes obtained form the RAPGAP. Red triangles correspond to the default setting of fragmentation parameters of RAPGAP, blue squares correspond to the COMPASS tuning of those parameters.

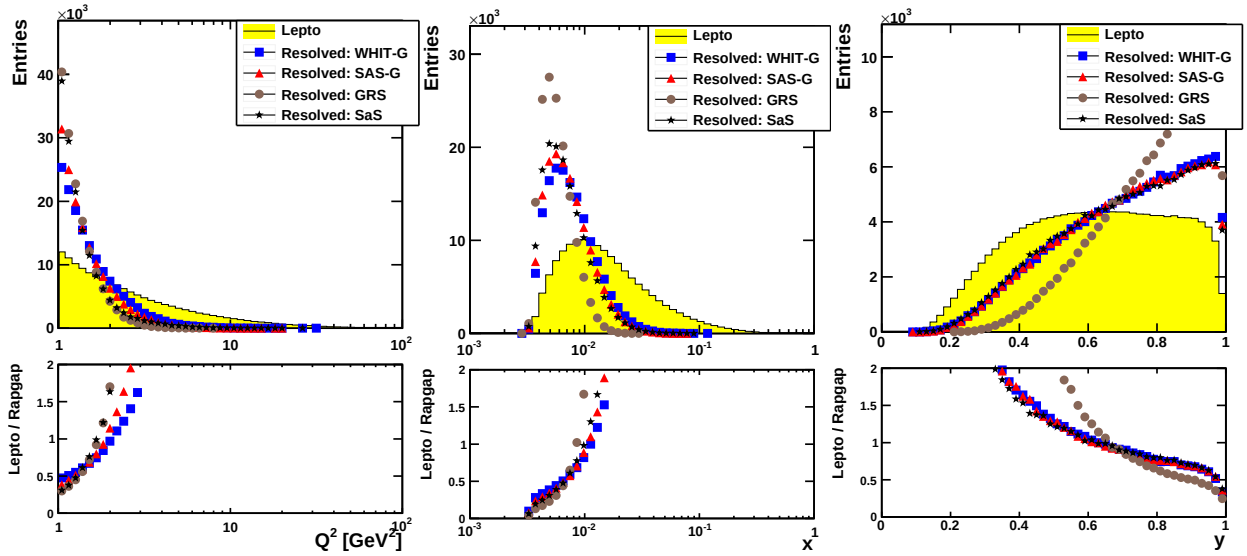

Figure 10.15: Comparison of kinematic distributions of events generated by the LEPTO with distributions of events originating from resolved photon processes obtained form the RAPGAP. Different points correspond to several selections of the photon PDFs.

if one neglects the resolved photon contribution (Fig. 10.14). Then, the kinematic distributions of events originating from the resolved photon were compared to the distributions of LEPTO events. As shown in Fig. 10.15 they differ significantly. This allowed to estimate the fraction of resolved photon events in the *high* p_T sample. To obtain the fraction of resolved photon events a sum of LEPTO and resolved photon distributions was fitted to the experimental data with one free parameter f

$$S = f \cdot LEPTO + (1 - f) \cdot Resolved\,photon. \tag{10.11}$$

Both distributions were first normalised to the number of events in the data sample. The fits were performed in a 2D space (Q^2, y) for nine different photon PDFs[1] and for three different μ^2 scale selections. In total twenty seven MC simulations of resolved photon events were considered. The scale μ^2 is equal to the factorisation and renormalisation scales, μ_R^2 and μ_F^2, which are assumed to be equal. It also regulates the occurrence of resolved photon events; in the simulation they are allowed for $\mu^2 > Q^2$. The three considered scales were the following: $\mu^2 = 4 \cdot m^2 + p_T^2$, $\mu^2 = Q^2 + p_T^2$ and $\mu^2 = \hat{s}$.

To account for the spectrometer acceptance the events generated by LEPTO were processed by a full MC simulation including the apparatus description and the algorithm for event reconstruction. On the other hand the output of RAPGAP cannot be used currently by COMGEANT to perform a full simulation. To circumvent this the obtained RAPGAP distributions were weighted with 2D $\left(Q^2, y\right)$ acceptance obtained from the full LEPTO simulation. As the resolved photon contributions depend on the kinematic region the fits were performed for each trigger independently.

Selected fits are presented in Fig. 10.16 and the obtained resolved photon contributions are summarised in Table 10.7. The biggest resolved photon contribution is observed for the IT sample which is consistent with the results of the low Q^2 *high* p_T analysis [11, 100], where this trigger was dominant. For $Q^2 > 1\,\mathrm{GeV}^2$, the IT corresponds to 0.4% of the data sample. For the OT sample, which comprise most of the available

[1] GRS (1), SASGAM (2): the numbers in brackets correspond to the values of the 'INGA' option of the RAPGAP generator [130]. DO-G (311), LAC-G (331), GS-G (341), GRV-G (351), ACFGP-G (361), WHIT-G (381), SaS-G (391): the numbers in brackets correspond to the ID number of a PDF in the LHAPDF library [131].

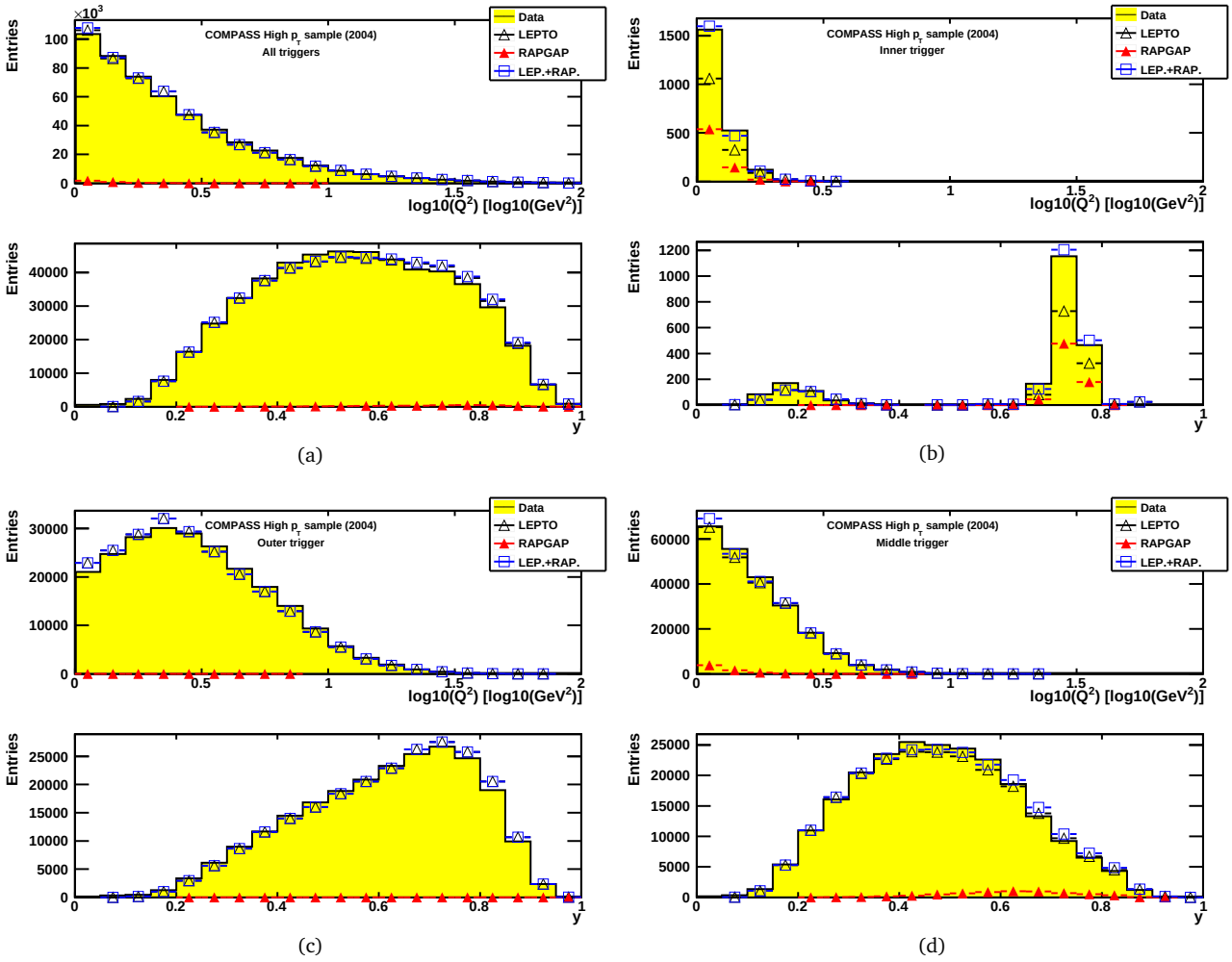

Figure 10.16: Q^2 and y distributions for the LEPTO LO and the RAPGAP resolved photon simulations compared to the experimental data. The RAPGAP simulations are done with the photon PDFs of Ref. [132] and with scale $\mu^2 = m^2 + p_T^2$. The MC distributions are normalised to the fraction obtained from 2D fit to data (*cf.* text for details). The results are presented for four samples: a) All triggers, b) Inner Trigger, c) Outer Trigger, d) Middle Trigger. The green circles represent the sum of LEPTO and RAPGAP distributions.

	Data samples by trigger						
	All	IT	LT	MT	incMT	OT	pCT
Maximum resolved photon fraction for samples with $\mu^2 = m^2 + p_T^2$ scale	0.005	0.43	0.05	0.04	0.04	~ 0	0.06
Maximum resolved photon fraction for all samples	0.005	0.59	0.19	0.10	0.08	~ 0	0.06
Resolved photon fractions for sample with default values of fragmentation parameters ($\mu^2 = m^2 + p_T^2$ scale, photon PDF from Ref. [132])	0.05	0.44	0.10	0.09	0.08	0.02	0.06
Fraction of all events	1.0	0.004	0.15	0.44	0.23	0.45	0.05
$< Q^2 >$		1.19	1.80	1.66	1.67	3.01	13.45

Table 10.7: Fractions of resolved photon events, obtained from fits of kinematic distributions to the data, presented for different trigger samples. The first row presents maximal fractions obtained for the $m^2 + p_T^2$ scale which is the most suitable in our case. The second row contains maximal fractions obtained from all simulations. The third row shows the fractions obtained from MC samples with the default values of fragmentation parameters. In the fourth row the relative sizes of the trigger samples are presented, while the last row contains average Q^2 for the considered samples.

statistics, the resolved photon contribution is negligible. For the second most populated trigger MT it was found to be below 10%. However, for the whole sample the contribution is well below 1%.

The values of fragmentation parameters were tuned to obtain a better description of the experimental data. When doing this we might compensate for not simulated resolved photon events by an artificial change of fragmentation parameters. To test this another fit was performed using distributions obtained from simulations with the default setting of fragmentation parameters. The obtained fraction is $\sim 5\%$, however with obtained quality of the fits it is not possible to judge if such MC simulation would describe data better than the one used for extraction of the final result.

In the low Q^2 analysis [11], where resolved photon events correspond to a half of the sample, the systematic effect due to the lack of knowledge about polarised photon PDFs leads to about 10% relative error on $\Delta G/G$. In our case we can safely neglect the resolved photon contribution, both to the final result and to the systematic error.

10.8 Simplification of the formula for $\Delta G/G$ extraction

During the extraction of $\Delta G/G$ we assume for simplicity that in Eq. 7.21 $\bar{x}_C^{'}$ equals to $\bar{x}_C$. Where $x_C^{'}$ corresponds to a value of the nucleon momentum fraction carried by struck quark in the QCDC process for a sample of events where $\bar{x} = \bar{x}_C$; x_C is the nucleon momentum fraction carried by struck quark in the QCDC process for inclusive sample. The impact of this assumption was estimated in two tests. In the first one $x_C^{'}$ was assumed to be proportional to x_C, $x_C^{'} = 1.6 \cdot x_C$. In the second one $x_C^{'}$ was approximated by using Neural Network. The NN that is used to estimate x_C based on values of Q^2 and x was given as an input the value of x_C for given event instead of x. Thus it effectively estimated $x_C^{'}$. The resulting change of $\Delta G/G$ was 0.007 and 0.012 respectively. For the systematic error estimate we assumed that the contribution due to the approximate formula for $\Delta G/G$ is $\sigma(\Delta G/G)_{formula} = 0.012$.

10.9 Summary of the systematic contributions

An extensive study of the systematic uncertainties was performed. It covered both experimental and theoretical contributions. For the estimate of the experimental systematic error we considered possible contributions from: the false asymmetries, uncertainties due to parametrisations of beam polarisation, dilution factor, cross section spin asymmetry A_1, uncertainty due to measurement of the target polarisation. The theoretical uncertainty comprise the contribution related to the neural networks, the uncertainty due to variation of MC parameters settings, the effects due to Radiative Corrections and Resolved Photon processes, and uncertainty due to approximate formula for $\Delta G/G$.

The systematic contributions are summarised in Table 10.8. As described in Sec. 7.2.4 the D-wave state correction for the deuteron was taken into account. All contributions were summed in quadrature and the obtained total systematic error is $\sigma(\Delta G/G)_{syst} = 0.049$. The two largest systematic uncertainties are due to false asymmetries and the MC.

$\sigma(\Delta G/G)_{NN}$	0.009
$\sigma(\Delta G/G)_{MC}$	0.040
$\sigma(\Delta G/G)_{f,P_b,P_t}$	0.006
$\sigma(\Delta G/G)_{false}$	0.021
$\sigma(\Delta G/G)_{A_1^d}$	0.008
$\sigma(\Delta G/G)_{formula}$	0.013
TOTAL	0.049

Table 10.8: Summary of the major systematic contributions.

Chapter 11

Results for $\Delta G/G$

The gluon polarisation $\Delta G/G$ in the nucleon was extracted from the sample of events with pairs of hadrons with high transverse momenta. The COMPASS data taken in 2002-2004 were split into periods of data taking each corresponding to about one week. The selection of events and grouping of the data is detailed in Sec. 7.4. The $\Delta G/G$ for a given period is extracted using a second order weighted method introduced in Sec. 7.3.5. Event weights were determined using the parametrisation of process fractions and parton kinematics based on the Neural Networks approach (Sec. 9.2).

The value of $\Delta G/G$ averaged over the muon kinematic variables for a given year was obtained as the weighted average of $\Delta G/G$ values calculated for each period of the data taking. The results presented on period-by-period basis as well as the combined results for the three years of data are shown in Fig. 11.1. The numerical results for all periods are listed in Appendix .

The direct measurement provided by COMPASS using hadron pairs with high transverse momenta for $Q^2 > 1\,\text{GeV}^2$ data results in

$$\frac{\Delta G}{G} = 0.08 \pm 0.1(stat.) \pm 0.05(syst.)$$

at $< x_G >= 0.083^{+0.052}_{-0.034}$ and $< \mu^2 >= 1.94\,\text{GeV}^2$, which is consistent with zero within the statistical error. It is worth to note that the systematic uncertainty is small compared to the statistical error. The different contributions to the systematic error are discussed in Chapter 10 and are summarised in Table 10.8. The two largest contributions originate from the Monte Carlo and from false asymmetries. A further increase of statistical precision, after inclusion of 2006 data, is expected to improve the estimation of the systematic uncertainties due to false asymmetries.

Besides this result other results from direct measurements of the gluon polarisation are also available. The two of them are complementary measurements performed by COMPASS. One with high p_T hadron pairs at $Q^2 < 1\,\text{GeV}^2$ [11, 65] (shown as red circle in Fig. 11.2) and the second one with open charm production at $< \mu^2 >= 13\,\text{GeV}^2$ [10, 50] (shown as red star in Fig. 11.2). Moreover the HERMES [56, 58] and the SMC [12] have previously measured gluon polarisation with high p_T hadron pairs for all Q^2 and $Q^2 > 1\,\text{GeV}^2$, respectively. The different results obtained in fixed target experiments are summarised in Fig. 11.2. The figure also displays five different curves with predictions for the x-dependence of $\Delta G/G$. The three solid, blue curves were obtained using the parametrisations from Ref. [61] and they correspond to three different values of the gluon contribution to the nucleon spin, $\Delta G = \int_0^1 \Delta G(x)dx$, quoted on the right-hand side of the diagram. The dashed and dotted, black curves show the results from Ref. [9] that correspond to a positive and negative polarisation of the gluons. The two curves correspond to $\left|\int_0^1 \Delta G(x)dx\right| = 0.2$–$0.3$.

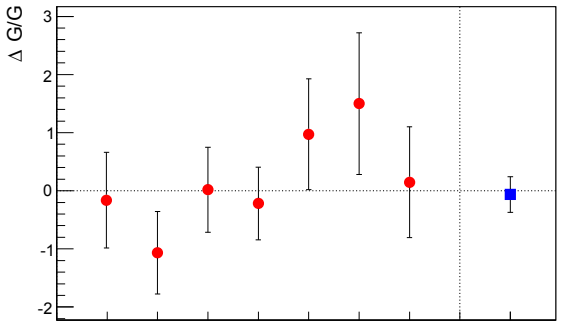

(a) 2002

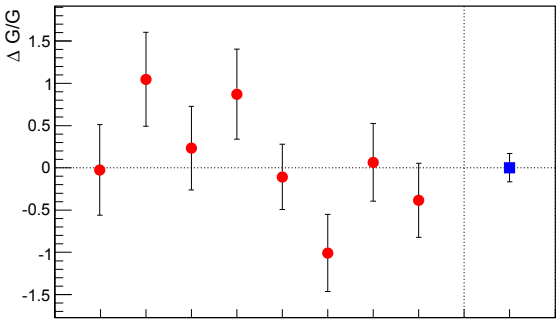

(b) 2003

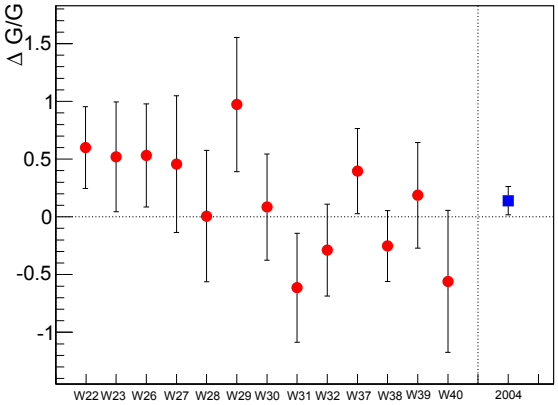

(c) 2004

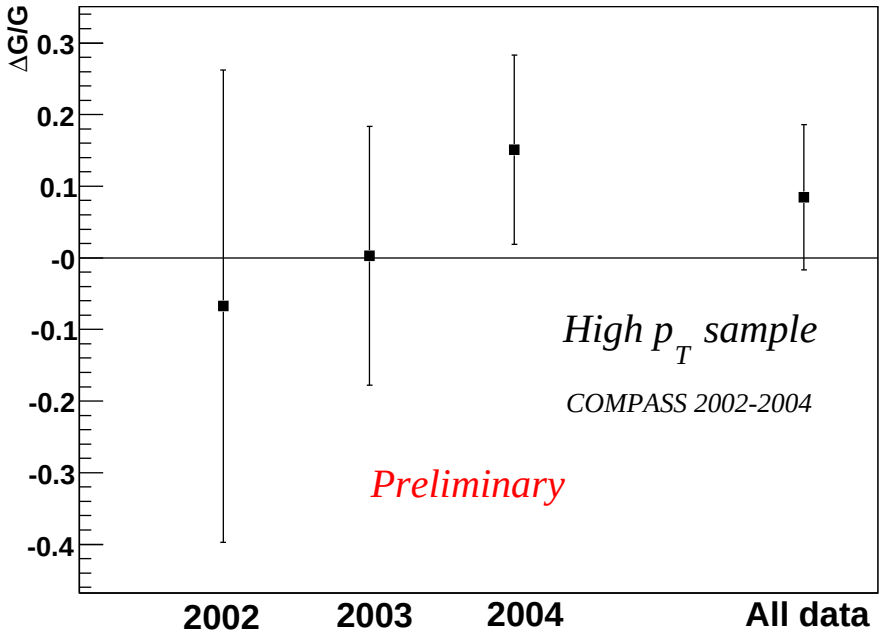

(d) All data

Figure 11.1: Results of $\Delta G/G$ extraction presented for each period of data taking in 2002 (a), 2003 (b) and 2004 (c) years. The combined values from the three years yield the final value of $\Delta G/G$ (d).

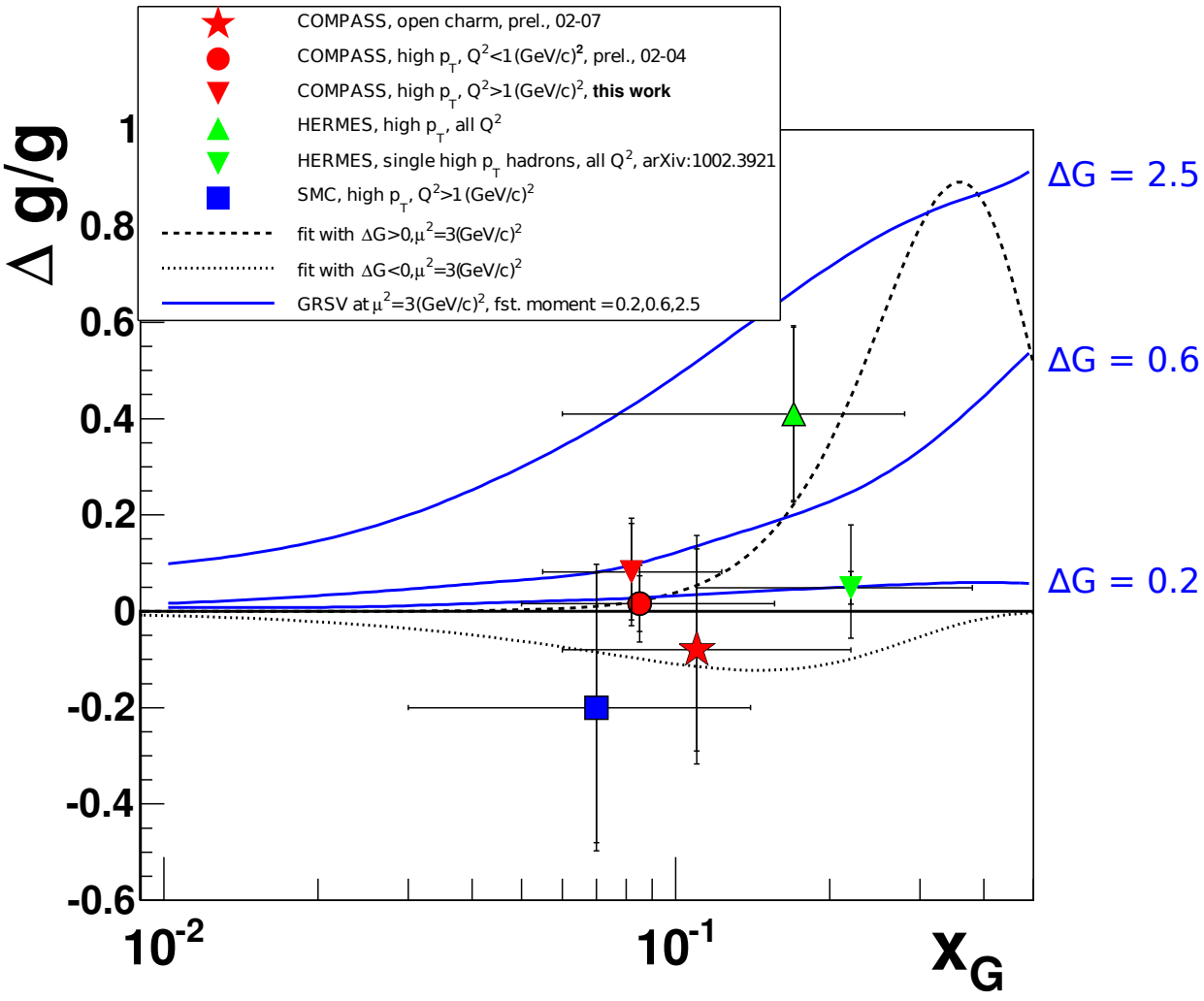

Figure 11.2: Comparison of existing direct measurements of $\Delta G/G$. The red triangle is the result of analysis presented in this thesis. The red star and the circle correspond to preliminary results of the two complementary analyses of COMPASS, the open charm and the high p_T pairs for $Q^2 < 1\,\mathrm{GeV}^2$ analyses, respectively. The other points represent results from the HERMES and SMC high p_T pairs analyses. The blue solid curves show the predicted functions of $\Delta G/G(x)$ for three different gluon polarisations ΔG obtained with parametrisation from Ref. [61]. The black dashed and dotted lines show the results of the QCD-analysis [9] of the inclusive measurements performed by COMPASS. The two curves correspond to two fit solutions of equal significance but yielding opposite sign of the ΔG.

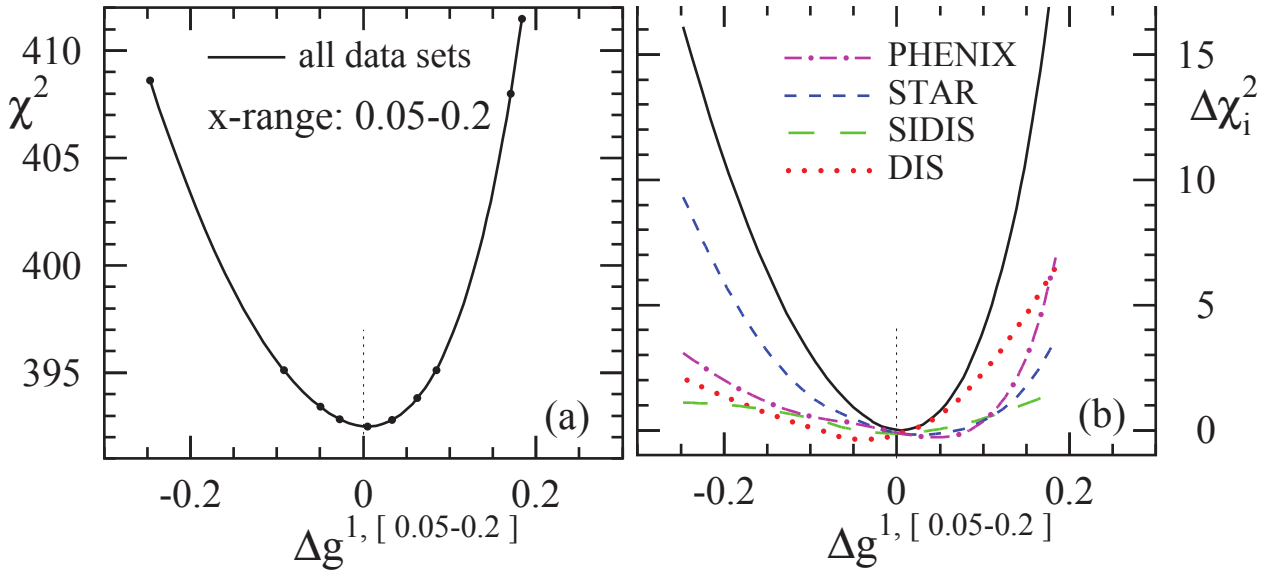

Figure 11.3: The χ^2 profile (left) as a function of the truncated first moment of $\Delta G(x)$, and partial contributions $\Delta\chi^2_i$ (right) of the different data sets. The results are obtained from a global analysis of the inclusive and the semi-inclusive lepton-nucleon spin asymmetries and the polarised proton-proton asymmetries [133].

A direct comparison between the high p_T pairs measurement and results from the polarised proton-proton scattering at RHIC is not possible. This is due to a different experimental procedure. However, a QCD-analysis including not only the inclusive and semi-inclusive DIS measurements, but also different measurements from the RHIC was performed [36, 133] and can be compared to the result of this thesis. This QCD-analysis used the p_T-dependence of the measured asymmetries for the polarised proton-proton scattering to constrain the polarised gluon distribution in the region of x covered by the RHIC data. This range of x almost coincides with the range covered by the COMPASS data. The result of the QCD analysis is presented in Fig. 11.3. It shows the χ^2 distribution for the QCD fit as a function of the value of the truncated first moment of $\Delta G(x)$, $\Delta g^{1,[0.05-0.2]} = \int_{0.05}^{0.2} \Delta G(x,Q^2)dx$, at $Q^2 = 10\,\text{GeV}^2$. It is seen that the polarised proton-proton scattering results favour small values of ΔG in the covered x range. This result is compatible with the measurement presented in this thesis and the other direct measurements of $\Delta G/G$ shown in Fig. 11.2.

The presented results clearly suggest that the value of $\Delta G/G$ in the covered range of x_G is compatible with zero. The precise results from the high p_T analyses of COMPASS as well as recent HERMES result disfavour high values of the first moment of $\Delta G(x)$ unless $\Delta G(x)$ has a node in the measured region [134].

Chapter 12

Summary and outlook

The spin composition of the nucleon is studied in polarised lepton-nucleon scattering, measured by dedicated experiments since the 70-ties. Still the covered kinematical range is small compared to the unpolarised measurements. This limits the precision of polarised parton distribution functions obtained in QCD analyses. While the polarised quark distributions are relatively well constrained in recent QCD-fits, the polarised gluon distribution, and thus the gluon spin contribution to the nucleon spin, remain uncertain.

In this thesis a complementary approach to determine the gluon polarisation in the nucleon is pursued using a direct measurement. It is done my measuring double spin asymmetries of events with high p_T hadron pairs in polarised lepton-nucleon scattering. To access the gluons in the nucleon the photon-gluon fusion process (PGF) is used. In this process, the virtual photon interacts with a gluon from the nucleon creating a quark-antiquark pair. To enrich the analysed data sample with events originating from the PGF process a hadron pair with high transverse momenta in the final state is requested. However, this requirement does not fully suppress leading process (LP) and QCD-Compton (QCDC) events. Such events contribute to the measured asymmetry as a background to the PGF as they do not probe the gluons in the nucleon, but the quarks. A Monte Carlo simulation is used to estimate the fractions of the PGF, LP and QCDC events as well as the parton kinematics in order to determine their contributions to the measured asymmetry.

The analysis presented in this thesis is based on the data taken by the COMPASS experiment at CERN during the years 2002-2004. The polarised lepton-nucleon scattering is studied using the naturally polarised μ^+ muon beam of $160\,\text{GeV}$ energy and the longitudinally polarised ^{6}LiD target. The selected $Q^2 > 1\,\text{GeV}^2$ kinematic region ensures that the perturbative QCD is applicable. For the necessary MC simulations the LEPTO event generator was used.

In this thesis we presented a novel approach to determine the gluon polarisation from deep inelastic scattering of muons on nucleons. The $\Delta G/G$ is extracted using the second order weighted method directly from the counting rate asymmetry with weights based on the Neural Network parametrisation of the parton kinematics and the processes fractions. The proposed approach allows for correct treatment of the background processes as well as increases the statistical sensitivity of the measurement.

In order to extract the required information from the MC simulations it is essential that they reasonably describe the experimental data. A detailed study of the description of the spectrometer by GEANT MC simulation was performed by the author. With gained confidence in the MC model for the apparatus, several LEPTO parameters had to be adjusted to improve the description of the experimental data by the MC simulations. The impact of changes of LEPTO parameters on the extracted gluon polarisation was in-

cluded in the determination of systematic uncertainties. With the best obtained MC settings we estimate that the analysed data sample contains a fraction $R_{PGF} = 0.31$ of PGF events with average analysing power $< a_{LL}^{PGF} >= 0.63 \pm 0.3$.

The result for the gluon polarisation measured by the COMPASS experiment in the years 2002-2004 is

$$\frac{\Delta G}{G} = 0.08 \pm 0.1(stat.) \pm 0.05(syst.)$$

at $< x_G >= 0.083^{+0.052}_{-0.034}$ and $< \mu^2 >= 1.94\,\text{GeV}^2$. Within the present statistical accuracy this value is consistent with zero and consistent with QCD-fits to the present data for the inclusive and the semi-inclusive polarised deep inelastic scattering. Also the two complementary analyses performed by COMPASS, with the high p_T pairs for $Q^2 < 1\,\text{GeV}^2$ and the open charm production, have obtained value of $\Delta G/G$ which are consistent with zero.

The combined analysis of data collected in 2002-2006 years for the high p_T pairs, $Q^2 > 1\,\text{GeV}^2$ channel is ongoing. It is expected that adding additional data and improvements to the events selection will lead to reduction of the statistical uncertainty by factor 2. We expect to present the new result by the end of the 2010.

The result of this work together with current results from other fixed target experiments as well as collider experiments at RHIC indicate that the $\Delta G/G$ is consistent with zero for x_G around 0.1. To further constrain the spin dependant distribution function of gluons a measurement in wider range of x_G is needed. In a near future, the data on polarised proton-proton scattering at RHIC higher energy, $\sqrt{s} = 500\,\text{GeV}$, may further constrain the gluon spin contribution at smaller x_G. An essential increase of accuracy of $\Delta G(x)$ may be achieved with a polarised lepton-nucleon collider, due to significant increase of covered kinematical domain, both in x and Q^2. Currently such project is under consideration in the USA [135].

As the recent measurements indicate that the gluon contribution to the nucleon spin is small it leads to a conclusion that the orbital angular momentum of the partons in the nucleon is probably significant. An experimental evaluation of this quantity would be an important test of the QCD improved Parton Model of the nucleon. An access to the orbital angular momentum of quarks is possible with exclusive processes: Deeply Virtual Compton Scattering (DVCS) and Deeply Virtual Meson Production. Such studies are already pursued at the Jefferson Laboratory and by the HERMES experiment. Recently the COMPASS collaboration has presented a proposal of such measurements at CERN [136] in an extended range of x and Q^2.

In conclusion, the present understanding of the spin structure of the nucleon is far from being complete. With the well established evidence that the quark spins contribute only to about 30% of the nucleon spin, and experimental hints that the gluon spin contribution is probably small, the “Nucleon Spin Crisis” remains unsolved. The new experimental activities planned for a next decade are certainly expected to provide interesting answers.

Appendix A

Tables

A.1 Monte Carlo settings

Table A.1: Versions of the software and the input files used in MC simulations.

	Value[1]
Software versions	CORAL(prod-2005-4-12-slc3), COMGEANT(0-0-7.03.1[2]), ROOT(5.10.00), LEPTO(6.5.1), EXTGEN(9), PHAST(7.054)
Beam file	beam_halo.35513.data
Background file	random/muplus160/2004/fz/random_rich.2004.00.outpipe.fz.1[2]
Solenoid map	smctgt_solenoide.fieldmap
SM1 map	SM1M.map.172.data
SM2 map	SM2.map.4000.data
COMGEANT geometry version	geom_general_072.ffr, geom_muon_2004.00.real.ffr

1) The input files are available at gridka.fzk.de (/grid/fzk.de/compass/compass3/users/conrad/compassusr/compass/COMPASS_FILES).

2) COMGEANT 0-0-7.03 was modified to allow non-binary values in the coincidence matrices, available at gridka.fzk.de (/grid/fzk.de/compass/compass3/users/conrad/compassusr/software/comgeant/0-0-7.03.1).

Table A.2: LEPTO and COMGEANT settings.

LEPTO	Value
LST12 (# of flavours of sea quarks)	3
LST13 (# of flavours in the final state)	4
LST15 (PDF)	20452 (MRST04 LO 3 flavours from LHAPDF library)
Q^2 cut	> 0.9
High p_T sample	
Pre-cuts on two leading hadrons	$p_T > 0.6$ GeV, $\theta < 0.25$
COMPASS fragmentation tuning	
Fragmentation p_T	PARJ21=0.3, PARJ23=0.02, PARJ24=3.5
Fragmentation function parameters	PARJ41=0.6, PARJ42=0.1
Parton shower OFF	
LST8 (Turn off PS)	1
LST20 (Cut-off scheme)	1 (Select JADE cut-off scheme[1])
PARL8	0.0050 (Default JADE cut-off setting)
PARL9	2.0000 (Default JADE cut-off setting)

1) The $z\,\hat{s}$ cutoff scheme causes LEPTO to crash with PS OFF

COMGEANT	Value
Low calorimeter thresholds	HCAL1 $= 5$ GeV, HCAL1 $= 7$ GeV
High calorimeter thresholds	HCAL1 $= 17.5$ GeV, HCAL2 $= 21$ GeV
Coincidence matrices	The matrices include the efficiencies of the Hodoscope detector planes *cf.* Ref. *[137]*

A.2 Event statistics

Table A.3: Number of events contained in the different periods. "mDST" refers to the number of events in the "mini Data Summary Tapes", *i.e.* events with at least one (primary or secondary) vertex. "Selected events" corresponds to the final selected sample. Last column contains the extracted value of $\Delta G/G$. Note that results presented in the Table **are not** corrected for D-wave state admixture in deuteron.

	mDST	Selected events	$\Delta G/G$
02P1C	$117 \cdot 10^6$	6032	-0.203 ± 0.823
02P2A	$151 \cdot 10^6$	8496	-1.065 ± 0.710
02P2D	$135 \cdot 10^6$	8495	0.018 ± 0.733
02P2E	$182 \cdot 10^6$	11679	-0.217 ± 0.626
02P2F	$87 \cdot 10^6$	5792	0.973 ± 0.953
02P2G	$58 \cdot 10^6$	3276	1.500 ± 1.219
02P3G	$106 \cdot 10^6$	5815	0.148 ± 0.953
2002	$836 \cdot 10^6$	49585	-0.064 ± 0.305
03P1A	$163 \cdot 10^6$	17312	-0.028 ± 0.536
03P1B	$136 \cdot 10^6$	14350	1.048 ± 0.557
03P1C	$141 \cdot 10^6$	17995	0.233 ± 0.496
03P1D	$196 \cdot 10^6$	15789	0.871 ± 0.533
03P1E	$213 \cdot 10^6$	30760	-0.108 ± 0.387
03P1F	$192 \cdot 10^6$	24509	-1.008 ± 0.457
03P1I	$196 \cdot 10^6$	22649	0.065 ± 0.459
03P1J	$297 \cdot 10^6$	27579	-0.385 ± 0.439
2003	$1.53 \cdot 10^9$	170943	0.001 ± 0.167
04W22	$402 \cdot 10^6$	32958	0.593 ± 0.354
04W23	$245 \cdot 10^6$	17439	0.519 ± 0.476
04W26	$236 \cdot 10^6$	20850	0.531 ± 0.447
04W27	$136 \cdot 10^6$	12104	0.457 ± 0.592
04W28	$185 \cdot 10^6$	12720	0.006 ± 0.569
04W29	$167 \cdot 10^6$	13091	0.973 ± 0.582
04W30	$225 \cdot 10^6$	19192	0.085 ± 0.461
04W31	$210 \cdot 10^6$	19086	-0.614 ± 0.472
04W32	$306 \cdot 10^6$	27710	-0.288 ± 0.397
04W37	$333 \cdot 10^6$	31525	0.396 ± 0.368
04W38	$349 \cdot 10^6$	44276	-0.253 ± 0.308
04W39	$204 \cdot 10^6$	23784	0.186 ± 0.456
04W40	$151 \cdot 10^6$	11950	-0.559 ± 0.616
2004	$3.15 \cdot 10^9$	286685	0.188 ± 0.105
total	$5.52 \cdot 10^9$	507213	0.077 ± 0.094

Bibliography

[1] M. Breidenbach *et al.* . *Phys. Rev. Lett.* **23**, 935–939 (1969).

[2] M. J. Alguard *et al.* . *Phys. Rev. Lett.* **37**, 1261 (1976).

[3] J. Ashman *et al.* (European Muon Collaboration). *Phys. Lett.* **B206**, 364 (1988).

[4] J. Ashman *et al.* (European Muon Collaboration). *Nucl. Phys.* **B328**, 1 (1989).

[5] B. Adeva *et al.* (Spin Muon Collaboration). *Phys. Rev.* **D58**, 112002 (1998).

[6] K. Abe *et al.* (E143 Collaboration). *Phys. Rev.* **D58**, 112003 (1998).

[7] P. L. Anthony *et al.* (E155 Collaboration). *Phys. Lett.* **B493**, 19–28 (2000).

[8] A. Airapetian *et al.* (HERMES Collaboration). *Phys. Rev.* **D71**(1), 012003 (2005).

[9] V. Y. Alexakhin *et al.* (COMPASS Collaboration). *Phys. Lett.* **B647**, 8–17 (2007).

[10] M. Alekseev *et al.* (COMPASS Collaboration). *Phys. Lett.* **B676**, 31–38 (2009).

[11] E. S. Ageev *et al.* (COMPASS Collaboration). *Phys. Lett.* **B633**, 25–32 (2006).

[12] B. Adeva *et al.* (Spin Muon Collaboration). *Phys. Rev.* **D70**, 012002 (2004).

[13] E. Leader. *Spin in Particle Physics*, volume 15 of *Cambridge Monographs on Particle Physics, Nuclear Physics and Cosmology*. Cambridge University Press, (2001).

[14] F. Halzen and A. D. Martin. *Quarks and leptons: an introductory course in modern particle physics*. John Wiley & Sons, (1984).

[15] D. Griffiths. *Introduction to elementary particles*. Wiley-VCH, (2008).

[16] E. S. Ageev *et al.* (COMPASS Collaboration). *Phys. Lett.* **B647**, 330–340 (2007).

[17] M. G. Alekseev *et al.* (COMPASS Collaboration). *The Spin-dependent Structure Function of the Proton g_1^p and a Test of the Bjorken Sum Rule*. arXiv:hep-ex/1001.4654, (2010). Accepted Phys. Lett. B.

[18] R. P. Feynman. *Phys. Rev. Lett.* **23**(24), 1415–1417 (1969).

[19] J. D. Bjorken and E. A. Paschos. *Phys. Rev.* **185**(5), 1975–1982 (1969).

[20] J. D. Bjorken. *Phys. Rev.* **179**(5), 1547–1553 (1969).

[21] M. Anselmino, A. Efremov, and E. Leader. *Phys. Rep.* **261**(1-2), 1–124 (1995).

[22] S. L. Adler. *Phys. Rev.* **177**(5), 2426–2438 (1969).

[23] R. L. Jaffe. *Phys. Lett.* **B193**(1), 101–104 (1987).

[24] G. Altarelli and G. G. Ross. *Phys. Lett.* **B212**(3), 391–396 (1988).

[25] R. D. Carlitz, J. C. Collins, and A. H. Mueller. *Phys. Lett.* **B214**(2), 229–236 (1988).

[26] E. Leader and D. B. Stamenov. *Phys. Rev.* **D67**(3), 037503 (2003).

[27] C. Amsler *et al.* (Particle Data Group Collaboration). *Phys. Lett.* **B667**, 1 (2008).

[28] J. Kodaira, S. Matsuda, T. Muta, T. Uematsu, and K. Sasaki. *Phys. Rev.* **20**(3), 627–629 (1979).

[29] J. Kodaira, S. Matsuda, K. Sasaki, and T. Uematsu. *Nucl. Phys.* **B159**(1-2), 99–124 (1979).

[30] J. Kodaira. *Nucl. Phys.* **B165**(1), 129–140 (1980).

[31] W. A. Bardeen, A. J. Buras, D. W. Duke, and T. Muta. *Phys. Rev.* **D18**(11), 3998–4017 (1978).

[32] S. D. Bass. *The Spin structure of the proton*. World Scientific, (2007).

[33] T. D. Averett. *AIP Conf. Proc.* **675**, 88–97 (2003).

[34] M. Hirai, S. Kumano, and N. Saito (Asymmetry Analysis Collaboration). *Phys. Rev.* **D69**(5), 054021 (2004).

[35] E. Leader, A. V. Sidorov, and D. B. Stamenov. *Phys. Rev.* **D73**(3), 034023 (2006).

[36] D. de Florian, R. Sassot, M. Stratmann, and W. Vogelsang. *Phys. Rev.* **D80**(3), 034030 (2009).

[37] J. D. Bjorken. *Phys. Rev.* **148**(4), 1467–1478 (1966).

[38] J. D. Bjorken. *Phys. Rev.* **D1**(5), 1376–1379 (1970).

[39] Y. L. Dokshitzer. *Sov. Phys. JETP* **46**, 641–653 (1977).

[40] V. N. Gribov and L. N. Lipatov. *Sov. J. Nucl. Phys.* **15**, 438–450 (1972).

[41] G. Altarelli and G. Parisi. *Nucl. Phys.* **B126**(2), 298–318 (1977).

[42] R. Mertig and W. L. van Neerven. *Z. Phys.* **C70**(4), 637–653 (1996).

[43] W. Vogelsang. *Phys. Rev.* **D54**(3), 2023–2029 (1996).

[44] W. Vogelsang. *Nucl. Phys.* **B475**(1-2), 47–72 (1996).

[45] R. D. Ball, S. Forte, and G. Ridolfi. *Phys. Lett.* **B378**(1-4), 255–266 (1996).

[46] M. Alekseev *et al.* (COMPASS Collaboration). *Phys. Lett.* **B680**(3), 217–224 (2009).

[47] D. de Florian, R. Sassot, and M. Stratmann. *Phys. Rev.* **D75**(11), 114010 (2007).

[48] G. Brona. *Hadron production and polarisation of gluons in the nucleon in the $\mu \to N$ interactions in the COMPASS experiment at CERN*. PhD thesis, University of Warsaw, (2007). `http://wwwcompass.cern.ch/compass/publications/theses/2007_phd_brona.ps.gz`.

[49] S. Koblitz. *Determination of the Gluon Polarisation from Open Charm Production at COMPASS*. PhD thesis, University Mainz, (2008). `http://wwwcompass.cern.ch/compass/publications/theses/2008_phd_koblitz.pdf`.

[50] C. Franco *et al.* . *Measurement of $\Delta g/g$ via Open Charm using [2002, 2007] data*. COMPASS release note, April (2010).

[51] C. Franco. *New COMPASS results on the gluon polarisation using D0 production asymmetries*. In *Proceedings of XVIII International Workshop on Deep-Inelastic Scattering and Related Subjects (DIS 2010)*, (2010).

[52] A. A. Sokolov and I. M. Ternov. *Sov. Phys. Dokl.* **8**, 1203–1205 (1964).

[53] K. Ackerstaff *et al.* (HERMES Collaboration). *Nucl. Instrum. Meth.* **A417**, 230–265 (1998).

[54] T. Sjostrand, S. Mrenna, and P. Skands. *J. High Energy Phys.* **05**, 026 (2006).

[55] G. Ingelman, A. Edin, and J. Rathsman. *Comput. Phys. Commun.* **101**, 108–134 (1997).

[56] A. Airapetian *et al.* (HERMES Collaboration). *Phys. Rev. Lett.* **84**, 2584–2588 (2000).

[57] P. Leibing. *Can the gluon polarisation in the nucleon be extracted from HERMES data on single high-p_T hadrons?* PhD thesis, Hamburg University, (2004). `http://www-hermes.desy.de/notes/pub/04-LIB/pattythesis.ps.gz`.

[58] P. Liebing (HERMES Collaboration). *AIP Conf. Proc.* **915**, 331–334 (2007).

[59] D. Adams *et al.* (Spin Muon Collaboration). *Phys. Rev.* **D56**, 5330–5358 (1997).

[60] C. Bourrely, J. Soffer, F. M. Renard, and P. Taxil. *Phys. Rep.* **177**, 319 (1989).

[61] M. Gluck, E. Reya, M. Stratmann, and W. Vogelsang. *Phys. Rev.* **D63**, 094005 (2001).

[62] M. Gluck, E. Reya, and A. Vogt. *Eur. Phys. J.* **C5**, 461–470 (1998).

[63] M. Gluck, E. Reya, and I. Schienbein. *Phys. Rev.* **D60**, 054019 (1999).

[64] M. Gluck, E. Reya, and C. Sieg. *Eur. Phys. J.* **C20**, 271–281 (2001).

[65] C. Bernet *et al.* . *Measurement of $\Delta G/G$ in the production of high p_T hadron pairs at low Q^2 (2004 data)*. COMPASS note 2006-8, (2006).

[66] K. H. Ackermann *et al.* (STAR Collaboration). *Nucl. Instrum. Meth.* **A499**, 624–632 (2003).

[67] K. Adcox *et al.* (PHENIX Collaboration). *Nucl. Instrum. Meth.* **A499**, 469–479 (2003).

[68] A. Adare *et al.* (PHENIX Collaboration). *Phys. Rev. Lett.* **103**, 012003 (2009).

[69] B. I. Abelev *et al.* (STAR Collaboration). *Phys. Rev. Lett.* **100**, 232003 (2008).

[70] P. Abbon *et al.* (COMPASS Collaboration). *Nucl. Instrum. Meth.* **A577**, 455–518 (2007).

[71] G. Baum, J. Kyynäräinen, and A. Tripet (COMPASS Collaboration). *COMPASS: a proposal for a common muon and proton apparatus for structure and spectroscopy*. Technical Report CERN-SPSLC-96-14. SPSLC-P-297, CERN, (1996). http://cdsweb.cern.ch/record/298433?ln=en.

[72] G. Baum, J. Kyynäräinen, and A. Tripet (COMPASS Collaboration). *COMPASS: Common Muon and Proton Apparatus for Structure and Spectroscopy; Add. 1*. Technical Report CERN-SPSLC-96-30. SPSLC-P-297-Add-1, CERN, (1996). http://cdsweb.cern.ch/record/304136?ln=en.

[73] N. Doble, L. Gatignon, G. von Holtey, and F. Novoskoltsev. *Nucl. Instrum. Meth.* **343**(2-3), 351–362 (1994).

[74] B. Adeva *et al.* (Spin Muon Collaboration). *Nucl. Instrum. Meth.* **A343**(2-3), 363–373 (1994).

[75] D. Adams *et al.* (Spin Muon Collaboration). *Nucl. Instrum. Meth.* **A443**(1), 1–19 (2000).

[76] O. A. Rondon-Aramayo. *Phys. Rev.* **C60**, 035201 (1999).

[77] A. Abragam and M. GoldMan. *Nuclear Magnetism: Order and Disorder*. Clarendon Press, Oxford, (1982).

[78] G. Mallot. *The Spin Structure of the Nucleon from the SMC Experiments*. Habilitation thesis, Fachbereich Physik der Johannes Gutenberg-Universität Mainz, (1993). http://wwwcompass.cern.ch/compass/publications/theses/1996_hab_mallot.pdf.

[79] C. Bernet *et al.* . *Nucl. Instrum. Meth.* **A550**, 217–240 (2005).

[80] W. Carena *et al.* . *ALICE DAQ and ECS User's Guide*. Technical Report ALICE-INT-2005-015, CERN, (2005). https://edms.cern.ch/document/616039.

[81] T. Nagel. *Cinderella: an Online Filter for the COMPASS experiment*. Master's thesis, Technische Universität München, (2005). http://wwwcompass.cern.ch/compass/publications/theses/2005_dpl_nagel.pdf.

[82] C. Bernet. *Caractérisation des Mircomégas et mesure de la polarisation des gluons sur COMPASS*. PhD thesis, Université Paris 7 - Denis Diderot, (2005). http://wwwcompass.cern.ch/compass/publications/theses/2005_phd_bernet.ps.gz.

[83] *DCS*. http://compass-dcs.web.cern.ch/compass-dcs/scripts/welcome.asp.

[84] *CORAL*. http://coral.web.cern.ch/coral.

[85] *PHAST*. http://ges.home.cern.ch/ges/phast/index.html.

[86] *POLGRID*. http://www.polgrid.pl/.

[87] M. von Hodenberg. *A first Reconstruction of COMPASS Data*. Master's thesis, Albert-Ludwigs-Universität Freiburg, (2002). http://hpfr02.physik.uni-freiburg.de/arbeiten/diplomarbeiten/vonHodenberg.ps.gz.

[88] M. von Hodenberg. *First measurement of the gluon polarisation in the nucleon using D mesons at COMPASS*. PhD thesis, Albert-Ludwigs-Universität Freiburg, (2005). `http://wwwcompass.cern.ch/compass/publications/theses/2005_phd_von_hodenberg.ps.gz`.

[89] R. Joosten. *Performance of the BMS upgrade in 2003. Plans for the 2004 run*. Talk given at COMPASS Analysis Meeting, December (2003).

[90] L. Smith. *A tutorial on Principal Components Analysis*. `http://www.cs.otago.ac.nz/cosc453/student_tutorials/principal_components.pdf`, (2002).

[91] J. Shlens. *A Tutorial on Principal Component Analysis*. `http://www.snl.salk.edu/~shlens/pca.pdf`, (2005).

[92] M. O'Connel. *Economical function fitting for momentum determination*. Technical Report rl-73-081, Rutherford Laboratory, (1973).

[93] M. Hansroul *et al.* . *The application of multi-dimensional analysis techniques to the processing of event data from large spectrometers*. Technical Report dd-73-31, CERN, (1973). `http://cdsweb.cern.ch/record/1050923`.

[94] Y. Bedfer. *COMPASS's track reconstruction algorithm*. COMPASS Note 2004-1, (2004).

[95] H. Pereira and J.-M. Le Goff. *COMPASS spectrometer alignment*. COMPASS Note 2003-4, (2004).

[96] M. Stolarski. *Spin structure of the nucleon at low x and low Q^2 in the COMPASS experiment at CERN*. PhD thesis, University of Warsaw, (2005). `http://wwwcompass.cern.ch/compass/publications/theses/2006_phd_stolarski.pdf`.

[97] V. Blobel and C. Kleinwort. *A new method for the high-precision alignment of track detectors*. arXiv:hep-ex/0208021, (2002).

[98] R. Brun and F. Rademakers. *ROOT – An Object Oriented Data Analysis Framework*. In *Proceedings AIHENP'96 Workshop*, volume A389 of *Nucl. Instrum. Meth.*, 81–86, (1997). `http://root.cern.ch`.

[99] R. Lowry. *Concepts and Applications of Inferential Statistics*. (1999). `http://faculty.vassar.edu/lowry/webtext.html`.

[100] S. Procureur. *Détermination de la polarisation des gluons dans le nucléon par la production de hadrons a grande impulsion transverse a COMPASS,*. PhD thesis, Universite Paris XI, U.F.R. Scientifique d'Orsay, (2006). `http://wwwcompass.cern.ch/compass/publications/theses/2006_phd_procureur.pdf`.

[101] A. Bravar, D. von Harrach, and A. Kotzinian. *Phys. Lett.* **B421**, 349–359 (1998).

[102] K. Kurek. *Status of high-pT analysis*. Talk given at COMPASS Analysis Meeting, Aug (2008).

[103] K. Kowalik. *Selection of the photon gluon fusion process by requiring high-p_T hadrons in muon nucleon scattering*. PhD thesis, Soltan Institute for Nuclear Studies, (2004).

[104] S. Hedicke. *Determination of the gluon polarisation in the nucleon using hadron pairs with high transverse momentum at COMPASS*. PhD thesis, Albert-Ludwigs-Universität Freiburg, (2005). `http://wwwcompass.cern.ch/compass/publications/theses/2005_phd_hedicke.pdf`.

[105] K. Gustafsson. *Computation of the Dilution Factor for the Year 2002 COMPASS Data*. COMPASS Note 2003-3, (2003).

[106] A. A. Akhundov, D. Y. Bardin, L. Kalinovskaya, and T. Riemann. *Fortsch. Phys.* **44**, 373–482 (1996).

[107] J. Kiryluk. *Spin Asymmetries A_1 and Structure Functions g_1 of the Proton and the Deuteron at Low x and Low Q^2 from Polarized High Energy Muon Scattering*. PhD thesis, University of Warsaw, (2000).

[108] R. Windmolders. *An introduction to the evaluation of spin structure functions from experimental data*. arXiv:hep-ph/0211350, (2002).

[109] J.-M. Le Goff. *Asymmetry extraction*. COMPASS note 2004-3, (2004).

[110] J. Pretz. *A New Method for Asymmetry Extraction*. COMPASS note 2004-11, (2004).

[111] J.-M. Le Goff and J. Pretz. *Statistical errors and correlations for semi-inclusive asymmetries*. COMPASS note 2004-4, (2004).

[112] M. Arneodo *et al.* (New Muon Collaboration). *Nucl. Phys.* **B483**, 3–43 (1997).

[113] A. D. Martin, W. J. Stirling, and R. S. Thorne. *Phys. Lett.* **B636**, 259–264 (2006).

[114] H. L. Lai *et al.* (CTEQ Collaboration). *Eur. Phys. J.* **C12**, 375–392 (2000).

[115] T. Sjostrand. *Comput. Phys. Commun.* **82**, 74–90 (1994).

[116] T. Sjostrand. *Pythia 5.7 and jetset 7.4 physics and manual*. Technical Report CERN-TH-7112/93, CERN, (1994). `http://cdsweb.cern.ch/record/287231/`.

[117] A. Hillenbrand (HERMES Collaboration). *Tuning of the Lund model for fragmentation functions and purities*. In *11th International Workshop on Deep Inelastic Scattering (DIS 2003)*, (2003).

[118] M. Bengtsson and T. Sjostrand. *Z. Phys.* **C37**, 465 (1988).

[119] *COMGEANT*. `http://valexakh.web.cern.ch/valexakh/wwwcomg/index.html`.

[120] R. Brun *et al.* . *GEANT Detector description and simulation tool: CERN Program Library Long Writeup*. Technical Report W5013, CERN, (1994). `http://consult.cern.ch/writeups/geant`.

[121] M. Leshno, V. Y. Lin, A. Pinkus, and S. Schocken. *Neural Networks* **6**(6), 861–867 (1993).

[122] W. S. Mc Culloch. *Bulletin of Mathematical Biophysics* **5**, 115–133 (1943).

[123] D. Rutkowska, M. Piliński, and L. Rutkowski. *Sieci neuronowe, algorytmy genetyczne i systemy rozmyte*. Wydawnictwo Naukowe PWN, (1997).

[124] R. Sulej, K. Zaremba, K. Kurek, and E. Rondio. *Measur. Sci. Tech.* **18**, 2486–2490 (2007). `http://www.ire.pw.edu.pl/~rsulej/NetMaker`.

[125] A. Bravar, K. Kurek, and R. Windmolders. *Comput. Phys. Commun.* **105**, 42–61 (1997).

[126] C. Bernet *et al.* . *Measurement of high p_T asymmetries on 2002 data.* COMPASS note 2004-7, (2004).

[127] K. Pearson. *Biometrika* **5**, 181–183 (1906).

[128] V. Y. Alexakhin *et al.* (COMPASS Collaboration). *Eur. Phys. J.* **C52**, 255–265 (2007).

[129] B. Badelek, D. Y. Bardin, K. Kurek, and C. Scholz. *Z. Phys.* **C66**, 591–600 (1995).

[130] H. Jung. *Comp. Phys. Commun.* **86**, 147–161 (1995).

[131] M. R. Whalley, D. Bourilkov, and R. C. Group. *The Les Houches Accord PDFs (LHAPDF) and Lhaglue*. In *Proceedings of HERA and the LHC: A Workshop on the Implications of HERA and LHC Physics*, (2005). `http://hepforge.cedar.ac.uk/lhapdf`.

[132] M. Gluck, E. Reya, and M. Stratmann. *Phys. Rev.* **D54**, 5515–5522 (1996).

[133] D. de Florian, R. Sassot, M. Stratmann, and W. Vogelsang. *Phys. Rev. Lett.* **101**, 072001 (2008).

[134] T. Gehrmann and W. J. Stirling. *Phys. Rev.* **D53**, 6100–6109 (1996).

[135] C. Aidala *et al.* . *A High Luminosity, High Energy Electron-Ion-Collider*. `http://web.mit.edu/eicc/DOCUMENTS/EIC_LRP-20070424.pdf`. (The EIC Working Group).

[136] The COMPASS Collaboration. *COMPASS-II Proposal*. Technical Report SPSC-2010-014, CERN, (2010). `http://cdsweb.cern.ch/record/1265628?ln=en`.

[137] K. Klimaszewski. *Trigger Hodoscope Efficiencies in 2004*. Talk given at COMPASS Analysis Meeting, Jan (2008).

Acknowledgements

I would like to thank my supervisors Jan Paweł Nassalski and Andrzej Sandacz for the support they offered, for motivating me to go further when it seemed impossible and for countless and inspiring discussions about experimental physics. I am thankful to Professor Nassalski for introducing me to the fascinating world of high energy physics and for the possibility to work at the CERN laboratory. I am in great debt to Krzysztof Kurek and Marcin Stolarski for their great patience and I would like to thank them for many interesting discussions and comments on experimental and theoretical physics as well as on statistics. I will hold fond memories of those disputes.

My thanks go to Luis Silva from LIP Lisbon, my cross-checker, for his swift help and constructive criticism. I am grateful to my colleagues from the Warsaw COMPASS group for a friendly atmosphere at work and a helpful hand when it was needed. I would also like to thank all my COMPASS colleagues - it was a real pleasure to be a part of this wonderful community. Last but not least, I would like to thank: Barbara Badełek, Yann Bedfer, Sergei Gerassimov, Rainer Joosten and Jean-Francois Rajotte.

This work has been partially supported by Polish Ministry of Science and Higher Education grant No. NN 202 259534 and by KBN grant No. 621/E-78/SPUB-M/CERN/P-03/DZ/298/2000, No. 621/E-78/SPB/CERN/P-03/DWM 576/2003-2006.

I wish to thank my wife Kasia for her patience and support throughout my studies and most especially during writing this thesis. Without her help I would have never been able to finish this work. Thank you my darling.